THE UNIVERSITY OF WARWICK

University of Warwick institutional repository: http://go.warwick.ac.uk/wrap

A Thesis Submitted for the Degree of PhD at the University of Warwick

http://go.warwick.ac.uk/wrap/55048

This thesis is made available online and is protected by original copyright.

Please scroll down to view the document itself.

Please refer to the repository record for this item for information to help you to cite it. Our policy information is available from the repository home page.

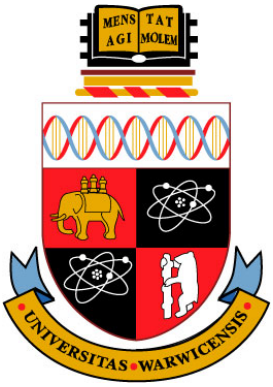

Advanced Electronics for Fourier-Transform Ion Cyclotron Resonance Mass Spectrometry

by

Tzu-Yung Lin

A thesis submitted in partial fulfilment of the requirements for the degree of Doctor of Philosophy in Engineering

School of Engineering

THE UNIVERSITY OF WARWICK

November 2012

For my grandpa, Mong.

Acknowledgements

There are many people who have helped me along the way toward the completion of this work. Especially, I would like to thank my supervisors, Prof. Peter B. O'Connor (Department of Chemistry) and Prof. Roger J. Green (School of Engineering), for their patient guidance, support, and their valuable time. They offered a unique opportunity for me to look at the mass spectrometry instrumentation problems from an engineering point of view. Furthermore, the relocation with Prof. O'Connor extends my experience to the magnificent cultures of the British Isles and continental Europe.

Meanwhile, Prof. Ronald W. Knepper (Department of Electrical and Computer Engineering) and Prof. Catherine E. Costello (Cardiovascular Proteomics Center) from Boston University, Massachusetts, USA, provided useful suggestions and support, especially during the time when I was conducting research within Boston University. Useful discussions from other Boston University members, such as Dr. Konstantine Aizikov, Dr. Raman Mathur, Dr. Cheng Lin, Dr. Weidong Cui, Dr. Chunxiang Yao, Dr. Xiaojuan Li, and Dr. Nadezda Sargaeva

are also acknowledged.

My appreciation is also extended to staff and student members here at the University of Warwick, Coventry, UK. Dr. David P. A. Kilgour helped with the generation of the data used to plot the Mathieu equation stability diagram, and shared much knowledge about quadrupole/ion trap mass spectrometry. Dr. Mark P. Barrow and Dr. Alex W. Colburn provided useful information and suggestions about the research field of mass spectrometry and the related electronics. Huilin Li helped with the interpretation of the IR-ECD spectra, and allowed me to participate in and to learn from some of her proteomics research projects. Rod Wesson kindly suggested some design ideas for the quadrupole power supply. He also helped with some of the circuit drawings and the making of the power supply printed circuit boards. Ian Griffith helped with the manufacturing of the preamplifier boards. Robert Day provided insight for the preamplifier stabilization. There were also many helpful discussions between the members of the Ion Cyclotron Resonance Laboratory. They are Rebecca H. Wills, Yulin Qi, Pilar Perez Hurtado, Andrea F. Lopez-Clavijo, Andrew Soulby, Juan Wei, and Samantha L. Benson.

Some of the conversations during the conferences were inspiring too. Especially, I would like to thank Prof. Ron M. A. Heeren, Prof. I. Jon Amster and Dr. Don Rempel for their helpful discussions in the BMSS (British Mass Spectrometry Society) 3-Day Meeting, the EFTMS (European Fourier Transform Mass Spectrometry) Conference, and the ASMS (American Society for Mass Spectrometry)

Conference on Mass Spectrometry and Allied Topics.

Finally, I'd like to emphasize on my special thanks to my family and my friends, especially my grandparents, my parents, my brothers, and Joanna, with their great support throughout my PhD experience. The financial support from Department of Chemistry, Warwick Centre for Analytical Science (EPSRC (Engineering and Physical Sciences Research Council): EP/F034210/1), School of Engineering, and NIH (National Institutes of Health) (NIH/NCRR-P41 RR10888; NIH/NIGMS-R01GM078293) are also gratefully appreciated.

Abstract

With the development of mass spectrometry (MS) instruments starting in the late 19th century, more and more research emphasis has been put on MS related subjects, especially the instrumentation and its applications. Instrumentation research has led modern mass spectrometers into a new era where the MS performance, such as resolving power and mass accuracy, is close to its theoretical limit. Such advanced performance releases more opportunities for scientists to conduct analytical research that could not be performed before.

This thesis reviews general MS history and some of the important milestones, followed by introductions to ion cyclotron resonance (ICR) technique and quadrupole operation. Existing electronic designs, such as Fourier-transform ion cyclotron resonance (FT-ICR) preamplifiers (for ion signal detection) and radio-frequency (RF) oscillators (for ion transportation/filtering) are reviewed. Then the potential scope for improvement is discussed.

Two new FT-ICR preamplifiers are reported; both preamplifiers operate at room temperature. The first preamplifier uses an operational amplifier (op amp)

in a transimpedance configuration. When a 18-kΩ feedback resistor is used, this preamplifier delivers a transimpedance of about 85 dBΩ, and an input current noise spectral density of around 1 pA/$\sqrt{\text{Hz}}$. The total power consumption of this circuit is around 310 mW when tested on the bench. This preamplifier has a bandwidth of ∼3 kHz to 10 MHz, which corresponds to the mass-to-charge ratio, *m/z*, of approximately 18 to 61k at 12 T for FT-ICR MS. The transimpedance and the bandwidth can be adjusted by replacing passive components such as the feedback resistor and capacitor. The feedback and bandwidth limitation of the circuit is also discussed. When using an 0402 type surface mount resistor, the maximum possible transimpedance, without sacrificing its bandwidth, is approximated to 5.3 MΩ. Under this condition, the preamplifier is estimated to be able to detect ∼110 charges.

The second preamplifier employs a single-transistor design using a different feedback arrangement, a T-shaped feedback network. Such a feedback system allows ∼100-fold less feedback resistance at a given transimpedance, hence preserving bandwidth, which is beneficial to applications demanding high gain. The single-transistor preamplifier yields a low power consumption of ∼5.7 mW, and a transimpedance of 80 dBΩ in the frequency range between 1 kHz and 1 MHz (*m/z* of around 180 to 180k for a 12-T FT-ICR system). In trading noise performance for higher transimpedance, an alternative preamplifier design has also been presented with a transimpedance of 120 dBΩ in the same frequency range.

The previously reported room-temperature FT-ICR preamplifier had a volt-

age gain of about 25, a bandwidth of around 1 MHz when bench tested, and a voltage noise spectral density of $\sim$7.4 nV/$\sqrt{\text{Hz}}$. The bandwidth performance when connecting this preamplifier to an ICR cell has not been reported. However, from the transimpedance theory, the transimpedance preamplifiers reported in this work will have a bandwidth wider by a factor of the open-loop gain of the amplifier.

In a separate development, an oscillator is proposed as a power supply for a quadrupole mass filter in a mass spectrometer system. It targets a stabilized output frequency, and a feedback control for output amplitude stabilization. The newly designed circuit has a very stable output frequency at 1 MHz, with a frequency tolerance of 15 ppm specified by the crystal oscillator datasheet. Within this circuit, an automatic gain control (AGC) unit is built for output amplitude stabilisation. A new transformer design is also proposed. The dimension of the quadrupole being used as a mass filter will be determined in the future. This circuit (in particular the transformer and the quadrupole connection/mounting device) will be finalised after the design of the quadrupole.

Finally, this thesis concludes with a discussion between the gain and the noise performance of an FT-ICR preamplifier. A brief analysis about the correlation between the gain, cyclotron frequency, and input capacitance is performed. Future work is also suggested for extending this research.

List of Awards, Publications, & Presentations

Awards

Thales Sponsorship for ICTON 2012 for Joint Best Research Student Paper from the University of Warwick, July 2012.

School of Engineering Travel Bursary, University of Warwick, February 2012.

BMSS Travel Grants (twice), British Mass Spectrometry Society,
August 2011, & February 2012.

Patent

Tzu-Yung Lin, Roger J. Green, and Peter B. O'Connor. Transimpedance amplifier. University of Warwick. UK Patent Application GB1205775.8, 30 March 2012.

Journal/Conference Papers

Tzu-Yung Lin, Roger J. Green, and Peter B. O'Connor. A low noise single-transistor transimpedance preamplifier for Fourier-transform mass spectrometry

using a T feedback network. *Review of Scientific Instruments*. 83(9):094102, 2012.

Tzu-Yung Lin, Roger J. Green, and Peter B. O'Connor. Use of optical receiver circuit design techniques in a transimpedance preamplifier for high performance mass spectrometry. In *14th International Conference on Transparent Optical Networks (ICTON)*, pages 1–4. Coventry, UK, 2–5 July 2012.

Tzu-Yung Lin, Roger J. Green, and Peter B. O'Connor. A gain and bandwidth enhanced transimpedance preamplifier for Fourier-transform ion cyclotron resonance mass spectrometry. *Review of Scientific Instruments*, 82(12):124101, 2011.

Huilin Li, **Tzu-Yung Lin**, Steve L. Van Orden, Yao Zhao, Mark P. Barrow, Ana M. Pizarro, Yulin Qi, Peter J. Sadler, and Peter B. O'Connor. Use of top-down and bottom-up Fourier transform ion cyclotron resonance mass spectrometry for mapping calmodulin sites modified by platinum anticancer drugs. *Analytical Chemistry*, 83(24):9507–9515, 2011.

Huilin Li, Yao Zhao, Hazel I. A. Phillips, Yulin Qi, **Tzu-Yung Lin**, Peter J. Sadler, and Peter B. O'Connor. Mass spectrometry evidence for cisplatin as a protein cross-linking reagent. *Analytical Chemistry*, 83(13):5369–5376, 2011.

Konstantin Aizikov, Donald F. Smith, David A. Chargin, Sergei Ivanov, **Tzu-Yung Lin**, Ron M. A. Heeren, and Peter B. O'Connor. Vacuum compatible sample positioning device for matrix assisted laser desorption/ionization Fourier transform ion cyclotron resonance mass spectrometry imaging. *Review of Scientific Instruments*, 82(5):054102, 2011.

Selected Oral Presentations

Tzu-Yung Lin, Roger J. Green, and Peter B. O'Connor. Novel Electronics for Fourier-Transform Ion Cyclotron Resonance Mass Spectrometry Mass Spectrometry Group, Max-Planck-Institut für Kohlenforschung Mülheim, Germany, 4 October 2012.

Tzu-Yung Lin, Roger J. Green, and Peter B. O'Connor. An improved low-noise preamplifier design for Fourier-transform ion cyclotron resonance mass spectrometry. Environmental Molecular Sciences Laboratory, Pacific Northwest National Laboratory. Richland, WA, USA, 5 September 2012.

Tzu-Yung Lin, Roger J. Green, and Peter B. O'Connor. Advanced front-end electronics for Fourier-transform ion cyclotron resonance mass spectrometry. Ion Cyclotron Resonance Program, National High Magnetic Field Laboratory. Tallahassee, FL, USA, 27 August 2012.

Tzu-Yung Lin, Roger J. Green, and Peter B. O'Connor. Low noise front-end electronics for Fourier-transform ion cyclotron resonance mass spectrometry. In *Department of Chemistry Postgraduate Research Symposium*. University of Warwick. Coventry, UK, 30 May 2012.

Selected Poster Presentations

Tzu-Yung Lin, Roger J. Green, and Peter B. O'Connor. An improved low-noise preamplifier design for Fourier-transform ion cyclotron resonance mass spectrometry. In *60th ASMS Conference on Mass Spectrometry and Allied Topics*. Vancouver, BC, Canada, 20–24 May 2012.

Tzu-Yung Lin, Roger J. Green, and Peter B. O'Connor. Advanced front-end electronics for Fourier-transform ion cyclotron resonance mass spectrometry. In *10th European Fourier Transform Mass Spectrometry Conference*. Coventry, UK, 1–5 April 2012.

Tzu-Yung Lin, Roger J. Green, David P. A. Kilgour, and Peter B. O'Connor. Circuit design of a high power rf oscillator for multipole ion guide mass filtering. In *32nd BMSS 3-Day Meeting*. Cardiff, UK, 11–14 September 2011.

Tzu-Yung Lin, Roger J. Green, and Peter B. O'Connor. A new preamplifier design for Fourier-transform ion cyclotron resonance mass spectrometry. In *59th ASMS Conference on Mass Spectrometry and Allied Topics*. Denver, CO, USA, 5–9 June 2011.

Tzu-Yung Lin, Raman Mathur, Cheng Lin, Konstantin Aizikov, Ronald W. Knepper, and Peter B. O'Connor. An amplitude and frequency stabilized high power oscillator for mass filtering and multipole ion guides. In *57th ASMS Conference on Mass Spectrometry and Allied Topics*. Philadelphia, PA, USA, 31 May–4 June 2009.

Konstantin Aizikov, Jason J. Cournoyer, Cheng Lin, **Tzu-Yung Lin**, Nadezda P. Sargaeva, and Peter B. O'connor. Experimental evidence of ion cyclotron resonance frequency modulations induced by inhomogeneities of the trapping electric field. In *56th ASMS Conference on Mass Spectrometry and Allied Topics*. Denver, CO, USA, 1–5 June 2008.

Contents

Acknowledgements **iii**

Abstract **vi**

List of Awards, Publications, & Presentations **ix**

List of Tables **xvii**

List of Figures **xviii**

List of Abbreviations **xxiii**

1 Introduction **1**

1.1 FT-ICR Preamplifier Problems to Be Solved 2

1.2 Quadrupole Power Supply Problems in Mass Filtering 3

1.3 Thesis Outline 4

2 Fourier-Transform Ion Cyclotron Resonance Mass Spectrometry **8**

2.1 Introduction to Mass Spectrometry 9

2.1.1 Brief History & Milestones 9

2.1.2 Mass Spectrometry Composition 14

2.2 Ion Cyclotron Resonance Technique 16

2.2.1 ICR Cell Operation 18

2.2.2 In-Cell Ion Motion 18

2.3 Signal Processing 22

2.3.1 Ion Detector 22

2.3.2 Data System 25

2.4 Advantages of FT-ICR MS . . . 25
2.4.1 Resolving Power . . . 27
2.4.2 Mass Accuracy . . . 30
2.4.3 Flexibility . . . 30
2.5 Front-End Electronics . . . 33
2.5.1 Signal & Gain . . . 34
2.5.2 Amplifier Noise . . . 37
2.5.3 Existing FT-ICR Preamplifier Designs . . . 40
2.6 Conclusion . . . 46

3 Quadrupole Ion Guide & Mass Filter 48
3.1 Introduction . . . 48
3.2 Theory of the Quadrupole Operation . . . 51
3.2.1 Quadrupolar Potential . . . 51
3.2.2 Mathieu Equation . . . 52
3.2.3 Stability Diagram . . . 53
3.3 Mass Filter . . . 55
3.4 Existing Power Supply Designs . . . 57
3.5 Quadrupole Power Supply Problems in Mass Filtering . . . 65
3.6 Conclusion . . . 68

4 Test Equipment & Software Programs 70
4.1 Introduction . . . 70
4.2 NI PXI Platform . . . 71
4.3 NI LabVIEW . . . 73
4.3.1 I-V Characteristics . . . 73
4.3.2 AC Analysis . . . 74
4.4 Noise Performance . . . 80
4.5 Other Software/Hardware Used . . . 81
4.6 Conclusion . . . 82

5 Transimpedance Preamplifier Using an Operational Amplifier 83
5.1 Introduction . . . 84
5.2 Transimpedance Amplifier . . . 86
5.2.1 Bandwidth Extension . . . 86
5.2.2 Cyclotron Frequency Correlation . . . 89
5.3 Transimpedance Preamplifier Circuit Design . . . 92

5.3.1 Main Stage . . . 95
5.3.2 Input Stage . . . 97
5.3.3 Printed Circuit Board . . . 98
5.4 Computer Simulation . . . 98
5.5 Transimpedance Preamplifier Testing Results . . . 100
5.5.1 Frequency Response . . . 100
5.5.2 Noise Performance . . . 104
5.6 Discussions . . . 105
5.6.1 Bandwidth & Feedback Impedance . . . 105
5.6.2 Noise & Feedback Impedance . . . 106
5.7 Conclusion . . . 107

6 Single-Transistor Transimpedance Preamplifier Using a T Feedback Network 109
6.1 Introduction . . . 110
6.2 Transimpedance Amplifier Transfer Function . . . 111
6.2.1 Single-Resistor Feedback . . . 111
6.2.2 T Feedback Network . . . 114
6.3 Single-Transistor Preamplifier Circuit Design . . . 116
6.3.1 Common-Source Amplifier . . . 116
6.3.2 Feedback Loop Configuration . . . 121
6.3.3 Printed Circuit Board . . . 125
6.4 Circuit Testing . . . 126
6.5 Results & Discussions . . . 127
6.6 Conclusion . . . 132

7 Radio-Frequency Oscillator for a Quadrupole Mass Filter 135
7.1 Introduction . . . 136
7.1.1 Component Selection . . . 137
7.1.2 Circuit Testing . . . 138
7.2 RF Oscillator Design . . . 139
7.2.1 Crystal Oscillator . . . 139
7.2.2 Bandpass Filter . . . 142
7.2.3 Gain Control Scheme . . . 142
7.2.4 RF Oscillator Printed Circuit Board . . . 144
7.2.5 Testing Results . . . 145

7.3 Precision Rectifier Design 149
7.3.1 Precision Rectifier Printed Circuit Board 151
7.4 Power Amplifier Design 152
7.4.1 Power Amplifier Board 154
7.5 Transformer 155
7.5.1 Testing Results (Power Amplifier & Transformer) 157
7.5.2 Future Transformer Modification 159
7.6 Conclusion & Future Work 160

8 Conclusion **162**
8.1 FT-ICR Preamplifier 163
8.1.1 Preamplifier Using an Operational Amplifier 163
8.1.2 Single-Transistor Preamplifier Using a T Feedback Network 163
8.1.3 Cyclotron Frequency Correlation 164
8.2 Power Supply for a Quadrupole Mass Filter 165

9 Future Work **166**
9.1 Preamplifier 167
9.1.1 T Feedback Network 167
9.1.2 Preamplifier Noise Performance 168
9.1.3 Cyclotron Frequency Correlation 169
9.1.4 System Test 169
9.2 Power Supply for a Quadrupole Mass Filter 170

References **171**

A Appendix **190**
A.1 Datasheet: JFET BF862 191
A.2 Datasheet: Operational Amplifier AD8099 201
A.3 Datasheet: Operational Amplifier LT6205/06/07 225
A.4 Datasheet: Bipolar Power Transistor MJE18008 244

List of Tables

2.1 Summary of the existing FT-ICR preamplifiers. 43
3.1 Summary of the existing RF power supplies. 65

List of Figures

2.1 Sir Joseph J. Thomson's apparatus for measuring the charge-to-mass ratio of cathode rays. 10
2.2 Replica of Francis W. Aston's third mass spectrometer. 11
2.3 Apparatus for the multiple acceleration of ions. 12
2.4 The composition of a modern mass spectrometer. 15
2.5 Components inside the mass analyser, ion detector, and data system illustrated in Fig. 2.4. 15
2.6 The cyclotron principle. 17
2.7 The operation of a cylindrical ICR cell. 19
2.8 Three types of ion motions in an ICR cell. 20
2.9 Ion trajectory in a cubic Penning trap 22
2.10 A typical schematic of the detection signal processing chain for an FT-ICR system. 23
2.11 The signal processing procedure of an FT-ICR data system. . . . 26
2.12 The Bruker 12-T solariX FT-ICR mass spectrometer in the Ion Cyclotron Resonance Laboratory, University of Warwick. 27
2.13 Full width at half maximum (FWHM) Δm. 28
2.14 Tuning mix m/z 922 peak with ∼1-minute transient and ∼5.8M resolving power using a 12-T FT-ICR system. 29
2.15 Overlapped isotopic distributions of two ions being identified by an FT-ICR mass spectrometer. 31

2.16 IR-ECD spectra of the Substance P m/z 449.9 peak. 32
2.17 Different ICR cell configurations. 34
2.18 Gain and noise distribution in a three-stage amplifier system. . . . 35
2.19 Equivalent circuits of the thermal noise for a resistor R. 39
2.20 The noise model for an amplifier. 40
2.21 A conventional FT-ICR preamplifier. 42
2.22 The room-temperature FT-ICR amplifier system designed by Mathur and co-workers in 2007. 44
2.23 The cryogenic FT-ICR preamplifier reported by Mathur and co-workers in 2008. 45
3.1 Three major stages of a quadrupole ion guide power supply, and the schematic of a quadrupole ion guide illustrating the electrical connections. 49
3.2 The Mathieu stability diagram. 54
3.3 The first stability region in a stability diagram. 55
3.4 Schematic of the simplified RF source designed by Jones and Anderson. 58
3.5 Schematic of the RF oscillator designed by Mathur and O'Connor. 59
3.6 Principle schematic of the RF power supply designed by Cermak . 60
3.7 (a) (b) Schematic of the frequency stabilized RF generator for ion traps designed by Chang and Mitchell. 61
3.7 (c) Schematic of the clamp circuit of the frequency stabilized RF generator for ion traps designed by Chang and Mitchell. 62
3.8 Detailed schematic of the RF circuit designed by Robbins *et al.* . 63
3.9 The ion trap driving circuit using CMOS inverters, designed by Jau *et al.* 64
3.10 The feedback scheme with common-base setup for oscillation in the 2002 design by O'Connor *et al.* 67
3.11 The 215-V regulator and the 15-V DC voltage supply in the 2002 design by O'Connor *et al.* 68

4.1 NI PXI platform and DC power supplies for circuit test. 72
4.2 Schematic of the transistor I-V characteristic testing circuit. . . . 74
4.3 Front panel of the LabVIEW program for obtaining I-V characteristics of a transistor. 75
4.4 Block diagram of the LabVIEW program for obtaining I-V characteristics of a transistor. 76
4.5 Front panel of the LabVIEW program for the AC analysis. 78
4.6 Block diagram of the LabVIEW program for the AC analysis. . . 79
5.1 Components inside the ion detector of a modern mass spectrometer. 84
5.2 Two types of preamplifier systems. 88
5.3 Noise power spectral densities of four types of transistors. 93
5.4 Schematic of the transimpedance preamplifier using an operational amplifier AD8099. 94
5.5 Average noise level of chip resistors. 95
5.6 Single layer printed circuit board of the AD8099 preamplifier. . . 99
5.7 SPICE simulations of the AD8099 preamplifier transimpedance. . 101
5.8 Voltage gain frequency response of the main (AD8099) stage. . . . 102
5.9 Transimpedance frequency response of the preamplifier system in three feedback conditions. 103
5.10 One of the input/output waveforms fetched by the NI PXI system. 104
5.11 Measured input current noise spectral density with 18 kΩ transimpedance. 105
6.1 Transimpedance amplifiers with two feedback arrangements. . . . 113
6.2 Schematic of the single-transistor transimpedance preamplifier using a single-resistor feedback. 118
6.3 Common-source amplifier using the JFET BF862: (a) SPICE simulated correlations between the source resistance and voltage gain/ drain current; (b) measured BF862 current-voltage characteristic. 120
6.4 (a) Schematic of the single-transistor transimpedance preamplifier using a T feedback network. 123

6.4 (b) Measured transimpedance frequency response of the single-transistor transimpedance preamplifier using a T feedback network. 124
6.5 Printed circuit board for single-transistor preamplifiers and AD8099 voltage amplifiers. 126
6.6 (a) Schematic of the AD8099 preamplifier with a T feedback network, and the AD8099 voltage amplifier (VA). 128
6.6 (b) Measured transimpedance of the AD8099 preamplifier with three feedback systems. 129
6.6 (c) SPICE simulation of the AD8099 preamplifier frequency response in different permutations of the presence of two 8-pF feedback capacitors in the T feedback network. 130
7.1 Block diagram of the newly designed RF power supply for a quadrupole mass filter. 137
7.2 (a) Block diagram of the schematic shown in Fig. 7.2b. 140
7.2 (b) Schematic of the fixed frequency RF oscillating source with output amplitude control. 141
7.3 The frequency response simulation of the Deliyannis-Friend bandpass filter in Fig. 7.2. 143
7.4 A transformer in which its secondary coil is canter-tapped. 145
7.5 Printed circuit board of of the fixed frequency RF oscillating source with output amplitude control. 146
7.6 The oscilloscope screen snapshots of the output waveforms and their FFT results from both the crystal oscillator and the bandpass filter. 147
7.7 Measured RF oscillator output peak-to-peak amplitude and the power consumption correlated to the applied feedback voltage. . . 148
7.8 Schematic of the precision rectifier. 150
7.9 Two-layer printed circuit board of the precision rectifier. 151
7.10 Schematic of the power amplifier stage. 153
7.11 Power amplifier board with components mounted. 156

7.12 Winding of a bifilar coil with current flowing in the same direction. 157
7.13 Photo of the hand-wound air-core bifilar transformer. 158
7.14 The oscilloscope screen snapshot of the power amplifier output. . 159
7.15 Cross-section view of a Litz wire 160

List of Abbreviations

AC	.....	Alternating Current
ADC	.....	Analogue-to-Digital Converter
AGC	.....	Automatic Gain Control
BJT	.....	Bipolar Junction Transistor
CAD	.....	Collision-Activated Dissociation
CID	.....	Collision-Induced Dissociation
CMOS	.....	Complementary Metal-Oxide-Semiconductor
ESI	.....	Electrospray Ionization
FET	.....	Field-Effect Transistor
FFT	.....	Fast Fourier Transform
FT-ICR	.....	Fourier-Transform Ion Cyclotron Resonance
FTMS	.....	Fourier-Transform Mass Spectrometry
FWHM	.....	Full Width at Half Maximum
GC	.....	Gas Chromatography

ICR	.....	Ion Cyclotron Resonance
IR	.....	Infrared
IRMPD	.....	Infrared Multiphoton Dissociation
JFET	.....	Junction Field-Effect Transistor
LC	.....	Liquid Chromatography
LMCO	.....	Low-Mass Cut Off
MALDI	.....	Matrix-Assisted Laser Desorption/Ionization
MOSFET	.....	Metal-Oxide-Semiconductor Field-Effect Transistor
MS	.....	Mass Spectrometry
MS/MS	.....	Tandem Mass Spectrometry
NS-CAD	.....	Nozzle-Skimmer CAD
Op Amp	.....	Operational Amplifier
PCB	.....	Printed Circuit Board
PCI	.....	Peripheral Component Interconnect
PXI	.....	PCI eXtensions for Instrumentation
RF	.....	Radio Frequency
SNR	.....	Signal-to-Noise Ratio
SORI-CAD	.....	Sustained Off-Resonance Irradiation CAD
SPICE	.....	Simulation Program with Integrated Circuit Emphasis
TTL	.....	Transistor-Transistor Logic
UVPD	.....	Ultraviolet Photodissociation
VA	.....	Voltage Amplifier

CHAPTER 1

Introduction

The late 19th century marks the start of the mass spectrometry (MS) instrument development. MS instrumentation research has led to a continuous improvement in mass spectrometer performance, especially the resolving power and mass accuracy. This advanced performance allows scientists to conduct analytical research in new areas that could not be performed before.

This thesis focuses on the electronics for Fourier-transform ion cyclotron resonance (FT-ICR) MS, in hope that the new designs proposed here contribute to the MS community, resulting in better mass spectrometer designs in the future, for solving more complicated analytical problems. In this work, existing FT-ICR preamplifiers (for ion signal detection) and radio-frequency (RF) oscillators (for ion transportation/filtering) are reviewed. Then the potential scope for future improvement is suggested.

1.1 FT-ICR Preamplifier Problems to Be Solved

For improving FT-ICR performance, single-charge detection is proposed to be one of the solutions to minimise the space charge issue in an ion cyclotron resonance (ICR) cell. The sensitivity and the signal-to-noise performance of an FT-ICR system has to be improved to achieve the goal of single-charge detection. More advanced ICR cell designs are also introduced for improving FT-ICR performance. In such a case, more parasitic capacitance will be seen by the input node of the preamplifier, and such capacitance at input node limits the bandwidth. Therefore, an FT-ICR preamplifier with improved bandwidth, noise performance, and signal sensitivity is essential.

Among the exiting FT-ICR preamplifier designs reviewed in Section 2.5.3, the signal current from the FT-ICR mass analyser, an ICR cell, is converted into a voltage using a large input resistor, which unfortunately acts as a major noise source at the input node. Meanwhile, the parasitic capacitance from the ICR cell and cabling shunts such a large input resistor, causing the bandwidth to be limited. The parasitic capacitance from the ICR cell in an FT-ICR system can vary from around 10 pF to over 100 pF (Kaiser et al., 2011a), depending on the cell dimensions, feedthroughs, and cabling. The preamplifier circuit reported by Mathur and co-workers in 2008 used a 10-MΩ input resistor (Mathur et al., 2008). A 100-pF capacitance shunting a 10-MΩ resistance causes a $1/RC$ corner at ∼160 Hz. However, a 12-T FT-ICR system demands a bandwidth of around 1 MHz.

With the newly designed preamplifiers reported in Chapters 5 and 6, this work presents solutions to preserve preamplifier bandwidth using both transimpedance and the T feedback techniques. Components with excellent noise performance are used for improving the signal-to-noise ratio (SNR) of the system, hence improving the FT-ICR sensitivity.

The design constraints of an FT-ICR preamplifier, such as the gain, sensitivity, noise performance, and cyclotron frequency correlation are also studied in this work. In the future, it is planned to use these new designs to test the potential of performing single-charge detection at room temperature.

1.2 Quadrupole Power Supply Problems in Mass Filtering

A quadrupole mass filter is a commonly used ion filtering device in MS. When operated in the RF-only mode (details will be discussed in Section 3.2), it can be used as an ion guide to transfer ions in a mass spectrometer. Such a device is also commonly used in an FT-ICR system. Among the existing quadrupole power supply designs reviewed in Section 3.4, many of the ion guide power supplies use a similar feedback scheme to start the oscillation. Those systems oscillate at the resonant frequency of the output stage. Such frequency is determined by the equivalent output reactance, which depends on the output transformer size, tuning capacitors, cabling, and ion guide dimensions. As the impedance varies with operation conditions, the output frequency is unstable. Meanwhile, the output amplitude of most of those circuits is also instable. For instance, the

design reported by Mathur and co-workers (Mathur and O'Connor, 2006) has been tested to have a more than 1% output amplitude variation in less than one minute.

As discussed later in Chapter 3, to drive a mass filter with 0.1-Da resolution, RF oscillator output amplitude and frequency variations of less than 5.0×10^{-4} are necessary. In Chapter 7, a new oscillator design is proposed and tested. Such an oscillator targets a stabilized output frequency, and a feedback control for output amplitude stabilisation. The newly designed circuit has a very stable output frequency at 1 MHz, with a frequency tolerance of 15 ppm specified by the crystal oscillator datasheet. For output amplitude stabilization, an automatic gain control (AGC) unit is built in this circuit. It is believed that the new design will produce a stable RF power supply for driving a quadrupole mass filter.

1.3 Thesis Outline

This thesis consists of three major parts. The first part of this thesis comprises Chapters 1, 2, 3, and 4, covering the research questions, theories, and the testing methods used for this work. Chapter 2 reviews the general MS related history and some of the important milestones, followed by the introduction of the composition of a modern mass spectrometer. Then, the theories of the ICR technique, one of the mass analysing methods, is reviewed. This is followed by the introduction of the FT-ICR signal processing method. To understand the electronic detection limit for an ICR cell in an FT-ICR system, the nature of the ion signal and

electronic noise have been studied. Then the existing preamplifiers for ICR signal detection are reviewed. Finally, the potential scope for improvement is suggested by the end of this chapter.

In Chapter 3, the theory of operating a quadrupole ion guide is provided, followed by an introduction to the Mathieu equation, stability diagram, and quadrupole mass filtering theory. Existing quadrupole power supply designs are reviewed. Then the problems of building a power supply for a quadrupole mass filter are discussed in this chapter, whilst a new power supply design will be reported in Chapter 7.

Chapter 4 reports the testing equipment and the computer softwares used in this work, followed by the presentation of the methods used to test the designed circuits reported in the second part of this thesis, including Chapters 5, 6, and 7.

The second part of this dissertation reports the new electronic designs, including two FT-ICR preamplifiers, and an oscillator for a quadrupole mass filter. In Chapter 5, a preamplifier using an operational amplifier (op amp) in a transimpedance configuration is reported. This chapter starts with a brief review of the transimpedance technique and the input capacitance tolerance of a transimpedance amplifier. Then the correlation between the cyclotron frequency of the signal form an ICR cell and the transimpedance (gain) of the preamplifier is reviewed to understand the preamplifier design constraints. This is followed by the presentations of the newly designed preamplifier and its printed circuit board (PCB) for testing. The preamplifier has been computer simulated and tested on

the bench. The tested frequency response and the noise performance are shown. This chapter concludes with a discussion between the feedback impedance, bandwidth, noise performance, and the estimated numbers of ions to be detected in a 12-T FT-ICR system.

Chapter 6 begins with a discussion of the theories of two feedback arrangements, a single-resistor feedback and a T-shaped feedback network, for transimpedance amplifiers. Then a single-transistor transimpedance preamplifier design is proposed to extend further the noise performance. Biasing conditions, input/output impedance, and over-all transimpedance of such a design is studied. A PCB for testing purpose has been manufactured. Then, this is followed by the bench testing report of the proposed T feedback network and the single-transistor transimpedance preamplifier. This chapter concludes with a discussion of the gain and noise performance of a preamplifier, and a suggestion of possible constructing elements for a T feedback network for circuit optimization.

Chapter 7 presents a RF oscillator as a quadrupole mass filter power supply, which has a stabilised output frequency, and a feedback control for output amplitude stabilisation. This chapter first introduces the building blocks of the new quadrupole mass filter power supply, and is followed by the reports of the electronic details of each building block. Three PCBs have been built for testing the following parts of this power supply: a RF oscillator, a bandpass filter, a gain control circuit, a power amplifier, and a feedback control circuit. Then a transformer design is suggested, followed by the discussion of the correlation between

resonant frequency and impedance of the output stage.

Finally, the third part of this thesis contains the conclusion, suggested future works, reference and appendices. Chapter 8 and Chapter 9 present the conclusion and the suggested future works for extending this research, respectively. In particular, a discussion between the preamplifier gain and noise performance is presented. A brief analysis of the correlation between the gain, cyclotron frequency for FT-ICR MS, and input capacitance is also performed.

In the reference, the page number labeled in the parentheses indicates where the citation is mentioned in this thesis. In the appendices, datasheets of the key components of this work are included.

CHAPTER 2

Fourier-Transform Ion Cyclotron Resonance Mass Spectrometry

This chapter first reviews the general MS related history and some of the important milestones, followed by the introduction of the composition of a modern mass spectrometer. In Section 2.2, the theories of the ion cyclotron resonance (ICR) technique, one of the mass analysing methods, is reviewed. This is followed by the introduction of the method for FT-ICR signal processing. Section 2.4 introduces the advantages of an FT-ICR mass spectrometer. The nature of the ion signal and the electronic noise have been studied to understand the electronic detection limit for an ICR cell in an FT-ICR system. Then the existing preamplifiers for ICR signal detection is reviewed, followed by the suggested potential scope for improvement.

2.1 Introduction to Mass Spectrometry

After positively or negatively charged ions (from samples which are introduced either directly, or from a gas chromatography (GC)/liquid chromatography (LC) system) are generated and sent into a mass spectrometer, a mass spectrometer separates those charged ions according to their mass-to-charge ratios, m/z, and records the m/z with relative abundances. Because of its selectivity, specificity, and sensitivity to a given sample substance, mass spectrometry (MS) is generally recognized as one of the essential microanalytical tools for determining elemental composition or structural information in chemical, biological, or other areas of research.

2.1.1 Brief History & Milestones

The development of a mass spectrometer can be traced back to the late 19th century, when Sir Joseph J. Thomson used a vacuum tube to measure the charge-to-mass ratio of cathode rays, and was awarded the Nobel Prize in Physics in 1906 "in recognition of the great merits of his theoretical and experimental investigations on the conduction of electricity by gases."[1] However, Thomson's curiosity about the electrical discharge behaviors originated from the discovery of "Kanalstrahlen" (canal rays) by Eugene Goldstein at Berlin Observatory (Watson and Sparkman, 2008). Figure 2.1 (Beynon and Morgan, 1978) shows his apparatus for such measurement, in which the letter "M" means the magnet that generates

[1] See http://www.nobelprize.org/nobel_prizes/physics/laureates/1906/ for information about the Nobel Prize in Physics 1906, accessed 10 August 2012.

a magnetic field perpendicular to the plane of Fig. 2.1.

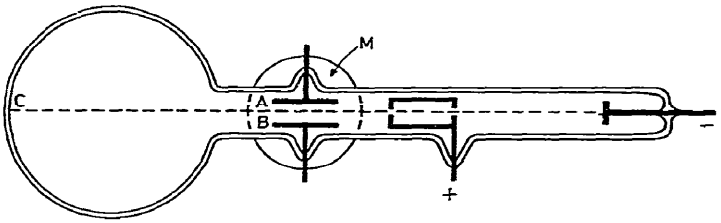

Figure 2.1: Sir Joseph J. Thomson's apparatus for measuring the charge-to-mass ratio of cathode rays (Beynon and Morgan, 1978).

The discovery and research of isotopes are also widely recognized as milestones in the mass spectrometry history. In particular, Frederick Soddy and Francis W. Aston received their Nobel Prizes in Chemistry in 1921 and 1922, respectively, for Soddy's "contributions to our knowledge of the chemistry of radioactive substances, and his investigations into the origin and nature of isotopes,"[2] and for Aston's "discovery, by means of his mass spectrograph, of isotopes, in a large number of non-radioactive elements, and for his enunciation of the whole-number rule."[3] Figure 2.2 (Watson and Sparkman, 2008) shows the mass spectrometer designed by Aston.

The oil drop experiment performed in 1909 leads Robert A. Millikan to the Nobel Prize in Physics in 1923 for his "work on the elementary charge of electricity and on the photoelectric effect."[4] Some believe that the oil drop experiment can be considered the first example of the electrospray ionization (ESI) method,

[2]See http://www.nobelprize.org/nobel_prizes/chemistry/laureates/1921/ for information about the Nobel Prize in Chemistry 1921, accessed 10 August 2012.

[3]See http://www.nobelprize.org/nobel_prizes/chemistry/laureates/1922/ for information about the Nobel Prize in Chemistry 1922, accessed 10 August 2012.

[4]See http://www.nobelprize.org/nobel_prizes/physics/laureates/1923/ for information about the Nobel Prize in Physics 1923, accessed 10 August 2012.

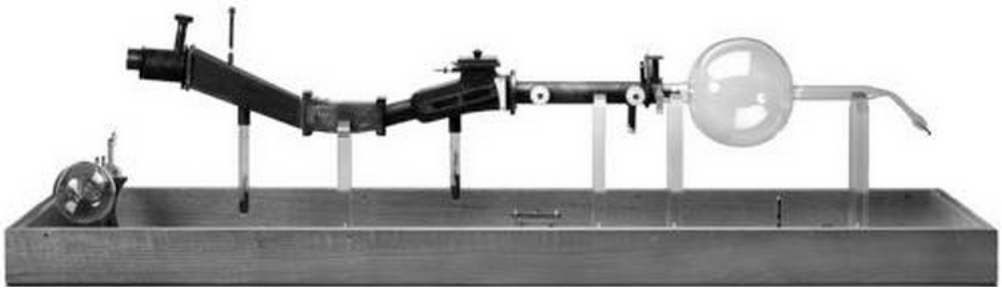

Figure 2.2: Replica of Francis W. Aston's third mass spectrometer, commissioned by the American Society for Mass Spectrometry (Watson and Sparkman, 2008).

which is now a widely used ionization method for MS. A U.S. patent was granted to Ernest O. Lawrence in 1934 for the invention of the cyclotron (Lawrence, 1934), and later in 1939 the Nobel Prize in Physics was awarded to Lawrence "for the invention and development of the cyclotron and for results obtained with it, especially with regard to artificial radioactive elements."[5] Figure 2.3 (Lawrence and Livingston, 1932) shows the ion acceleration apparatus developed by Lawrence. The cyclotron concept was later adapted, and in 1974 the mass analysis method of Fourier-transform ion cyclotron resonance (FT-ICR) was invented by Comisarow and Marshall (Comisarow and Marshall, 1974a).

Although it was not until 1989 that the next MS related Nobel laureates of Hans G. Dehmelt and Wolfgang Paul were recognized (one half awarded in Physics) "for the development of the ion trap technique,"[6] the interests toward the MS related topics remained active in between the Nobel "gap years" (Wat-

[5]See http://www.nobelprize.org/nobel_prizes/physics/laureates/1939/ for information about the Nobel Prize in Physics 1939, accessed 10 August 2012.

[6]See http://www.nobelprize.org/nobel_prizes/physics/laureates/1989/ for information about the Nobel Prize in Physics 1989, accessed 10 August 2012.

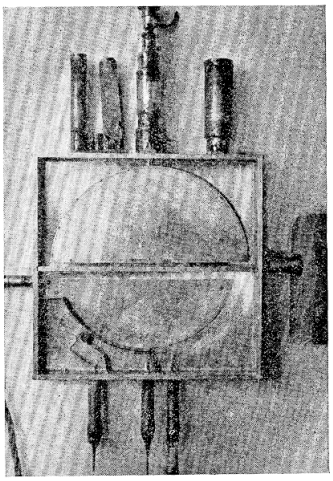

(a) Photo of the vacuum tube with cover removed.

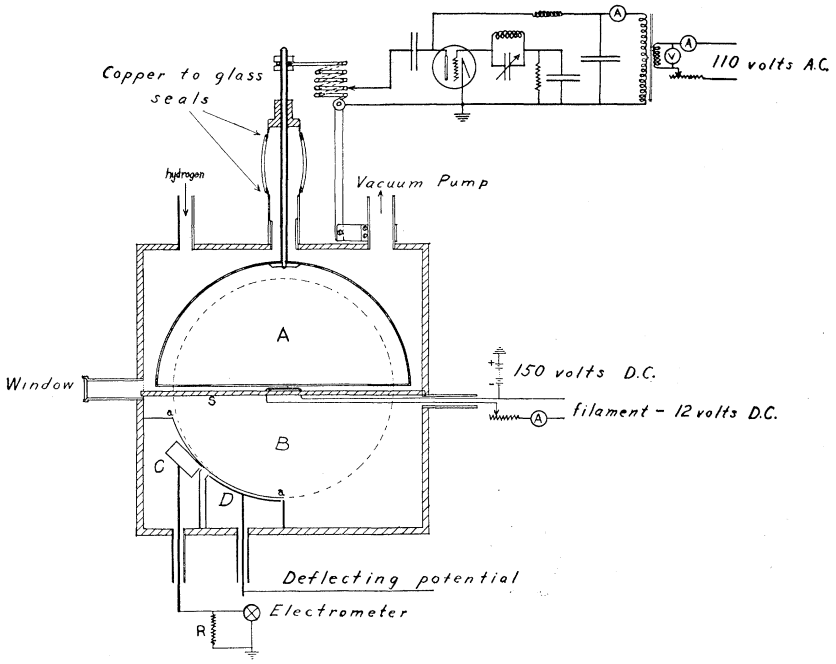

(b) Apparatus diagram.

Figure 2.3: Apparatus for the multiple acceleration of ions, invented by Lawrence (Lawrence and Livingston, 1932).

son and Sparkman, 2008). One of the evidences can be found in the MS review paper written by Hipple and Shepherd and published in the journal of *Analytical Chemistry* in 1949 (Hipple and Shepherd, 1949), in which 176 references were cited. Later in 1998, another MS review paper in *Analytical Chemistry* written by Burlingame and co-workers became a 70-page report with 1409 citations (Burlingame et al., 1998).

Later, in 1996 Robert F. Curl Jr., Sir Harold W. Kroto, and Richard E. Smalley were awarded the Nobel Prize in Chemistry in 1996 "for their discovery of fullerenes,"[7] where the C_{60} signal was first recorded by a time-of-flight (TOF) mass spectrometer in 1985 (Kroto, 1997). The Nobel Prize in Chemistry 2002 was received "for the development of methods for identification and structure analyses of biological macromolecules."[8] Whilst one half of the prize was for the development of the nuclear magnetic resonance (NMR) spectroscopy method, the other half went jointly to John B. Fenn and Koichi Tanaka "for their development of soft desorption ionization methods for mass spectrometric analyses of biological macromolecules,"[8] in which the ionization techniques of ESI and matrix-assisted laser desorption/ionization (MALDI) were developed.

Nowadays, there are many good references about the history of MS. The review sections and book sections/chapters mentioned in this thesis can be excellent starting points for researchers to investigate further.

[7] See http://www.nobelprize.org/nobel_prizes/chemistry/laureates/1996/ for information about the Nobel Prize in Chemistry 1996, accessed 10 August 2012.

[8] See http://www.nobelprize.org/nobel_prizes/chemistry/laureates/2002/ for information about the Nobel Prize in Chemistry 2002, accessed 10 August 2012.

2.1.2 Mass Spectrometry Composition

"A modern mass spectrometer is constructed from elements which approach the state-of-the-art in solid-state electronics, vacuum systems, magnet design, precision machining, and computerized data acquisition and processing" (Ligon, 1979). In general, a mass spectrometer is composed of an inlet system for sample introduction, an ion source to create charged ions, a mass analyser to measure the mass-to-charge ratio, m/z, of the charged sample, a signal detector, and a data processing system. Usually the ion source, mass analyser, and ion detector are located in a vacuum chamber, as shown in Fig. 2.4.

The components inside the mass analyser, ion detector, and data system are listed in Fig. 2.5. Generally, in an FT-ICR system, a mass analyser contains an ion transferring/filtering/accumulating system and an ICR cell. A quadrupole ion filter can be used here for ion filtering. The operation of a quadrupole ion filter will be introduced in Chapter 3, and a proposed new electronic device for running a quadrupole ion filter will be presented in Chapter 7. An ion detector consists of electronic devices for processing the analogue signal coming from the mass analyser. The signal is amplified and filtered here, before being sent into an analogue-to-digital converter (ADC) in the data system. The preamplifier in an ion detector system is believed to be one of the key components for improving signal-to-noise performance electronically. Later in this chapter, the operation theory of an ICR cell and the signal processing in the ion detector will be discussed, and newly designed preamplifiers will be presented in Chapter 5

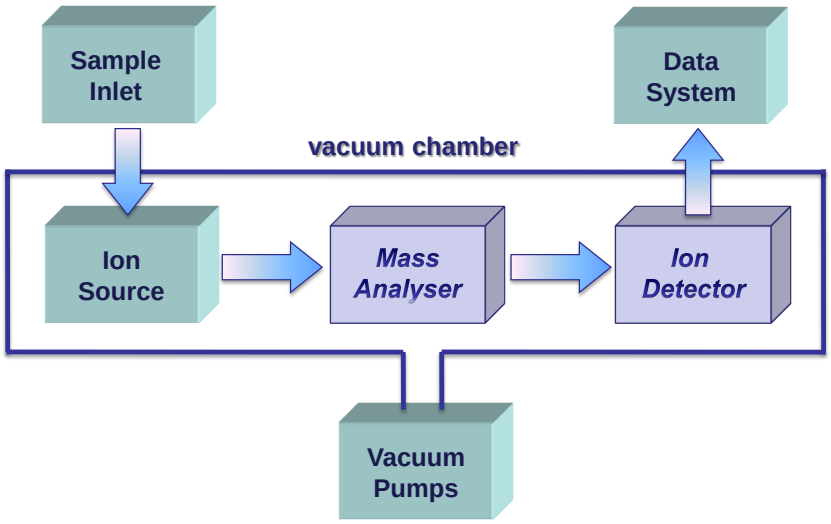

Figure 2.4: The composition of a modern mass spectrometer.

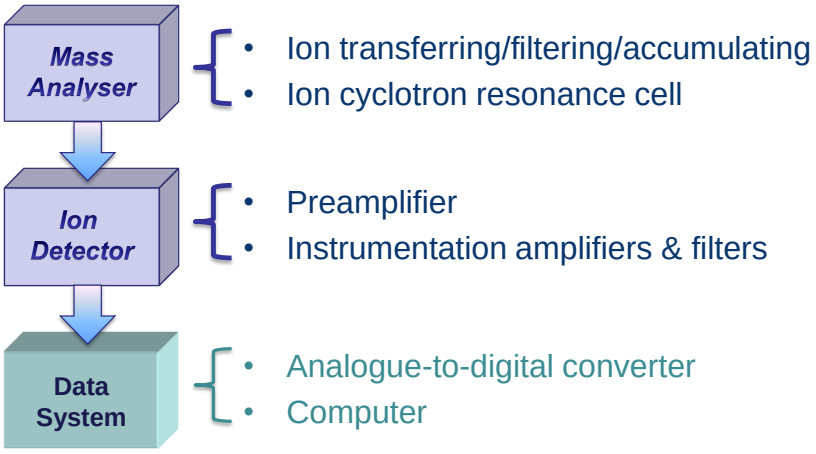

Figure 2.5: Components inside the mass analyser, ion detector, and data system illustrated in Fig. 2.4. In particular, this thesis will cover the designs of the preamplifier (Chapters 5 & 6) and the power supply for ion filtering (Chapter 7).

and Chapter 6.

Depending on the type of analysers, there are different types of mass spectrometers, such as sector instruments, ion traps, time-of-flight (TOF) instruments, and Fourier-transform mass spectrometers. Each of them offers different performance features in terms of sensitivity, speed, resolving power, and mass accuracy. Among them, the FT-ICR MS, one type of the Fourier-transform mass spectrometry (FTMS) (Amster, 1996), offers excellent flexibility, the highest resolving power, and the best mass accuracy. As a result, the FT-ICR MS has become the instrument of choice for proteomics (Li et al., 2011b; Li et al., 2011a; Lourette et al., 2010; Cui et al., 2011), biological imaging (Aizikov et al., 2011; McDonnell et al., 2010; Smith et al., 2011; Taban et al., 2007), petroleum (Hsu et al., 2011), and environmental research (Barrow et al., 2010; Headley et al., 2011). The FT-ICR MS approach also shows promise for archeological dating (Perez Hurtado and O'Connor, 2012). Here, the mass analyser of an FT-ICR mass spectrometer will be discussed in Section 2.2, whilst the ion detector will be mentioned in Section 2.3.

2.2 Ion Cyclotron Resonance Technique

Positioned within an ultra high vacuum chamber ($< 10^{-9}$ mbars) with a homogeneous magnetic field, an ion cyclotron resonance (ICR) cell is the main analysing component of FT-ICR MS. The detecting technique of ion cyclotron resonance (ICR) was introduced by Comisarow and Marshall in 1974 at Univer-

sity of British Columbia, Vancouver, Canada (Comisarow and Marshall, 1974a; Comisarow and Marshall, 1974b). The operation of the ICR can be derived from the cyclotron principle recognized by Lawrence (Lawrence and Livingston, 1932), and is illustrated in Fig. 2.6 (Comisarow, 1993). In a homogeneous magnetic field B, charged ion with ionic charge q, ionic mass m, and velocity v, can be constrained to orbit circularly with a characteristic angular cyclotron frequency ω_{cyc} (Comisarow and Marshall, 1976; Comisarow, 1993), where

$$\omega_{cyc} = 2\pi f_{cyc} = \frac{qB}{m} \ . \tag{2.1}$$

Note that here f_{cyc} is the cyclotron frequency. The correlations between the cyclotron frequency and the ion mass in a 3-T magnetic field is also shown in Fig. 2.6.

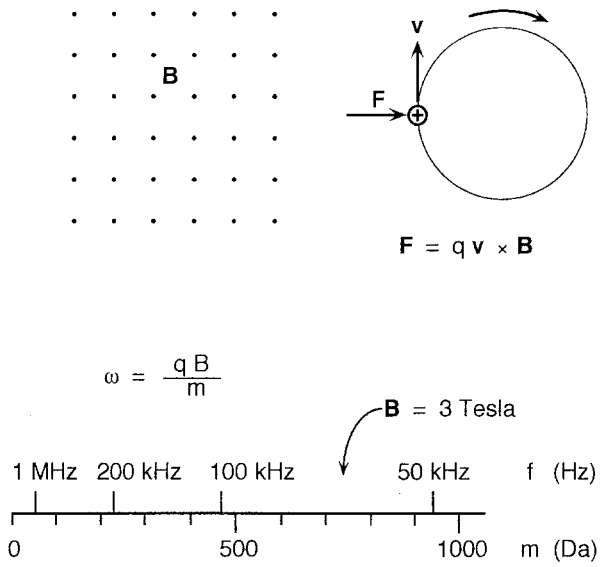

Figure 2.6: The cyclotron principle (Comisarow, 1993).

2.2.1 ICR Cell Operation

Figure 2.7 shows the operation of a cylindrical ICR cell. Ions are first transported and trapped in the cell, as shown in Fig. 2.7(a). At this stage, ions may oscillate with incoherent, low, thermal amplitude. Then as Fig. 2.7(b) indicates, an oscillating electric field is applied to the excitation plates to excite the ions into a higher rotating radius for detection. The ions which have their angular cyclotron frequency ω_{cyc} the same as the excitation frequency will be "irradiated" to a larger, coherent cyclotron orbit closer to the detection plates. The excitation signal will be a sweep of frequency to excite all ions of interests to their rotation orbit. The ICR cell detects such ion rotating motion in the magnetic field (perpendicular to the plane of Fig. 2.7) by electrostatic induction, and the introduced "image current" will be picked up by the front-end electronics connected to the detection plates, as shown in Fig. 2.7(c). Note that the rotating ions may collide with neutral background air molecules, resulting in the loss of their kinetic energy. Then the radius of their rotating orbit is reduced. As the ions move further away from the detection plates, the intensity of the induced signal current is decreased. Therefore, an ultra high vacuum condition is required to delay such a signal decay due to the background air pressure in an ICR cell.

2.2.2 In-Cell Ion Motion

There are three types of ion motions that ions trapped in an ICR cell undergo, as shown in Fig. 2.8 (Schmid et al., 2000). The ion motion with frequency f_{cyc}

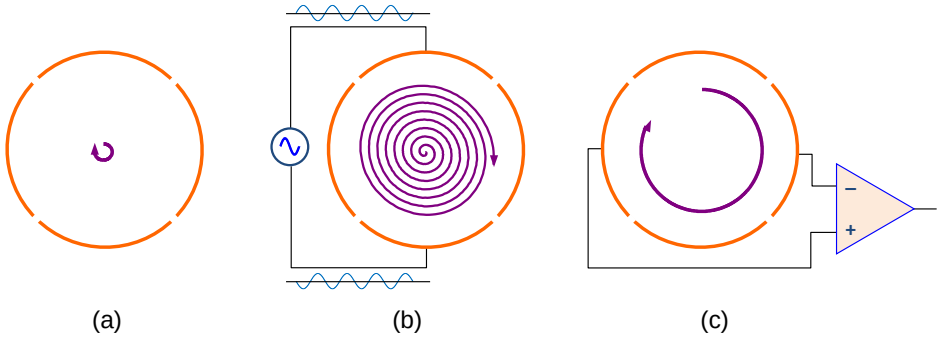

Figure 2.7: The operation of a cylindrical ICR cell.

characterized by Eq. (2.1) is called the cyclotron motion. In the ICR cell, ideally ions are trapped in the center of the cell, but in reality, undergo harmonic oscillations along the injection-axis (z-direction). Such a oscillating motion is called the trapping motion or z-motion. Meanwhile, ICR frequencies are a function not only of the magnetic force, but also of the electrostatic trapping field, which is ideally hyperbolic. The motion caused by this radial component of the trapping field is called the magnetron motion. In reality, with the ICR cell typically used in commercial instruments, the electrostatic trapping field is a good approximation of a hyperbolic field only near the center of the cell. Thus, with those different ion motions and the imperfect electric fields typically used, the observed ICR frequencies are modulated as the ions orbit in the cell.

To describe such frequency quantitatively, one should start with the Lorentz force described in Fig. 2.6, in which the force $\boldsymbol{F}$, the velocity $\boldsymbol{v}$, and the magnetic

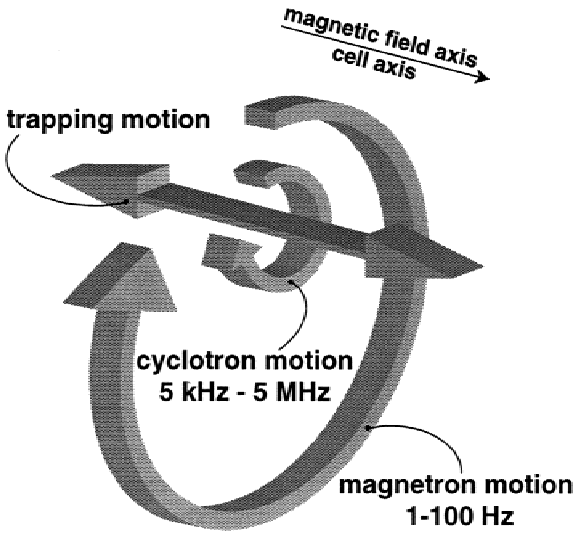

Figure 2.8: Three types of ion motions in an ICR cell (Schmid et al., 2000).

field $\boldsymbol{B}$ are perpendicular to each other and have the relation of

$$\boldsymbol{F} = m\frac{d\boldsymbol{v}}{dt} = q\boldsymbol{v} \times \boldsymbol{B} \ , \tag{2.2}$$

where m is the mass and q is the ionic charge of the ion. Then the magnitude of such force F can be a function of the angular velocity ω and the rotating radius r where

$$F = m\omega^2 r = qB\omega r \ . \tag{2.3}$$

In an ICR cell, the ions are trapped using a electrostatic trapping potential V_{trap}, which can be applied to two end electrodes that are positioned at $z = \pm a_z/2$ from the cell center along the z-axis. Such potential causes a radical force $q\boldsymbol{E}$ ($\boldsymbol{E}$ is the electric field) that opposites the Lorentz force described in Eq. (2.3).

Therefore the force becomes (Marshall et al., 1998)

$$F = m\omega^2 r = qB\omega r - \frac{qV_{trap}\alpha}{{a_z}^2} r \ , \tag{2.4}$$

where α is the geometrical constant depending on the ICR cell. Then by rearranging Eq. (2.4), the following equation can be obtained

$$\omega^2 - \frac{qB\omega}{m} + \frac{qV_{trap}\alpha}{m{a_z}^2} = 0 \ . \tag{2.5}$$

The solution, as shown in Eq. (2.6), to the quadratic Eq. (2.5) describes the perturbations applied to the cyclotron frequency ω_{cyc} mentioned in Eq. (2.1).

$$\omega_{\pm} = \frac{\omega_{cyc}}{2} \pm \sqrt{\left(\frac{\omega_{cyc}}{2}\right)^2 - \frac{{\omega_z}^2}{2}} \ , \tag{2.6}$$

where ω_+ is called the reduced cyclotron frequency, ω_- is the magnetron frequency of the magnetron motion shown in Fig. 2.8, and

$$\omega_z = \sqrt{\frac{2qV_{trap}\alpha}{m{a_z}^2}} \tag{2.7}$$

is the trapping oscillation frequency of the trapping motion. Figure 2.9 (Marshall et al., 1998) is an example of the ion trajectory with cyclotron motion (indicated by $\boldsymbol{v}_c$), magnetron motion (indicated by $\boldsymbol{v}_m$), and trapping motion (indicated by $\boldsymbol{v}_T$).

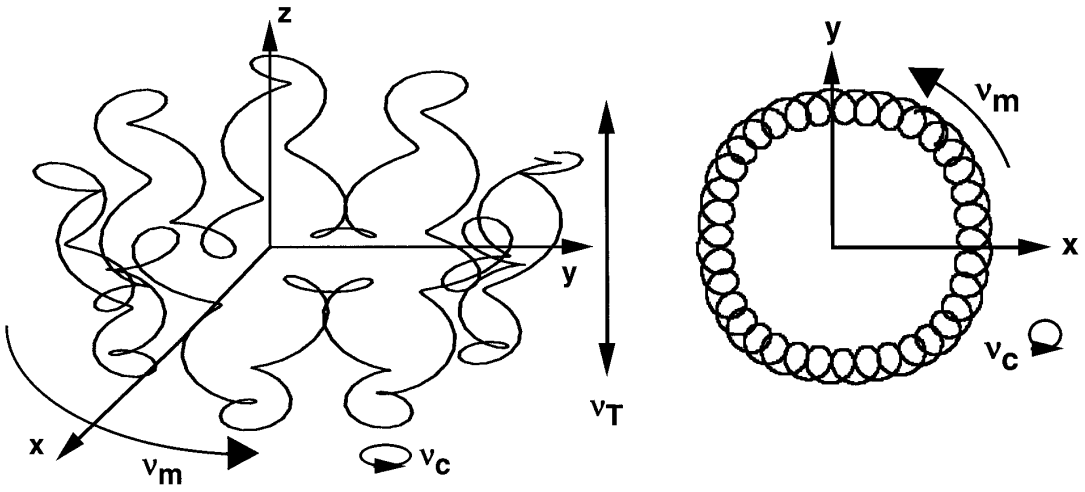

Figure 2.9: Ion trajectory in a cubic Penning trap, where $\boldsymbol{v_c}$ indicates the cyclotron motion, $\boldsymbol{v_m}$ indicates the magnetron motion, and $\boldsymbol{v_T}$ indicates the trapping motion (Marshall et al., 1998).

2.3 Signal Processing

2.3.1 Ion Detector

The ion detector shown in Fig. 2.4 takes the responsibility of sensing the electronic signals induced from a mass analyser. Figure 2.10 (Mathur and O'Connor, 2009) illustrates a typical schematic of the detection signal processing chain for an FT-ICR system. Before the digitized signal is sent into a computer for further analysis, the analogue signal is processed by a preamplifier, instrument amplifiers, filters, and an ADC.

A preamplifier, which is usually mounted inside the ultra high vacuum chamber as close as possible to the ICR cell, is the key front-end electronic component in FT-ICR MS. The preamplifier detects the image current (Comisarow, 1978) induced by the excited ion packets rotating at a coherent orbit in the cell. These

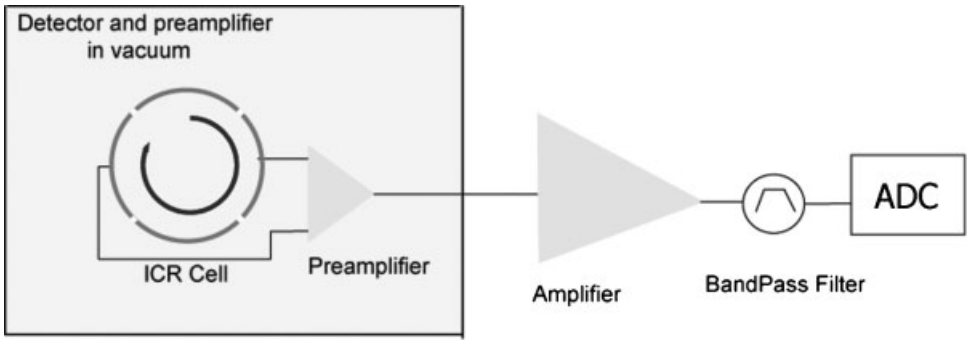

Figure 2.10: A typical schematic of the detection signal processing chain for an FT-ICR system (Mathur and O'Connor, 2009).

currents are generally on the scale of tens of femtoamps to a few hundred picoamps, depending of the number of ions trapped, and the radius of rotating orbit. The root mean square (RMS) signal current (Comisarow, 1978) from an ICR cell can be given by Eq. (2.8a).

$$I_{s\ (r.m.s)} = \frac{Nq^2B}{\sqrt{2}m} \times \frac{r}{d} \tag{2.8a}$$

$$= \frac{1 \times (1.60 \times 10^{-19})^2 \times 12}{\sqrt{2} \times 1000 \times 1.66 \times 10^{-27}} \times \frac{1}{4}$$

$$= 3.27 \times 10^{-14} \simeq 33 \ \ \text{(fA/charge)}, \tag{2.8b}$$

where N is the number of excited ions, q is the ionic charge, B is the magnetic field strength, m is the ion mass, r is the ion rotation orbital radius, and d is the cell diameter (spacing). For a singly-charged, 1000-Da ion rotating at the orbit radius of $\frac{1}{4}$ the cell diameter in a 12-T magnetic field, namely, $N = 1$, $B = 12$ T, $m = 1000$, and $\frac{r}{d} = \frac{1}{4}$, Eq. (2.8b) calculates a RMS current signal of about 33 fA/charge.

The amplified signal will be further processed in a signal processing chain involving second stage amplifiers, band pass filters, and an ADC, in air outside the vacuum system. The digitized signal then can be analysed by a computer. The total gain within such a signal chain should be carefully designed so that the amplified signal fits in the dynamic range of the ADC. Insufficient gain sacrifices the detection sensitivity, whereas overloaded gain causes saturation of the ADC, which results in the generation of artifact peaks by the Fourier transform (Mathur and O'Connor, 2009). Considering the worst-case scenario of single-charge detection, 1-bit change at the least significant bit of the ADC output is needed to detect this current signal of a single ion given by Eq. (2.8b). If the ADC has a resolution of 16 bits with an input range of ± 1 V, the minimum total gain, which is the transimpedance A_T in this case, of the full amplifier must be

$$A_T = \frac{2 \times \dfrac{1}{2^{16}}}{3.27 \times 10^{-14}} = 9.3 \times 10^8 \ (\Omega). \tag{2.9}$$

Note this calculation assumes a noiseless signal, but upon digitization, noise allows detection of periodic signals less than 1 bit change (Marshall and Verdun, 1990). With such an over-all transimpedance, theoretically the maximum signal current can be detected without saturation at the ADC is around 2.1 nA, namely, about 66000 1000-Da ions (at the orbit radius of $\frac{1}{4}$ the cell diameter in a 12-T magnetic field) being detected.

2.3.2 Data System

The induced image current from the ICR cell is recorded in the time domain after being sent to a data system computer. The data system Fourier transforms the recorded signal into the frequency domain. The frequency information is further calibrated to yield the mass spectrum in the mass-to-charge m/z domain. Such a procedure is illustrated in Fig. 2.11 using an tandem mass spectrometry (MS/MS), methods to gain different structural information, spectrum of the Substance P m/z 449.9 peak, recorded by the Bruker (Billerica, Massachusetts, USA) 12-T solariX FT-ICR mass spectrometer shown in Fig. 2.12.

Equation (2.6) can be revised to have a form of

$$f_{obs} \approx a(\frac{m}{z})^{-1} + bV_{trap} + cV_{trap}{}^{2}(\frac{m}{z}) \ , \tag{2.10}$$

as reported by Li and co-workers (Li et al., 1994; Zhang et al., 2005). The Eq. (2.10) presents one of the commonly used calibration functions for the FT-ICR MS.

2.4 Advantages of FT-ICR MS

The FT-ICR MS is currently the mass spectrometer with the highest resolving power and mass accuracy. Another greatest advantage of the FT-ICR MS is its flexibility to be equipped with different ion sources, inlet systems, and MS/MS methods.

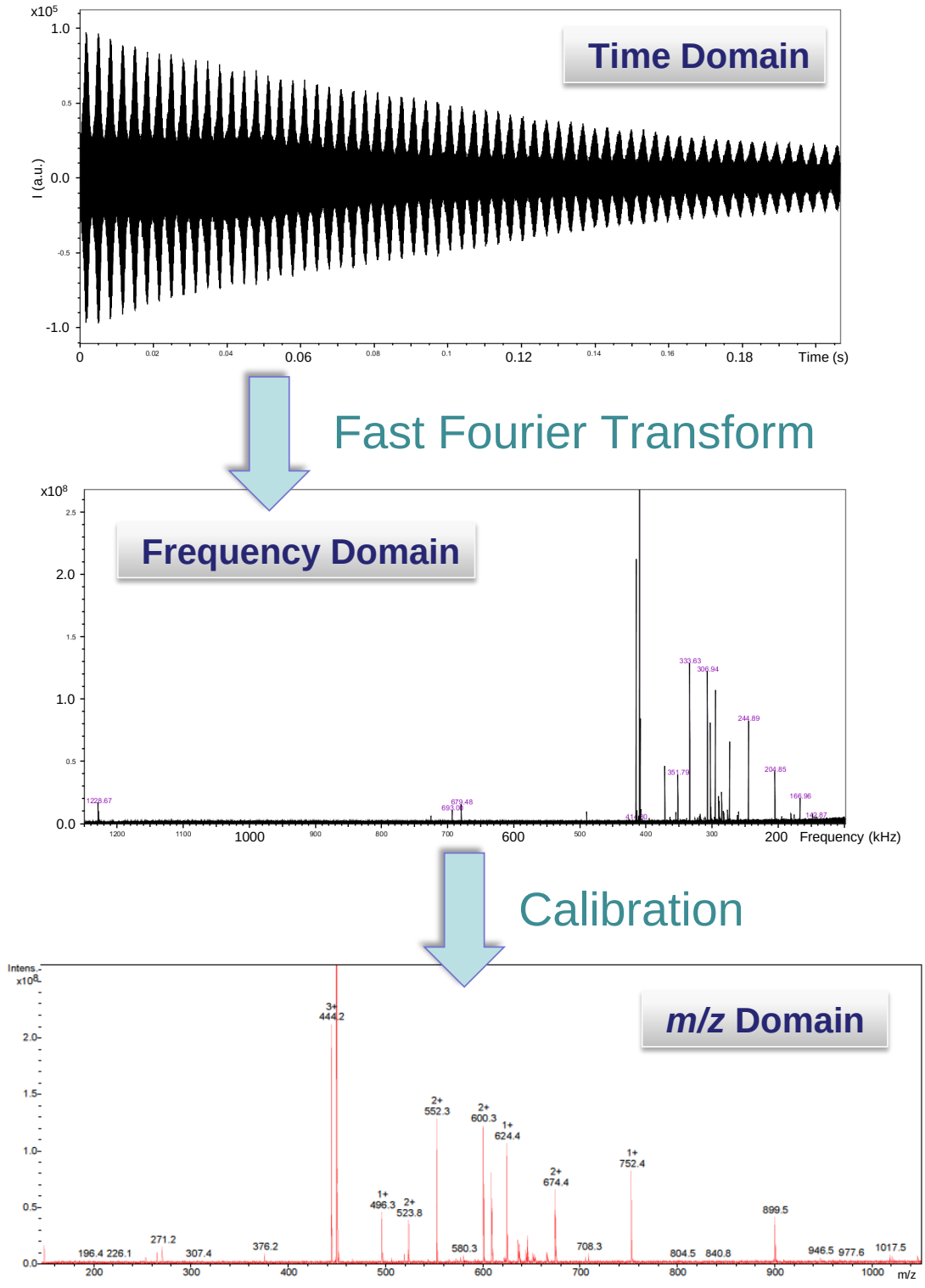

Figure 2.11: The signal processing procedure of an FT-ICR data system. First, the transient data are recorded, and then Fourier transformed into frequency domain. After calibration, the mass spectrum in the mass-to-charge m/z domain is shown.

Figure 2.12: The Bruker 12-T solariX FT-ICR mass spectrometer in the Ion Cyclotron Resonance Laboratory, University of Warwick.

2.4.1 Resolving Power

A mass spectrometer with higher resolution means the ability to obtain better separation of peaks in a given mass spectrum. Usually such ability is described as the resolving power, *R.P.* (Marshall et al., 1998; Watson and Sparkman, 2008),

$$R.P. = \frac{m}{\Delta m} \ , \tag{2.11}$$

where m is the mass, and Δm is the full width at half maximum (FWHM) of the peak, as illustrated by Fig. 2.13 (Watson and Sparkman, 2008). In Fig. 2.13 the peak of $m/z = 2000$ has a Δm of 0.5, so that the resolving power $R.P. = 2000/0.5 = 4000$.

Nowadays, a 12-T FT-ICR system can record spectra with resolving power routinely $>$ 1M. The maximum resolving power R_{FT-ICR} that an FT-ICR system

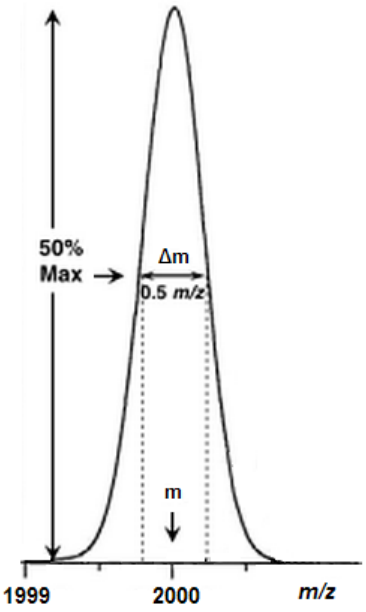

Figure 2.13: Full width at half maximum (FWHM) Δm (Watson and Sparkman, 2008) [modified].

can achieve for a data set is dependent on the transient duration t_{tran} and the cyclotron frequency f_{cyc}, where

$$R_{FT-ICR} \geq \frac{f_{cyc} \times t_{tran}}{2} \ . \tag{2.12}$$

Figure 2.14[9] shows a spectrum of a tuning mix[10] m/z 922 peak with ∼5.8M resolving power, obtained from a ∼1-minute transient after apodization, using the 12-T FT-ICR system shown in Fig. 2.12.

[9]The mass spectra reported in Fig. 2.14 and Fig. 2.16 were prepared using the Bruker Daltonics DataAnalysis Version 4.0 SP 4 and the FTMS Processing tool build 17 from Bruker Corporation (Billerica, Massachusetts, USA).

[10]The tuning mix was purchased from Agilent Technologies (Santa Clara, California, USA).

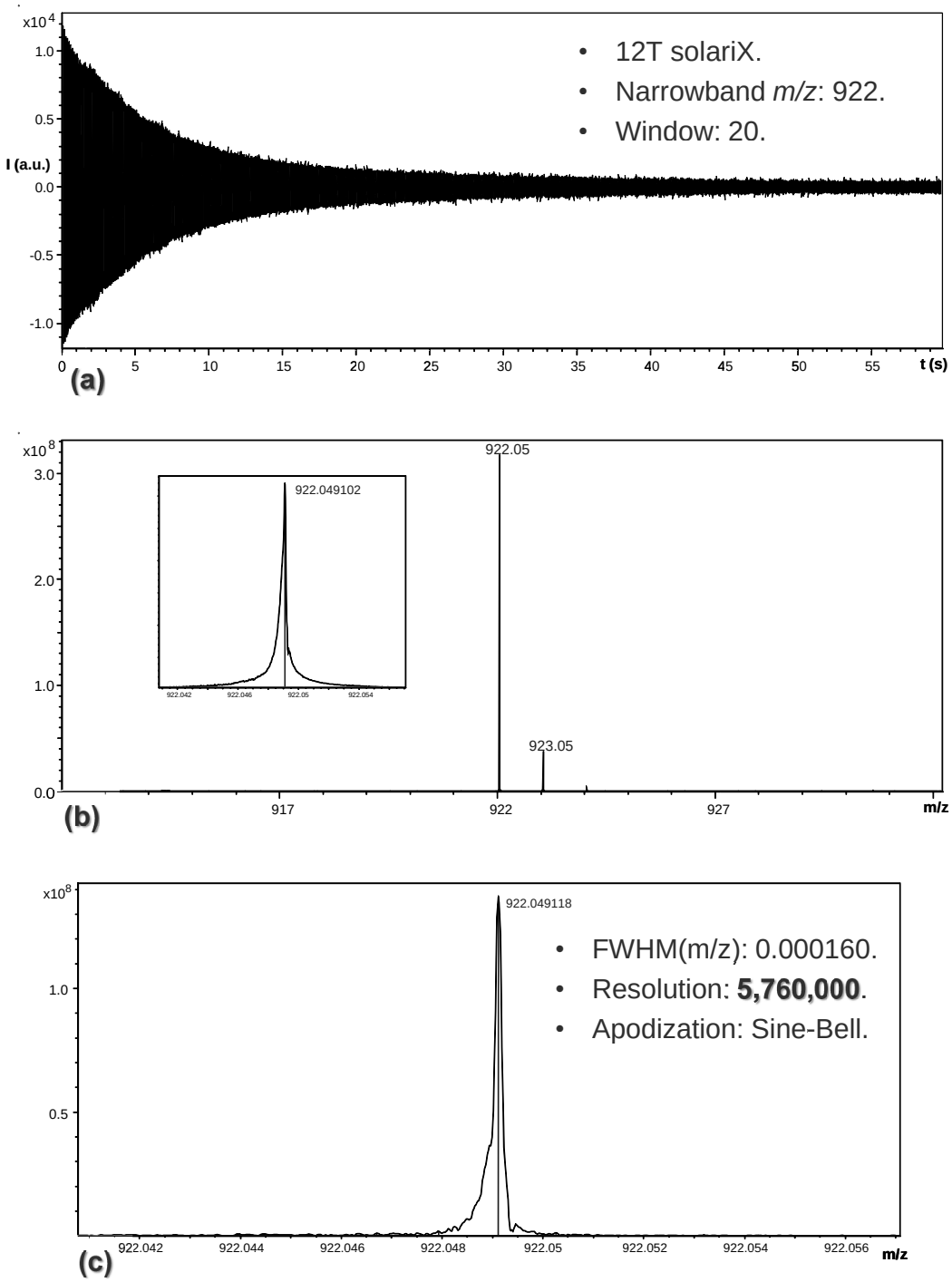

Figure 2.14: Tuning mix m/z 922 peak with (a) ∼1-minute transient and ∼5.8M resolving power using a 12-T FT-ICR system, obtained using a 12-T solariX FT-ICR mass spectrometer, with Narrowband mode (center mass 922; mass range 20) and Q1 isolation of mass 922 with isolation resolution of 20.

2.4.2 Mass Accuracy

Mass accuracy is the measurement to yield the error between the measured m/z and the true m/z in a given spectrum. Mass accuracy $M.A.$ can be calculated in parts per million (ppm) or parts per billion (ppb) as

$$M.A. = \frac{M_{obs} - M_{true}}{M_{true}} \times 10^6 \text{ (ppm)} = \frac{M_{obs} - M_{true}}{M_{true}} \times 10^9 \text{ (ppb)}, \qquad (2.13)$$

where M_{obs} is the experimentally observed, and M_{true} is the true mass values, respectively. Recently, the FT-ICR mass accuracy of around 200 ppb has been reported (Smith et al., 2012; Savory et al., 2011). With the improvement of electric field homogeneity (such as the introduction of a better cell design), the reduction of the space charge effect (to trap and detect one ion at a time), and the advanced method of mass calibration, mass accuracy can be pushed close to its theoretical value.

Ultra high resolving power and mass accuracy are required in different areas of research. For instance, Fig. 2.15 demonstrates the overlapped isotopic distributions of two ions (one labeled with the dots and the other labeled with crosses) being identified by an FT-ICR mass spectrometer (Li et al., 2011b).

2.4.3 Flexibility

An FT-ICR mass spectrometer has the flexibility to be coupled with different ion sources/inlet systems, and to perform many MS/MS techniques, such as electron-

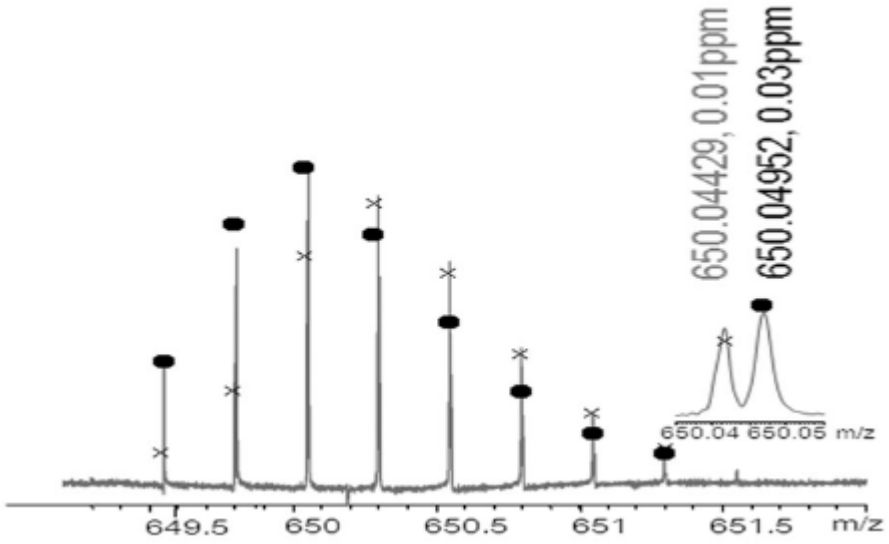

Figure 2.15: Overlapped isotopic distributions of two ions (one labeled with the dots and the other labeled with crosses) being identified by an FT-ICR mass spectrometer (Li et al., 2011b).

capture dissociation (ECD) (Zubarev et al., 1998; Zubarev et al., 2002), sustained off-resonance irradiation collision-activated/-induced dissociation (SORI-CAD/-CID) (Gauthier et al., 1991; Flora et al., 2001), infrared multiphoton dissociation (IRMPD) (Little et al., 1994), ultraviolet photodissociation (UVPD) (Ly and Julian, 2009), or double resonance (Comisarow et al., 1978; Lin et al., 2006), etc., for obtaining detailed structural information. The FT-ICR system shown in Fig. 2.12 has 5 different ion sources (APCI, APPI, EI/CI, ESI, & MALDI), and 6 MS/MS method classes (ECT, ETD, IRMPD, CAD, NS-CAD, & SORI-CAD), and has the potential of being equipped with more sources and MS/MS methods.

Figure 2.16[9] illustrates an example of injecting an infrared (IR) laser to the trapped precursor ions during an ECD process to increase the ECD efficiency. The first spectrum at the top indicates the isolated Substance P m/z 449.9 peak.

The second spectrum from the top shows the spectrum when IR laser is introduced but the energy is low enough not to break any covalent bond. The third spectrum from the top is the normal ECD spectrum of this Substance P m/z 449.9 peak. With the assistance of the "IR laser heating" during the ECD process, the spectrum at the bottom illustrates an increased product ion intensity.

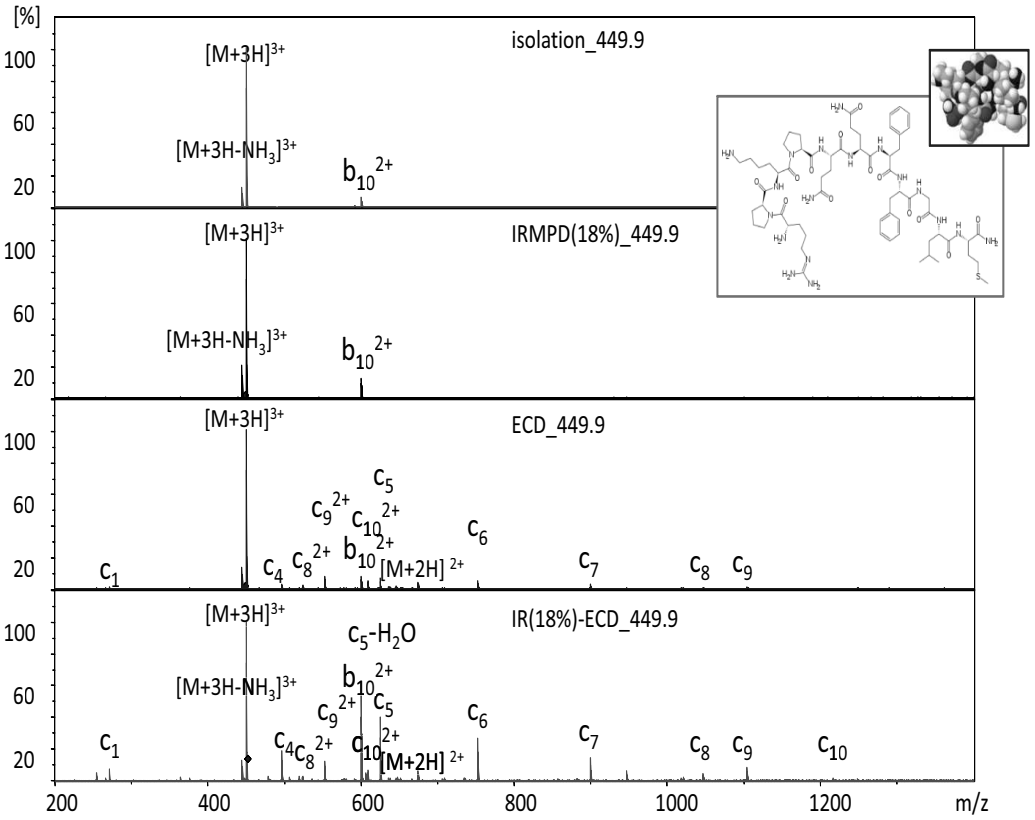

Figure 2.16: IR-ECD spectra of the Substance P m/z 449.9 peak to show the flexibility of the FT-ICR MS flexibility to perform ECD whilst injecting IR laser.

2.5 Front-End Electronics [11]

In the 80s and the 90s, different ICR cell designs were conceived (as shown in Fig. 2.17) to reduce the perturbation caused by the imperfect electrostatic trapping potential to improve performance (Caravatti and Allemann, 1991; Marshall et al., 1998). In recent years, cell design research remains active; a few modern designs have been reported to optimize the in-cell electric field (Brustkern et al., 2008; Tolmachev et al., 2008; Kim et al., 2008; Weisbrod et al., 2010; Misharin et al., 2010; Kaiser et al., 2011b; Nikolaev et al., 2011) to push the FT-ICR MS performance close to its theoretical limit.

With imperfect cells, ion packets experience an imperfect, non-hyperbolic electric field when rotating within an ICR cell at a 'higher' orbital radius. The space charge forces arising from the Coulombic interaction further dynamically perturb the electric fields experienced by the ions and thus affect both frequency and stability (peak width) of the peaks in the spectra thus limiting the mass accuracy. These effects can also result in a rapid loss of coherence in the transient which limits the resolving power (Aizikov et al., 2009). To avoid such phenomena, fewer ions are sent into the cell and excited to a 'lower' rotating orbit for detection. As a consequence, at the detection plates of the cell, the induced current due to the ion motions is smaller, resulting in a weaker signal being presented to the

[11] This section is partially reproduced from the following two journal articles, "A Gain and Bandwidth Enhanced Transimpedance Preamplifier for Fourier-Transform Ion Cyclotron Resonance Mass Spectrometry," *Review of Scientific Instruments*, in 2011 (Lin et al., 2011), and "A Low Noise Single-Transistor Transimpedance Preamplifier for Fourier-Transform Mass Spectrometry Using a T Feedback Network," *Review of Scientific Instruments*, in 2012 (Lin et al., 2012).

front-end electronics.

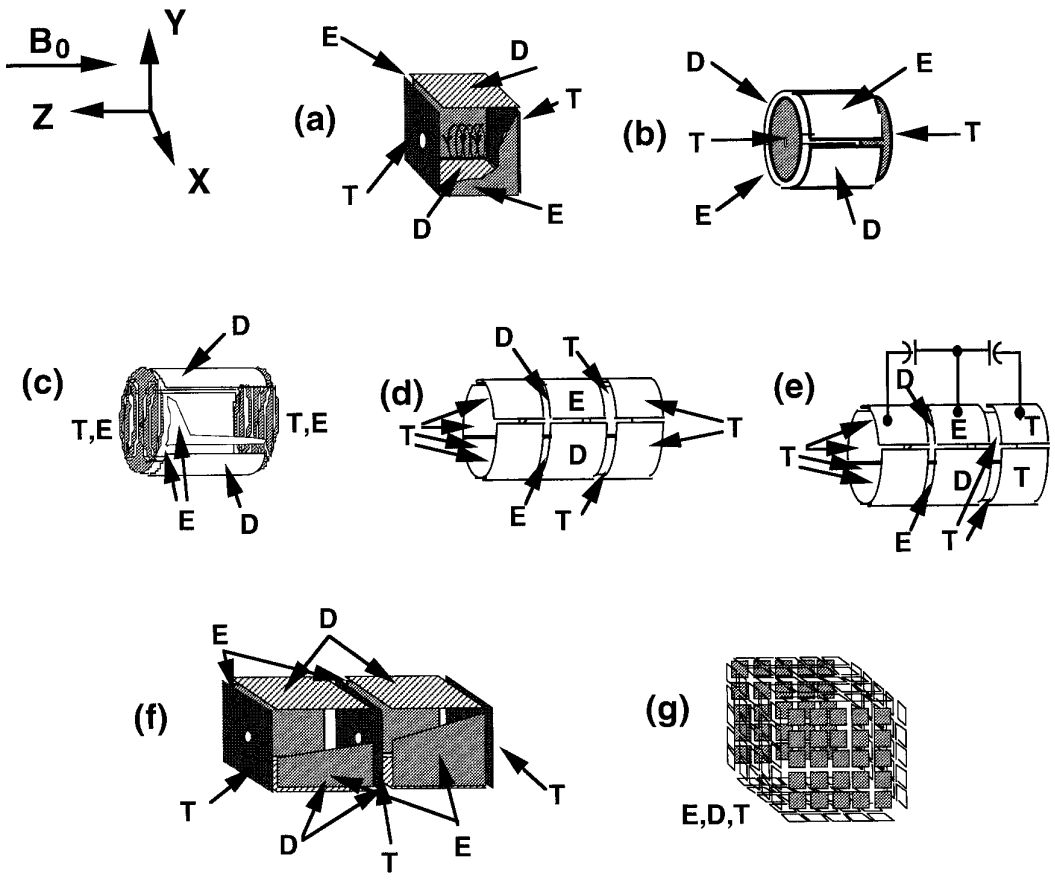

Figure 2.17: Different ICR cell configurations, where **D** indicates the detection, **E** indicates the excitation, and **T** indicates the trapping plates (Marshall et al., 1998).

2.5.1 Signal & Gain

As suggested by Eq. (2.8b), the image current signal from an ICR cell can be theoretically as low as 33 fA (for a singly-charged, 1000-Da ion rotating at the orbit radius of $\frac{1}{4}$ the cell diameter in a 12-T magnetic field) for the goal of single-charge detection. To have a 1-bit change at the least significant bit of the output of a 16-bit ADC with input range of ± 1 V, a transimpedance of 9.3×10^8 Ω

(∼180 dBΩ) is needed for the electronics between the ICR cell and the ADC. Such a large gain can be achieved by introducing several amplifying stages in series, including a preamplifier at the first stage, and several instrumentation amplifiers at the later stages. Figure 2.18 shows such a signal chain with three amplifying stages. The first stage amplifier provides transimpedance A_T for the input signal current s and the noise current n_0 coming from the ICR cell. The transimpedance preamplifier converts the input current into a voltage output for the following second and third stage voltage amplifiers. After the preamplifier, the signal is further amplified by voltage gains G_2 and G_3 at the second and third stage, respectively.

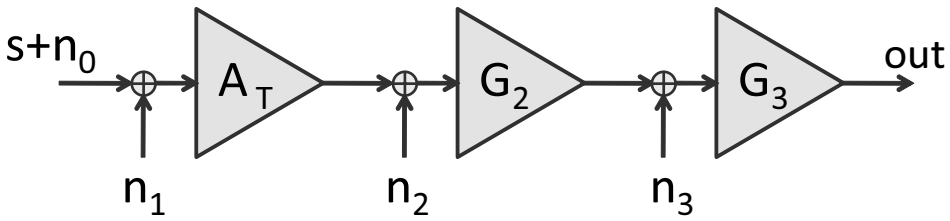

Figure 2.18: Gain and noise distribution in a three-stage amplifier system.

However, each amplifying stage adds its own intrinsic noise onto the signal. In Fig. 2.18 such noises are referred back to the inputs of the first, second, and third stage amplifiers and are represented by n_1, n_2, and n_3 respectively. Note that since the noise n_1, n_2, and n_3 are the referred noise of each amplifier, noise n_1 is current noise whilst the noise n_2 and n_3 are noise values in voltage. Here, for the interpretation convenience, in the following calculations the amplified output signal S, the output noise N, and all other symbols (A_T, G_2 and G_3; s, n_0, n_1,

n_2, and n_3) indicate only the magnitudes (without any dimension or unit) of each of them, respectively.

Here, after the signal processing chain, the output contains not only the amplified signal, S, where

$$S = sA_T G_2 G_3 \ , \tag{2.14}$$

but also the noise, N, where

$$N = (n_0 + n_1)A_T G_2 G_3 + n_2 G_2 G_3 + n_3 G_3 \ . \tag{2.15}$$

The gains G_2 and G_3 are generally greater than 1. With large transimpedance A_T, where $A_T \gg n_2$ and $A_T \gg n_3$, the signal-to-noise ratio (SNR), S/N, at the output can be obtained by dividing Eqn. (2.14) by Eqn. (2.15), and can be approximated as:

$$\begin{aligned} S/N &= \frac{sA_T G_2 G_3}{(n_0 + n_1)A_T G_2 G_3 + n_2 G_2 G_3 + n_3 G_3} \\ &= \frac{s}{n_0 + n_1 + \dfrac{n_2}{A_T} + \dfrac{n_3}{A_T G_2}} \simeq \frac{s}{n_0 + n_1} \ . \end{aligned} \tag{2.16}$$

To conclude, by having significant gain at the first amplifying stage, the contribution of the electronic noise is limited to the first stage, namely, the intrinsic noise of the preamplifier and detection components. To electronically improve the signal-to-noise performance, it is required that the first stage amplifier has not only as much gain as possible within the bandwidth of interest, but also minimal

noise (n_1), so that the preamplifier design is crucial for best performance.

2.5.2 Amplifier Noise

Reducing the noise from a preamplifier can be a major difficulty for a circuit designer. Typically, noise consists of all of the voltages and currents which accompany a signal of interest, and includes (Letzter and Webster, 1970):

- *Johnson-Nyquist noise (thermal noise).* Thermal noise is the electronic noise caused by electron's thermal agitation inside any electrical conductor, first measured and explained by John B. Johnson and Harry Nyquist (Johnson, 1928; Nyquist, 1928).

- *Noise from electronic components or amplifiers (such as shot noise or flicker noise).* Shot noise is caused by the random fluctuation of current (due to the discrete nature of charges) at semiconductor junctions. It was first introduced in 1918 by Walter H. Schottky who studied the current fluctuations in vacuum tubes (Schottky, 1918). Flicker noise was first measured by John B. Johnson (Johnson, 1925) and thereafter Walter H. Schottky provided a theoretical explanation about such noise[12] (Schottky, 1926).

- *Environmental noise.* It includes the interference from the lightning, automotive ignition, structure vibration, etc. Environmental noise can be limited to a negligible level when proper grounding/shielding is provided.

[12]See http://arxiv.org/abs/physics/0204033v1 for information about the history of flicker noise, accessed 15 August 2012.

- *Statistical fluctuations.* It is the noise from the quantization nature of all measurements.

As proper grounding and shielding to the amplifier circuitry minimise the interference from the environmental noise, and the noise of statistical fluctuations rarely becomes a problem, the other two types of noise, thermal noise and amplifier noise, are the major noise sources to be minimised for improving noise performance in a given amplifier design (Letzter and Webster, 1970).

Caused by the thermal agitation of electrons inside conductors, thermal noise can be described as the noise power P_n,

$$P_n = k_B T \Delta f \ , \tag{2.17}$$

which is a function of Boltzmann's constant k_B, the absolute temperature T, and the bandwidth Δf. To describe the thermal noise output from a resistor, the equivalent circuit of a noisy resistor can be modeled by a noiseless resistor R, either coupling in series with a noise voltage source e_n, or shunting a noise current source i_n, shown in Fig. 2.19, where

$$e_n = \sqrt{4 k_B R T \Delta f} \ , \tag{2.18}$$

and

$$i_n = \sqrt{\frac{4 k_B T \Delta f}{R}} \ . \tag{2.19}$$

Note that here the e_n and i_n are the RMS voltage and current, respectively.

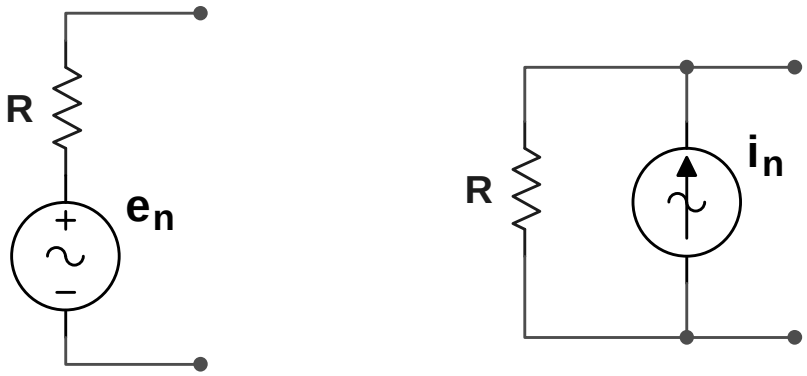

Figure 2.19: Equivalent circuits of the thermal noise for a resistor R.

Shot noise and flicker noise are considered electronic noise sources and are commonly seen in an active device. Usually, flicker noise dominates thermal and shot noise from the frequency of direct current (DC) to ∼100 Hz (Letzter and Webster, 1970). To characterize the noise performance of an amplifier, Letzter and Webster suggested a model comprising a noiseless amplifier with both voltage and current noise sources, e_{na} and i_{na}, respectively, connected to the input, and a noiseless source resistor, R, with its noise voltage source, e_n, coupled in series to the input (Letzter and Webster, 1970), as shown in Fig. 2.20.

From Eq. (2.17), thermal noise power can be decreased by cooling (T), or reducing the bandwidth (Δf). To design and cool a preamplifier to work in the cryogenic temperature of ∼4 K can significantly reduce the thermal noise by about 10 fold. At a given temperature (such as at room temperature), modifying the resistance value in an amplifier system can also reduce the thermal noise volt-

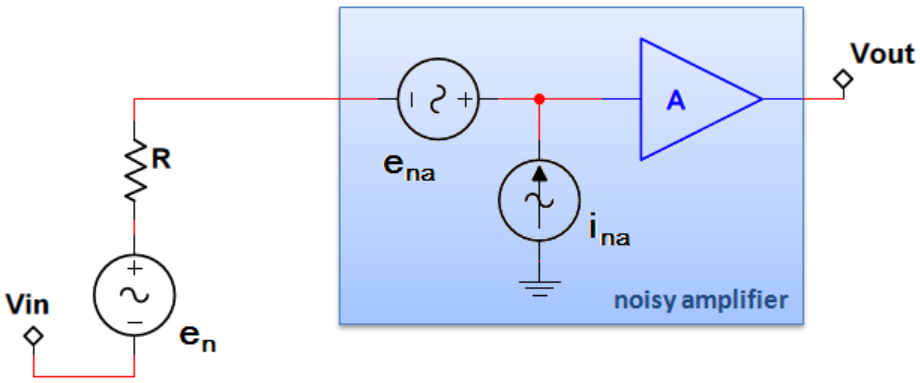

Figure 2.20: The noise model for an amplifier suggested by Letzter and Webster (Letzter and Webster, 1970), including a noiseless amplifier with gain A, an equivalent amplifier noise current generator i_{na}, an equivalent amplifier noise voltage generator e_{na}, and a noiseless source (the input signal source) resistor R with its noise voltage generator e_n.

age. To characterize such a change in an amplifier system illustrated by Fig. 2.20, the corresponding modification to either the noise current generator i_{na}, or the noise voltage generator e_{na}, or both, need to be evaluated carefully. Additionally, limiting the noise generated by the active components can be another approach to improve the signal-to-noise performance of a preamplifier. It can be done by reducing the number of active components being used, and by choosing ultra low noise components.

2.5.3 Existing FT-ICR Preamplifier Designs

As discussed earlier, in terms of sensitivity, the front-end electronics, especially the preamplifier, in an FT-ICR system plays a crucial role. The potential improvement scope for such preamplifiers remains significant. Conventional FT-ICR preamplifiers can provide a signal-to-noise limitation that requires at least 30–100

ions to achieve a signal-to-noise of 3 (Kaur and O'Connor, 2004; Limbach et al., 1993). To obtain the best system performance, the design goal for a preamplifier is generally to boost its gain to the maximum and to limit its noise to the minimum. New preamplifier designs may allow single-charge detection, which would maximize the potential dynamic range of FT-ICR instruments.

Figure 2.21 shows a conventional FT-ICR preamplifier, consisting of a large input resistor and a unity-gain stable operational amplifier (op amp) OPA627,[13] which has a gain-bandwidth product of 16 MHz and a reported noise of 4.5 $\mathrm{nV}/\sqrt{\mathrm{Hz}}$. The preamplifier is mounted close to the ICR cell inside a vacuum chamber to limit the capacitance from cabling, as shown in Fig. 2.21a. Figure 2.21b shows the preamplifier circuit board. Two sets of preamplifiers are sitting on a ceramic board. Each set is responsible for the signal from one of the two detection plates on the ICR cell. The schematic of such a preamplifier is shown in Fig. 2.21c. The current signal I from the ICR cell is converted to voltage by the large input resistor R, and then buffered by a unity-gain voltage follower. The capacitance C indicates the effective parasitic capacitance at the op amp input.

Recently, efforts have been made toward the enhancement of the performance of preamplifiers for FT-ICR MS. In 2007, Mathur *et al.* reported a room temperature differential preamplifier (Mathur et al., 2007), which was based on the Jefferts and Walls' design (Jefferts and Walls, 1989) updated with modern components, with similar configuration shown in Fig. 2.21c. The amplifier system

[13] See http://www.ti.com/product/opa627 for information about op amp OPA627, accessed 15 August 2012.

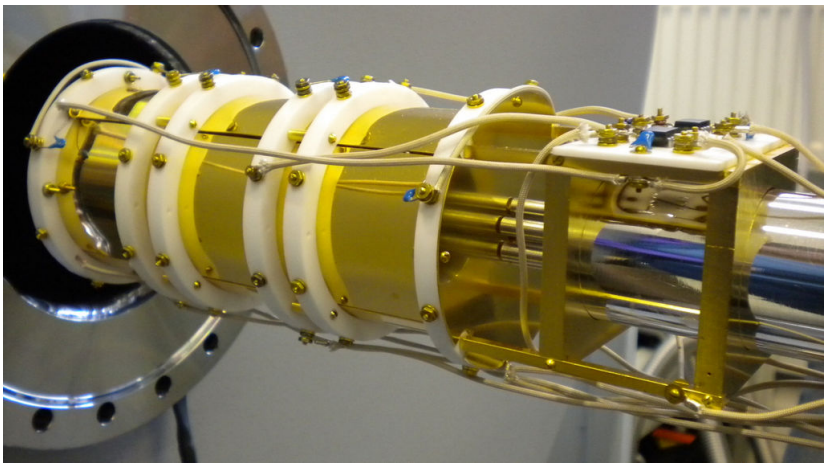

(a) The ICR cell and the mounted preamplifier board.

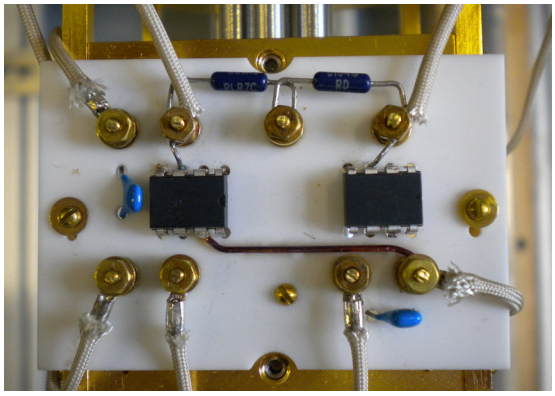

(b) Top view of the preamplifier board.

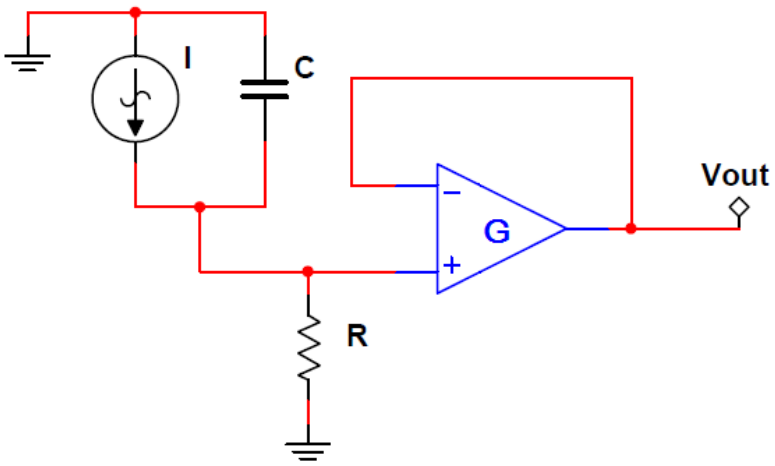

(c) Schematic of the preamplifier.

Figure 2.21: A conventional FT-ICR preamplifier.

(a preamplifier, shown in Fig. 2.22a, and an instrumentation amplifier, shown in Fig. 2.22b) designed by Mathur *et al.* figures a voltage noise spectral density of 7.4 nV/$\sqrt{\text{Hz}}$ at 100 kHz, and a total gain of about 3500 (around 25 at the first stage) between the frequency of 10 kHz and 1 MHz.

In 2002, O'Connor proposed an idea of holding the vacuum system of the FT-ICR MS inside a helium cooled cold bore at the temperature of 4.2 K (O'Connor, 2002). Significantly reducing the thermal noise, the preamplifier design (shown in Fig. 2.23) reported in 2008 (using gallium arsenide (GaAs) field-effect transistors (FETs) to avoid the semiconductor mobility "freezing out" at cryogenic temperature) showed about 20 times improvement in SNR, and had a voltage gain of 250 with 3-dB frequency of 850 kHz (Mathur et al., 2008). Later in 2011, Ivanov and co-workers designed another cryogenic amplifier using a silicon germanium (SiGe) transistor, with a reported input voltage noise spectral density of about 35 pV/$\sqrt{\text{Hz}}$ (Ivanov et al., 2011). However, the high cost of maintaining liquid helium to preserve the 4-K environment prevents such a cryogenic FT-ICR system from being popularized.

Designer	Operating Temperature	Voltage Gain	Bandwidth	Noise Spectral Density
conventional	room	unity	16 MHz	4.5 nV/$\sqrt{\text{Hz}}$
(Mathur et al., 2007)	room	25	1 MHz	7.4 nV/$\sqrt{\text{Hz}}$
(Mathur et al., 2008)	cryogenic	250	850 kHz	–

Table 2.1: Summary of the existing FT-ICR preamplifiers.

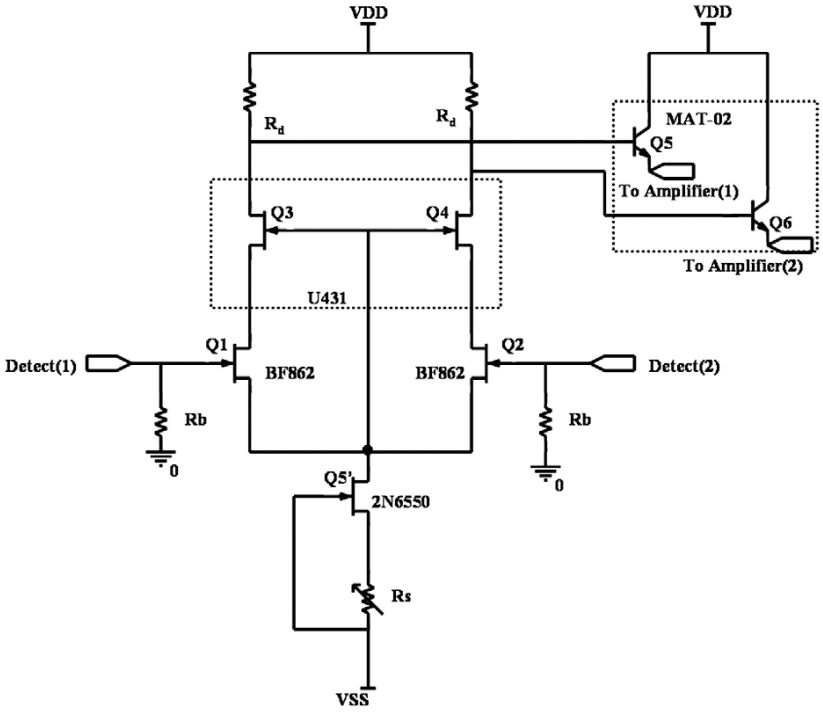

(a) Schematic of the preamplifier.

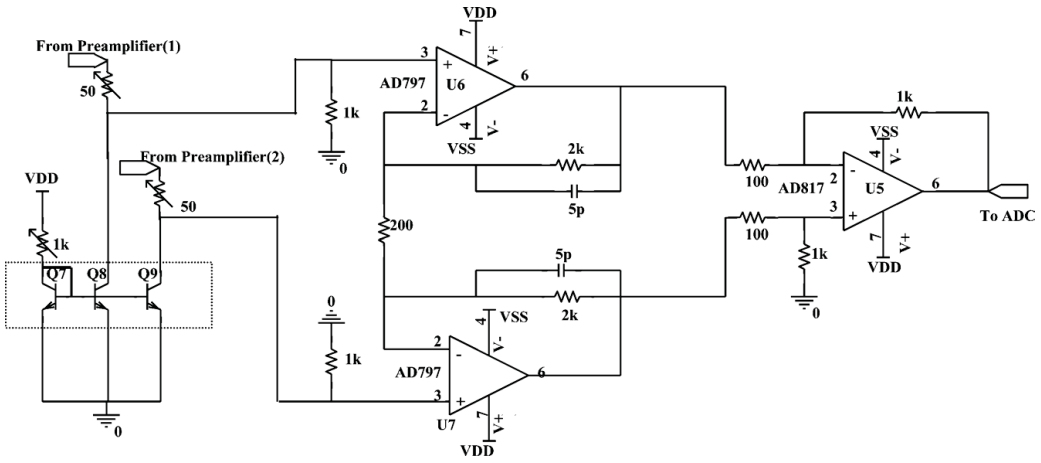

(b) Schematic of the instrumentation amplifier.

Figure 2.22: The room-temperature FT-ICR amplifier system designed by Mathur and co-workers in 2007 (Mathur et al., 2007).

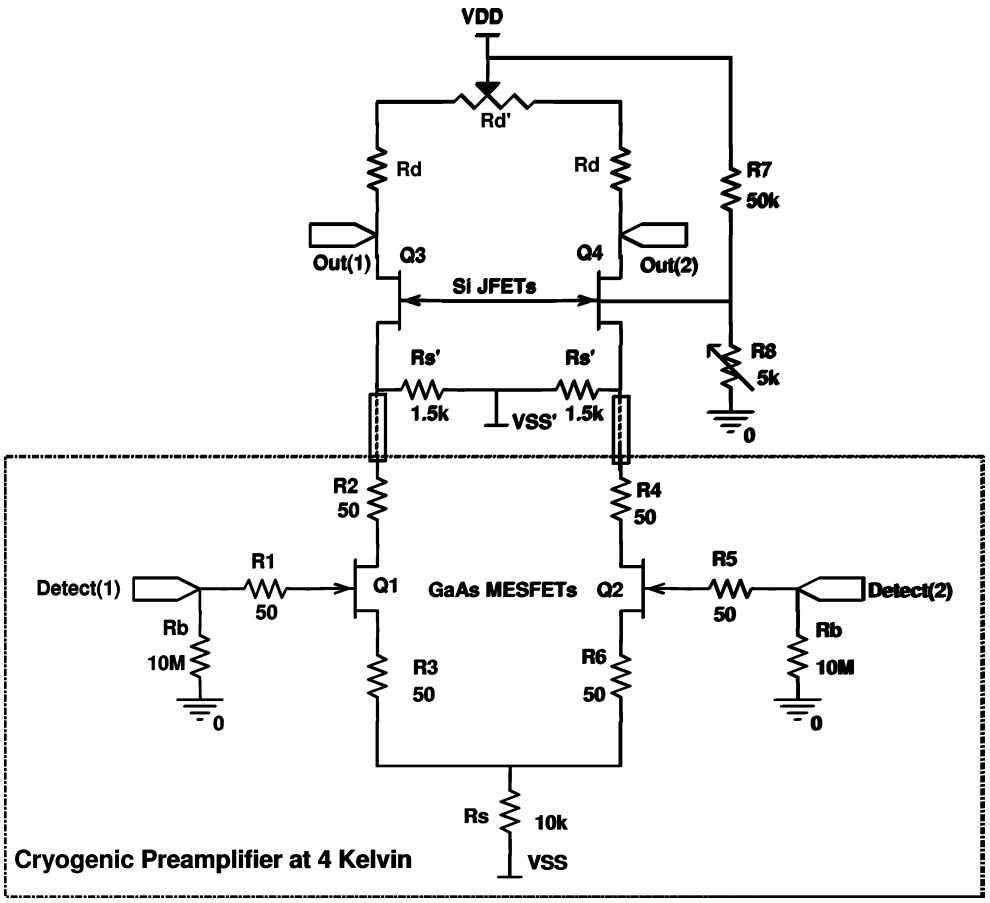

Figure 2.23: The cryogenic FT-ICR preamplifier reported by Mathur and coworkers in 2008 (Mathur et al., 2008).

Among the designs mentioned above, the signal current is converted into a voltage by a large input resistor, which acted as a major noise source at the input node, before being further processed by the following voltage amplifiers. As single-charge detection is one of the solutions to avoid space charge issues in an ICR cell, a preamplifier with improved signal sensitivity and noise performance is essential for such a goal.

The parasitic capacitance from the ICR cell and cabling shunts such a large input resistor, which limits the bandwidth. The parasitic capacitance from the ICR cell in an FT-ICR system can vary from around 10 pF to over 100 pF (Kaiser et al., 2011a), depending on the cell dimensions, feedthroughs, and cabling. The preamplifier circuit reported by Mathur and co-workers in 2008 used a 10-MΩ input resistor (Mathur et al., 2008). A 100-pF capacitance shunting a 10-MΩ resistance causes a $1/RC$ corner at ∼160 Hz. However, a 12-T FT-ICR system demands a bandwidth of at least 1 MHz. Meanwhile, more complicated modern ICR cell designs introduce more input capacitance to the preamplifier. As a result, a preamplifier with an enhanced tolerance to the input capacitance is demanded for further FT-ICR systems.

2.6 Conclusion

This chapter first reviews the general MS related history and the theory of the FT-ICR operation. The nature of the ion signal and the electronic noise have also been studied to understand the electronic detection limit for an ICR cell

in an FT-ICR system. In particular, the cyclotron frequency equation and the calculated theoretical current signal intensity from a 12-T FT-ICR system serve as important references for designing the MS ion detector and data system. Then the existing preamplifiers for ICR signal detection is reviewed, followed by the suggested potential scope for improvement. New FT-ICR preamplifier designs and their testing results will be reported later in Chapter 5 (a transimpedance preamplifier using an op amp) and Chapter 6 (a single-transistor transimpedance preamplifier using a T feedback network).

CHAPTER 3

Quadrupole Ion Guide & Mass Filter

This chapter introduces the theory of operating a quadrupole ion guide is provided, followed by the introduction of the Mathieu equation, stability diagram, and quadrupole mass filtering theory. Then this chapter reviews the existing quadrupole power supply designs. The problems of building a power supply for a quadrupole mass filter are discussed in this chapter, whilst a new power supply design will be presented in Chapter 7.

3.1 Introduction

The linear quadrupole has been used for ion transportation and mass filtering in scientific apparatus since the late 50s (Paul, 1990; Douglas, 2009), and is still widely used in mass spectrometers. The history of quadrupoles and the theory of the motion of charged particles in radio-frequency (RF) fields have been comprehensively reviewed in many excellent papers and books, in particular, by Gerlich (Teloy and Gerlich, 1974; Gerlich, 1992), Dawson (Dawson, 1976), Paul

(Paul, 1990), March (March, 1997) and Todd (March and Todd, 2009), and Douglas (Douglas, 2009) and co-workers (Douglas et al., 2005).

A quadrupole comprises ideally hyperbolic but commonly cylindrical electrodes in a square formation, as shown in Fig. 3.1. Two pairs of rods are connected with opposite-polarity RF signal applied electrically, and establish a two-dimensional field in the x-y plane. Ions oscillate in the x-y plane whilst traveling along the z direction (March and Todd, 2005).

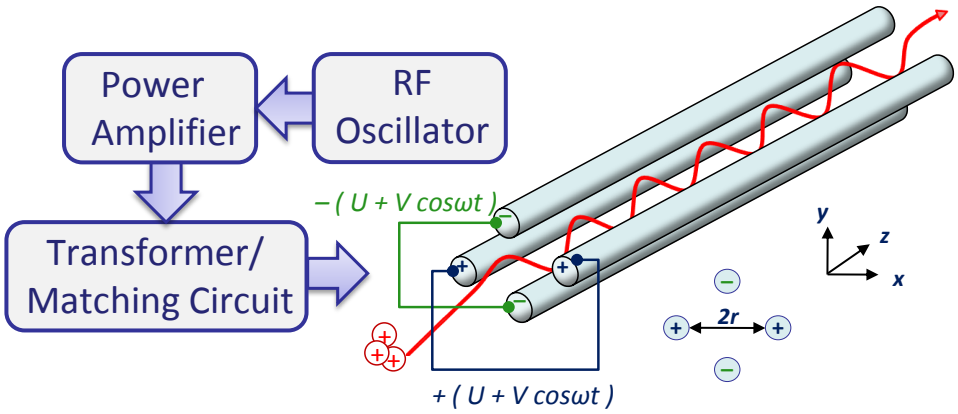

Figure 3.1: Three major stages of a quadrupole ion guide power supply, and the schematic of a quadrupole ion guide illustrating the electrical connections.

To operate a quadrupole with radius r (the inscribed circle tangential to the rods' surfaces), opposite polarity RF signals $\pm\phi(t)$ with amplitude V, angular frequency ω, and a superimposed direct current (DC) offset U, are applied to the adjacent rods of a quadrupole, where

$$\phi(t) = \pm(U + V\cos\omega t) \ . \tag{3.1}$$

The RF signals mentioned in Eq. (3.1) are generated by a "power supply" which comprises three major stages/parts, as illustrated by Fig. 3.1:

- *RF Oscillator (First Stage)*: the oscillating source. In some circuits, such as the power supply reported by O'Connor and co-workers (O'Connor et al., 2002), this is a feedback system involving the next stage power amplifier. By feeding the output the amplifier back to the input, the circuit will oscillate at a self-tuned resonant frequency.

- *Power Amplifier (Second Stage)*: the main driving stage to amplify the signal generated by the source to drive the quadrupole ion guide.

- *Transformer/Matching Circuit (Third Stage)*: the output stage after the power amplifier. It is usually either a transformer to convert the output voltage of the power amplifier to a higher value, or a matching circuit for resonant frequency tuning or impedance matching, or both. If a DC offset is to applied to the quadrupole, the offset voltage can be introduced in this stage.

Due to the strict requirement of the output frequency and amplitude tolerances, to design a power supply for a quadrupole mass filter requires more attention than for a ion guide. The details of such design requirements will be discussed later.

3.2 Theory of the Quadrupole Operation

The theory of operating a quadrupole device is widely reviewed. The basic concepts will be summarized here, based on the interpretation in the book written by March and Todd (March and Todd, 2005).

3.2.1 Quadrupolar Potential

To simplify the following derivation, the assumption has to be made that there is only one gas-phase ion travels in a quadrupole with hyperbolic electrodes, infinite rod length, and complete absence of background gas. The potential in the electric field of a quadrupolar device in the Cartesian co-ordinates $\phi_{x,y,z}$ has a general form of

$$\phi_{x,y,z} = \frac{\phi_0}{2r^2}(\lambda x^2 + \sigma y^2 + \gamma z^2) \ , \tag{3.2}$$

where λ, σ, and γ are weighting constants for the x, y, and z coordinates, respectively; ϕ_0 is the net potential applied to the single ion in the quadrupole, where

$$\phi_0 = \phi_{x-pair} - \phi_{y-pair} = 2(U + V\cos\omega t) \ . \tag{3.3}$$

To satisfy the Laplace condition of

$$\nabla^2\phi_{x,y,z} = 0 \ , \tag{3.4}$$

the numbers of

$$\lambda = -\sigma = 1 \; ; \qquad \gamma = 0 \tag{3.5}$$

can be assigned for the two-dimensional devices. As a result, the quadrupolar potential at point (x, y) can be expressed as

$$\phi_{x,y} = \frac{\phi_0}{2r^2}(x^2 - y^2) \; . \tag{3.6}$$

3.2.2 Mathieu Equation

According to Eq. (3.3), if only the component of motion in the x-direction is considered, the force acting on this ion at the point (x, 0), F_x, is

$$F_x = m\frac{d^2x}{dt^2} = -ze(\frac{d\phi_{x,y}}{dx})_{y=0} = -ze\frac{\phi_0 x}{r^2} \; , \tag{3.7}$$

where z is the number of charges on the ion, e is the electron charge, m is the mass of the ion, and the negative sign suggests that the force acting on the ion is in the opposite direction of the increasing x. By substituting Eq. (3.3) into Eq. (3.7), the equation can be expanded to

$$\frac{d^2x}{dt^2} + (\frac{2zeU}{mr^2} + \frac{2zeVcos\omega t}{mr^2})x = 0 \; , \tag{3.8}$$

which is a canonical form of the Mathieu Equation

$$(\frac{d^2u}{d\xi^2}) + (a_u - 2q_u cos2\xi)u = 0 \ . \tag{3.9}$$

By substituting $u = x$ and $\xi = \omega t/2$, the dimensionless stability parameters a_x and q_x become

$$a_x = \frac{8zeU}{mr^2\omega^2} \qquad \text{and} \qquad q_x = \frac{-4zeV}{mr^2\omega^2} \ , \tag{3.10}$$

where U, V, ω, and r are the previously mentioned DC voltage, RF signal amplitude, angular frequency, and the inscribed circle radius, respectively. Because of the conditions given by Eq. (3.5), the derivation of the force on the traveling ion in the y-direction can be obtained as $a_y = -a_x$ and $q_y = -q_x$.

3.2.3 Stability Diagram

As a result, the ion motion (in either x or y direction) in such electric fields can be described by the Mathieu equation with parameters a_u and q_u, where u represents the co-ordinate axis x or y depending on the geometrical direction to be considered. The solutions to the Mathieu equation can be interpreted in terms of ion trajectory stability in the stability diagram, as shown in Fig. 3.2 (de Hoffmann and Stroobant, 2007). A stable ion trajectory can be obtained when the parameters a_u and q_u fall into one of the stability regions, where the traveling ion is stable in both x and y-directions, of the Mathieu equation. It is

shown in Fig. 3.2 that there are a few regions that are stable along both x and y-directions, such areas A, B, C, and D.

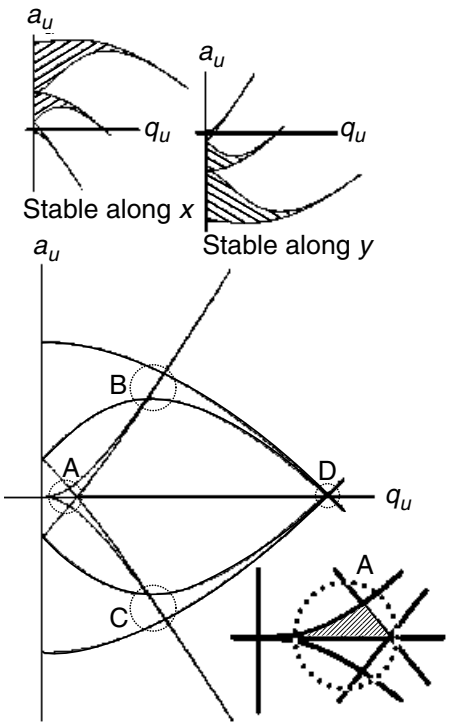

Figure 3.2: The Mathieu stability diagram (de Hoffmann and Stroobant, 2007).

It is common to run a quadrupole in the first stability region (area A in Fig. 3.2), though to run the quadrupole device in other stable regions was also reported (Hiroki et al., 1991). Figure 3.3 illustrates the first stable region. The area confined by q-axis and both blue and red solid lines is the stable region. When running a quadrupole as an ion guide, in the so-called "RF-only" mode, the DC voltage U is set to 0 to operate the quadrupole so that ions are positioned along the q-axis, which allows any ion to be transported stably in a given quadrupole system as long as its mass-to-charge ratio (m/z) satisfies the low-mass cut off (LMCO) condition of $q_u \leq 0.908$. For instance, a quadrupole with size r

of 5 mm operating at the frequency of 1 MHz and the supplied RF amplitude V of 200 V has a LMCO of 86 Da for a singly-charged ion.

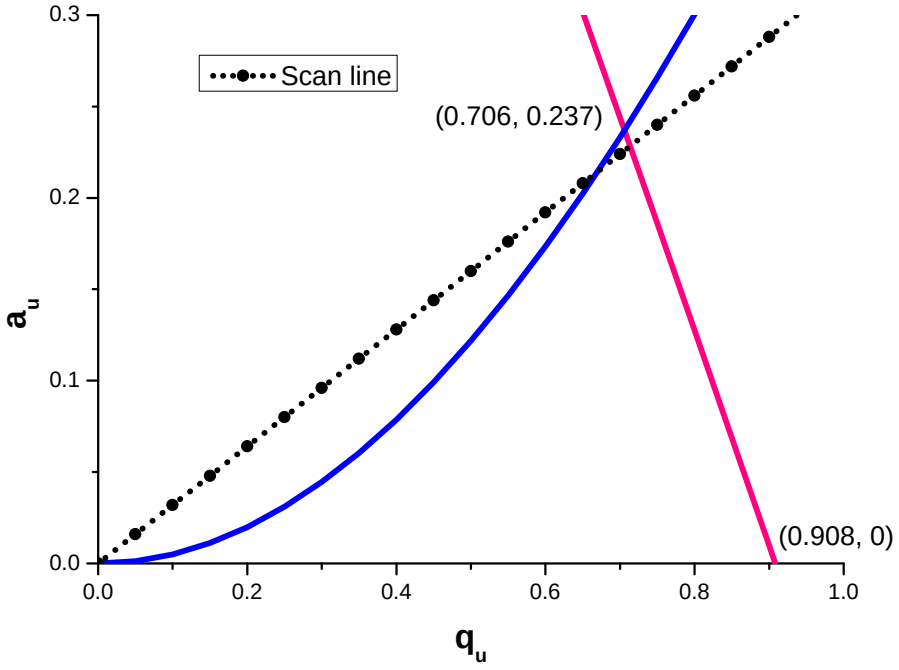

Figure 3.3: The first stability region in a stability diagram.

3.3 Mass Filter

To run a quadrupole as a mass filter, a DC voltage (U in Eq. (3.1)) is superimposed on the RF signal supplying the system. In general, the quadrupole is tuned and run along certain "scan line" (the dotted line shown in Fig. 3.3). On the scan line, heavier ions lie closer to the origin. With a fixed running frequency, the slope of the scan line can be adjusted by changing the ratio of DC voltage U and RF amplitude V. When the parameters of the system are set so that the

scan line is inside the stable region but very close to the tip, where $q_u = 0.706$ and $a_u = 0.237$, only ions within a very narrow window of m/z values can be transported. The closer to the tip, the higher the potential resolving power of the mass filter. To tune the system electronically closer to this tip of the stability diagram, signals of very stable values of U, V, and ω have to be generated to supply the quadrupole mass filter. This requirement becomes more stringent as one increases the masses of the ions one wishes to resolve. Specifically, the variation of the output amplitude and frequency of a mass filter power supply has to be limited to narrow the filtering window. The requirements for precise mass selection was described by Austin and co-workers in a quadrupole mass spectrometry book edited by Dawson in 1976 (Austin et al., 1976) as

$$\frac{\Delta m}{m} = \frac{\Delta V}{V} - \frac{2\Delta\omega}{\omega} \ . \tag{3.11}$$

It was also stated by Austin *et al.* (Austin et al., 1976) that over the operating range of 0–200 Da, a mass stability of better than 0.1 Da can be achieved if $\Delta\omega/\omega$ and $\Delta V/V$ are below 2.5×10^{-4} and 5.0×10^{-4}, respectively. As a result, most of the reported quadrupole power supplies are capable of driving an ion guide, but only a few of them have the potential to drive a mass filter with 0.1-Da resolution.

3.4 Existing Power Supply Designs

In 1976, some basic building blocks, such as a rectifier, a crystal oscillator, a RF output circuit, for a mass filter power supply were given by Austin *et al.* in the book edited by Dawson in 1976 (Austin et al., 1976). Such circuit intended to supply a 4-MHz signal up to 1000 V.

Since the late 90s, a series of power supplies for ion guides have been designed for mass spectrometry instrumentation. In 1997, Jones *et al.* reported a simple RF power supply for ion guides (Jones et al., 1997), using a pair of 6146B transmitter vacuum tubes in a push-pull configuration. The operating frequency was set by the output impedance, which was a combination of the output tank coil and the total shunting capacitance, and could be tuned up to ∼30 MHz. The output could be switched off by a transistor-transistor logic (TTL) signal, and the RF amplitude could be adjusted from 50 to 600 V by computer or manually, while the maximum power dissipation was ∼140 W. Such design was further improved by Jones and Anderson in 2000, as shown in Fig. 3.4 (Jones and Anderson, 2000), with reduced complexity, size, and cost.

In 2002, O'Connor *et al.* reported a high voltage RF oscillator for driving multipole ion guides (O'Connor et al., 2002). This oscillator was a modification based on Jones and Anderson's design, to (a) replace the vacuum tubes by the bipolar junction transistors (BJTs) 2SC5392, (b) introduce a tightly coupled air-core transformer to separate the DC offset from the power supply voltage, while providing feedback signal, and (c) include an automatic gain control (AGC) to

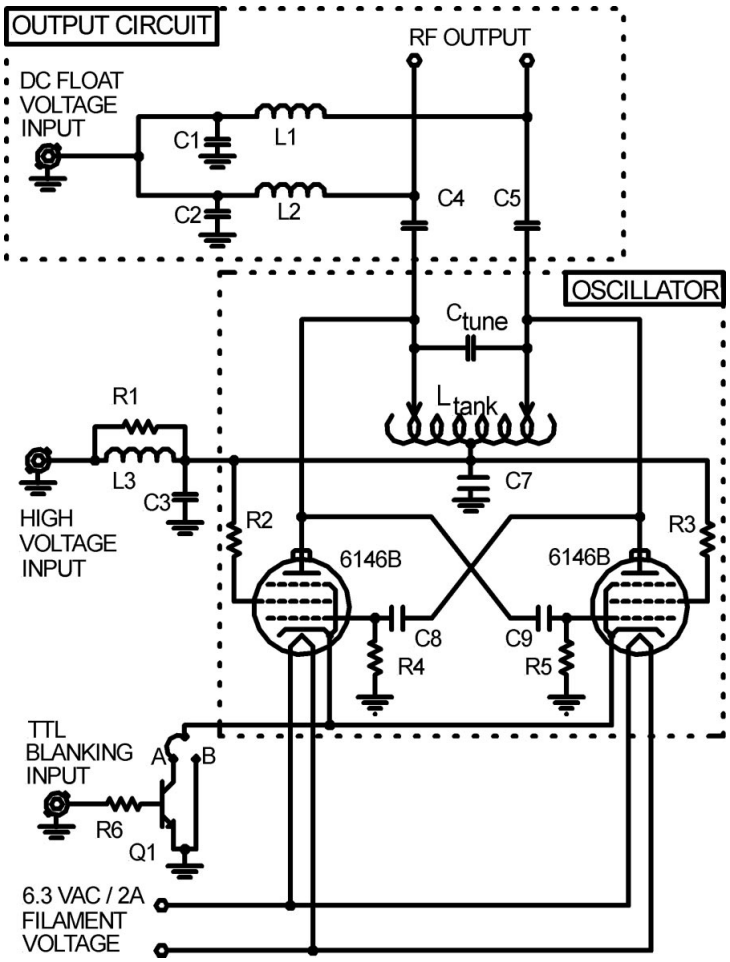

Figure 3.4: Schematic of the simplified RF source designed by Jones and Anderson (Jones and Anderson, 2000).

linearly correlate the output RF amplitude of 0–500 V with a reference DC voltage of 0–10 V. The output frequency was tunable from 500 kHz to 1.5 MHz by changing the impedance of the matching components. In their report, a simple regulating circuit was also provided for an unregulated power supply. Later in 2006, Mathur and O'Connor implemented a similar oscillator, in which the BJT BUH51 replaced 2SC5392, on a printed circuit board (PCB) (Mathur and O'Connor, 2006). The circuit of such a design is shown in Fig. 3.5 (Mathur and

O'Connor, 2006). Mathur and O'Connor further studied the PCB design constraints, such as track spacing and width, heat dissipation, parasitic impedance, and electromagnetic interference. The details and the PCB files can be downloaded from the Internet.[14]

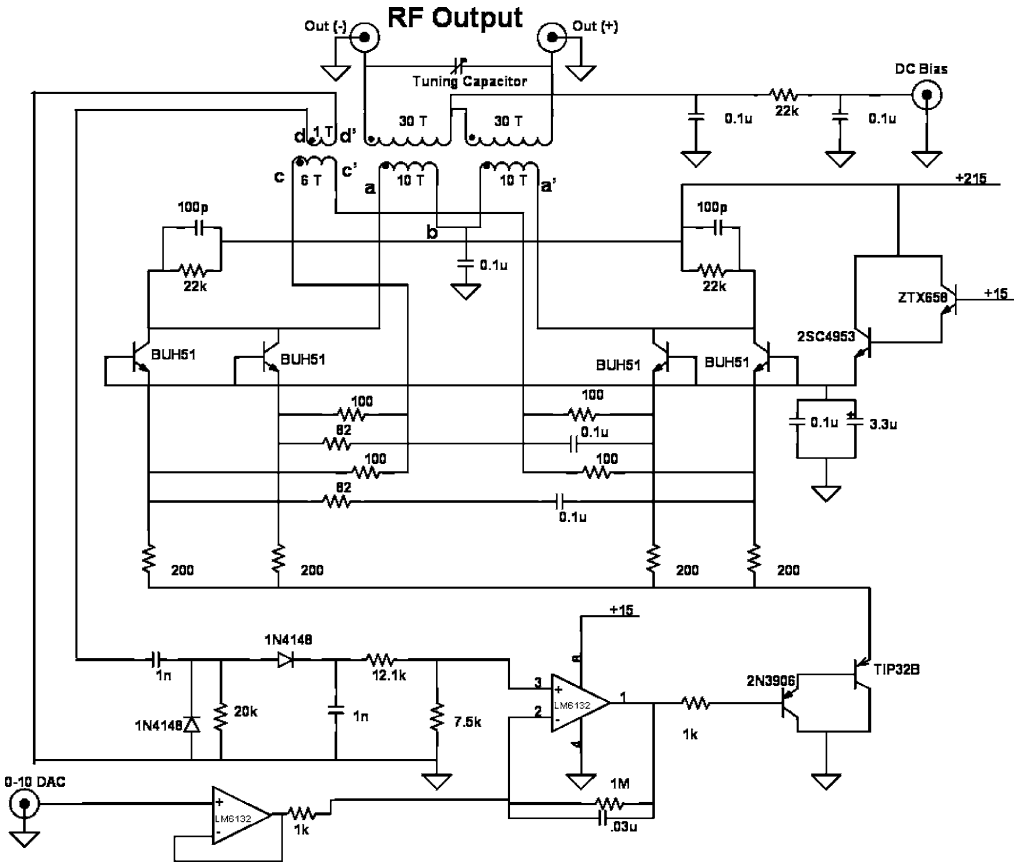

Figure 3.5: Schematic of the RF oscillator designed by Mathur and O'Connor (Mathur and O'Connor, 2006).

In 2005, Cermak designed a compact RF power supply that could be run between the frequency range of 4 to 8 MHz, depending on the output transformer and capacitors (Cermak, 2005). In this design, two power metal-oxide-

[14]See http://warwick.ac.uk/oconnorgroup/research/rfoscillator/ for information about the RF oscillator PCB designed by Mathur and O'Connor in 2006, accessed 10 August 2012.

semiconductor field-effect transistors (MOSFETs) were used as the main power amplification stage, which was driven by externally synchronized oscillators derived monostable flip-flops and buffers, as shown in Fig. 3.6 (Cermak, 2005). A stable operation, when the amplitude was 200 V with ∼50 W power consumption, was reported.

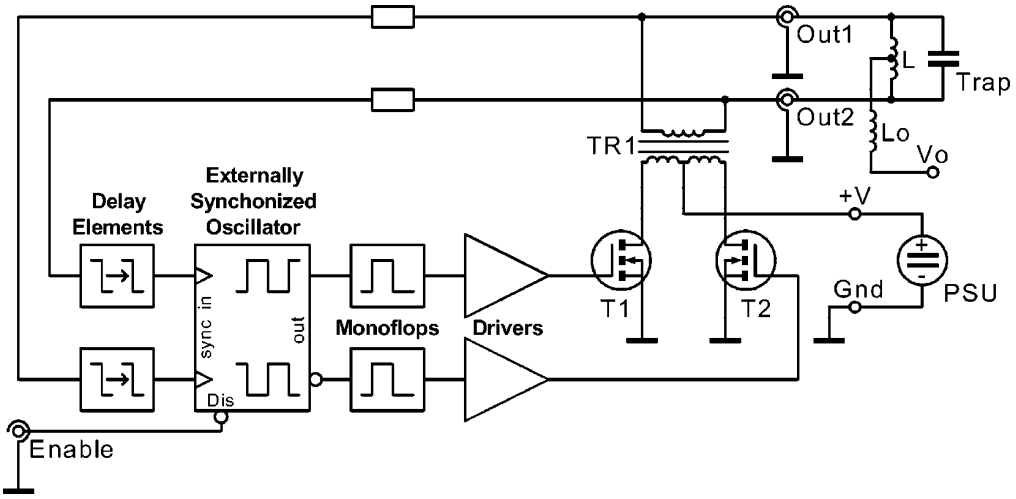

Figure 3.6: Principle schematic of the RF power supply designed by Cermak (Cermak, 2005).

In 2006, Chang and Mitchell reported a frequency stabilized RF generator to drive ion traps. Vacuum tubes 6146W were used, and the oscillation frequency was phase locked to an external reference oscillator (Chang and Mitchell, 2006). With the presence of an amplitude gain control unit, the circuit, as shown in Fig. 3.7, was set to run at the frequency of ∼800 kHz, with amplitude of 8–400 V.

In 2008, Robbins and co-workers designed a computer-controlled, variable-frequency power supply that allowed an output RF amplitude of 5–500 V over

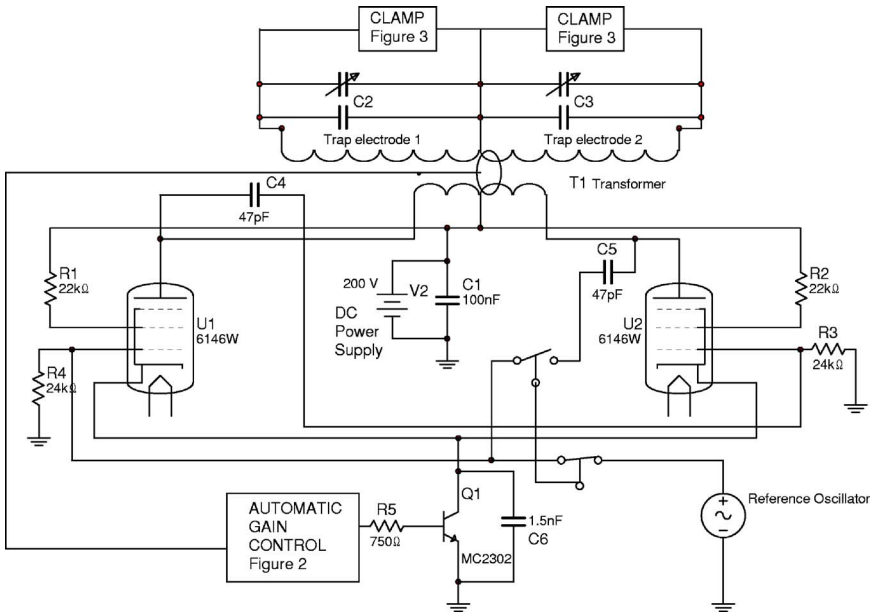

(a) Principle schematic.

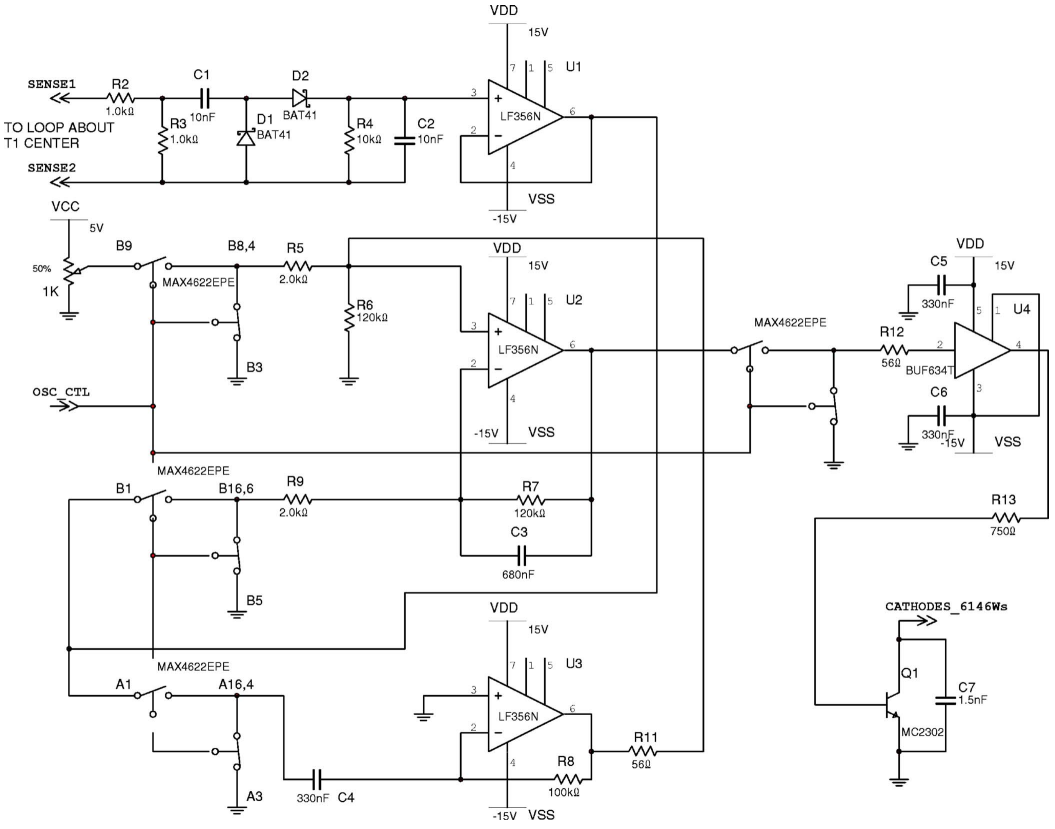

(b) Gain control unit.

Figure 3.7: Schematic of the frequency stabilized RF generator for ion traps designed by Chang and Mitchell (Chang and Mitchell, 2006)

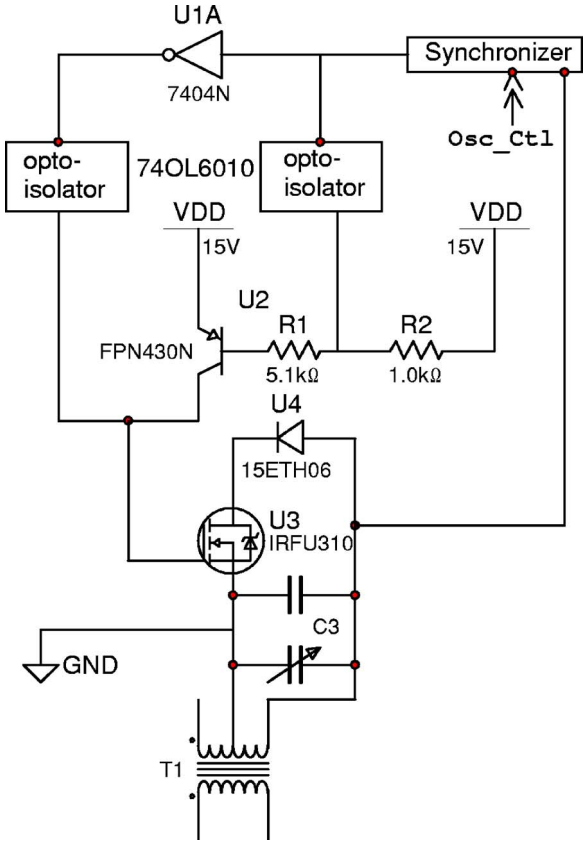

(c) Clamp circuit.

Figure 3.7: Schematic of the frequency stabilized RF generator for ion traps designed by Chang and Mitchell (Chang and Mitchell, 2006).

the frequency range of 350–750 kHz (Robbins et al., 2008). In such system, the reference waveform was produced by a computer-controlled waveform generator, as shown in the detailed schematic in Fig. 3.8 (Robbins et al., 2008). At the transformer output stage, a computer-controlled stepper motor was used to change the shaft angular position of an air-gap variable tuning capacitor to match the output impedance to a resonant frequency assigned by the computer.

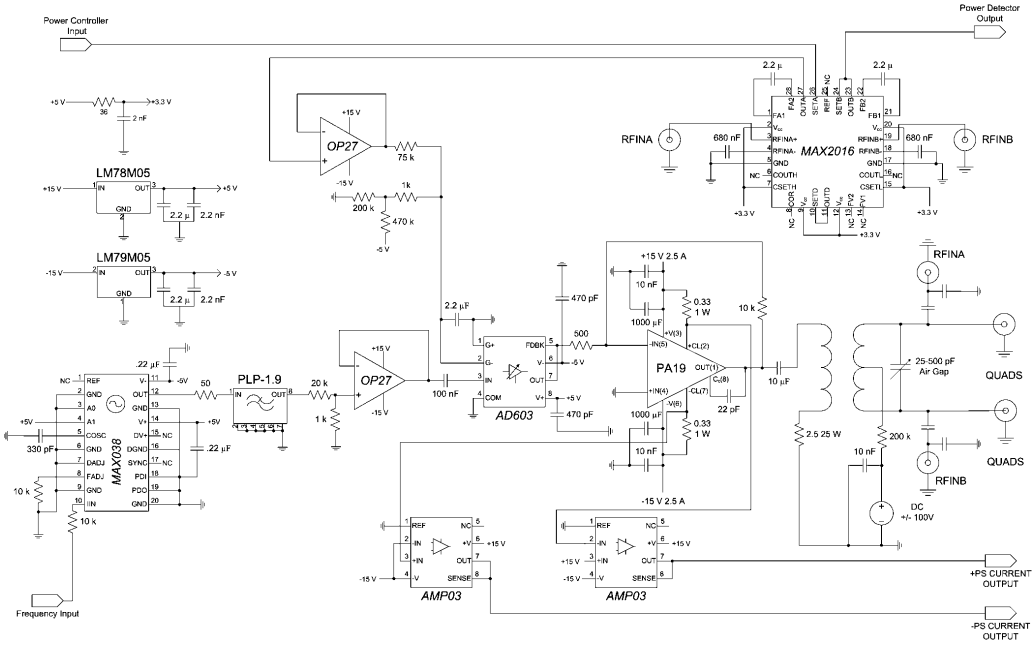

Figure 3.8: Detailed schematic of the RF circuit designed by Robbins *et al.* (Robbins et al., 2008).

In 2011, Jau *et al.* reported a low power RF oscillator using complementary metal-oxide-semiconductor (CMOS) logic gates, which was utilized on a 2×2 cm PCB for driving a small ion trap ($2 \times 2 \times 10$ mm) (Jau et al., 2011). This design delivered frequencies from 0.1 to 10 MHz, and the output RF amplitude was tested up to 400 V while the DC voltage supply to the system could be lower than 7 V. The circuit is shown in Fig. 3.9 (Jau et al., 2011).

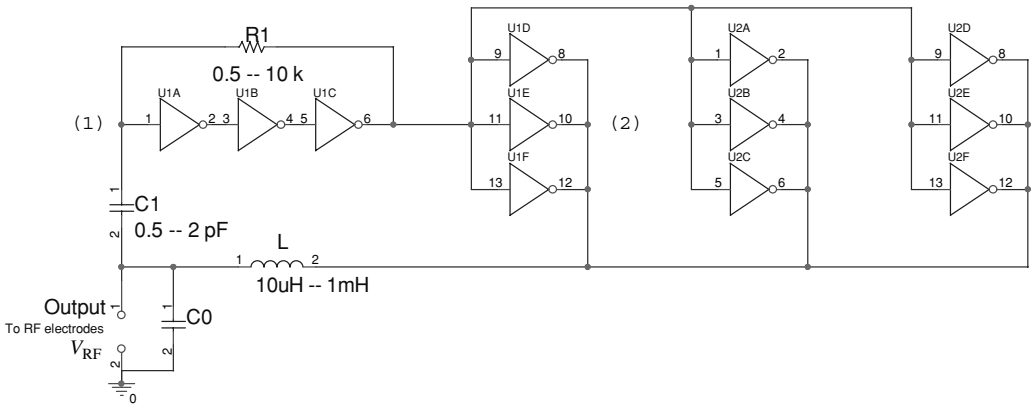

Figure 3.9: The ion trap driving circuit using CMOS inverters, designed by Jau *et al.* (Jau et al., 2011).

As described by Eq. (3.10), the dimension of a quadrupole (r, the inscribed circle radius) plays a role when one tries to tune the operation of a quadrupole system into the stability regions of the stability diagram. Therefore, the specifications (in particular, the output frequency and amplitude) of the reviewed existing power supply designs are different. The power supply circuits mentioned above are summarised in Table 3.1.

Apart from the power supply circuits, a zero-method control circuit to regulate the DC and RF voltages was reported by Tsukakoshi *et al.* in 2000 (Tsukakoshi et al., 2000). In 2007, Franceschi *et al.* reported a matching network, with capability to provide a DC offset, to match the output impedance of a commercial RF generator to an ion guide system with high Q (Franceschi et al., 2007). Another LC coupling network was reported by Canterbury *et al.* in 2010 for high field asymmetric waveform ion mobility spectrometry (Canterbury et al., 2010).

Designer / Year Reported	Output Frequency (Hz)	Output Amplitude (V)	Main Component
(Austin et al., 1976)	4M	1000	vacuum tube
(Jones et al., 1997) (Jones and Anderson, 2000)	30M	50–600	vacuum tube
(O'Connor et al., 2002) (Mathur and O'Connor, 2006)	0.5–1.5M	0–500	BJT
(Cermak, 2005)	4–8M	200	MOSFET
(Chang and Mitchell, 2006)	800k	8–400	vacuum tube
(Robbins et al., 2008)	350–750k	5–500	power op amp
(Jau et al., 2011)	0.1–10M	400	CMOS logic gate

Table 3.1: Summary of the existing RF power supplies.

3.5 Quadrupole Power Supply Problems in Mass Filtering

Among the designs mentioned in Section 3.4, transformers are commonly used at the output stage of the RF oscillator circuitry. Potentially, the output RF amplitude can be modified by changing the turns ratio of the transformer. However, the impedance of a transformer changes with its dimensions and the number of turns of the coil. Quadrupole ion guides are capacitive loads. The resonant frequency of the oscillator output is determined by the equivalent output inductance and capacitance, which depend on the transformer size, tuning capacitors, cabling, and the ion guide dimensions and resultant capacitance. When the operating

frequency is fixed, increasing the output-to-input turns ratio of the output transformer may theoretically increase the output amplitude, but the offset resonant frequency due to the output impedance change could result in a dramatic amplitude decrease. It was commonly reported that the output RF amplitude was changed after connecting the oscillator circuit to the quadrupole. The impedance mismatch is believed to be the main reason causing such amplitude loss. On the other hand, if the transformer is part of the resonance circuit, such impedance change will modify the output frequency. Therefore, if in the RF oscillator stage (the first stage, as shown in the diagram in Fig. 3.1) of a power supply, a LC resonance circuit is used for generating the RF signal, such a power supply can only drive an ion guide, not a mass filter.

Many of the ion guide power supply designs previously reported (Jones et al., 1997; Jones and Anderson, 2000; O'Connor et al., 2002; Mathur and O'Connor, 2006) used a similar feedback scheme to start the oscillation. Those oscillators operated with a self-tuned resonant frequency, which was set by the output transformer and the shunting capacitance. For instance, Fig. 3.10 (O'Connor et al., 2002) shows the basic building block of the differential common-base power amplifier of the design by O'Connor and co-workers. The output transformer forms part of the resonance circuit, and also generates feedback signal for the oscillation. As a result, the oscillation frequency of such a circuit depends on the impedance of the LC tank circuit, which is a combination of the impedance of the transformer, the tuning capacitor, the quadrupole load to be connected, and

other stray impedance, at the output. However, in practice, a change in the operating temperature will alter the capacitance of the components, causing a resonant frequency drift.

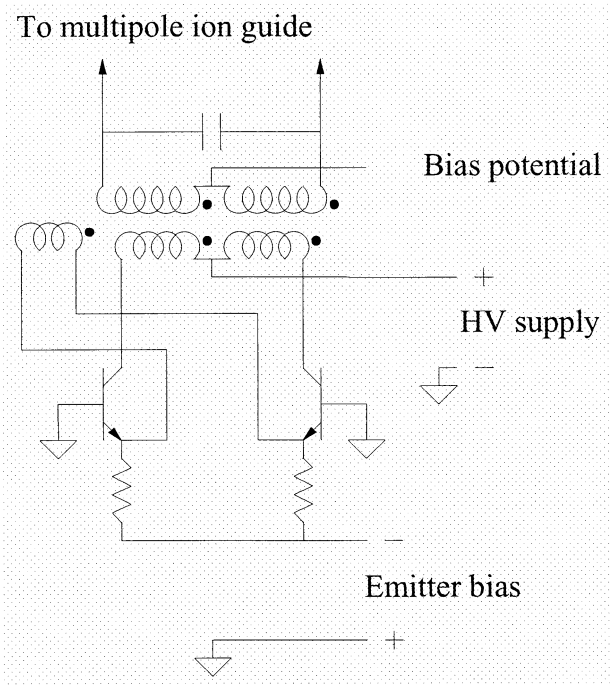

Figure 3.10: The feedback scheme with common-base setup for oscillation in the 2002 design by O'Connor *et al.* (O'Connor et al., 2002).

Meanwhile, in Mathur and O'Connor's design (Mathur and O'Connor, 2006), an AGC unit was built to sense the output at the transformer/matching circuit third stage to modify the gain at the power amplifier second stage. The AGC unit seemed to stabilize the output amplitude. However, a Zener diode was used in the regulator circuit (shown in Fig. 3.11) reported in 2002 (O'Connor et al., 2002) to provide the +15-V DC voltage in the 2006 circuit (Mathur and O'Connor, 2006). The output voltage after a Zener diode is a function of the biasing current, which changes according to the load shunting this Zener diode.

Therefore, such a supply voltage drift changes the DC conditions of not only the operational amplifiers (op amps) in both the AGC unit and the regulator circuit, but also the amplifying transistors. Such instabilities cause a constant, more than 1% change to the output amplitude.

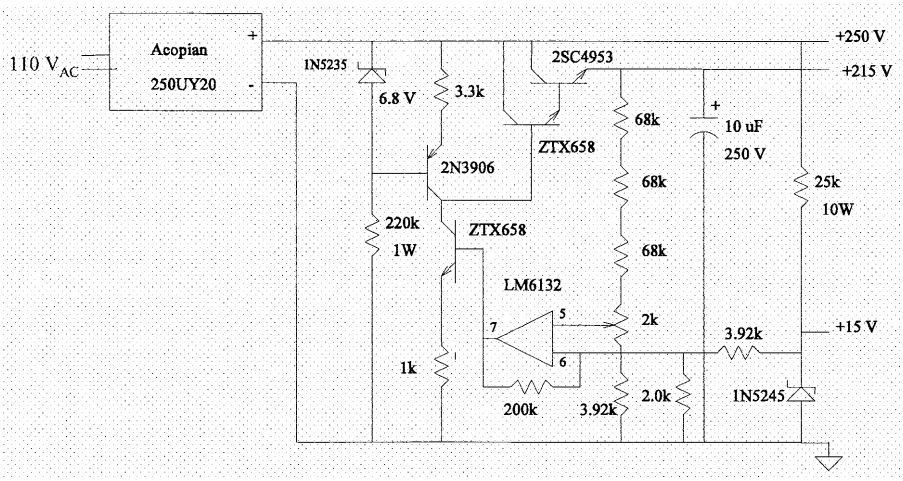

Figure 3.11: The 215-V regulator and the 15-V DC voltage supply in the 2002 design by O'Connor *et al.* (O'Connor et al., 2002).

As a result, Mathur and O'Connor's oscillator can be a good power supply to operate an ion guide, but for driving a mass filter with narrow mass window, the output frequency and amplitude stabilities have to be improved. In Chapter 7, a new oscillator design is proposed and partially tested. It is believed that the new design can be a RF power supply for driving a quadrupole mass filter.

3.6 Conclusion

In this chapter, the theory of operating a quadrupole as a ion guide or a mass filter is introduced. A stable ion trajectory can be obtained when the stability

parameters are tuned to be inside the stability regions.

Existing power supplies for a quadrupole system are reviewed. Most of them operate at a frequency below 10 MHz and has an output amplitude less than 500 V, and are suitable for ion transportation. When a quadrupole is used for mass filtering, very stable output frequency (ω) and amplitude (V) have to be generated by the power supply. In particular, it is preferred to have $\Delta\omega/\omega$ and $\Delta V/V$ below 2.5×10^{-4} and 5.0×10^{-4}, respectively, for a 0.1-Da resolution. The design of a new RF power supply for driving a quadrupole mass filter will be proposed later in Chapter 7.

CHAPTER 4

Test Equipment & Software Programs

Test automation was widely used to test the circuits in this thesis. This chapter presents the testing equipment, computer softwares, and testing methods used to test the designed circuits reported in the following chapters (Chapters 5, 6, and 7).

4.1 Introduction

The PCI (Peripheral Component Interconnect) eXtensions for Instrumentation (PXI) platform[15] and the control software LabVIEW from National Instruments (Austin, Texas) were utilized to test the performance of the designed circuits. It allowed faster circuit test execution and reporting, and a larger number of sampling points for an more accurate results after averaging.

Apart from the National Instruments (NI) system, the direct current (DC) power supply TTi EL301R from Thurlby Thandar Instruments Ltd. (Hunting-

[15]See http://www.ni.com/white-paper/4811/en for information about the PXI system, accessed 15 August 2012.

don, UK), and the lead-acid battery LC-R067R2P from Panasonic Corporation (Osaka, Japan) were used as power supplies. The spectrum analyser IFR A-7550 from Aeroflex Inc. (Plainview, New York, USA) was used for noise analysis. The oscilloscope Tektronix (Beaverton, Oregon, USA) DPO2014 was also used both to monitor, and to perform the fast Fourier transform (FFT) on the output waveforms. Simulation Program with Integrated Circuit Emphasis (SPICE) simulation was carried out by using the computer simulation software NI Multisim v11.0.2. The circuit schematics reported in Chapters 5 and 6 were drawn also using NI Multisim.

4.2 NI PXI Platform

The NI PXI system used for this report includes a PXI-5122 oscilloscope, a PXI-5421 arbitrary waveform generator, a PXI-6733 analogue output card, a PXI-8336 control card, and a PXI-1042 chassis. Figure 4.1 shows this PXI system and two DC power supplies. The 2-channel NI PXI-5122 oscilloscope provides a sampling rate of 100 MS/s and a 14-bit resolution with 100-MHz bandwidth.[16] The NI PXI-6733 analogue output card has a output voltage range between -10 and +10 V and a current driving ability of 5 mA.[17] The combination of the PXI-5122 and the PXI-6733 can be very useful for testing the I-V characteristics of a transistor. NI PXI-5421 arbitrary waveform generator can generate any arbitrary waveform

[16]See http://sine.ni.com/nips/cds/view/p/lang/en/nid/12615 for information about the NI PXI-5122 oscilloscope, accessed 20 August 2012.

[17]See http://sine.ni.com/nips/cds/view/p/lang/en/nid/11311 for information about the NI PXI-6733 analogue output card, accessed 20 August 2012.

between the frequency range of DC and 43 MHz.[18] The frequency response of a amplifier system can be measured by setting up an alternating current (AC) analysis using both PXI-5122 and PXI-5421. The controlling and data collecting programs used with the PXI system will be discussed in the next section.

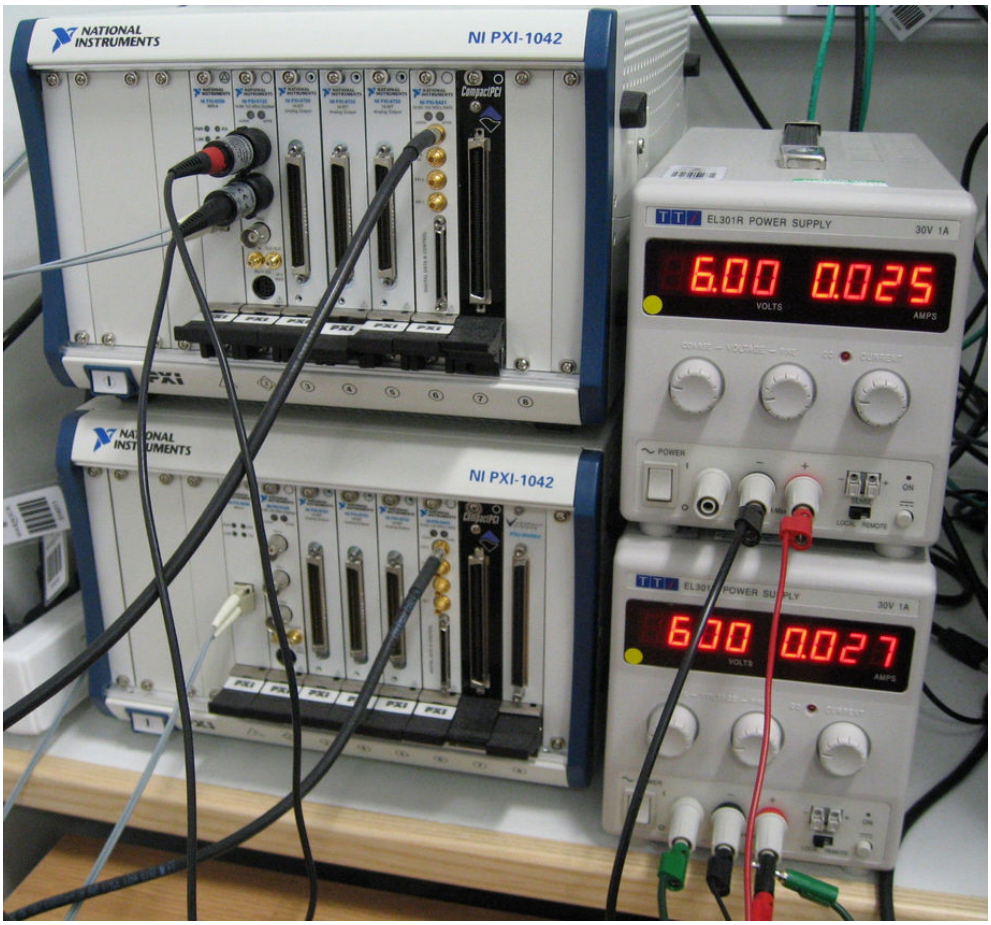

Figure 4.1: NI PXI platform and DC power supplies for circuit test.

[18]See http://sine.ni.com/nips/cds/view/p/lang/en/nid/12714 for information about the NI PXI-5421 arbitrary waveform generator, accessed 20 August 2012.

4.3 NI LabVIEW

The software NI LabVIEW 2009 (Service Pack 1) was used to control and to collect data from the PXI system shown in Fig. 4.1.

4.3.1 I-V Characteristics

The I-V characteristics of transistors reported in the later chapter was measured using the NI PXI-5122 oscilloscope (for measuring DC voltages) and PXI-6733 analogue output card (for supplying DC voltages). Figure 4.2 illustrates the schematic of the circuit used for transistor I-V characteristic testing. The drain node of the transistor being tested is coupled to an output channel of the PXI-6733 card through a resistor R. The gate node of the transistor is coupled directly to another output channel of the PXI-6733 card. The voltage values at both the drain node and the gate node of the transistor (V_{DS} and V_{GS}, respectively) are monitored by the PXI-5122 oscilloscope.

The LabVIEW program utilized for control and data collection is shown in both Fig. 4.3 (front panel) and Fig. 4.4 (block diagram). The parameters at the front panel control both PXI-5122 and PXI-6733 cards. The program scans both voltages applied to nodes 'DC 1' and 'DC 2' shown in Fig. 4.2 according to the settings at the front panel. The window 'Measurements' shown in Fig. 4.3 is not used, since only one measurement is recorded for each voltage step. The recorded voltage information will be converted to data sets of gate-source voltage V_{GS}, drain-source voltage V_{DS}, and drain current I_D, for plotting the I-V

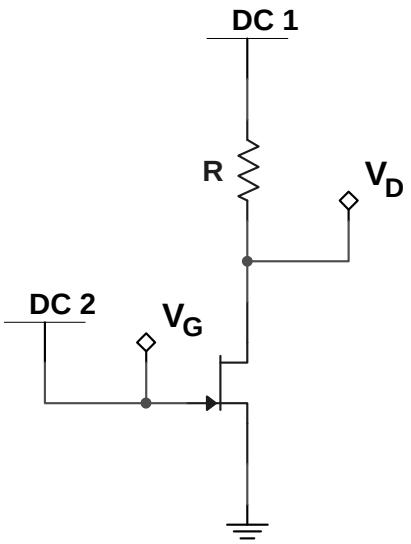

Figure 4.2: Schematic of the transistor I-V characteristic testing circuit.

characteristics.

4.3.2 AC Analysis

The AC analyses reported in the following chapters were carried out with the NI PXI-5122 oscilloscope and PXI-5421 arbitrary waveform generator. The DC voltages needed were supplied by the DC power supplies. The LabVIEW program for reporting frequency responses is shown in both Fig. 4.5 (front panel) and Fig. 4.6 (block diagram).

This AC analysis program uses PXI-5421 arbitrary waveform generator to send out specified waveforms. The frequency of the waveform is scanned according to the specified starting/stop frequency and frequency steps. Multiple measurements are taken for each frequency step, according to the parameter 'no. of measurements' at the front panel shown in Fig. 4.5. Peak-to-peak voltage

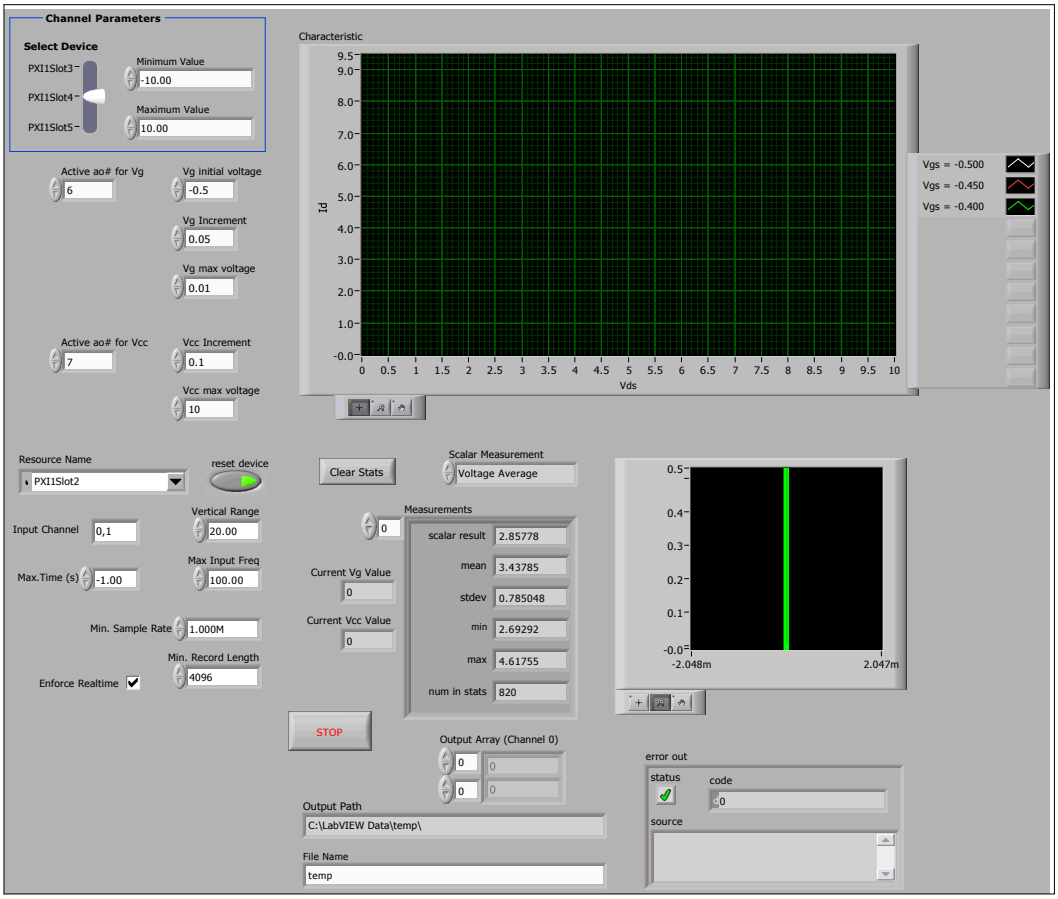

Figure 4.3: Front panel of the LabVIEW program for obtaining I-V characteristics of a transistor.

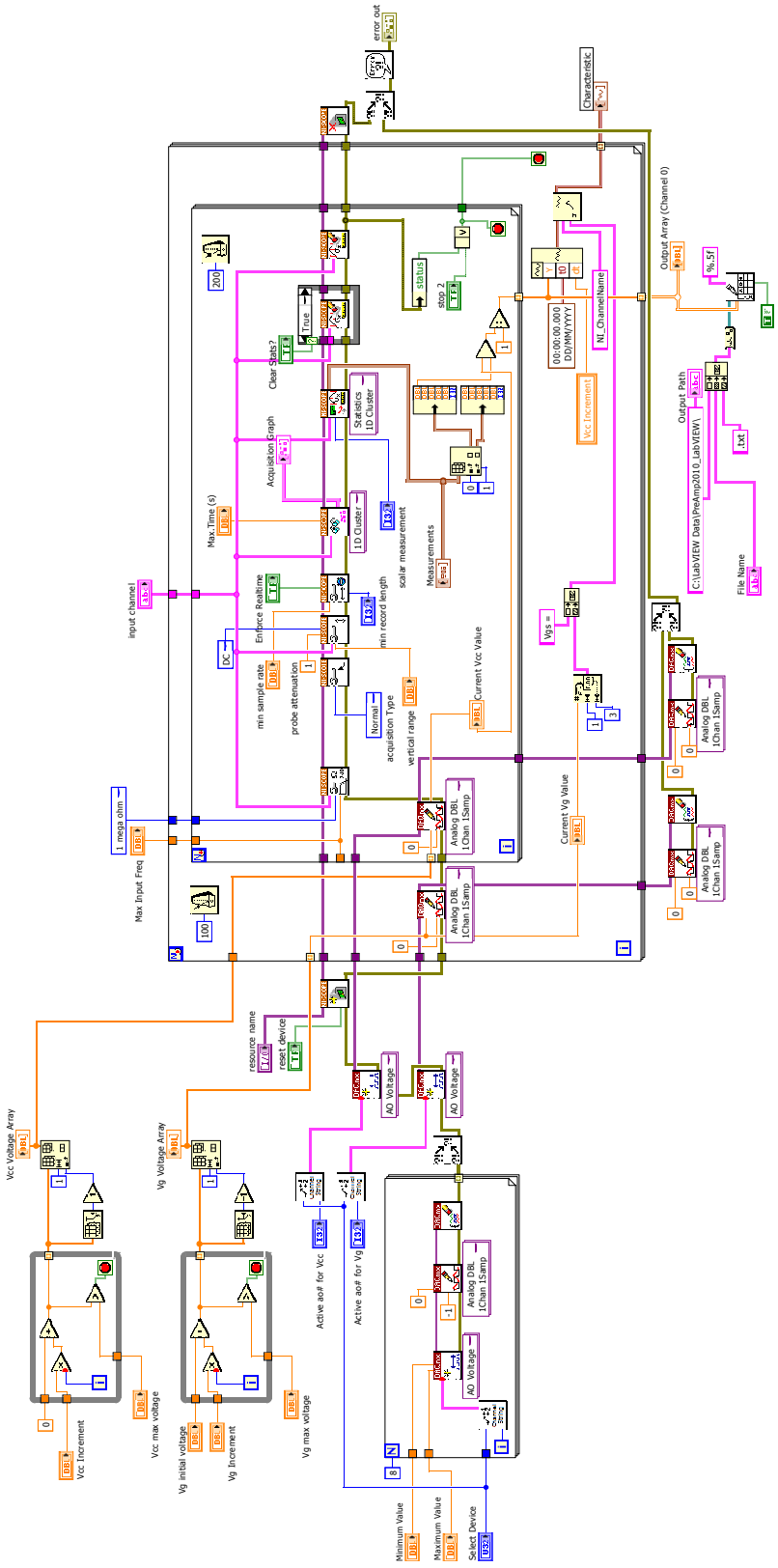

Figure 4.4: Block diagram of the LabVIEW program for obtaining I-V characteristics of a transistor.

amplitude is measured by the PXI-5122 oscilloscope. After all the measurements are completed, the mean, standard deviation, and minimum/maximum values of each frequency step will be recorded. Since the memory size of the computer used was big enough, the maximum sampling rate of 100 MS/s was always used for both channels of the PXI-5122 oscilloscope. Twenty points were measured and averaged to obtain both the input current going into the node I_{in} and the output voltage measured at node V_{out} in the schematic figures shown in the later chapters.

The transimpedance measured by the NI PXI system is reported using the commonly used form of Bode magnitude plots. The magnitude axis of such a plot is often reported in decibel scale. Since the transimpedance (gain) of a transimpedance amplifier has a unit of $V/A = \Omega$, in a Bode plot, the transimpedance is reported using dBΩ, where dBΩ is defined as X (dBΩ) $= 20 \times log[Y\ (\Omega)]$, in which X and Y are the transimpedance in dBΩ and Ω, respectively (Lin et al., 2012).

For the frequency response reported in Chapter 5, the peak-to-peak amplitude of the testing input sinusoidal current is 0.12 mA, whereas in Chapter 6 the peak-to-peak amplitude of the testing input sinusoidal current is 120 μA for circuits with estimated overall transimpedance below 20 kΩ, and 20 μA for circuits with estimated transimpedance above 1 MΩ.

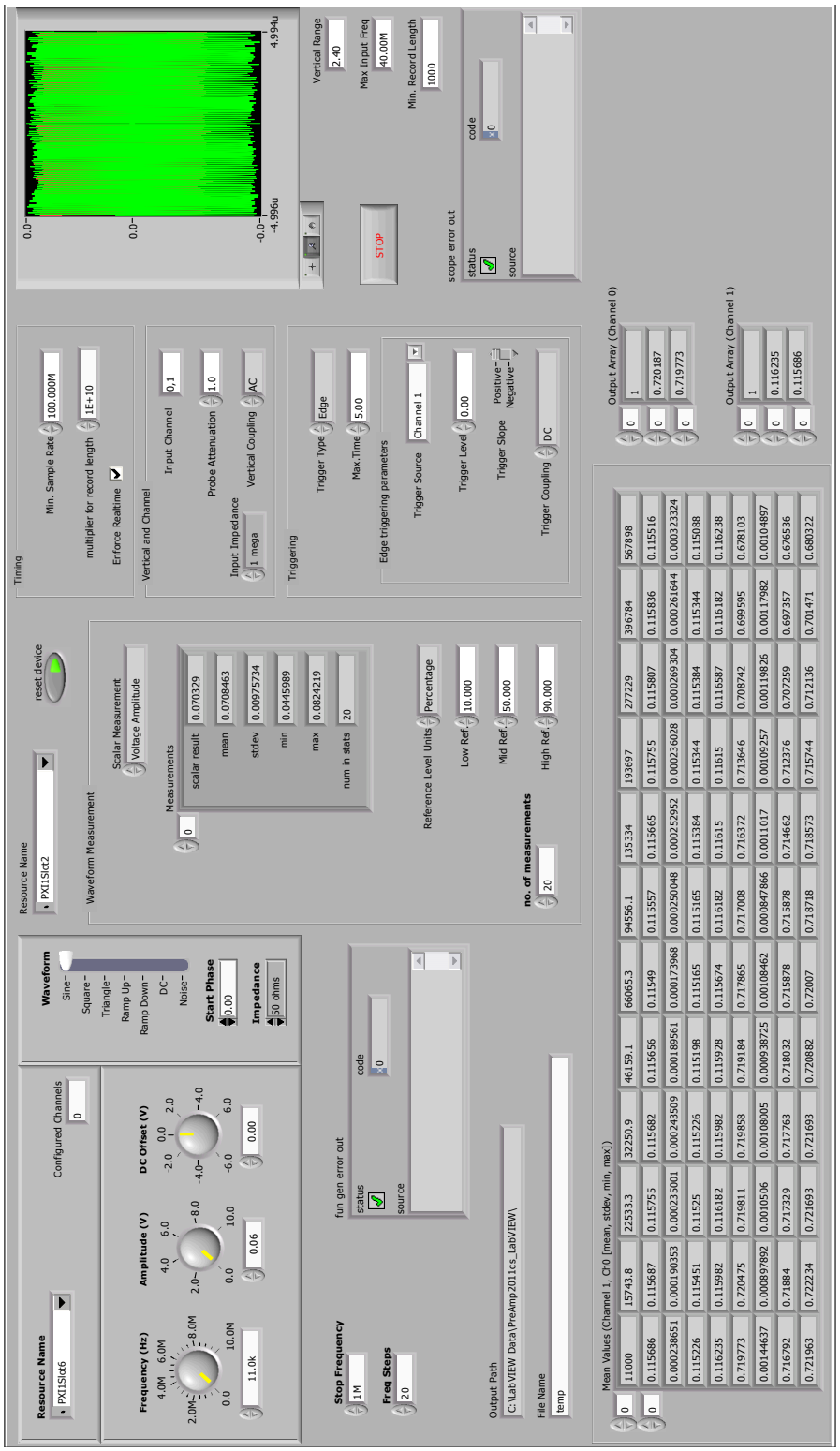

Figure 4.5: Front panel of the LabVIEW program for the AC analysis.

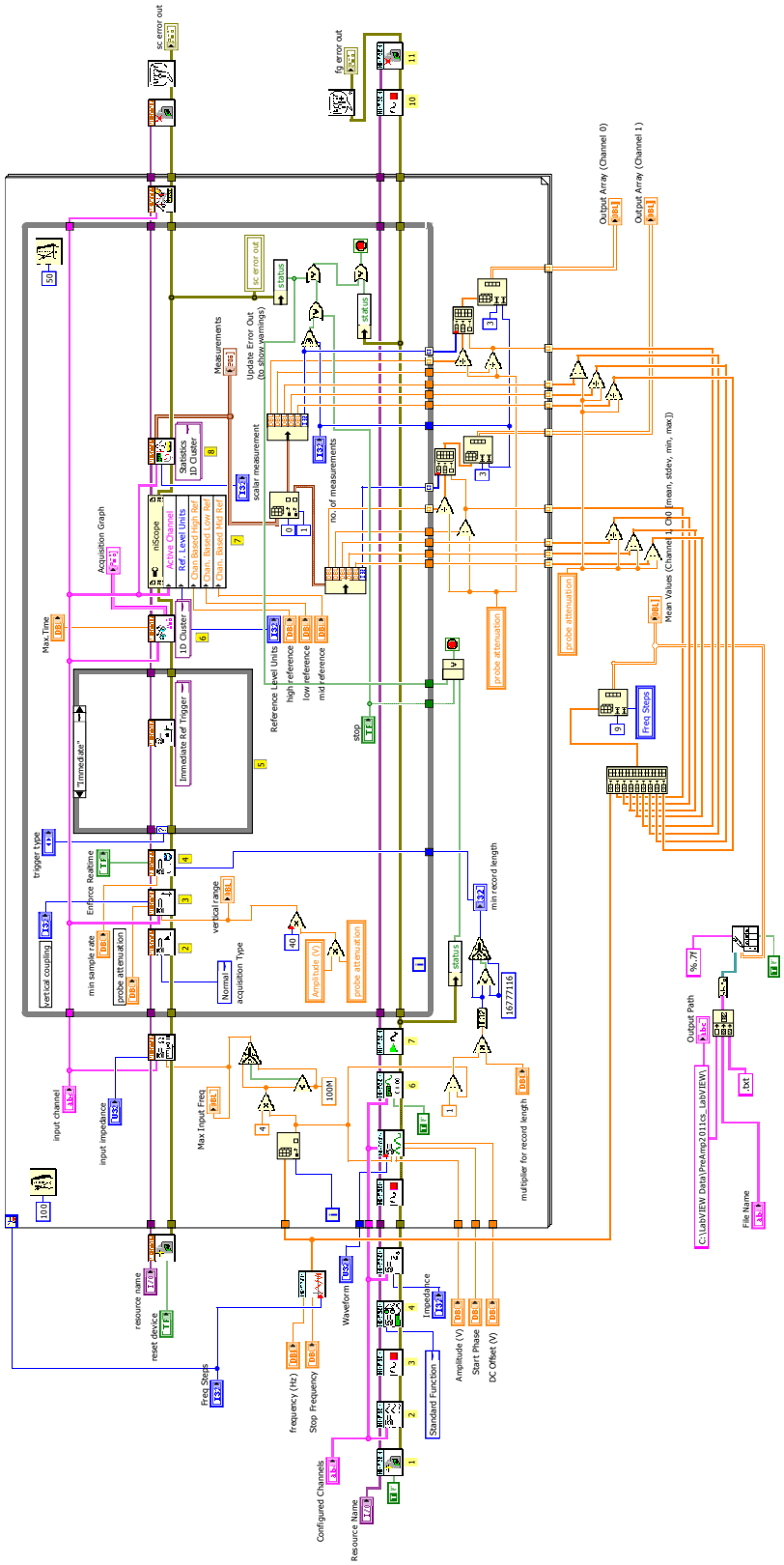

Figure 4.6: Block diagram of the LabVIEW program for the AC analysis.

4.4 Noise Performance [19]

It had been reported that the RF noise from the switching power supply may affect the noise performance of a preamplifier (Mathur et al., 2007; Wu et al., 2010). The lead-acid batteries mentioned above were introduced to compare the noise performance. Noise performance tests were conducted at an unshielded environment using the preamplifier reported in Chapter 5. Such test concluded that no difference in noise performance was observed, when using either the switching power supplies or the lead-acid batteries as the power supplies to the preamplifier used. It could be the results of the proper grounding and bypass/decoupling capacitors used.

The noise performance reported in the following chapters was measured when the amplifier input was floating and a DC blocking capacitor was coupled between the output and the spectrum analyser. The noise power was measured in dBm. The noise power in dBm, $P_{n(dBm)}$, can be calculated from the noise power in watts, $P_{n(W)}$, by

$$P_{n(dBm)} = 10 \times log(\frac{P_{n(W)}}{1 \times 10^{-3}}) \ . \tag{4.1}$$

On the contrary, the measured noise power in dBm can be converted back to Watts, and can be referred to the output voltage V_{out} by

$$P_{n(W)} = 10^{(\frac{P_{n(dBm)}-30}{10})} = \frac{(V_{out})^2}{R_{load}} \ , \tag{4.2}$$

[19] This section is partially reproduced from the journal article, "A Gain and Bandwidth Enhanced Transimpedance Preamplifier for Fourier-Transform Ion Cyclotron Resonance Mass Spectrometry," *Review of Scientific Instruments*, in 2011 (Lin et al., 2011).

where R_{load} is the load resistance of the spectrum analyser. The transimpedance A_T of the preamplifier and the resolution bandwidth (Res) of the spectrum analyser have to be considered to further correlate the output voltage V_{out} of the preamplifier back to the input current spectral density i_n, where

$$i_n = \sqrt{\frac{P_{n(W)} \times R_{load}}{(Res) \times (A_T)^2}} \quad (\text{pA}/\sqrt{\text{Hz}}) \; . \tag{4.3}$$

By using Eq. (4.2) and Eq. (4.3), the input current noise spectral density i_n (in pA/$\sqrt{\text{Hz}}$) data were calculated from the measured noise power $P_{n(dBm)}$ (in dBm) and the transimpedance A_T data collected using the AC analysis technique mentioned in Section 4.3.2.

4.5 Other Software/Hardware Used

Apart from the NI LabVIEW and Multisim mentioned previously, other software programs were used to assist other related works.

In Chapters 5 and 6, the printed circuit board (PCB) layouts were designed using the computer-aided design software, Altium Designer Build 8.4 (Service Pack 4) from Altium Limited (Sydney, Australia). The PCBs used in both chapters were manufactured in-house using the PCB prototyping plotter ProtoMat S62 from LPKF Laser & Electronics AG (Garbsen, Germany).

The software Proteus 7.10 from Labcenter Electronics (Grassington, UK) was used for some of the circuit drawings and all of the PCB designs reported in

Chapter 7. The designed PCBs reported in Chapter 7 were etched, and populated in-house.

4.6 Conclusion

In this chapter, the methods used to test the designed circuits reported in the following chapters are presented. The NI PXI system allows a reliable and efficient testing of circuits. The LabVIEW programmes used to control the PXI cards and to fetch data have a great flexibility for defining circuit testing conditions. When testing the noise performance of a circuit, proper shielding and power supply decoupling should be provided. As of the spectrum analyser, a more recent model with better sensitivity may be necessary when testing the noise behaviour of a circuit with excellent noise performance.

CHAPTER 5

Transimpedance Preamplifier Using an Operational Amplifier

This chapter reports a preamplifier using an operational amplifier in a transimpedance configuration, and is partially reproduced from the journal article, "A Gain and Bandwidth Enhanced Transimpedance Preamplifier for Fourier-Transform Ion Cyclotron Resonance Mass Spectrometry," *Review of Scientific Instruments*, in 2011 (Lin et al., 2011).

An ion detector is one of the components in a modern mass spectrometer, as discussed in Section 2.1.2. Usually, an ion detector consists of electronic devices for processing the analogue signal coming from the mass analyser, as shown in Fig. 5.1. The signal is amplified and filtered here, before being sent into an analogue-to-digital converter (ADC) in the data system. The preamplifier in an ion detector system is believed to be one of the key components for improving signal-to-noise performance electronically. Newly designed preamplifiers will be

presented in this chapter and Chapter 6.

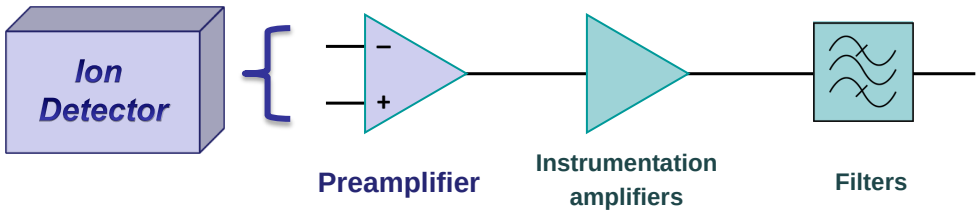

Figure 5.1: Components inside the ion detector of a modern mass spectrometer (the composition of a modern mass spectrometer is illustrated in Fig. 2.4). Chapters 5 & 6 report new preamplifier designs for a 12-T FT-ICR system.

This chapter begins with a brief review of the transimpedance technique and the input capacitance tolerance of a transimpedance amplifier. Then the correlation between the cyclotron frequency of the signal form an ICR cell and the transimpedance (gain) of the preamplifier is reviewed to understand the transimpedance amplifier design constraints. The newly designed preamplifier and its printed circuit board (PCB) for testing are presented. The preamplifier is SPICE simulated and is tested on the bench for its frequency response and its noise performance. Then this chapter concludes with a discussion between the feedback impedance, bandwidth, noise performance, and the estimated numbers of ions that can be detected in a 12-T FT-ICR system.

5.1 Introduction

It was discussed in Chapter 2, that in a signal processing chain, the noise performance is dominated by the noise from the signal source and from the first

stage 'signal processor,' the preamplifier, if the preamplifier is designed with significant gain. Similar to the photodiodes in optical communication systems, the signal analyser of a Fourier-transform ion cyclotron resonance (FT-ICR) mass spectrometer, an ICR cell, is a capacitive device. Electrostatically induced image currents are expected at the input of the preamplifier. The parasitic capacitance from the cell can vary from around 10 pF to over 100 pF (Kaiser et al., 2011a), depending on the cell dimensions, feedthroughs, and cabling. A high capacitance at the preamplifier input limits the bandwidth, causing potential signal intensity loss.

The nature of the ion signal from an FT-ICR mass spectrometer and the electronic noise were studied and reported in Chapter 2 to further understand the electronic detection limit. A new transimpedance preamplifier was designed, computer simulated, built, and tested. The preamplifier design featured its enhanced tolerance of the capacitance of the detection device, lower intrinsic noise, and larger flat mid-band gain (input current noise spectral density of around 1 pA/$\sqrt{\text{Hz}}$ when the transimpedance is about 85 dBΩ).

The designed preamplifier has a bandwidth of ∼3 kHz to 10 MHz, which corresponds to the mass-to-charge ratio, m/z, of approximately 18 to 61k for a 12-T FT-ICR system. The transimpedance and the bandwidth can be easily adjusted by replacing passive components. The feedback limitation of the circuit will be discussed in this chapter.

5.2 Transimpedance Amplifier

Since the signal to be detected in an FT-ICR system is a current due to the motion of ions, a transimpedance amplifier to convert the current input to a voltage output for further amplification is needed. As reviewed in Section 2.5.3, conventional preamplifiers convert the signal current into voltage by using an input resistor and a voltage amplifier. Such a current-voltage conversion can be also performed by a transimpedance amplifier.

5.2.1 Bandwidth Extension

A transimpedance amplifier is a widely used current-voltage converting solution for many applications such as optical communication (Green et al., 2008a; Chen et al., 2005; El-Diwany et al., 1981). The negative-feedback transimpedance technique has the advantages of reducing the effective input load capacitance to the amplifier and extending the bandwidth by a factor equal to the open-loop gain of the amplifier (Green and McNeill, 1989; Hullett and Moustakas, 1981). Therefore, it appears to be ideal for detecting ion signals from an ICR cell, which in general acts like a current source (Comisarow, 1978) with large capacitance (from ∼10 pF to over ∼100 pF, as mentioned earlier) depending on cabling and the size of the cell.

A typical FT-ICR preamplifier can be modeled from a circuit schematic such as Fig. 5.2a, where C is the total source capacitance from the ideal alternating current (AC) current source I, which represents the current signal from the ICR

cell. The operational amplifier (op amp) with open-loop gain G has an input resistor R, which is responsible for transforming the input current into voltage. The current-to-voltage transfer function $H(\omega)$ can be derived as

$$H(\omega) = \frac{R}{1 + j\omega(RC)} \ , \tag{5.1}$$

and the 3-dB bandwidth ω_{3dB} is given by

$$\omega_{3dB} = \frac{1}{RC} \ . \tag{5.2}$$

If the configuration of such an amplifier is replaced by a transimpedance amplifier with negative feedback, the circuit becomes what is shown in Fig. 5.2b. The transfer function becomes

$$H(\omega) = \frac{R}{1 + j\omega R(C/G)} \ . \tag{5.3}$$

Namely, the transimpedance technique effectively reduces the input capacitance by a factor of G, hence the 3-dB frequency is then extended to

$$\omega_{3dB} = \frac{G}{RC} \ . \tag{5.4}$$

With such bandwidth increment, the gain-bandwidth product is further pushed to higher frequency range and therefore higher gain can be introduced to the am-

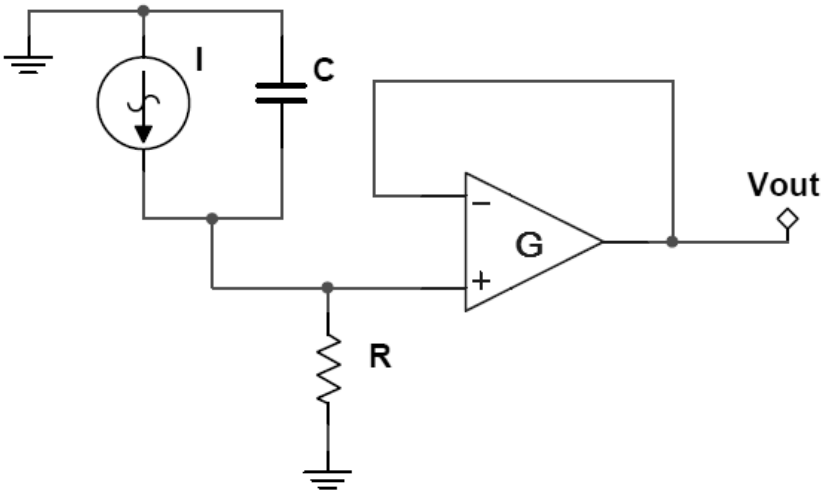

(a) A unity gain operational amplifier with an input resistor R to convert current signal into voltage.

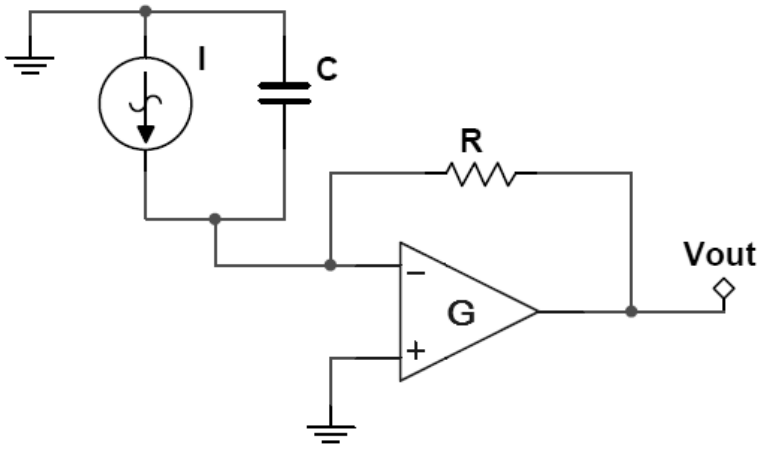

(b) A transimpedance amplifier with a feedback resistor R.

Figure 5.2: Two types of preamplifier systems. The ideal current source I represents the signal from the ICR cell. The capacitor C is the combination of the parasitic capacitance of the cell and cabling.

plifier system with the same 3-dB bandwidth. Equivalently, the tolerance to the parasitic capacitance of the cell and cabling is stronger. Therefore, the preamplifier can be located further away from the cell to isolate it from possible electrical perturbation induced by the high magnetic field. Such a stronger tolerance makes the transimpedance an ideal choice when a higher magnetic field, such as the 21-T magnet (Painter et al., 2006; Xian et al., 2012), or the technique of excitation and detection on the same ICR plate (Chen et al., 2012)[20] is introduced in the near future.

5.2.2 Cyclotron Frequency Correlation

The cyclotron frequency from the ion signal in an ICR cell is described in Chapter 2. It can be easily seen by rewriting Eq. (2.1) that the mass-to-charge ratio is inversely proportional to the cyclotron frequency ω_{cyc},

$$\frac{m}{q} = \frac{B}{\omega_{cyc}} \ , \tag{5.5}$$

where m is the ion mass, q is the ionic charge of the ion, and B indicates the magnetic field strength. Since the image current, I_s, induced by the rotating ions in an ICR cell is modeled by Eq. (2.8a), substituting the q/m in Eq. (2.8a) by Eq. (5.5) yields

$$I_{s\ (r.m.s)} = \frac{Nqr}{\sqrt{2}d}\ \omega_{cyc} \ , \tag{5.6}$$

[20]The method of excitation and detection on the same ICR plate introduced by Chen and co-workers uses a few protection diodes at the input node of the ICR preamplifier. Such diodes increase the capacitance seen by the preamplifier input.

where N is the number of excited ions, r is the ion rotation orbital radius, and d is the cell diameter (spacing). As described, the intensity of the induced image current in an ICR cell is a function of the cyclotron frequency. Such dependency can be either calibrated by the signal processing computer, or can be eliminated by the front-end circuitry under certain conditions.

When a transimpedance preamplifier is introduced as the front-end electronics solution, from Eq. (5.3), the magnitude of the transfer function $H(\omega)$ at the cyclotron frequency ω_{cyc} can be calculated as

$$|H(\omega_{cyc})| = \frac{R}{\sqrt{1 + [\omega_{cyc} R(C/G)]^2}} \ . \tag{5.7}$$

Recall that the magnitude of the output voltage $|V_{out}|$ after the transimpedance preamplifier is $|I_s||H(\omega)|$. Here, if $\omega_{cyc}R(C/G)$ is much greater than 1, namely, the magnitude of the feedback resistance is much greater than the magnitude of the reactance of the effective input capacitance,

$$R >> \frac{1}{\omega_{cyc}(C/G)} \ , \tag{5.8}$$

Eq. (5.7) can be approximated as

$$|H(\omega_{cyc})| \simeq \frac{1}{\omega_{cyc}(C/G)} \ . \tag{5.9}$$

From Eq. (5.6) and Eq. (5.9), the magnitude of the output voltage becomes

$$|V_{out}| = |I_s||H(\omega_{cyc})| \simeq \frac{Nqr}{\sqrt{2}d(C/G)} \ , \tag{5.10}$$

which is independent of the cyclotron frequency. On the contrary, if the magnitude of the feedback resistance is much smaller than the magnitude of the reactance of the effective input capacitance,

$$R << \frac{1}{\omega_{cyc}(C/G)} \ , \tag{5.11}$$

Eq. (5.7) can be approximated as

$$|H(\omega_{cyc})| \simeq R \ , \tag{5.12}$$

and the magnitude of the output voltage becomes

$$|V_{out}| = |I_s||H(\omega_{cyc})| \simeq \frac{Nqr}{\sqrt{2}d} R\omega_{cyc} \ . \tag{5.13}$$

In such a case, calibration will be necessary for maintaining the constancy of the gain for each peak in a spectrum.

The gain G for a generic op amp is typically greater than 10^4. Assuming an input capacitance of 10 pF and the cyclotron frequency f_{cyc} of signals between 10 kHz and 10 MHz (mass-to-charge ratio, m/z, of ∼18 to 18k for a 12-T FT-ICR

system), the reactance magnitude of the effective input capacitance $\frac{1}{\omega_{cyc}(C/G)}$ can be between 16M and 16G. As it is not practical to have a feedback resistance much larger than 16 GΩ, for simplicity, the condition described by Eq. (5.11) shall be fulfilled when designing a transimpedance preamplifier using an op amp for an FT-ICR system in which the input capacitance is ∼10 pF.

5.3 Transimpedance Preamplifier Circuit Design

The basic design of the transimpedance preamplifier uses a junction field-effect transistor (JFET) input stage and an op amp main stage for gain. It was reported that metal-oxide-semiconductor field-effect transistor (MOSFET) often has the smallest high-frequency noise, whilst JFET usually has the best low-frequency noise behavior (Fabris and Manfredi, 2002). An example is shown in Fig. 5.3. In comparison with the N-type JFET, the reported N-type MOSFET has better noise performance at the frequency range higher than 1 MHz. As in this application the frequency of interest mostly falls in the range between 1 kHz and 1 MHz, a JFET device can be one of the best front-end candidates with large input impedance.

The schematic of the preamplifier circuit is shown in Fig. 5.4. The overall feedback is controlled by a single resistor (R1 in Fig. 5.4), which determines the transimpedance of the preamplifier. The input node 'Iin' of the preamplifier is direct current (DC) coupled to the detection plate of the ICR cell. Therefore, the same resistor in the feedback loop also biases the detection plates of the ICR

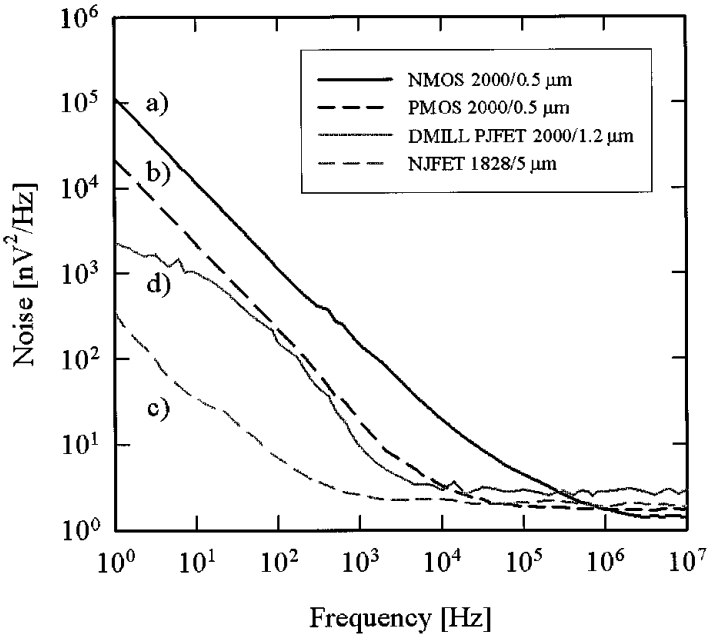

Figure 5.3: Noise power spectral densities of four types of transistors: a) a N-type MOSFET, b) a P-type MOSFET, c) a N-type JFET, and d) a P-type JFET (Fabris and Manfredi, 2002).

cell, in this case, to a virtual ground potential, which is necessary to preserve ion trajectories in the cell.

In order to limit the intrinsic noise from the passive components, low noise surface mount ceramic capacitors and surface mount thin-film chip resistors from Panasonic Corporation (Osaka, Japan) are selected to define the biasing conditions of the preamplifier system and to provide the transimpedance in the feedback loop. Figure 5.5 shows the average noise level of chip resistors reported in the Surface Mount Resistors Technical Guide Ver.3 from Panasonic.[21] As reported, a thin-film chip resistor has a lower noise level than a thick-film chip

[21]See http://industrial.panasonic.com/www-data/pdf/AOA0000/AOA0000PE36.pdf for the Surface Mount Resistors Technical Guide from Panasonic, accessed 30 August 2012.

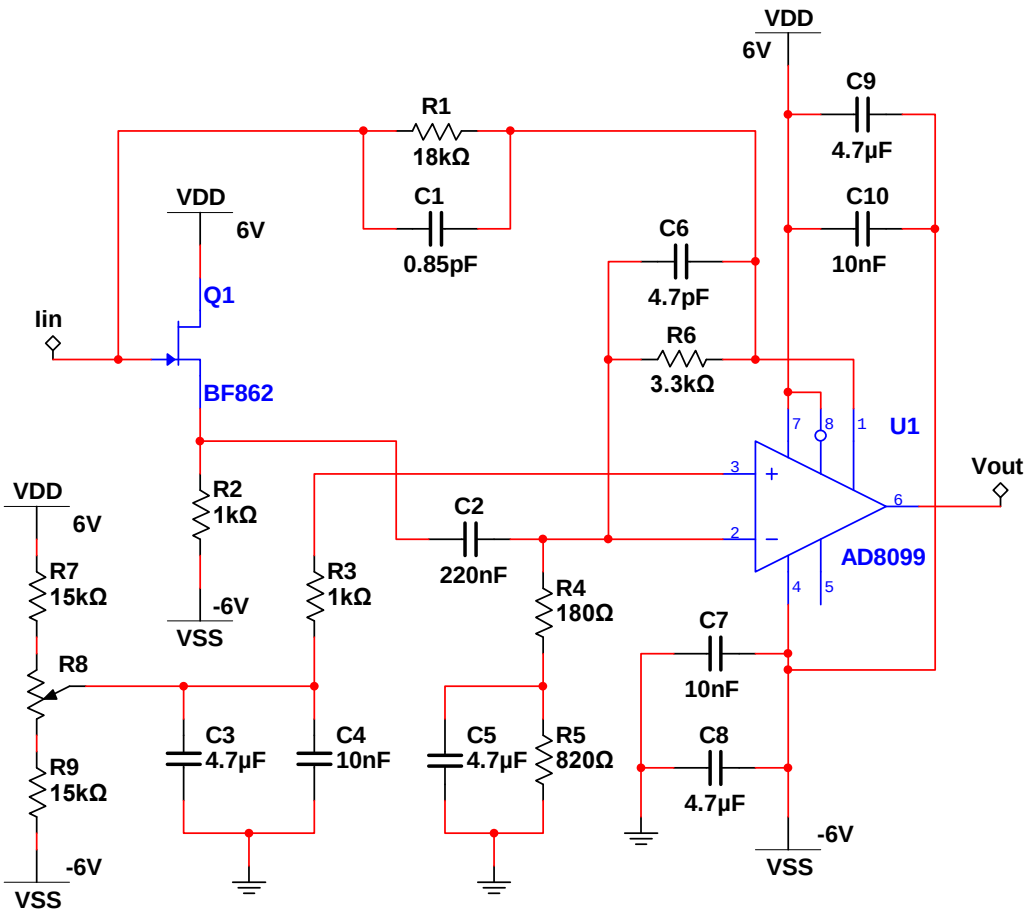

Figure 5.4: Schematic of the transimpedance preamplifier using an operational amplifier AD8099.

resistor.

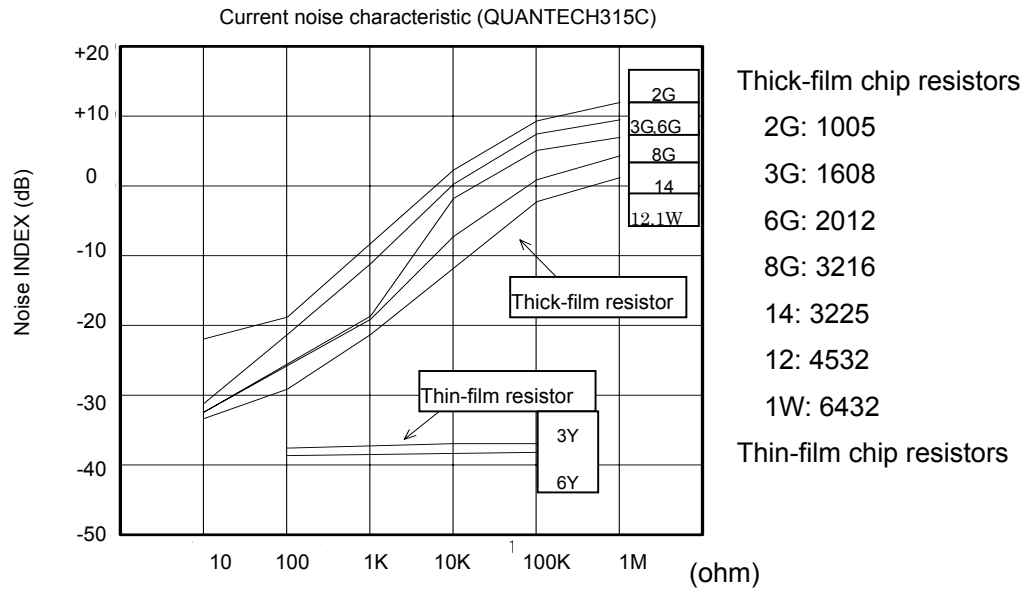

Figure 5.5: Average noise level of chip resistors, reported in the Surface Mount Resistors Technical Guide Ver. 3, Panasonic.[21]

5.3.1 Main Stage

The main stage is formed by an ultralow distortion op amp AD8099 from Analog Devices, Inc. (Norwood, Massachusetts),[22] biasing resistors R3–R5, bias adjustment resistors R7–R9, feedback resistor R6 and capacitor C6, DC blocking capacitor C2, and bypass capacitors C3–C5 and C7–C10. AD8099's ultralow noise input voltage spectral density of typically 0.95 nV/$\sqrt{Hz}$ (specified at 100 kHz), ultralow distortion (-92 dBc at 10 MHz), and wide bandwidth (700 MHz at the gain of 2) are specifically utilized in this preamplifier system. The AD8099's gain-bandwidth product of 3.8 GHz makes this op amp a good candidate for

[22] See Appendix A.2 for information about the op amp AD8099.

having a large gain at around 10 MHz. Pin 5 of the op amp is not connected, as suggested by the datasheet[22] when the gain is set to around 20. Pin 1 and pin 6 are internally connected inside the surface mount package to increase the routing flexibility on a PCB.

The AD8099 datasheet reports that AD8099 can operate stably when the gain is less than 20. As the gain-bandwidth product of this op amp is 3.8 GHz and only a 10-MHz bandwidth is required for this application, it is planed to set the gain of this main stage close to 20. Therefore, resistors R4 and R6 are used to set the AC signal gain of this main stage to 19 ($R6/R4 + 1$). On the contrary, one can change the resistance values of R4 and R6 if a gain of greater than 20 is needed, given that this op amp AD8099 is tested stable when gain is over 20. If a gain of greater than 20 causes a stability issue to this op amp, the introduction of multiple gain stages (such as connecting op amps in a cascade configuration), or other op amps should be considered in this application. The 3-dB bandwidth f_{3dB} (high frequency cut-off), which can be calculated by Eq. (5.14), is further limited by the capacitor C6 together with the feedback resistor R6 to 10 MHz.

$$f_{3dB} = \frac{1}{2\pi RC} \ . \tag{5.14}$$

The DC biasing conditions of both AD8099 inputs are balanced by R3 together with R4 and R5, and can be trimmed by the trimmer resistor R8 to maintain the output DC level at 0 V. In this application, pin 8 (the disable pin) is connected to +6V DC power rail so that the op amp remains on whenever the

power to the preamplifier system is on. Potentially, connecting this disable pin with a control signal can be a good solution when isolation between the ICR cell and the amplifying circuitry is necessary.

5.3.2 Input Stage

The large input impedance of the JFET BF862 from NXP Semiconductors N.V. (Eindhoven, The Netherlands)[23] makes such a transistor an ideal input stage, as the biasing and feedback circuitry at the input node of the op amp AD8099 lowers the input impedance of this op amp. The ultralow noise (noise input voltage spectral density of typically 0.8 nV/$\sqrt{Hz}$ at 100 kHz as specified on the datasheet)[23] characteristics of BF862 also limits the possible intrinsic noise added by this first stage buffer into the preamplifier system. According to the datasheet, the transition frequency of this JFET is 715 MHz. Such a bandwidth specification is suitable for this 12-T FT-ICR preamplifier application, where a bandwidth of less than 10 MHz is needed. Meanwhile, this BF862 was tested to be vacuum compatible and was proven stable when operates under a 7-T magnetic field. Such characteristics allow this JFET to be a good front-end choice, as the front-end device may be placed inside the vacuum chamber where high magnetic field exists.

The BF862 input stage can be configured either as a source follower or a common-source amplifier. A common-source amplifier provides more voltage gain

[23] See Appendix A.1 for information about the JFET BF862.

to increase the open-loop gain (G in Eq. (5.4)) to extend the 3-dB bandwidth, but also results in an unwanted 180-degree phase shift before unity gain, causing the preamplifier to oscillate. Therefore, this BF862 input stage is designed to be a source follower with an 1-kΩ source resistor (R2 in Fig. 5.4) to set the drain current at around 6.5 mA.

5.3.3 Printed Circuit Board

The preamplifier circuit was built on a single-layer printed circuit board (PCB). The populated PCB (sized $\sim 65 \times 60$ mm) is shown in Fig. 5.6. On the PCB, all of the components are located inside a ground ring to shield them from environmental noise. Bypass capacitors are placed as close as possible to the AD8099 chip, as suggested by the AD8099 datasheet, for optimum distortion and power supply rejection performance. Note that this board is for bench testing purpose. When placing such a PCB into a vacuum chamber close to the ICR cell in an FT-ICR system, a smaller-sized, two-layer board with ground plane should be considered to limit the noise coupling and parasitic capacitance.

5.4 Computer Simulation

To test the designed bandwidth and noise performance, SPICE simulation has been carried out using NI Multisim. Initially, the designed bandwidth is at the range of 1 kHz to 10 MHz, which corresponds to an output mass-to-charge ratio, m/z, of roughly 18 to 180k for a 12-T FT-ICR mass spectrometry (MS) system.

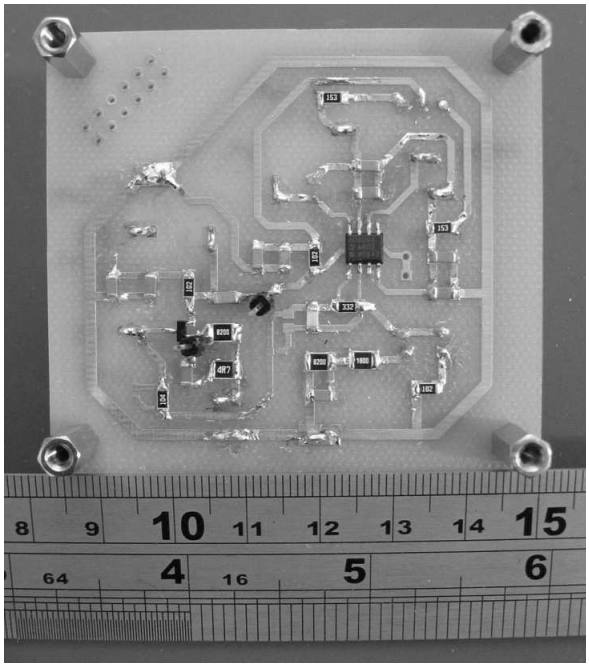

Figure 5.6: Single layer printed circuit board of the AD8099 preamplifier (sized $\sim 65 \times 60$ mm) with components fully populated.

Such a wide-band design goal offers enough buffer when the parasitic capacitance narrows the bandwidth. Use of a bandpass filtering configuration minimizes the artifacts, such as the signal aliasing caused by high frequency signal fold-over, and the offset in the signal (Mathur and O'Connor, 2009), in FT-ICR mass spectra. In this design, the low frequency cutoff is defined by the capacitor C2 and the effective resistance ($\sim$1 kΩ) in series with it, whereas the high frequency 3-dB point is defined by the feedback resistor R1 together with the capacitor C1. Both frequency poles can be estimated by using Eq. (5.14).

The AC analysis simulations are performed to show the transimpedance with different feedback resistance and capacitance values. Two feedback resistors, 180 Ω and 18 kΩ, are chosen to show the gain variance. Figure 5.7a shows the results when feedback capacitor C1 is not connected to the system. In the simula-

tion program, the parasitic capacitance of the 0805 sized surface mount feedback resistor R1 is set to 85 fF. The AC analysis simulation when C1 is 0.85 pF is shown in Fig. 5.7b. As expected, the low frequency cut-off is independent of the feedback impedance and is slightly below 1 kHz for both cases. When the feedback capacitance of C1 is fixed at 0.85 pF, from Eq. (5.14) the 3-dB bandwidth occurs at around 10 MHz and 1.0 GHz when R1 is 18 kΩ and 180 Ω, respectively. The simulation results support such estimations.

In Fig. 5.7a, the peakings around 20 MHz and 200 MHz of the 18-kΩ and 180-Ω curves, respectively, are the results of the phase shift caused by the LC resonance of the op amp output impedance, and can be eliminated by introducing the 3-dB poles before the peakings. As shown by the 18-kΩ curve in Fig. 5.7b, the 0.85-pF feedback capacitor and the 18-kΩ feedback resistor cause a pole at around 10 MHz, thus the transimpedance drops before the peak at 20 MHz. For the 180-Ω curve, the same feedback capacitance of 0.85 pF generates a 3-dB pole at about 1.0 GHz, and the 200-MHz peak remains.

5.5 Transimpedance Preamplifier Testing Results

5.5.1 Frequency Response

The voltage gain of the main stage and the overall transimpedance performance have been measured. The voltage gain of the op amp AD8099 was tested when the first stage (BF862 and its source resistor R2 in Fig. 5.4) was not mounted to

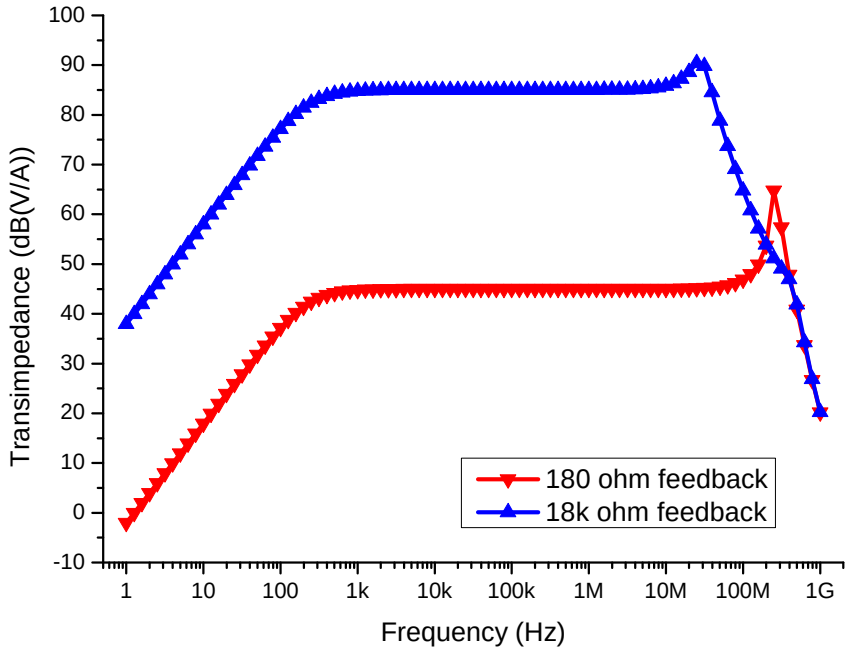

(a) Frequency response without the feedback capacitor C1 in Fig. 5.4.

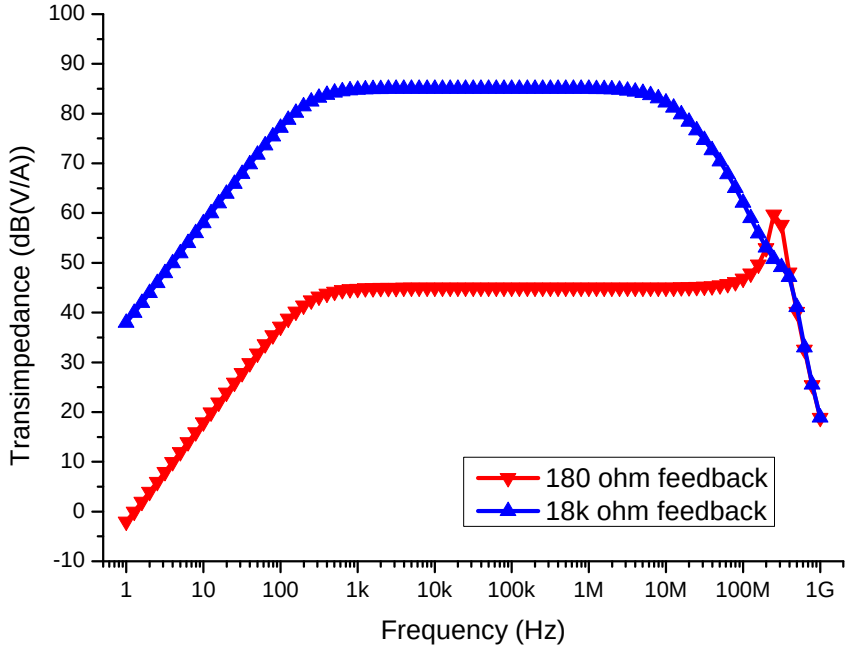

(b) Frequency response with 0.85-pF feedback capacitor.

Figure 5.7: SPICE simulations of the AD8099 preamplifier transimpedance.

the PCB, to ensure that the performance of this main stage matches the designed conditions of providing a voltage gain of 19 between 1 kHz and 10 MHz. The test signal was fed into the system via the DC blocking capacitor C2, and the output was measured directly from the output of AD8099. The result shown in Fig. 5.8 demonstrates an agreement with the designed voltage gain of 19 (about 25 dB) and designed 3-dB bandwidth of 10 MHz.

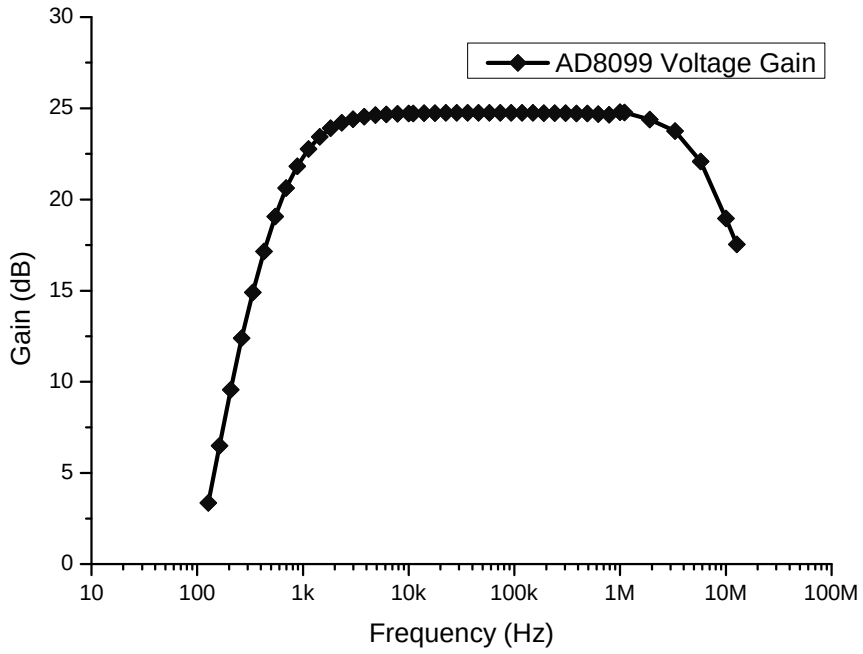

Figure 5.8: Voltage gain frequency response of the main (AD8099) stage.

Figure 5.9 shows the transimpedance of the entire preamplifier system in three conditions when different feedback resistors and capacitor are soldered onto the system: (i) only a 180-Ω resistor, (ii) only an 18-kΩ resistor, and (iii) an 18-kΩ resistor together with a 0.8-pF capacitor. It can be seen that the peaking of the 18-kΩ single-resistor feedback curve agrees with the SPICE simulation results

shown in Fig. 5.7. Shunting a 0.8-pF capacitor with the 18-kΩ feedback is a solution to avoid this peak.

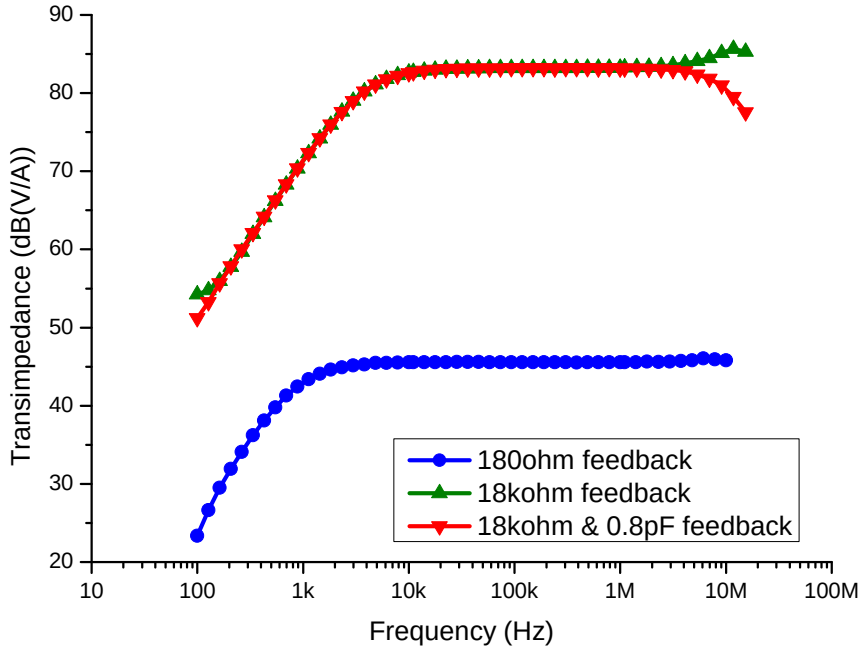

Figure 5.9: Transimpedance frequency response of the preamplifier system in three feedback conditions: (i) only a 180-Ω resistor, (ii) only an 18-kΩ resistor, and (iii) an 18-kΩ resistor together with a 0.8-pF capacitor.

Figure 5.10 illustrates one of the input/output waveforms fetched by the NI PXI system. It corresponds to the transimpedance measured at 10 kHz reported in Fig. 5.9 (iii), in which the preamplifier feedback system is an 18-kΩ resistor shunting a 0.8-pF capacitor. The large green line indicates the output waveform, whilst the red line represents the input waveform. The peak-to-peak amplitude of the measured output voltage is around 1.5 V, whilst the peak-to-peak input current amplitude is about 0.1 mA.

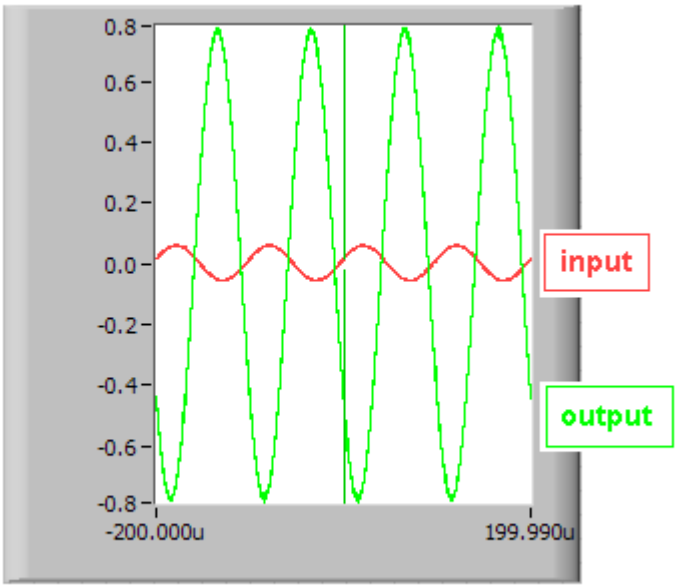

Figure 5.10: One of the input/output waveforms fetched by the NI PXI system. This is the waveform of the preamplifier system reported in Fig. 5.9 (iii), in which the preamplifier feedback system is an 18-kΩ resistor shunting a 0.8-pF capacitor. The testing frequency is 10 kHz, whilst the output voltage (green line) is ∼1.5 V (peak-to-peak) and input current (red line) is ∼0.1 mA (peak-to-peak).

5.5.2 Noise Performance

The noise performance was tested when the input node was floating. The total output power was recorded, converted into input current noise spectral density by Eq. (4.2) and Eq. (4.3), and then plotted in Fig.5.11. As reported, at the frequency of 1 MHz, the noise spectral density is around ∼1 pA/$\sqrt{\text{Hz}}$. The measured noise performance of this preamplifier system agrees with the general noise characteristics of an op amp, where the noise spectral density curve is the combination of low frequency *1/f noise* and high frequency *white noise*.

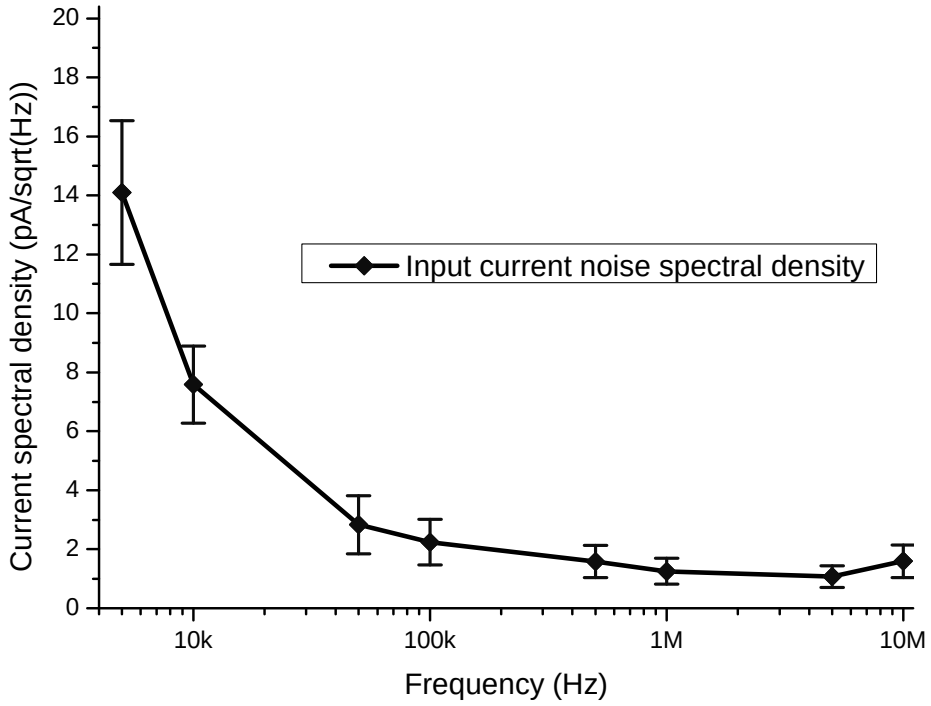

Figure 5.11: Measured input current noise spectral density with 18 kΩ transimpedance.

5.6 Discussions

5.6.1 Bandwidth & Feedback Impedance

The feedback resistor sets the transimpedance of the preamplifier system. Nevertheless, the parasitic capacitance within the feedback resistor itself limits the maximum value of the feedback resistance. Theoretically, the resistance of the feedback resistor (R1 in Fig. 5.4) shall be as large as possible due to a required large transimpedance (assuming that the condition described by Eq. (5.11) is ignored here). This limits the capacitance of C1 to a range that may be similar

to the parasitic capacitance contributed by the resistor R1. In reality, when R1 is large enough, the feedback capacitor C1 may not be necessary to meet the required high frequency cutoff. For example, a ∼200 kΩ 0805 surface mount package resistor, which can have the parasitic capacitance of about 80 fF, will set the 3-dB point (according to Eq. (5.14)) at around 10 MHz. When a smaller package is used, such parasitic capacitance can be limited to a lower value. For instance, a 0402 surface mount resistor has a typical parasitic capacitance value of around 30 fF . As a result, by introducing a resistor with 0402 package, the transimpedance of this system can be pushed to 530 kΩ for a 10-MHz bandwidth, or to 5.3 MΩ for 1 MHz.

5.6.2 Noise & Feedback Impedance

The measured noise power is independent of the feedback resistance, namely, the transimpedance of this preamplifier. If a 5.3 MΩ 0402 surface mount resistor is used as the feedback whilst narrowing the bandwidth to 1 MHz, the equivalent input current noise spectral density will become 3.7 fA/$\sqrt{\text{Hz}}$, rather than the reported ∼1 pA/$\sqrt{\text{Hz}}$ (shown in Fig. 5.11) at 1 MHz. Meanwhile, the bandwidth can be easily adjusted by changing the capacitance of C1 (for high frequency cut-off) and C2 (for low frequency cut-off) in Fig. 5.4. When the bandwidth is narrowed to 1.0 MHz (commonly used m/z region of having a low mass cut-off at ∼180 m/z for a 12-T FT-ICR MS system), with a 5.3 MΩ feedback resistor the electronic noise generated by this preamplifier referred back to the input current

will become roughly 3.7 pA.

The detection bandwidth can be traded for sensitivity by narrowing the detection window, which can be done by introducing filtering technique or by changing the preamplifier bandwidth. At threshold, the signal current has to be at least equal to the noise level in order to be detected, which means from Eqn. (2.8), around 110 singly-charged, 1000-Dalton ions (assuming the rotating orbit radius of $\frac{1}{4}$ the cell diameter, in a 12-T magnetic field) to be in the ICR cell for detection. In lieu of detecting the 1-MHz bandwidth in one detection using a 1-MHz detection window, a narrower 100-kHz window can be introduced to finish the same task in 10 detections. In which case, with a 5.3 MΩ feedback resistor ~ 35 charges ($= 3.7 \times 10^{-15} \times \sqrt{100 \times 10^3} \div 33 \times 10^{-15}$) can be detected in one scan. In reality, techniques such as multiple acquisition can be introduced to allow a weaker signal than noise.

5.7 Conclusion

As the key front-end electronic component, the preamplifier plays a critical role in pushing the unmatched FT-ICR MS performance to the limit. Following the studies of the ICR signal model from Comisarow (Comisarow, 1978), the gain and noise distribution in a multistage amplifier system, and the electronic noise, this chapter reports a preamplifier with transimpedance configuration to have not only stronger tolerance to the intrinsic capacitance of the cell, but also higher designed gain as a result of the bandwidth increment.

The improved preamplifier has a good flexibility of adjusting its transimpedance and bandwidth, whilst maintaining flat mid-band gain at the frequency of interest. The total power consumption of this circuit is around 310 mW when tested on the bench. With the chosen 18-kΩ feedback resistor, 0.8-pF feedback capacitor, and 220-nF DC blocking capacitor, the transimpedance of the preamplifier is around 85 dBΩ between 3 kHz and 10 MHz; the input current spectral density is about 1 pA/$\sqrt{\text{Hz}}$ at 1 MHz. When using a 0805 type feedback resistor, this preamplifier has been tested stable of providing a transimpedance between 45 and 85 dBΩ (depending on the feedback resistance value used), whist maintaining a bandwidth of 10 MHz. When using a 0402 type feedback resistor, this preamplifier is estimated to provide a transimpedance up to 5.3 MΩ for a 1-MHz bandwidth. In the near future, this preamplifier will be further mounted onto an FT-ICR MS system to test the performance.

CHAPTER 6

Single-Transistor Transimpedance Preamplifier Using a T Feedback Network

This chapter is partially reproduced from the journal article, "A Low Noise Single-Transistor Transimpedance Preamplifier for Fourier-Transform Mass Spectrometry Using a T Feedback Network," *Review of Scientific Instruments*, in 2012 (Lin et al., 2012).

This chapter starts with a discussion of the theories and the comparison of two different feedback arrangements, a single-resistor feedback and a T-shaped feedback network, for transimpedance amplifiers. Then it reports a single-transistor transimpedance preamplifier design to push the noise performance further. This is followed by the study of the biasing conditions, input/output impedance, and over-all transimpedance of such a design. A PCB for testing purpose is man-

ufactured. Then this is followed by the bench testing reports of the proposed T feedback network (using the transimpedance amplifier reported in Chapter 5) and the single-transistor transimpedance preamplifier. This chapter concludes with the discussion of the gain and noise performance of a preamplifier, and a suggestion of possible constructing elements for a T feedback network for circuit optimization.

6.1 Introduction

In the previous chapter, a transimpedance preamplifier was designed and tested for a Fourier-transform ion cyclotron resonance (FT-ICR) system. With the ability of effective input capacitance reduction over existing voltage amplifier designs, a transimpedance preamplifier can potentially provide an ideal preamplifier solution for many mass spectrometry systems, including FT-ICR mass spectrometry (MS). Here, efforts have been taken to further lower the noise generated by the active components of an operational amplifier (op amp) in a preamplifier. One way is to introduce a very low noise first-stage and to use only one active component.

Consequently, a novel single-transistor transimpedance preamplifier with a lower power consumption is introduced. A low noise, high input impedance JFET, BF862 from NXP Semiconductors N.V. (Eindhoven, The Netherlands),[24] is used as the main amplification stage of this transimpedance preamplifier. The noise generated by the active components in the previous design reported in

[24]See Appendix A.1 for information about the JFET BF862.

Chapter 5 is now limited. Only one transistor, which is the low noise JFET, BF862, with the equivalent noise input voltage of typically 0.8 nV/$\sqrt{\text{Hz}}$ specified on the datasheet, in the new design is responsible for such noise. Furthermore, a T-shaped feedback network is introduced as both the feedback and the gate biasing solutions to avoid a large gate biasing resistor, and to increase the bandwidth flexibility. The T feedback network is studied using the previously reported AD8099 preamplifier. Such a feedback system allows ∼100-fold less feedback resistance at a given transimpedance, hence preserving bandwidth, which is beneficial to applications demanding high gain.

6.2 Transimpedance Amplifier Transfer Function

6.2.1 Single-Resistor Feedback

A basic transimpedance amplifier is constructed out of an op amp with a feedback resistor, as shown in Fig. 6.1a. An op amp senses the voltage difference between its non-inverting input (V_+) and inverting input (V_-), and amplifies it with its open-loop gain (A). Consequently, the voltage at output becomes

$$V_{out} = A \times (V_+ - V_-). \tag{6.1}$$

An ideal op amp has a few particular characteristics, including infinite input impedance and infinite open-loop gain. In reality, the open-loop gain, A, is a finite large value of typically greater than 10^4. When analysing the op amp

circuit, it is common to assume that the input impedance is large so that the current flowing into either the inverting or non-inverting input is negligible.

With the hypotheses mentioned above, for a basic transimpedance amplifier with open-loop gain A, a feedback resistor R_f, a ideal current signal source I_{in}, and a grounded non-inverting input node ($V_+ = 0$), as shown in Fig. 6.1a, the voltage at the inverting input, V_-, can be rewritten as

$$V_- = \frac{-V_{out}}{A}. \tag{6.2}$$

There is no current flowing into the inverting input, so the input I_{in} will flow completely through the feedback resistor R_f,

$$I_{in} = \frac{V_- - V_{out}}{R_f}. \tag{6.3}$$

From Eq. (6.2) and Eq. (6.3), the transfer function, or the transimpedance, $T_{single-resistor}$ of this negative-feedback op amp circuit can be rewritten as

$$T_{single-resistor} = \frac{V_{out}}{I_{in}} = \frac{-R_f}{1 + \frac{1}{A}} \simeq -R_f. \tag{6.4}$$

Thus the closed-loop gain of this transimpedance amplifier system is independent of the op amp characteristics (its open-loop gain A), but is a function of the characteristics of the passive components (the feedback resistance R_f in this case) used to 'close' the loop.

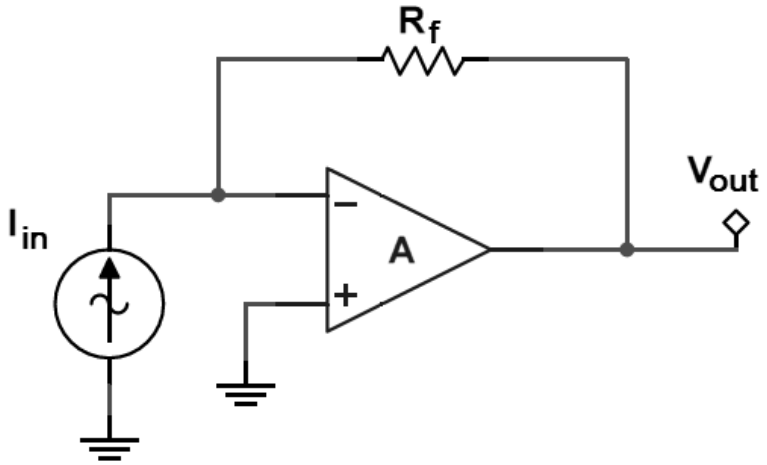

(a) Transimpedance amplifier with single-resistor feedback.

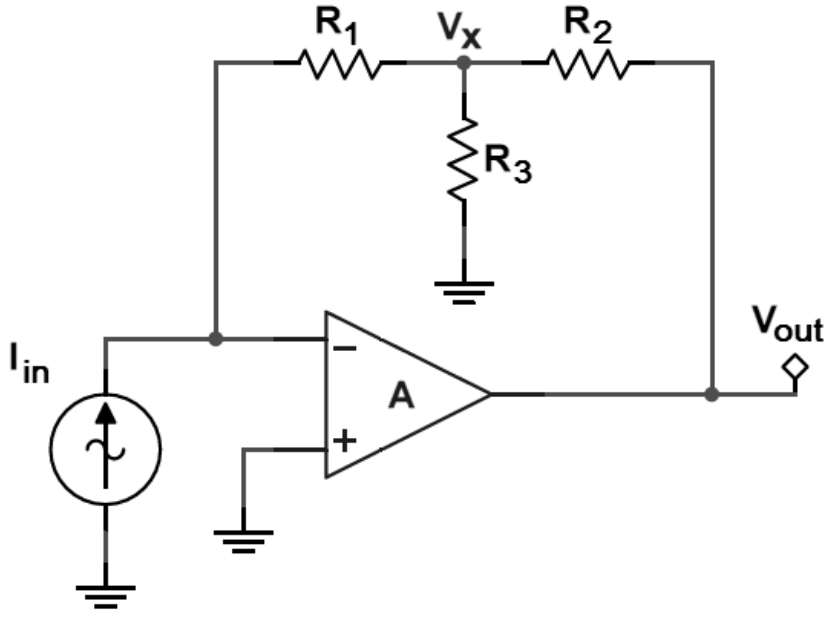

(b) Transimpedance amplifier with T-shaped feedback network.

Figure 6.1: Transimpedance amplifiers with two feedback arrangements (I_{in} indicates an ideal current signal source).

6.2.2 T Feedback Network

The single feedback resistor can be replaced by a three-resistor T-shaped feedback network (Barros, 1982; Fish and Katz, 1977) consisting of two resistors connected in series, and a third resistor coupled between the junction node of the two series resistors and a reference potential (ground in this case), as shown in Fig.6.1b. Then the circuit analysis shall be started with assuming that the voltage at the joint node of the T network, where the resistors R_1, R_2, and R_3 are connected, is V_x. The current flowing into the resistor R_1 is still I_{in}, and can be expressed as

$$I_{in} = \frac{V_- - V_x}{R_1} \ . \tag{6.5}$$

By substituting Eq. (6.2) into Eq. (6.5), V_x can be expressed as

$$V_x = V_- - R_1 I_{in} = \frac{-V_{out}}{A} - R_1 I_{in} \ . \tag{6.6}$$

At the joint node of the T network, the current flowing from the resistor R_1 is equal to the current flowing into both R_2 and R_3, namely,

$$I_{in} = \frac{V_x - 0}{R_3} + \frac{V_x - V_{out}}{R_2} \ . \tag{6.7}$$

By substituting V_x from Eq. (6.6), I_{in} can be rewritten as

$$I_{in} = \frac{\frac{-V_{out}}{A} - R_1 I_{in}}{R_3} + \frac{\frac{-V_{out}}{A} - R_1 I_{in} - V_{out}}{R_2} \ , \tag{6.8}$$

and so

$$(1 + \frac{R_1}{R_3} + \frac{R_1}{R_2})I_{in} = -[\frac{1}{A}(\frac{1}{R_2} + \frac{1}{R_3}) + \frac{1}{R_2}]V_{out} \ . \tag{6.9}$$

If it is chosen that $R_2 = 100R_3$, the equivalent resistance of $R_2 \parallel R_3$ will be about the same as R_3 ($[R_2 \parallel R_3] = [100R_3 \parallel R_3] = \frac{100}{101}R_3 \simeq R_3$). Since typically $A > 10^4$,

$$\frac{A}{R_2}(R_2 \parallel R_3) \simeq A\frac{R_3}{R_2} = \frac{A}{100} \gg 1 \ . \tag{6.10}$$

Then the transimpedance of the system becomes

$$T_{T-network} = \frac{V_{out}}{I_{in}} = -\frac{1 + \frac{R_1}{R_3} + \frac{R_1}{R_2}}{\frac{1}{A(R_2 \parallel R_3)} + \frac{1}{R_2}} = -\frac{R_1 + R_2 + \frac{R_1R_2}{R_3}}{1 + \frac{1}{\frac{A}{R_2}(R_2 \parallel R_3)}} \tag{6.11}$$

$$\simeq -(R_1 + R_2 + \frac{R_1R_2}{R_3}) \ . \tag{6.12}$$

As a result, by replacing the single feedback resistor with the T feedback network, the resistance of the feedback system can be reduced without sacrificing the overall transimpedance in a negative-feedback transimpedance amplifier system. For instance, using the designed resistance values of 47 kΩ , 18 kΩ , and 180 Ω for R_1, R_2, and R_3, respectively, the transimpedance becomes about 4.8 MΩ. Thus, with roughly the same theoretical transimpedance, the resistance values of the feedback resistors can be dropped by about 100 fold. Since the bandwidth of a transimpedance amplifier is a function of the feedback impedance, reducing the feedback resistance increases the bandwidth. Despite different technologies

being introduced for amplifier bandwidth extension (Green, 1986; Green et al., 2008a; Analui and Hajimiri, 2004; Mohan et al., 2000; Chien and Chan, 1999), the T feedback network is undoubtedly another simple approach to preserve the bandwidth without sacrificing the transimpedance. Note that here, the resistors R_1, R_2 and R_3 can be replaced by complex impedances (such as Z_1, Z_2, and Z_3) in order to obtain transimpedance characteristics which vary with frequency according to particular requirements in a given application.

6.3 Single-Transistor Preamplifier Circuit Design

6.3.1 Common-Source Amplifier

The first attempt to design a single-transistor transimpedance preamplifier was made by adjusting the impedance values of passive components, to adjust the DC conditions and to fulfill the requirement of having a large transimpedance between the frequency of 1 kHz and 1 MHz, which corresponds to the mass-to-charge ratio, m/z, between ∼180 and ∼180k in a 12-T FT-ICR system.

Voltage Gain

A common-source JFET amplifier with source degeneration is usually formed by a single JFET, a drain resistor R_D, a gate resistor R_G, and a source resistor R_S (Q1, R4, R3, and R6, respectively, in Fig. 6.2). The drain current is modulated by the JFET, according to the input voltage signal applied to the gate, and voltage

output is expected after such modulated current is converted into voltage by the drain resistor (or the load resistor), R_D. The voltage gain A_v of a common-source amplifier can be written as

$$A_v = -\frac{g_m R_{out}}{1 + g_m R_S} \simeq -\frac{g_m R_D}{1 + g_m R_S} \ , \tag{6.13}$$

where g_m is the transconductance of the transistor, and R_{out} is the equivalent output resistance, which can be approximated as R_D, when any resistance shunting the drain resistor R_D is significantly larger than the resistance of R_D. Note that datasheets often specify the transconductance g_m as the forward transfer admittance y_{fs}, where 'y' means the admittance, 'f' stands for forward transfer, and 's' indicates the common-source configuration (Deshpande, 2008), and $y_{fs} = dI_d/dV_{gs}$, the ratio of the drain current change over the change of the gate-source voltage.

Biasing Condition

In particular, the forward transfer admittance, y_{fs}, of the JFET BF862 increases with its drain current, as suggested by the datasheet. Reduction of the resistance of the resistor R6 results in increase of the drain current, causing a larger transfer admittance. Although this larger transfer admittance leads to larger gain, it sacrifices the advantages of not only the low power consumption characteristic (due to the low drain current) to lower the heat dissipation, but also the large voltage gain variation between the DC and AC signals to make this design a better

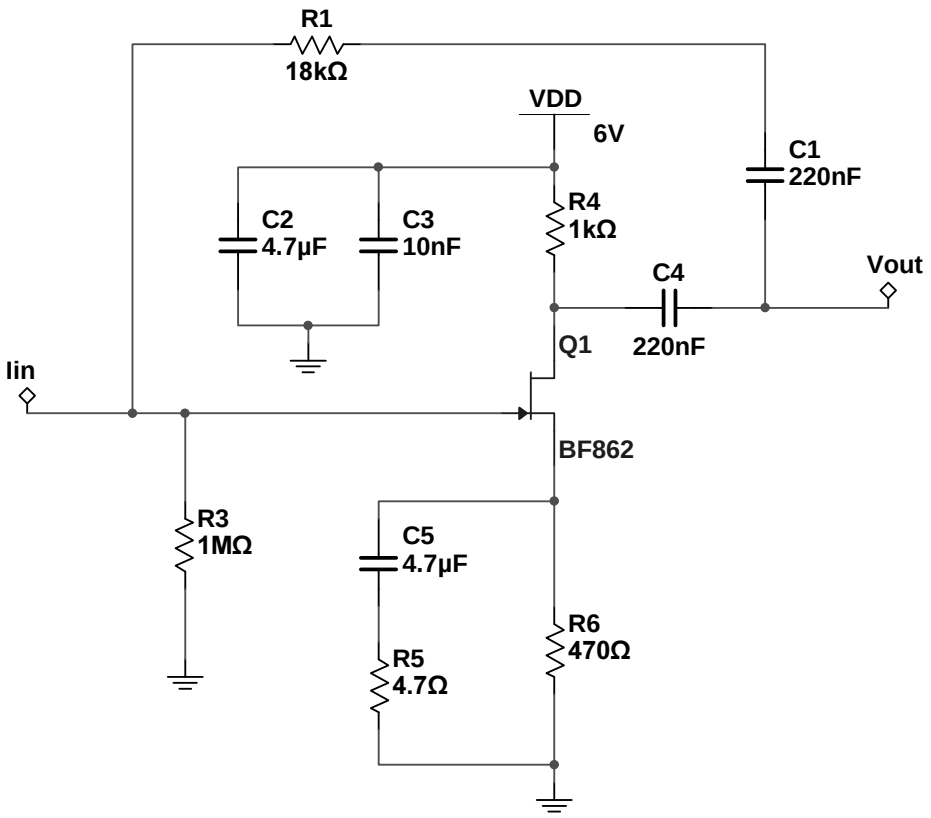

Figure 6.2: Schematic of the single-transistor transimpedance preamplifier comprised by a feedback loop (consisting of a feedback resistor R1 and a DC blocking capacitor C1), and a common-source JFET amplifier with source degeneration.

high-pass filter. Figure 6.3a shows the computer simulated correlations between the voltage gain, drain current I_D, and power consumption of this common-source JFET amplifier (the circuit of Fig. 6.2 without the feedback loop) with the permutation of five different source resistors (R6 in Fig. 6.2). As expected, the AC voltage gain is higher when a smaller source resistor is selected, at the cost of both higher DC drain current, and less DC and AC voltage gain difference.

The 470-Ω source resistor has been selected for this common-source JFET amplifier. An observed drain current of around 1.0 mA when testing this common-

source amplifier agreed with the SPICE simulation reported in Fig. 6.3a. Since this low DC drain current was below typical operating current of between 10 and 25 mA suggested by the datasheet, the characteristic curve was measured (shown in Fig. 6.3b) to test that the JFET was working in its saturation region without being pinched off.

From the measured drain current of ∼1.0 mA, the DC drain voltage V_D of 5.0 V and the source voltage V_S of around 0.47 V can be calculated. Therefore, the operation point of this design is slightly above the red (rhombus) line when V_{DS} is around 4.5 V in Fig. 6.3b. It can be noticed that this operation point is very close to the x-axis, where the JFET is off. However, the AC input signal from an ICR cell of a Fourier-transform mass spectrometer is far below the threshold to turn this transistor off. Since a 33 fA/charge current for a singly-charged 1000-Da ion in a 12-T FT-ICR system can be estimated by Eq. (2.8b), and typically less than 10^6 ions are expected for detection, a maximum of 33 nA current (assuming ions are singly charged) may be fed into the preamplifier. The calculated input voltage from the signal can be as high as 33 mV when using this common-source amplifier (as shown in Fig. 6.2, but without the feedback loop consisting of the capacitors C1, C4, and the resistor R1) with a 1 MΩ gate resistor. Such input condition makes the operation of this JFET still above the $V_{gs} = -0.5$ V trace in Fig. 6.3b. It can be concluded that this biasing condition matches the design goal of being benefit from both the low power consumption (∼5.7 mW) and the better low-frequency filtering (DC and AC voltage gain difference of ∼16 dB, as

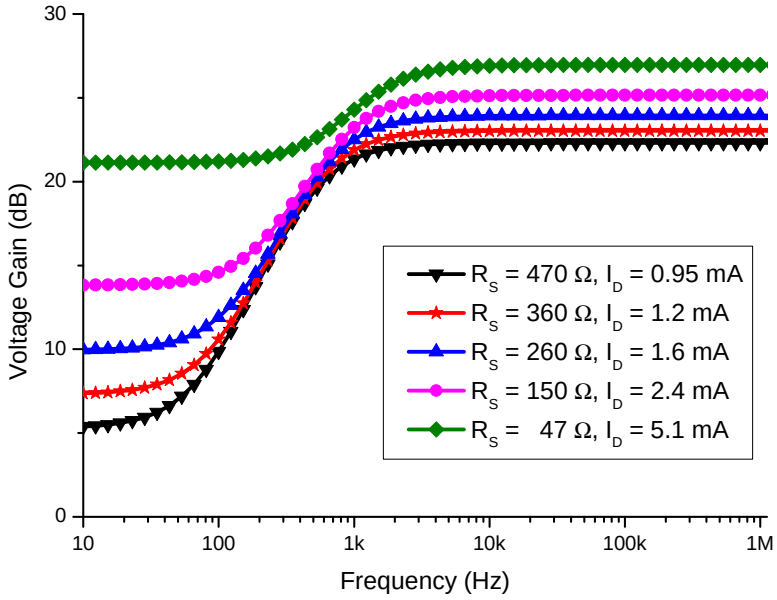

(a) SPICE simulated correlations between the source resistance R_S (R6 in Fig. 6.2) and voltage gain/drain current I_D of the BF862 common-source amplifier (as shown in Fig. 6.2, but without the feedback loop).

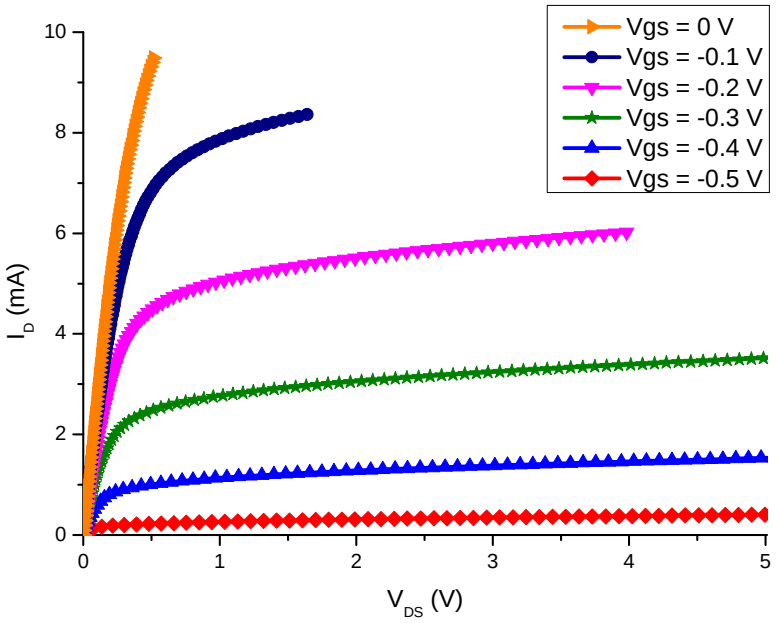

(b) JFET BF862 current-voltage characteristic curve (measured by the NI PXI system) to test the BF862 for very low DC drain currents. The operation point of this design will be slightly above the red (rhombus) line when V_{DS} is around 4.5 V.

Figure 6.3: Common-source amplifier using the JFET BF862.

shown in Fig. 6.3a).

6.3.2 Feedback Loop Configuration

When a feedback resistor (R1 in Fig. 6.2) is added into this common-source amplifier to modify this circuit into a transimpedance amplifier, not only the DC blocking capacitor C1 is needed to separate the DC potentials of the gate and the drain nodes, but there are loading issues to be carefully considered. It can be seen clearly from Eq. (6.13) that the drain resistance R_D plays a role when determining the voltage gain A_v. With the feedback loop coupled between the input and the output, the feedback resistor R1 becomes part of shunting resistance to R_D. As a result, there will be a minimum threshold resistance for R1 to keep the voltage gain A_v at a reasonable scale for a given application.

Input/Output Impedance

At the input node (the gate of the JFET), it is expected that the majority of the input signal current flows into the the feedback resistor R1 instead of the gate biasing resistor R3. Assuming the input resistance of the JFET is too large (in comparison to R1 and R3) to be considered, the ratio of R3 over R1 should be so large that the input current grounded via R3 can be negligible. For a larger transimpedance, a larger feedback resistor R1 is desired, resulting in a desired much larger R3 to push the signal into the feedback loop. Thus there is also a maximum threshold resistance of R1 or R3, such that the JFET input resistance

can be neglected. Therefore, to push the transimpedance of this single-transistor preamplifier, namely, to further increase the feedback resistance value, such gate biasing resistor has to be removed.

An effort has been made to re-locate the biasing gate resistor into the feedback network. Consequently, the single feedback resistor of R1 in Fig. 6.2 is replaced by a three-resistor, T-shaped feedback system, consisting of R1, R2, and R3 shown in Fig. 6.4a. The schematic shown in Fig. 6.4a represents the low noise single-transistor transimpedance preamplifier with a T feedback network. Without a gate resistor, the gate can still be properly biased to a fixed potential (ground in this case) through both resistors of R1 and R3. Note that the input of the preamplifier is DC coupled to the detection plates of the ICR cell, and thereby provides the ground potential needed for stable ion trajectories.

Moreover, the output impedance of this Single-transistor transimpedance preamplifier needs to be matched to the impedance of a 50-Ω transmission line in an FTMS system. A voltage amplifier (VA), such as the AD8099 VA shown in Fig. 6.6a, can be introduced for this purpose.

Effective Transimpedance Using a T feedback network

An overall transimpedance of 4.8 MΩ can be estimated by Eq. (6.12). However, by using a common-source amplifier instead of an op amp as the main amplification stage, the assumption of the open-loop gain $A > 10^4$ is no longer valid, causing the actual transimpedance [calculated by Eq. (6.11)] smaller than the estimated value

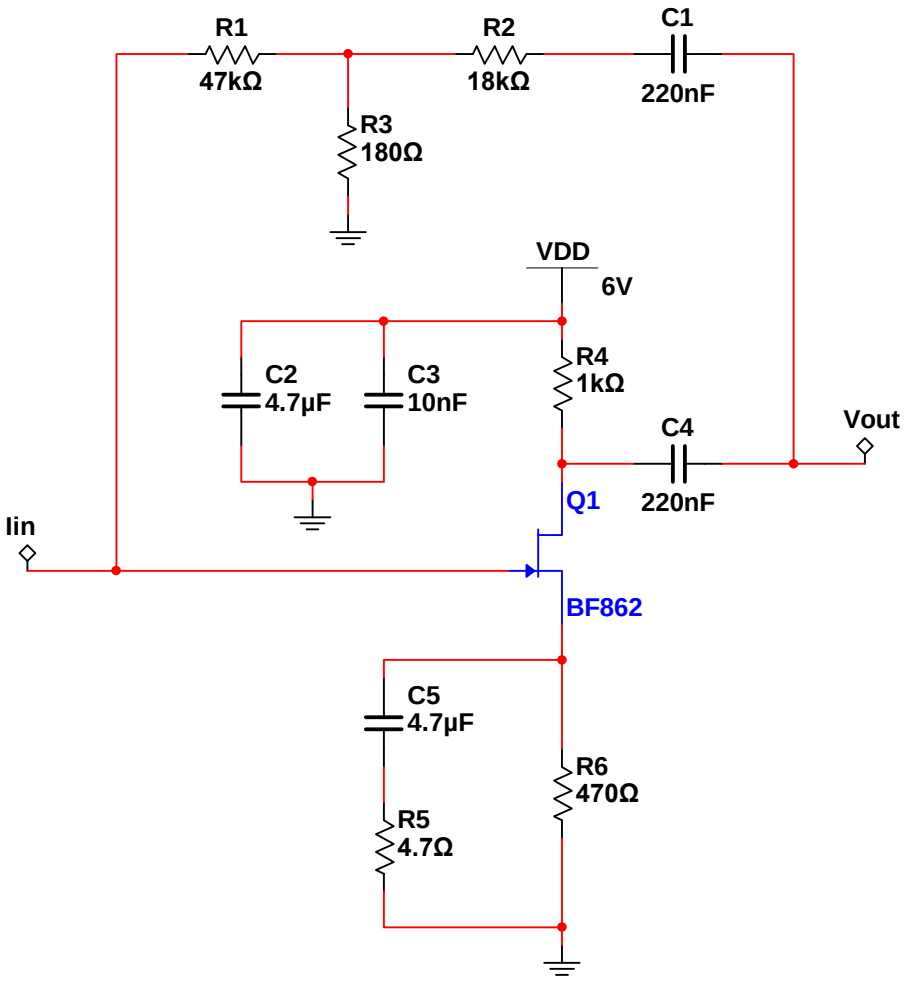

(a) Schematic of the single-transistor transimpedance preamplifier using a T feedback network.

Figure 6.4: Single-transistor transimpedance preamplifier.

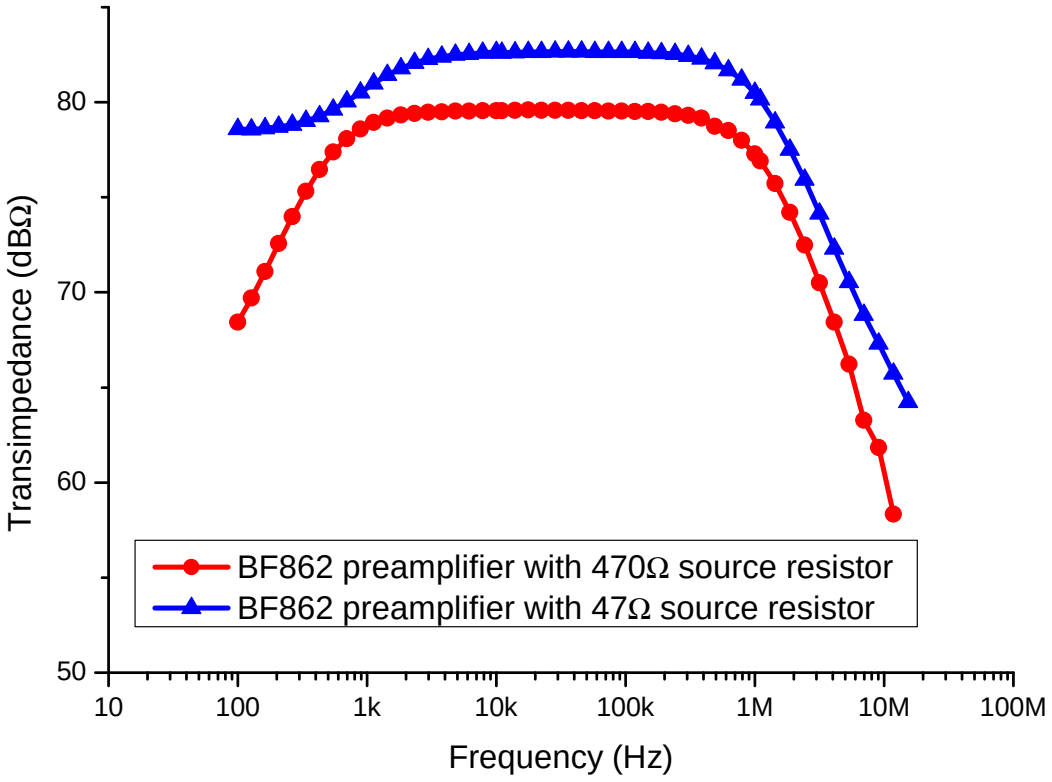

(b) Measured transimpedance frequency response of the single-transistor transimpedance preamplifier using a T feedback network (schematic shown in Fig. 6.4a), where two resistance values of the source resistor R6 (47 Ω and 470 Ω) are tested to show the variation of transimpedance according to the biasing condition change.

Figure 6.4: Single-transistor transimpedance preamplifier.

from Eq. (6.12). Such results can be proved later by the measured transimpedance data.

In a single-feedback-resistor transimpedance amplifier system (as shown in Fig. 6.1a), the bandwidth can be limited by adding a capacitor in parallel with the feedback resistor R_f. The same technique can be used in a transimpedance amplifier system with the T feedback network. In Fig. 6.1b, such a capacitor can be added in parallel with either R_1 or R_2. Figure 6.6c shows the simulated

3-dB transimpedance bandwidth corners using two feedback capacitors in the T feedback network with several different permutations (shunting neither, one, or two of the consecutive resistors with an 8 pF capacitor). The AD8099 Preamplifier with the T feedback network shown in Fig. 6.6a was simulated. When no capacitor was connected onto the T feedback network, the 3-dB frequency corner was provided by the parasitic capacitance shunting the feedback system. When a 8 pF capacitor shunts either the resistor R11 or R12, a lower frequency 3-dB corner was expected. When both consecutive resistors (R11 and R12 in Fig. 6.6a) were shunted by a 8 pF capacitor, not only an earlier 3-dB corner was expected, but also the transimpedance after the 3-dB corner dropped more steeply with frequency.

6.3.3 Printed Circuit Board

A single-layer PCB was designed and manufactured in-house. All components were located inside a ground ring to assist shielding from environmental noise. Low noise surface mount thin-film chip resistors from Panasonic Corporation (Osaka, Japan) were selected to limit the intrinsic noise from the passive components.

The populated PCB (sized $\sim 100 \times 60\ mm^2$, where the single-transistor preamplifier occupies the areas of about $20 \times 15\ mm^2$), is shown in the Supplementary Fig. 6.5. This PCB is for bench testing purpose. To test the FT-ICR performance with this newly designed amplifier, a smaller sized board should be designed, so

that the stray impedance can be limited. The PCB manufactured for the previous design reported in Chapter 5 is also used here to test the performance of the T feedback network.

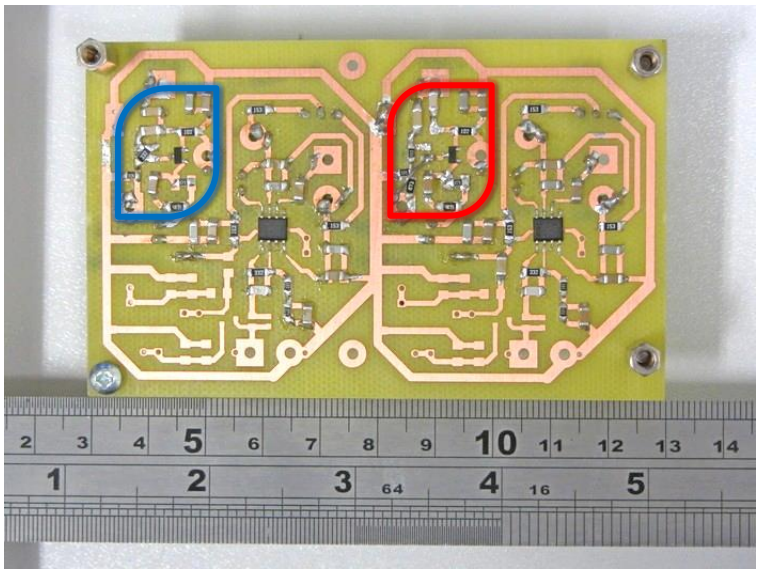

Figure 6.5: Printed circuit board of four sets of amplifier circuits: (i) the single-transistor preamplifier with a single-resistor feedback (inside the blue circle on the top-left corner); (ii) the single-transistor preamplifier with the T feedback network (inside the red circle on the right close to the center); (iii) two sets of AD8099 voltage amplifiers.

6.4 Circuit Testing

The T feedback network was tested using the previously reported AD8099 preamplifier reported in Chapter 5. Figure 6.6a illustrates the schematic of the AD8099 preamplifier with the T feedback network. A voltage amplifier using the same op amp AD8099 is also shown in Fig. 6.6a. In this report, when testing the T feedback network using the AD8099 Preamplifier, the resistance values were always R1 = 47 kΩ, R2 = 18 kΩ, and R3 = 180 Ω, with a 0.8-pF capacitor C1 shunting

R2. When testing the newly designed single-transistor transimpedance preamplifier with the T feedback network, the 0.8-pF capacitor was not connected. Since the AD8099 is a high speed op amp with gain-bandwidth product of about 3.8 GHz, the existence of the 0.8-pF capacitor (C1 in Fig. 6.6a) is to limit the bandwidth to around 1 MHz, which corresponds to the mass-to-charge ratio, m/z of ∼180 in a 12-T FT-ICR system. For the JFET BF862, its bandwidth characteristic will limit the 3-dB corner to around 1 MHz at a transimpedance of ∼80 dBΩ. To compare the performance of the T feedback network with a single resistor feedback, a feedback system with only a 4.7-MΩ resistor (in such case, the capacitor C1 and the resistor R1–R3 were replaced by a 4.7 MΩ resistor, coupling the I_{in} and V_{out} node in Fig. 6.6a) is also tested.

6.5 Results & Discussions

Figure 6.6b shows the frequency response using the AD8099 preamplifier in three feedback conditions: (i) an 18-kΩ resistor in parallel with a 0.8-pF capacitor (reported in Chapter 5) (ii) a single 4.7-MΩ feedback resistor, and (iii) the T feedback network as shown in Fig. 6.6a. The change of the DC blocking capacitor C2 could be also noticed. C2 was 220 nF in the previous design when the 18-kΩ curve was measured. In order to set the low corner frequency at around 1 kHz (m/z of 180k in a 12-T system), the 220-nF C2 is replaced by a 4.7-μF capacitor. A narrower bandwidth for the single 4.7-MΩ feedback curve can be noticed. It is caused by the parasitic capacitance of this 4.7-MΩ resistor.

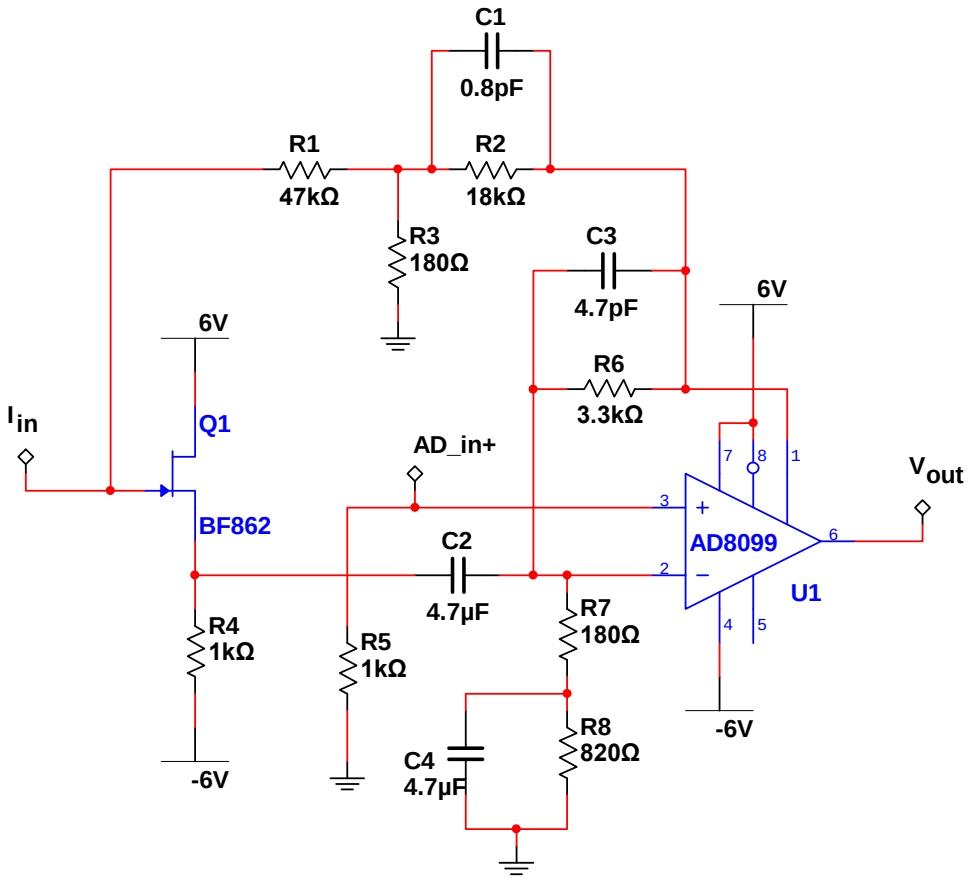

(a) Schematic of the AD8099 Preamplifier with a T feedback network. When the transistor Q1, capacitors C1, C2, and resistors R1–R4 are disconnected, the rest of the circuit forms an AD8099 VA, which can be used to match the output impedance of the single-transistor preamplifier to a 50-Ω transmission line in an FTMS system.

Figure 6.6: The AD8099 preamplifier with a T feedback network.

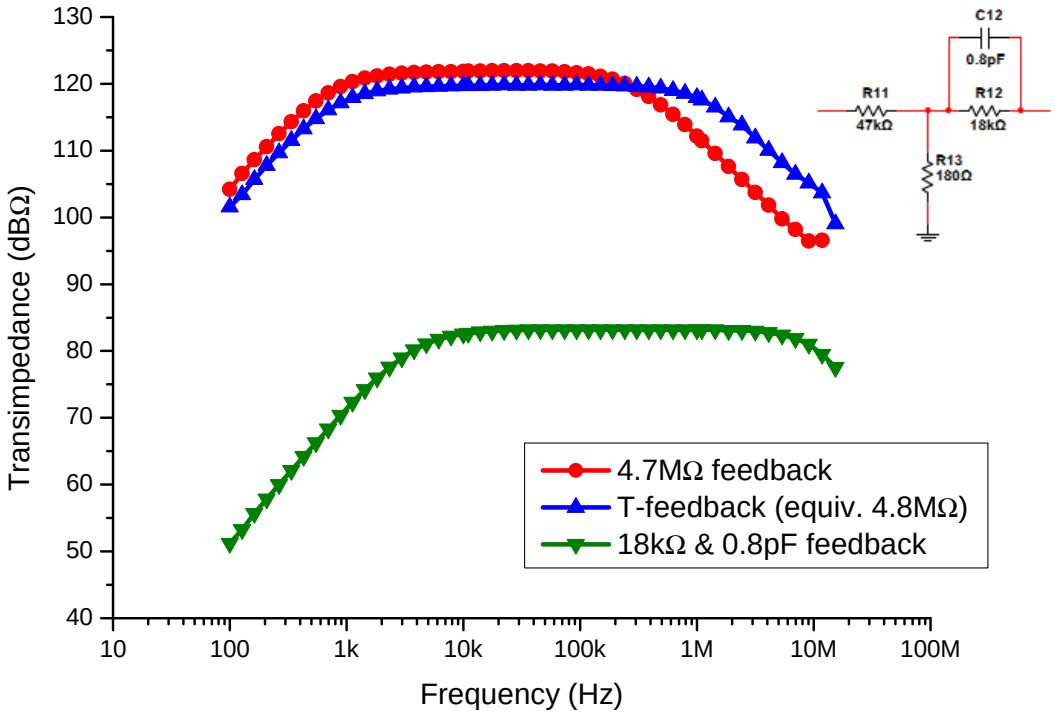

(b) Measured transimpedance of the AD8099 preamplifier with three feedback systems: (i) a single 18-kΩ feedback resistor shunting a 0.8-pF capacitor; (ii) a single 4.7-MΩ feedback resistor; (iii) the T feedback network as shown by the inset.

Figure 6.6: The AD8099 preamplifier with a T feedback network.

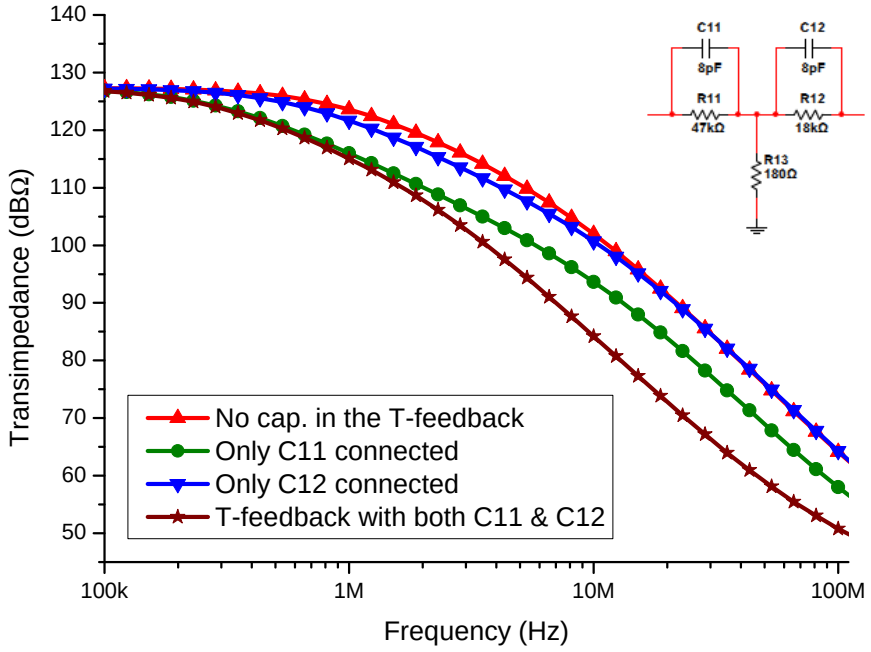

(c) SPICE simulation of the AD8099 preamplifier frequency response in different permutations of the presence of the two 8-pF feedback capacitors (C11 and C12 shown by the inset) in the T feedback network.

Figure 6.6: The AD8099 preamplifier with a T feedback network.

Despite the bandwidth variation, in Fig. 6.6b the measured transimpedance of the preamplifier using the T feedback network (consisting of 47-kΩ, 18-kΩ, 180-Ω resistors, and a 0.8-pF capacitor) shows a good agreement with the preamplifier using a single 4.7-MΩ feedback resistor.

The transimpedance frequency response of the single-transistor transimpedance preamplifier with the T feedback network is measured when a 470-Ω or a 47-Ω source resistor is used. As shown in Fig. 6.4b, the use of a 470-Ω source resistor shows a flat transimpedance of a few dBΩ less than the 47-Ω source-resistance preamplifier. However there is better filtering at low frequency for the 470-Ω source-resistance curve. As the DC drain current is about 0.95 mA and 5.1 mA

for the source resistance values of 470 Ω and 47 Ω, respectively, with the supplied voltage of 6 V, the power consumption when using a 47 Ω source resistor is about 25-mW more than, or around 5-fold of, the power used in a 470-Ω source-resistance preamplifier. More consumed power means more heat dissipation. Undesired heating can cause instability, so minimizing preamplifier power consumption in MS applications is important, especially when the preamplifier is located in vacuum close to the mass analyzing device for minimal parasitic capacitance from cabling.

The noise performance of the newly designed single-transistor transimpedance preamplifier with the T feedback network is not showed, since the noise spectrum is below the sensitivity of the spectrum analyser, IFR A-7550 (mentioned in Chpater 4), utilized to measured the noise performance. In such a single-transistor preamplifier design, this T feedback network replaces not only the feedback resistor, but also the biasing resistor (for biasing both the input (gate) terminal of the transistor and the detection plates of the ICR cell). Thus the amplifier noise cannot be simply modeled with a simple current or voltage noise source following a standard noise analysis procedures. Instead, the method suggested by Letzter and Webster (Letzter and Webster, 1970) must be employed for each resistor in the network, but calculating the "referred input noise current" and "referred input noise voltage" will be difficult as both the noise and the gain are affected. To predict the noise behavior in this case calls for further careful research. To test the resulting signal-to-noise behavior, a noise analysis system

with sensitivity better than the spectrum analyzer used for this report will be necessary.

The T feedback network provides more bandwidth for a given transimpedance, since the parasitic capacitance shunts a reduced resistance in this feedback system. The T feedback network also increases the transimpedance and the flexibility to obtain transimpedance characteristics for a given application. The single-transistor transimpedance preamplifier with a T feedback network provides a low-noise preamplification solution, but less gain in comparison to an op amp based preamplifier, such as AD8099 preamplifier. Recall that the signal-to-noise performance of the complete system can be maximized electronically by not only reducing the noise but also increasing the gain of a preamplifier. An optimized balance between the preamplifier gain and noise characteristics needs to be obtained for the best signal-to-noise performance in a given system.

6.6 Conclusion

A new low noise, low power consumption preamplifier for an FT-ICR mass spectrometer using a single-transistor transimpedance preamplifier with a T feedback network has been designed, manufactured and tested. The characteristics of using a resistive T feedback network is studied by using an op amp. The introduction of the T feedback network in an op amp based transimpedance system allows ∼100-fold less resistance (under the circumstance that the resistance value of R_2 in Fig. 6.1b is 100 times the resistance value of R_3) for a given transimpedance,

hence more bandwidth can be preserved.

In response to the need of the ultra low noise, in this preamplifier design, a very low noise common-source JFET amplifier is used as the main amplification stage. The very large open-loop gain offered by an op amp is traded with better noise performance and lower power consumption (∼5.7 mW). In such a case, the measured transimpedance of around 80 dBΩ between the frequencies of about 1 kHz and 1 MHz satisfies the need of a 12-T FT-ICR mass spectrometer with corresponding m/z of approximately 180 to 180k. Alternatively, using the AD8099 Preamplifier with the T feedback network, the transimpedance can be around 120 dBΩ with roughly the same bandwidth. To use the single-transistor transimpedance preamplifier with a T feedback network as the front-end electronics for the FT-ICR MS, the reported AD8099 VA can be a buffer candidate to match the output impedance to the impedance of a signal transmission cable.

Although here the preamplifier is designed for the application of FT-ICR MS, a similar technique can be introduced to other mass spectrometers such as the Orbitrap (Makarov, 2000), time-of-flight (TOF), and ion trap systems. Each of the three constructing elements in a T feedback network can be in any form of the combinations of resistive, capacitive, or inductive elements to create any complex impedance to have optimized frequency and transimpedance characteristics for the requirements of any particular application. Since this design can be an ideal front-end amplification solution to be applied to any charge/current detecting device, it can be introduced to other areas of applications, such as nuclear

magnetic resonance spectroscopy (Appelt et al., 2006), optical communication systems (Green et al., 2008b), or charge-coupled devices (CCDs), etc.

CHAPTER 7

Radio-Frequency Oscillator for a Quadrupole Mass Filter

A mass analyser is one of the components in a modern mass spectrometer, as discussed in Section 2.1.2. Generally, in an FT-ICR system, a mass analyser contains an ion transferring/filtering/accumulating system and an ion cyclotron resonance (ICR) cell. A quadrupole ion filter can be used here for ion filtering before sample ions being transferred into the ICR cell for detection. The operation of a quadrupole ion filter has been introduced in Chapter 3, and a proposed new electronic device for driving a quadrupole ion filter will be presented in this chapter.

This chapter reports a radio-frequency (RF) oscillator as a power supply for operating a quadrupole mass filter. The design reported here has a stabilised output frequency, and a feedback control for output amplitude stabilisation. This RF oscillator is designed to operate at room temperature. It can provide two out-

of-phase sinusoidal waveforms at the frequency of 1 MHz and the amplitude of 500 V to the quadrupole filter rods. A 200-V DC power supply will be used to supply this power amplifier. The chapter first introduces the building blocks of the new quadrupole mass filter power supply, and is followed by the report of the electronic details of each building block. Three PCBs are built for testing the RF oscillator, bandpass filter, gain control circuit, power amplifier, and feedback control circuits reported here. Then a transformer design is suggested, and is followed by the discussion of the correlation between the resonant frequency, and the impedance of the output stage. Future works for this project are also suggested at the end of this chapter.

7.1 Introduction

The theory of operating a quadrupole mass filter has been discussed in Chapter 3. The existing power supplies to quadrupole devices have also been briefly reviewed in Chapter 3. Here, efforts are made to design a new RF power supply for driving a quadrupole mass filter. The new design, as illustrated by the block diagram in Fig. 7.1, includes:

- a newly designed RF oscillator (the first stage in the mass filter power supply diagram shown in Fig. 3.1) with a new built-in automatic gain control (AGC) unit for output amplitude stabilization;

- a power amplifier (the second stage) modification from the design by Mathur

and O'Connor in 2006 (Mathur and O'Connor, 2006);

- a redesigned rectifier to generate feedback signal (based on the signal amplitude on the quadrupole rod) for the AGC;
- a proposed air-core transformer (the third stage) with better balance, and more cross-section area to carry the signal current.

Details of such a RF power supply design and the test results are presented in this chapter.

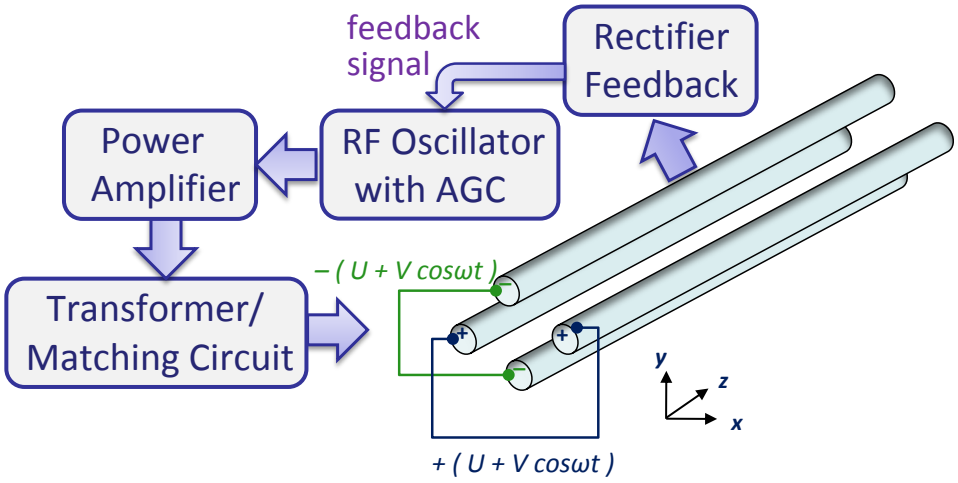

Figure 7.1: Block diagram of the newly designed RF power supply for a quadrupole mass filter.

7.1.1 Component Selection

The design goal for this RF power supply is to provide enough voltage and current to drive the mass filter rods at 1 MHz. As a result, the driving ability of each component at 1 MHz is very important.

The power amplifier second stage should be able to supply a 1-A current to drive the transformer third stage. The output sine wave after the transformer should have an amplitude of less than 500 V. It will be discussed in Section 7.2 that this power amplifier second stage is supplied by a 200-V DC voltage, and is driven by a current signal from a centre-tapped transformer (details are illustrated by Fig. 7.4). Therefore, as the input and output of this power amplifier second stage are both current signals, a power BJT becomes a better amplifying transistor candidate over a MOSFET. Details of the power amplifier design will be reported in Section 7.4.

As current signal is needed to drive the centre-tapped transformer mentioned above, another BJT is chosen for this purpose. Such a BJT is the output transistor of the RF oscillator first stage. Moreover, there is a crystal oscillator at this first stage. The crystal oscillator provides voltage signal and prefers a FET load, as suggested by the datesheet. As a result, a FET (instead of a BJT) is selected to be driven by the crystal oscillator here. Details of this first stage circuit will be discussed in Section 7.2.

7.1.2 Circuit Testing

For the circuit testing in this chapter, the DC power to the circuits is supplied by the TTi DC power supplies mentioned in Chapter 4. The oscilloscope Tektronix (Beaverton, Oregon) DPO2014 is used to measure the output of the oscillator, and to perform the fast Fourier transform (FFT) on the output waveforms.

7.2 RF Oscillator Design

A crystal oscillator is a good oscillating reference when designing a RF oscillator demanding very stable frequency output. The goal is to have a single-frequency sine wave at the output. Since most of the crystal oscillators output square waves, a low-pass or a bandpass filter is essential for eliminating the high frequency components in a square wave.

7.2.1 Crystal Oscillator

The schematic of the new RF oscillating source is shown in Fig. 7.2. A 1.000-MHz high-stability crystal oscillator, HG-2150CA-SVH, from Epson Toyocom (Tokyo, Japan),[25] is introduced as a square-wave generator with a frequency tolerance of $\pm 15 \times 10^{-6}$. A 5-V DC voltage for this crystal oscillator is supplied by a regulator, LM78L05, from Texas Instruments (Dallas, Texas, USA). The crystal drives a N-channel enhancement-mode FET, 2N7002, from Fairchild Semiconductor (San Jose, California). This FET has an input capacitance of around 20 pF at 1 MHz, which was tested drivable by the chosen crystal oscillator. Its maximum drain-source voltage rating of 60 V is also suitable for this application, in which less than 12 V drain-source voltage will be supplied to this FET. By varying the supply voltage to the FET 2N7002, the biasing drain current is changed, causing a transconductance g_m change. Therefore, the the output amplitude can be altered. Here, the OE (output enable) pin of the crystal oscillator is connected

[25] See http://www.epsontoyocom.co.jp/english/product/OSC/set01/hg2150ca/index.html for information about high-stability oscillator HG-2150CA-SVH, accessed 15 August 2012.

to the DC supply voltage (5 V in this case) to always enable this crystal oscillator. Potentially, this OE pin can be used as a control terminal to disable the oscillator output.

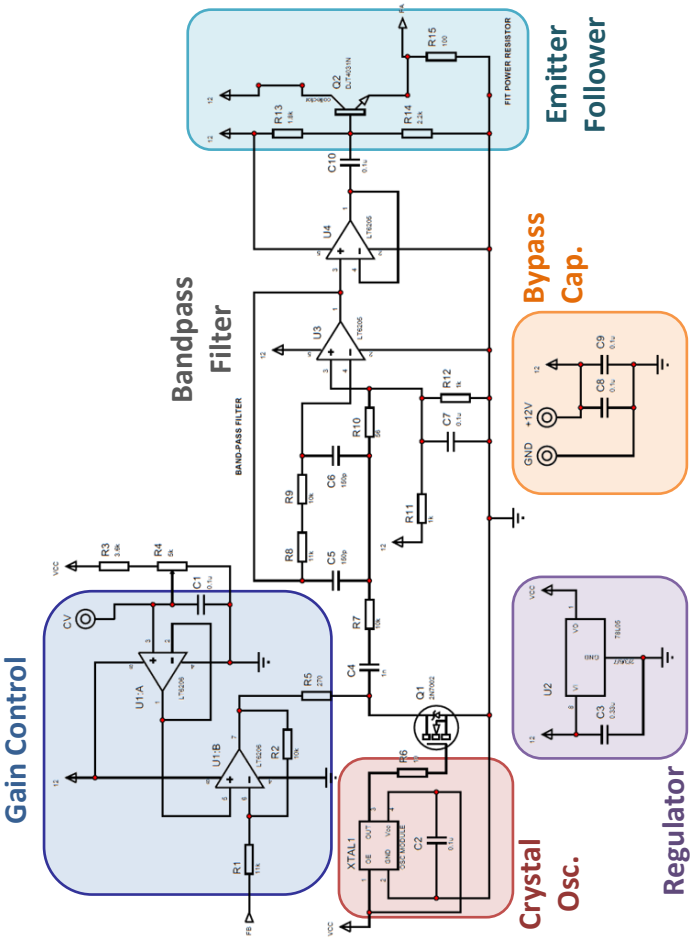

(a) Block diagram of the schematic shown in Fig. 7.2b.

Figure 7.2: Fixed frequency RF oscillating source with output amplitude control.

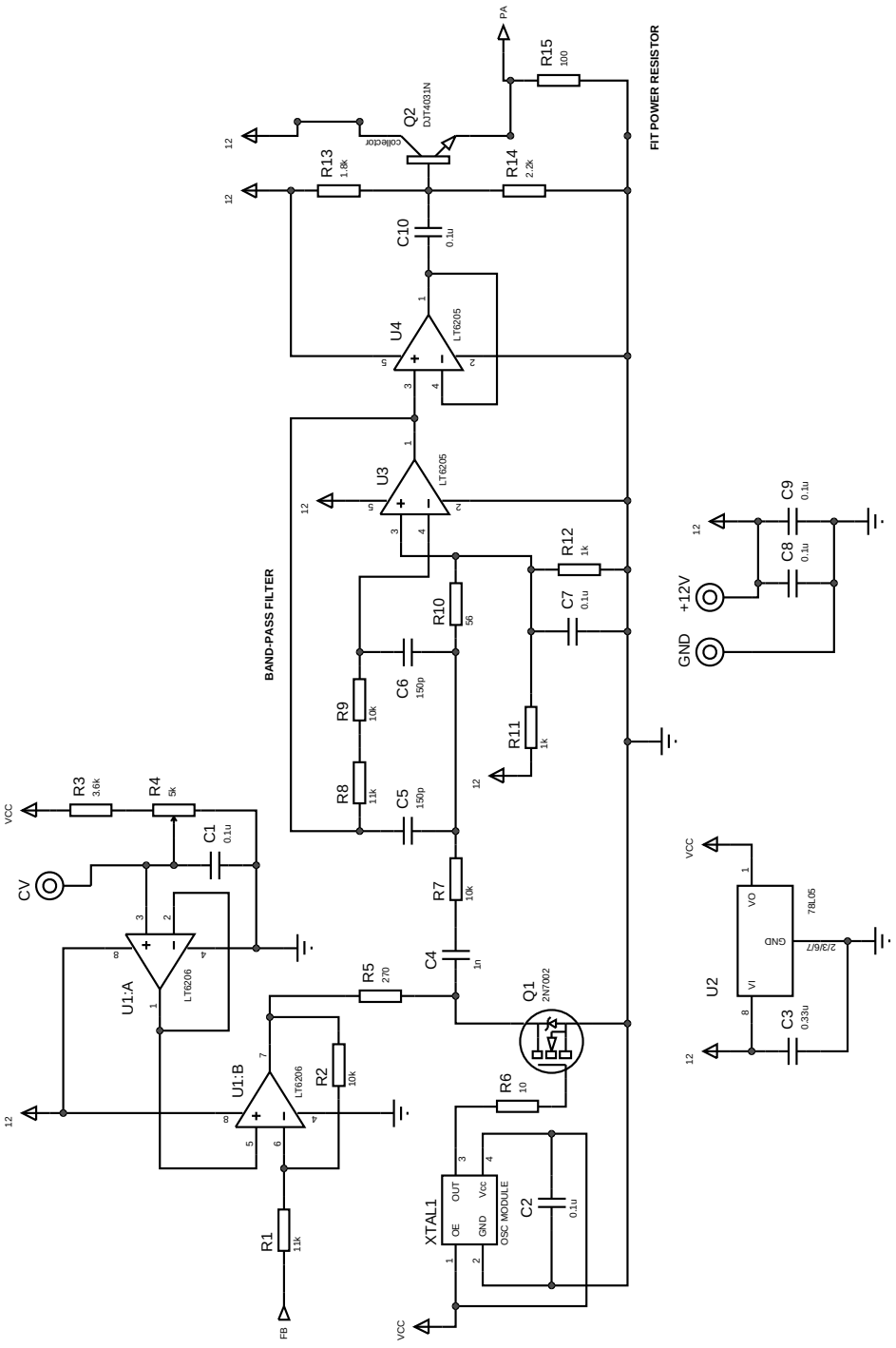

(b) Schematic.

Figure 7.2: Fixed frequency RF oscillating source with output amplitude control.

7.2.2 Bandpass Filter

In the schematic shown in Fig. 7.2, two LT6205 operational amplifiers (op amps) from Linear Technology (Milpitas, California, USA),[26] construct a bandpass filter and an output buffer. The op amp LT6205 has a gain-bandwidth product of 100 MHz, and can be supplied with DC voltage of 12 V. Therefore LT6205 (along with its dual version, LT6206, and quad version, LT6207) is widely used in this oscillator circuit. This commonly known Deliyannis-Friend bandpass filter (Deliyannis, 1968; Friend, 1970; Friend et al., 1975), consisting of the op amp U3, resistors R7–R12, and capacitors C5–C6, is designed to have both gain and Q around 10. A SPICE simulation is performed to test the frequency response of this bandpass filter. The result in Fig. 7.3 shows a very narrow window for the 1-MHz signal, which is ideal for reshaping the 1-MHz square wave into a mostly pure sine wave. The output of the bandpass filter fed a voltage follower op amp, U4, to prevent the following stages from interfering with the filter.

7.2.3 Gain Control Scheme

An AGC scheme, which is similar to what was used in the Mathur and O'Connor's oscillator (Mathur and O'Connor, 2006), is utilized partially by two op amps, LT6206.[27] In the schematic shown in Fig. 7.2, both op amps (U1:B and U1:A) are configured as comparators for the gain control signals, FB (feedback) and CV

[26] See Appendix A.3 for information about the op amp LT6205.

[27] Op amp LT6206 is the dual version of LT6205. See Appendix A.3 for information about the op amp LT6206.

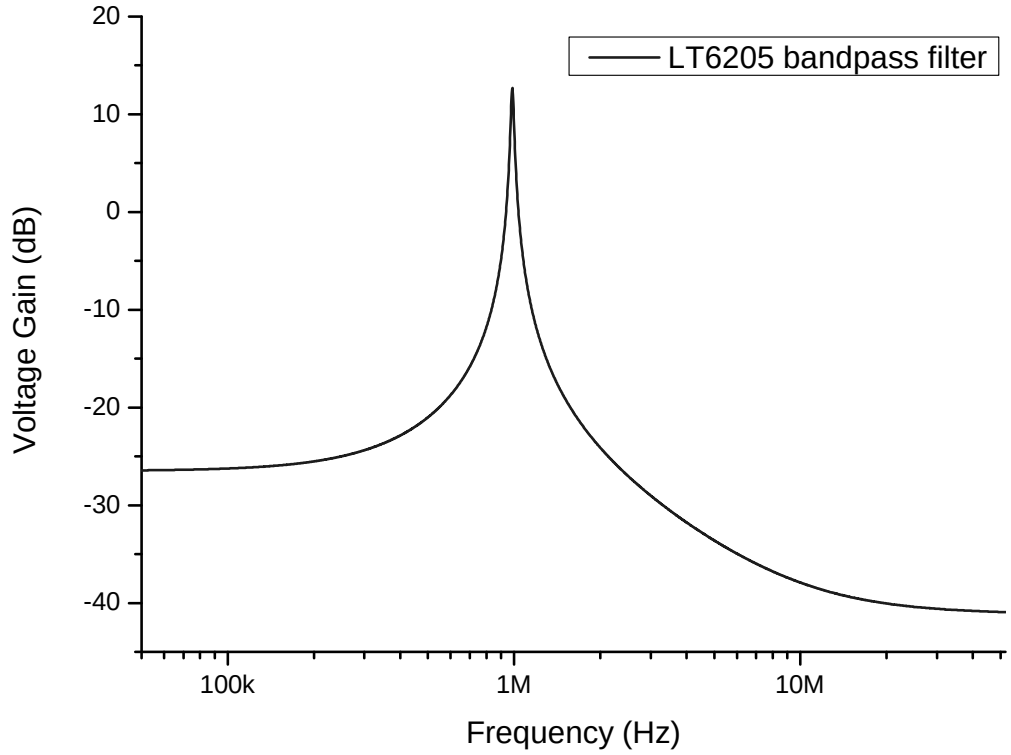

Figure 7.3: The frequency response simulation of the Deliyannis-Friend bandpass filter in Fig. 7.2.

(control voltage), respectively. Note that here the voltage at pin CV can be also generated by the resistor R3 and trimmer resistor R4. Pin CV is preserved for a control input to assign the output amplitude. The existence of R3 and R4 is just for testing convenience, and can be removed when a control voltage input is provided to pin CV.

Pin FB is preserved for the feedback signal, which is designed to be proportional to the amplitude of the RF signal applied to the quadrupole mass filter. With no input, op amp U2B generates a 3 V DC voltage, which was found a good value to prevent destabilization, for FET Q1. As the voltage on the FB

pin increases, the amplitude of the square wave output after Q1 will drop. In general, the signal from terminal FB is to stabilize the output amplitude to an assigned level, which is determined according to the voltage at terminal CV.

A power transistor, the NPN BJT, DJT4031N,[28] from Diodes Inc. (Plano, Texas), is able to be operated with a 3-A continuous collector current. The transition frequency of 105 MHz reported on the datasheet indicates that this BJT is suitable as a driving buffer for a 1 MHz signal here. This BJT is designed as an output stage for driving the primary coil of a transformer with a centre-tapped secondary winding to generate two symmetrical but 180-degree out of phase sinusoidal waveforms. Such a transformer is illustrated in Fig. 7.4. The 'RF Source' supplies a sine wave to the primary coil of this transformer. At the output node 'V_0' the output waveform will be a 180-degree out of phase of the output at the node 'V_180.' These waveforms can be used as the input signal for the power amplifier second stage (formed of power BJTs), which will be reported in Section 7.4.

7.2.4 RF Oscillator Printed Circuit Board

A single-layer PCB (sized roughly 72×25 mm), as shown in Fig. 7.5, is designed, etched, and populated in-house. This single-layer board is for the purpose of feedback signal testing. All components on the board are located inside a ground ring/ground plate. The noise-sensitive crystal oscillator and its power supply,

[28] See http://www.diodes.com/products/catalog/detail.php?item-id=6044 for information about BJT, DJT4031N, accessed 15 August 2012.

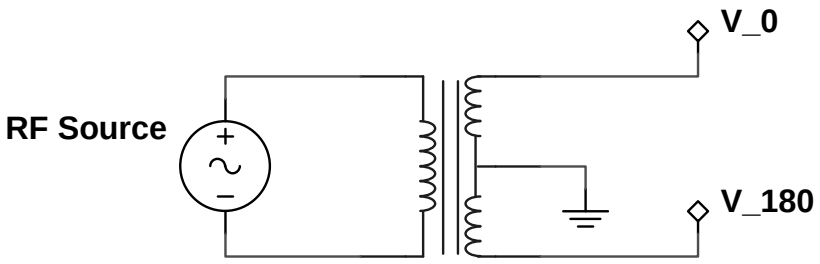

Figure 7.4: A transformer in which its secondary coil is centre-tapped. The RF Source represents the circuit shown in Fig. 7.2, and drives the primary coil of this transformer. The output nodes 'V_0' and 'V_180' will be connected to the power amplifier decried later in Section 7.4.

the 5-V DC regulator, (XTAL1 and U3 in the schematic shown in Fig. 7.2, respectively) are located further away from other components to minimise noise interference. The components of the Deliyannis-Friend bandpass filter are located as close as possible to minimize the length of the traces, so that the stray impedance from the traces is limited. For heat dissipation purpose, the collector of the BJT, DJT4031N, is soldered on a large 11 × 11 mm metal plate located around the top-right corner of the PCB inside the ground ring.

7.2.5 Testing Results

Figure 7.6 shows the output waveforms measured at (a) the OUT terminal of the crystal oscillator XTAL1 and (b) the output of the op amp U4. The feedback voltage at pin FB is set to around 2.0 V. At the OUT terminal of the crystal oscillator, a 1.0-MHz square wave with a peak-to-peak amplitude of 5.0 V is shown. The spectrum after FFT shows a 1.0-MHz peak with an amplitude of 7.2 dB, and a third harmonic at 3.0 MHz of -2.4 dB. After the FET Q1 and

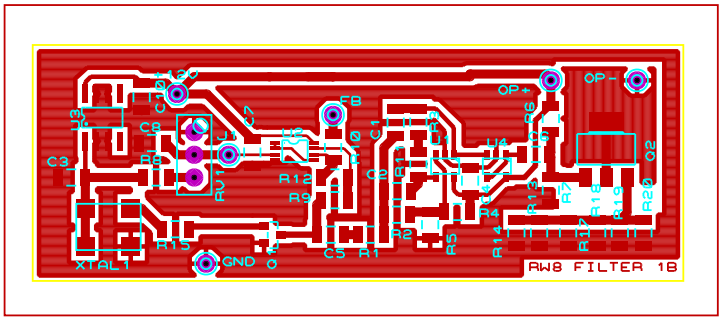

(a) Printed circuit board layout file.

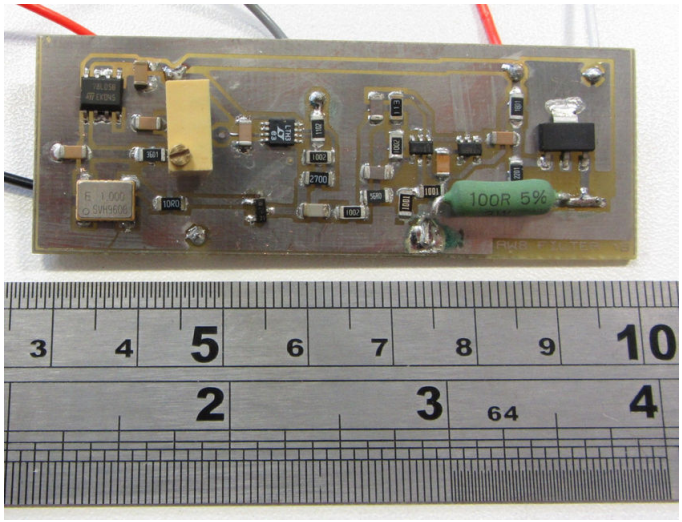

(b) Fully populated board, sized 72 × 25 mm.

Figure 7.5: Printed circuit board of of the fixed frequency RF oscillating source with output amplitude control.

the Deliyannis-Friend bandpass filter, the signal becomes a 1.0-MHz, 5.1-V sine wave with a measured first harmonic of 5.3 dB. The third harmonic is hard to be seen on the screen. However, the highest peak amplitude after 1.0 MHz is -43 dB located at around 3.2 MHz. The odd harmonics from the square wave generated by the crystal oscillator is effectively degraded. In particular, the third harmonic at the op amp output is at least ∼40-dB lower than the original signal, making the output of this oscillator an ideal fixed-frequency source for a mass filter power supply.

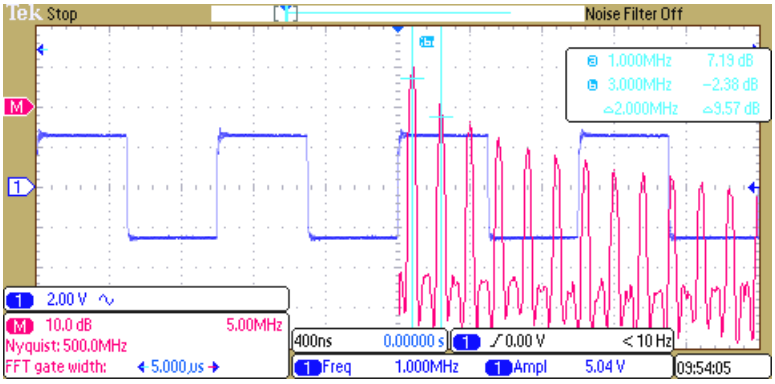

(a) The output of the crystal oscillator and the output waveform spectrum, measured at the OUT terminal of XTAL1 in Fig. 7.2.

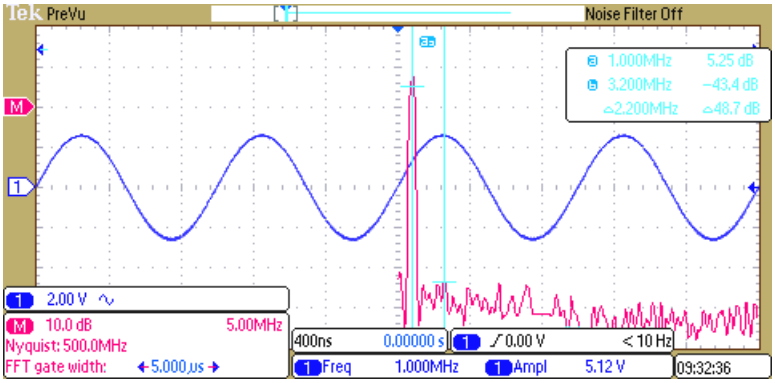

(b) The output and its spectrum, measured at the output of op amp U4 when a ∼2.0 V voltage applied to the FB node.

Figure 7.6: The oscilloscope screen snapshots of the output waveforms (shown in dark blue) from both the crystal oscillator and the bandpass filter. The measured amplitudes shown on the screen are peak-to-peak values, and the peek intensity after FFT (shown in red) is reported in dB.

Figure 7.7 shows the measured correlation between the feedback voltage at pin FB and the output peak-to-peak amplitude at the output of op amp U4. This is measured by using the oscilloscope DPO2014. Each point represents one measurement. The power consumption is also monitored and plotted using the y-axis on the right side. The power consumption of this RF oscillating source depends on the output amplitude, and is in general less than 0.70 W. When the feedback voltage is between 1.6 V and 2.4 V, an inversely linear relationship

is shown between the feedback voltage and the output amplitude. When the feedback voltage is below 1.6 V, the output starts to saturate.

This FB pin is part of the AGC unit, and will intake the control signal generated by the precision rectifier (reported in Section 7.3). The precision rectifier will be used to sense the output of the transformer stage (the third stage) of a mass filter power supply. The generated feedback signal has to be adjusted finely so that the feedback signal is limited between 1.6 V and 2.4 V and linearly correlates to the output signal.

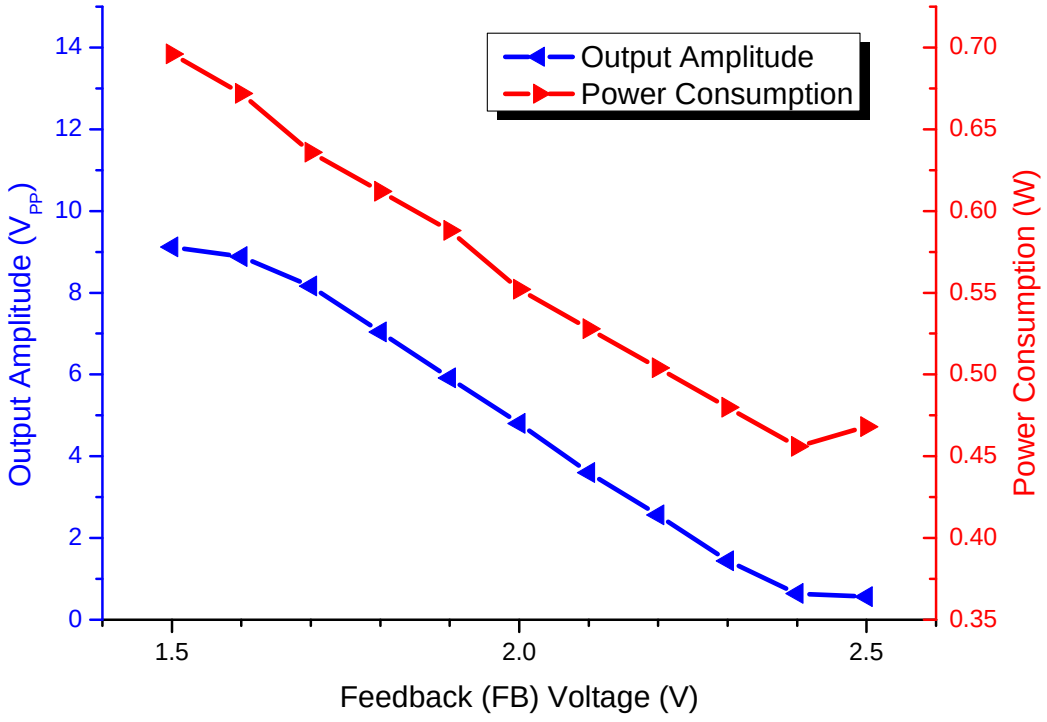

Figure 7.7: Measured RF oscillator output peak-to-peak amplitude (at the base terminal of Q2 in Fig. 7.2) and the power consumption correlated to the applied voltage at pin FB (for a feedback signal).

7.3 Precision Rectifier Design

The precision rectifier is formed of a commonly used full-waveform rectifier with op amps LT6207[29] and fast Schottky diodes HSMS-2800 from Avago Technologies (San Jose, California, USA). This precision rectifier unit is designed to monitor the output amplitude, and then convert the amplitude into a DC signal for the feedback signal FB shown in Fig. 7.2. The schematic of the precision rectifier is shown in Fig. 7.8.

The first part here is a commonly used precision rectifier design (Horowitz and Hill, 1989) to ensure that the behaviour of this rectifier is close to ideal, so that unwanted voltage drifting can be limited to achieve the output amplitude stabilization goal of having a $\Delta V/V$ below 2.5×10^{-4} (discussed in Section 3.3).

A unity-gain voltage follower formed by op amp U5:A is used to isolate the input of the precision rectifier. After the buffer, the op amp U5:D generates the first 1/2 wave, and the op amp U5:C finishes the full wave. Two more unity-gain buffers (the op amp U6:A and U6:B) are utilized for isolation and for DC offset removal. After the signal is smoothed by the capacitor C26 and the resistor R39, a feedback DC signal is generated according to the amplitude of the sine wave fed into the node ACFB shown in Fig. 7.8.

[29]Op amp LT6207 is the quad version of LT6205. See Appendix A.3 for information about the op amp LT6207.

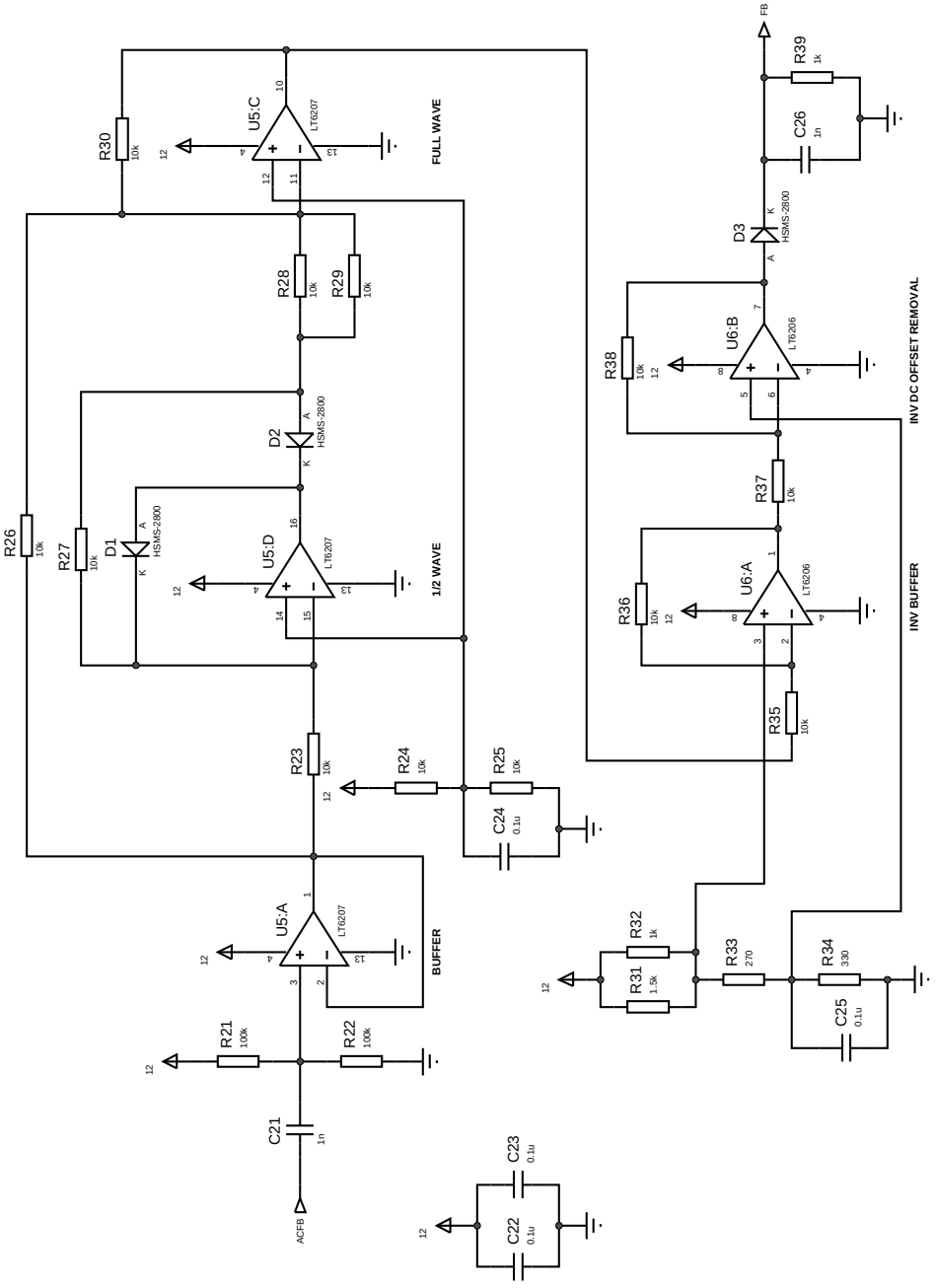

Figure 7.8: Schematic of the precision rectifier.

7.3.1 Precision Rectifier Printed Circuit Board

The PCB designed for the precision rectifier also houses the circuit reported in Section 7.2. Namely, the circuits shown in both Fig. 7.2 and Fig. 7.8 are on this board. This two-layer PCB (shown in Fig. 7.9) is sized about 75×58 mm and is designed, etched, and populated in-house, employing the same design concepts mentioned in Section 7.2.4 (large ground plate, small area for the bandpass filter, large heat dissipation plate for the output emitter follower Q2, and isolated area for the crystal oscillator XTAL1, etc.)

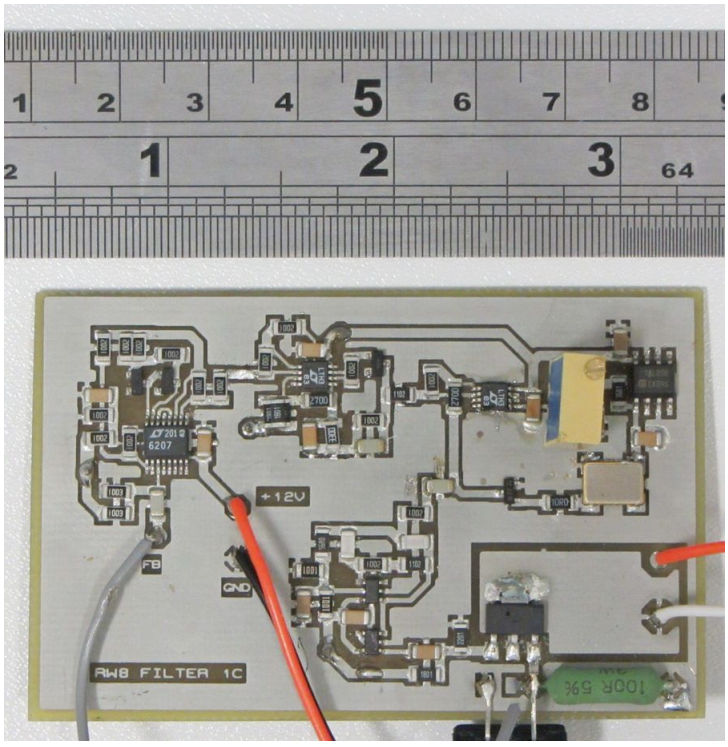

Figure 7.9: Two-layer printed circuit board of the precision rectifier (only the top layer is shown; the bottom layer is the ground/power plate.) This board also houses all of the components on the PCB shown in Fig. 7.5b.

When testing this board, the output of the emitter follower Q2 (pin PA in Fig. 7.2) is connected to the input of the precision rectifier (pin ACFB in Fig. 7.8).

An amplitude-stabilized sine wave similar to the waveform reported in Fig. 7.6b can be obtained. Note that such connection arrangement is for testing only. When the mass filter power supply circuit is finalized, the output of the emitter follower is feeding a power amplifier, and the input of the precision rectifier will be coupled to a voltage divider, which divides the voltage applied to the quadrupole rods to a reasonable level for the precision rectifier input.

7.4 Power Amplifier Design

The power amplifier stage employs the NPN bipolar power transistor, MJE18008, from ON Semiconductor (Phoenix, Arizona, USA),[30] because of its large maximum collector-emitter voltage rating of 450 V and its maximum collector current rating of 8 A. A 200-V DC power supply will be used to supply this power amplifier. This power amplifier is designed to be able to provide at least 1 A of current to drive an output transformer. A maximum output amplitude of 500 V after the transformer will be expected. A common-emitter configuration is set up, and a NPN Darlington pair, BU323Z (with collector-emitter voltage rating of 350 V and collector current rating of 10 A), from ON Semiconductor (Phoenix, Arizona, USA),[31] is utilized to supply the base current. Such characteristics enable the potential to deliver large voltage and current into the quadrupole system. This Darlington pair can provide a few amps of current, which may be necessary

[30] See Appendix A.4 for information about the bipolar power transistor MJE18008.

[31] See http://www.onsemi.com/PowerSolutions/product.do?id=BU323Z for information about the Darlington pair BU323Z, accessed 15 August 2012.

to drive base terminals of both MJE18008 transistors when the current gain of MJE18008 is set to around 10. The circuit schematic is shown in Fig. 7.10.

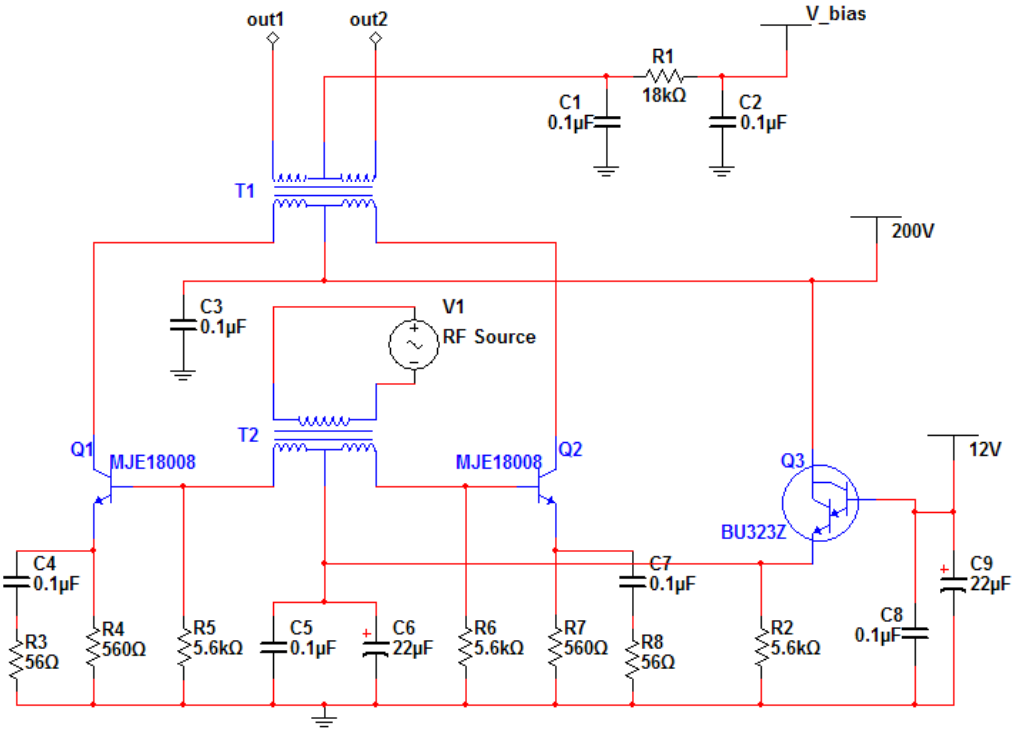

Figure 7.10: Schematic of the power amplifier stage.

The transformer mentioned in Section 7.2.3 (and illustrated in Fig. 7.4) is used here to couple the oscillating sine wave (generated by the RF oscillator described in Section 7.2) onto the base current supplied by the Darlington pair BU323Z (Q3 provides current for the transformer T2 in Fig. 7.10). Such a transformer has a ferrite core with three sets of 10-turn winding. Namely, the primary coil and the both sides of the secondary coil have a winding of 10 turns.

Similar to the design reported by Mathur and O'Connor in 2006 (Mathur and O'Connor, 2006), the load of the power transistor is an air-core transformer (T1)

in which both primary and secondary coils are centre-tapped. By increasing the secondary-to-primary turns ratio of the transformer (assuming the primary coil is the coil connected with the power BJT Q1 and Q1 in Fig. 7.10), the output voltage can be increased to fit the need of a given quadrupole system. A DC offset can be provided by the biasing voltage 'V_bias' to the centre-tap of the secondary coil of the transformer T1. Here the output waveforms at nodes 'out1' and 'out2' become the signals described by Eq. (3.1) (also shown in Fig. 7.1), where the U is the voltage supplied from the node 'V_bias,' and the V is the amplitude of the sinusoidal waveform controlled by the gain control function described in Section 7.2.3. In order to balance the outputs at node 'out1' and 'out2' (to have the same output amplitude on both sides), the left side (components C4, Q1, R3–R5 in Fig. 7.10) and right side (C7, Q2, R6–R8) of the oscillating circuitry should be made identical, which makes the layout of the power amplifier PCB crucial.

7.4.1 Power Amplifier Board

The PCB design follows the principle of making the layout of the oscillating pairs Q1 and Q2 in Fig. 7.10 symmetrical. Therefore the component placement and the routing have to be considered carefully. Figure 7.11 shows the fully populated two-layer PCB. There are two electrically isolated heat sinks attached to each other to ensure the working temperatures of the two power transistors remain roughly the same. The components on the right side of the heat sink form a

bridge rectifier, which is not shown in the schematic of Fig. 7.10. Such a bridge rectifier is for testing purpose and will be removed when the mass filter power supply circuit is finalised.

7.5 Transformer

For transformers with centre-tapped coils such as the transformer T1 shown in Fig. 7.10, it is easy to have a slightly mismatched turns ratio between the left and right half of the coils. To gain a better balance, the bifilar winding is introduced. A bifilar coil, as shown in Fig. 7.12, is wound with two closely spaced wires, which is an excellent solution to have identical coils on both sides of a canter tap of the transformer.

Figure 7.13 shows the photo of the hand-wound air-core bifilar transformer. The primary coil is a 10-turn bifilar winding. By connecting the left end of the first wire with the right end of the second wire, a centre tap is made, and it becomes a centre-tapped coil with theoretically identical 10-turn winding on both sides. Same method is employed for the 29-turn secondary coil, which is wound on top of the primary coil.

Since the transformer is the load of the power amplifiers Q1 and Q2, the impedance, determined by the the tubing dimension and the turns of winding, of the transformer decides the gain of this power amplifier. Meanwhile, the resonant frequency of the output system is a function of the impedance. The designed transformer impedance has to be carefully considered. When the quadrupole

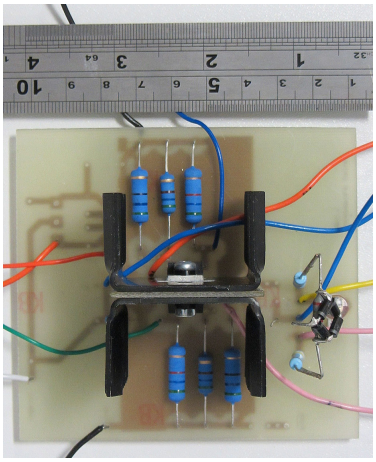

(a) Top view.

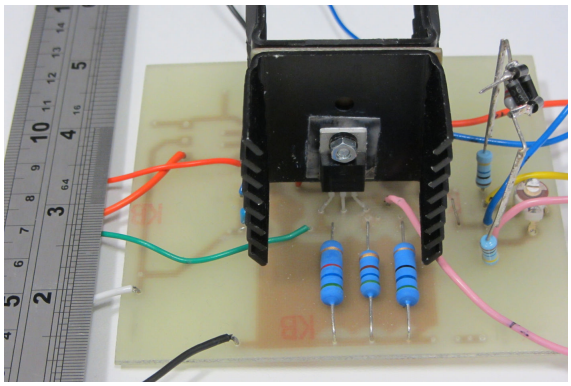

(b) Front view.

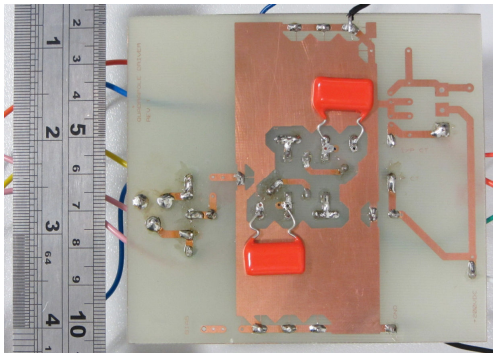

(c) Bottom layer.

Figure 7.11: Power amplifier board with components mounted.

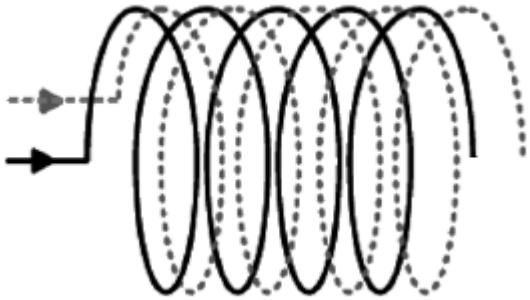

Figure 7.12: Winding of a bifilar coil with current flowing in the same direction (Ahn et al., 2011) [modified].

rods are connected, a resonant frequency of slightly less than 1 MHz is preferred so that unwanted higher-order harmonics can be filtered out. If it is designed that the resonant frequency of this output system is far away from 1 MHz, more power will be needed to drive the quadrupole rods.

7.5.1 Testing Results (Power Amplifier & Transformer)

Figure 7.14 shows the first test result of the power amplifier board and the air-core transformer. To simplify the testing, only the differential voltage of the two output nodes 'out1' and 'out2' in Fig. 7.10 is shown, and the centre tap of the secondary coil is not connected to the biasing circuit for a DC offset. As a result, for this test, the secondary-to-primary turns ratio of this output transformer T1 becomes 58:10. The input signal is a 1-MHz sine wave with the amplitude of ∼5.5 V (peak-to-peak value), generated by a function generator. Under such conditions, an output waveform of around 1 MHz with the peak-to-

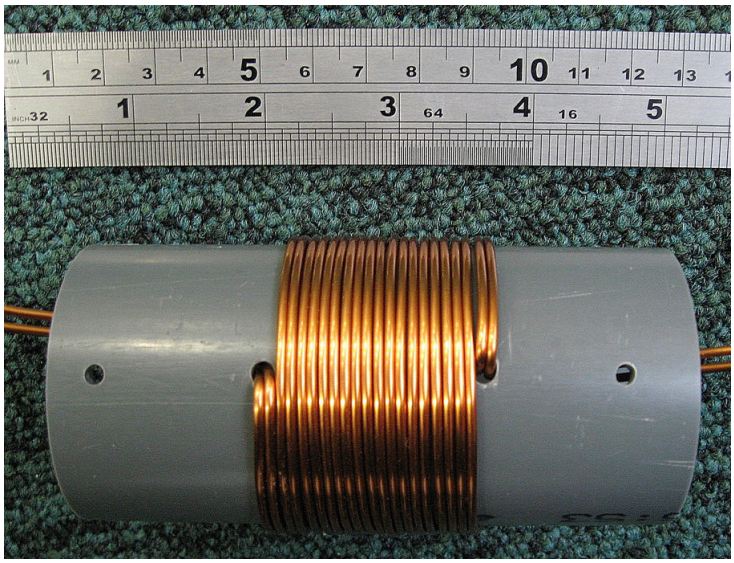

(a) Primary coil.

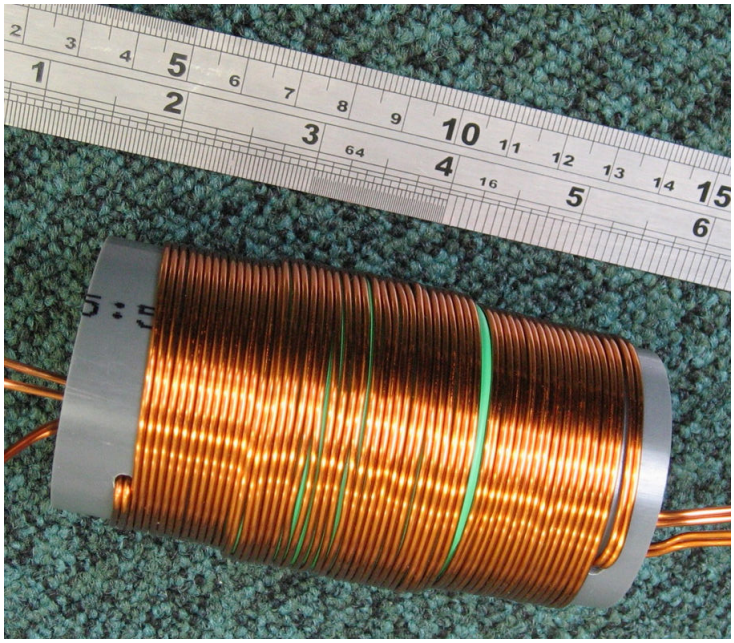

(b) Secondary coil.

Figure 7.13: Photo of the hand-wound air-core bifilar transformer.

peak amplitude of 328 V is obtained.

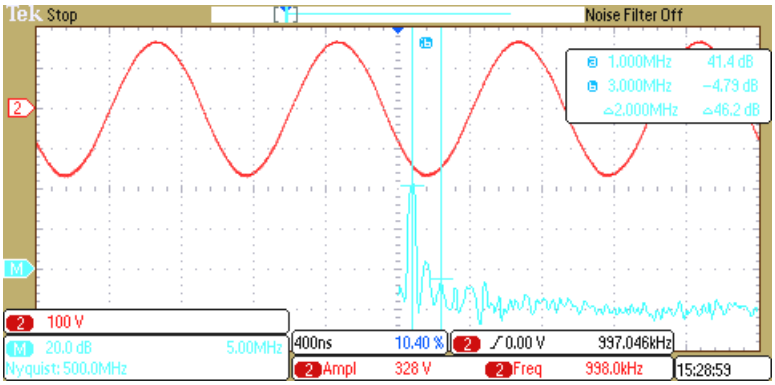

Figure 7.14: The oscilloscope screen snapshot of the power amplifier output (shown in red), differential signal measured between the nodes 'out1' and 'out2' after the output transformer (T1 in Fig. 7.10) with turns ratio of 58:10. The FFT result is shown in light blue.

7.5.2 Future Transformer Modification

In the first attempt of making a transformer, the enameled wire (or the magnet wire) with a size of American wire gauge (AWG) 16 was used. An AWG 16 wire has a diameter of about 1.3 mm. However, due to the skin effect, in copper, a 1-MHz signal is flowing within the skin depth of ∼66 μm. Therefore, most of the signal current only flows within the '66-μm skin' of the wire used in the home-made transformer mentioned above in Section 7.5. Alternatively, a Litz wire, containing multiple stands which are electrically insulated from each other, becomes a better choice when a large 1-MHz signal current is carried (more cross-section area can be used to carry such a current). Figure 7.15 shows the corss-section view of a Litz wire.[32]

[32]Figure 7.15 was obtained from the website http://www.rubadue.com/products/supplementary-2-layer-insulation-litz-wire-fep-insulation-double-insulated-wire, accessed 30 August 2012.

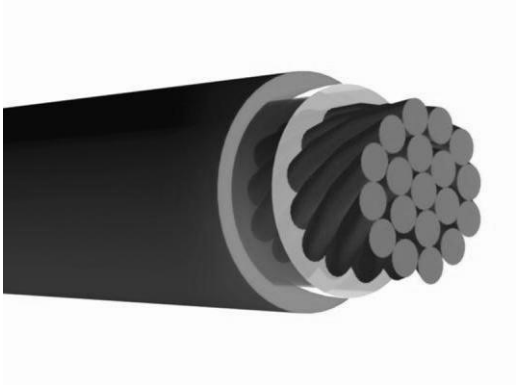

Figure 7.15: Cross-section view of a Litz wire.[32]

7.6 Conclusion & Future Work

As illustrated by Fig. 7.1, a completed quadrupole power supply consists of four sections, a RF oscillator with an AGC unit, a power amplifier, a trasformer, and a feedback signal generation system. Here, a RF oscillator with gain control unit has been built and tested (reported in Section 7.2). A power amplifier and a transformer has also been built and tested (reported in Section 7.4 and 7.5).

The rectifier feedback system shown in Fig. 7.1 has been partially built and tested (reported in Section 7.3). Depending on the designed maximum output amplitude being applied to the quadrupole rods, a voltage divider has to be made to complete the feedback system. To assign such a maximum output amplitude, those parameters, such as the quadrupole size and ion mass, mentioned in Section 3.2 have to be considered.

Recall that the impedance of the transformer and the quadrupole rods determine the resonant frequency at the power amplifier output. The transformer turns ratio also affects the output amplitude and transformer impedance. As a

result, to build a proper transformer that is suitable for a given mass filtering solution calls for more careful system tunings.

A solution to reduce such a complexity is to design a transformer with resonant frequency far away from the power supply frequency (1 MHz in this case). In such a case, one no longer worry about the system tuning to have the resonant frequency of the output system around 1 MHz. However, more current is needed for driving such a system, and under such a condition the heat dissipation has to be managed carefully. The dimension of the quadrupole to be used as a mass filter can affect the output impedance and the design specifications of the RF power supply. Since the dimension details have not been determined, this circuit (in particular, the transformer and the quadrupole connection/mounting structure) will be finalised after the design of the quadrupole.

CHAPTER 8

Conclusion

In this thesis, the history and important milestones of the mass spectrometry (MS) development are reviewed. It is then followed by the studies of the ion cyclotron resonance (ICR) technique, the ICR signal, and the quadrupole operation. Different electronic components for a high resolution/mass accuracy mass spectrometer have been investigated in hope that the new designs and the learned experiences contribute to the MS community. Two new preamplifiers for a 12-T Fourier-transform ion cyclotron resonance (FT-ICR) mass spectrometer have been designed, built and tested for the operation at room temperature. A new quadrupole mass filter power supply has also been designed, built, and tested.

8.1 FT-ICR Preamplifier

8.1.1 Preamplifier Using an Operational Amplifier

The first transimpedance preamplifier using an operational amplifier (op amp) AD8099 shows a tested transimpedance of around 85 dBΩ between the frequency of 3 kHz and 10 MHz (corresponding to the mass-to-charge ratio, m/z, of approximately 18 to 61k for a 12-T FT-ICR system), when a single 18-kΩ (shunting a 0.8-pF feedback capacitor) feedback resistor is employed. It also has an tested input current noise spectral density of around 1 pA/$\sqrt{\text{Hz}}$. The total power consumption of this circuit is around 310 mW when tested on the bench. The transimpedance and the bandwidth can be adjusted by replacing passive components. The feedback and bandwidth limitation of the circuit is discussed. With the maximum possible transimpedance of 5.3 MΩ when using an 0402 type surface mount resistor, the preamplifier is estimated to be able to detect ∼110 charges.

8.1.2 Single-Transistor Preamplifier Using a T Feedback Network

The second preamplifier employs a single-transistor design using a T-shaped feedback network. The T feedback network can bias the transistor gate and the ICR detection plate. This single-transistor preamplification solution provides a transimpedance of about 80 dBΩ between 1 kHz and 1 MHz (m/z, of around 180 to 180k for a 12-T FT-ICR system) and a low power consumption of ∼5.7 mW.

The T feedback system allows ∼100-fold less feedback resistance at a given transimpedance, hence preserving bandwidth, which is important for the introduction of a more complicated modern ICR cell (namely, more input capacitance is introduced by a modern ICR cell). In trading noise performance for higher transimpedance, an alternative preamplifier design has also been studied with a capability of a transimpedance of 120 dBΩ in the same bandwidth of about 1 MHz.

8.1.3 Cyclotron Frequency Correlation

The cyclotron frequency correlation has been discussed and estimated in Section 5.2.2. It has been concluded that, for a transimpedance preamplifier, when the magnitude of the feedback resistance is much greater than the magnitude of the reactance of the effective input capacitance, $R >> \frac{1}{\omega_{cyc}(C/G)}$, the magnitude of the output voltage after such a preamplifier is independent of the cyclotron frequency of the ion signal.

In a scenario when an input capacitance of 10 pF, and the cyclotron frequency f_{cyc} of signals between 10 kHz and 10 MHz (mass-to-charge ratio, m/z, of ∼18 to 18k for a 12-T FT-ICR system) is provided, a feedback resistance of much larger than 16 GΩ is necessary for the elimination of the cyclotron frequency dependency. However, with the introduction of protection circuitry at the input node for performing excitation and detection on the same ICR electrode (Chen et al., 2012), or the relocation of the preamplifier outside of the vacuum chamber

housing an ICR cell, more capacitance (from a longer cable and the feedthrough) is coupled onto the input node of a preamplifier. For instance, when the input capacitance is 200 pF, and the magnet is 21 T, (in which the cyclotron frequency of a m/z 18k ion is about ∼18 kHz), the magnitude of $\frac{1}{\omega_{cyc}(C/G)}$ becomes around 440M. With the employment of a T feedback network in an op amp based preamplifier, a transimpedance of much larger than 440 MΩ can be reachable. As a result, the voltage output can be independent of the cyclotron frequency when using a transimpedance preamplifier.

8.2 Power Supply for a Quadrupole Mass Filter

The oscillator reported in Chapter 7 is a simple solution to supply a quadrupole mass filter. The most challenging part of the quadrupole mass filter power supply design is the tuning after connecting each of the 'building blocks' together. As mentioned in Section 7.6, the design of the output transformer depends on many factors, such as the quadrupole dimension, the designed gain and output amplitude, and the resonant frequency, etc. More investigations are required before finalising such a design.

Furthermore, if the output transformer is designed not to resonant at the frequency of operation, the impedance tuning (to tune the resonant frequency of the output stage to the operating frequency of the RF power supply) may not be necessary. Instead, more current needs to be provided when operating the power supply system under such a condition.

CHAPTER 9

Future Work

This chapter suggests the future works to extend this research in the area of high performance MS related electronics. In the previous chapters, two transimpedance preamplifiers for a 12-T Fourier-transform ion cyclotron resonance (FT-ICR) mass spectrometer have been designed, built, and tested on the bench for the operation at room temperature. It is planned to test both preamplifiers using an electrically compensated ion cyclotron resonance (ICR) cell (Brustkern et al., 2008). In this work, a new quadrupole mass filter power supply has also been designed, built, and tested.

This thesis focus on reporting the bench testing results. It is hoped that in the future those newly designed electronic components can be tested on a 12-T FT-ICR mass spectrometer.

9.1 Preamplifier

The bandwidth of both preamplifiers reported in this work is designed for a 12 T FT-ICR system. A 1-MHz bandwidth corresponds to the mass-to-charge ratio, m/z, of approximately 180 at 12 T, which is suitable for most of the proteomics applications using an FT-ICR mass spectrometer. The bandwidth of both preamplifiers can be changed by replacing passive components, for the applications/tests in an FT-ICR system with different strength of magnetic field. The following tests are suggested to extend this research.

9.1.1 T Feedback Network

The T feedback network tested in Chapter 6 is a resistive network, in which a 47-kΩ and a 18-kΩ resistor are connected in series and a third 180-Ω resistor coupled between the junction node of the two series resistors and a reference potential. For such specified resistive values, the T feedback network is proven to have the ability to preserve bandwidth at a given transimpedance. For the use of this T feedback network in a single-transistor preamplifier, one also takes the advantage of the reference potential from the feedback network, which biases the gate terminal of the transistor and the detection plate of the ion cyclotron resonance (ICR) cell. One may claim that the lowered resistance value results in more thermal noise current. However, each of the component in a T feedback network can be replaced by reactive components to avoid thermal noise. It can be capacitive, inductive, or both, for obtaining transimpedance characteristics which

vary with frequency according to particular requirements in a given application. Therefore, further research should be conducted to obtain the best combination of the impedance values for each of the T feedback network components for noise/bandwidth performance optimization.

9.1.2 Preamplifier Noise Performance

As of the noise performance of a preamplifier system, the noise power of any given system can not be lower than the thermal noise power, which is a function of the temperature and bandwidth (as described by Eq. (2.17)).

One may be able to take advantage of the cooling system of the FT-ICR superconducting magnet to reduce the operating temperature of an FT-ICR preamplifier to a cryogenic level. The thermal noise power can be reduced by around 10 fold at the temperature of 4 K. With a much reduced noise level, a much improved signal-to-noise performance may make it possible to detect a singly-charged single ion in an ICR cell.

Reducing the bandwidth also limits the noise. In lieu of detecting the 1-MHz bandwidth in one detection using a 1-MHz detection window, a narrower 100-kHz window can be introduced to finish the same task in 10 detections.

Moreover, as reported in Chapter 5 and Chapter 6, the op amp based preamplifier provides more gain (transimpedance), whilst the single-transistor based preamplifier reduces the noise and the power consumption. The permutation between gain, bandwidth, noise performance, and power consumption (when a

preamplifier is placed inside a vacuum chamber, the heat dissipation can affect the vacuum condition) should be studied in the future for best system performance for an FT-ICR mass spectrometer.

9.1.3 Cyclotron Frequency Correlation

The correlation of the cyclotron frequency and the preamplifier gain/transimpedance is studied in Section 5.2.2 and in Section 8.1.3. The cyclotron frequency of the ICR signal and the preamplifier gain/transimpedance can affect the output signal of the FT-ICR ion detector. Best calibration functions for processing the ion signal should be studied when testing the transimpedance preamplifiers.

9.1.4 System Test

New compact PCBs using two layers should be built when testing the preamplifiers on an FT-ICR system. It is planned to first place the preamplifiers outside of the vacuum chamber and to connect the detection plates via feedthroughs. Then the performance variance when mounting the preamplifiers inside the vacuum chamber (here, the outgassing characteristics of the preamplifier components should be evaluated) should be compared. The bandwidth tolerance, number of ions being detected, dynamic range, and noise performance of the FT-ICR system using new preamplifiers should be evaluated.

9.2 Power Supply for a Quadrupole Mass Filter

As described in Chapter 7, a completed quadrupole power supply consists of four sections, a RF oscillator with built-in automatic gain control (AGC), a power amplifier, a transformer, and a feedback signal generation system. In this work, a RF oscillator, a rectifier feedback system, and a power amplifier have been built and tested. The dimension details of the quadrupole mass filter have not been determined. As a result, the maximum output amplitude of this power supply has not been defined. However, the output amplitude can be changed by changing the turns ratio of the output transformer. The output impedance of this system is defined by the transformer, quadrupole, and its connection/mounting component. The resonant frequency at the output stage is affected by such an output impedance. As a result, future investigations on those parameters are required before finalising the power supply.

References

Ahn, M. C., Jang, J. Y., Ko, T. K., and Lee, H. (2011). Novel design of the structure of a non-inductive superconducting coil. *IEEE Transactions on Applied Superconductivity*, 21(3):1250–1253. (In this thesis: page 157.)

Aizikov, K., Mathur, R., and O'Connor, P. B. (2009). The spontaneous loss of coherence catastrophe in Fourier transform ion cyclotron resonance mass spectrometry. *Journal of the American Society for Mass Spectrometry*, 20(2):247–256. (In this thesis: page 33.)

Aizikov, K., Smith, D. F., Chargin, D. A., Ivanov, S., Lin, T.-Y., Heeren, R. M. A., and O'Connor, P. B. (2011). Vacuum compatible sample positioning device for matrix assisted laser desorption/ionization Fourier transform ion cyclotron resonance mass spectrometry imaging. *Review of Scientific Instruments*, 82(5):054102. (In this thesis: page 16.)

Amster, I. J. (1996). Fourier transform mass spectrometry. *Journal of Mass Spectrometry*, 31(12):1325–1337. (In this thesis: page 16.)

Analui, B. and Hajimiri, A. (2004). Bandwidth enhancement for transimpedance amplifiers. *IEEE Journal of Solid-State Circuits*, 39(8):1263–1270. (In this thesis: page 116.)

Appelt, S., Kühn, H., Häsing, F. W., and Blümich, B. (2006). Chemical analysis by ultrahigh-resolution nuclear magnetic resonance in the earth's magnetic field. *Nature Physics*, 2(2):105–109. (In this thesis: page 134.)

Austin, W. E., Holme, A. E., and Leck, J. H. (1976). *The Mass Filter: Design and Performance, in P. H. Dawson (Ed.), Quadrupole Mass Spectrometry and Its Applications*, chapter 6, pages 121–152. American Institute of Physics, Woodbury, New York. Chapter VI. Reprinted as an "American Vacuum Society Classic" by American Institute of Physics. (In this thesis: page 56, 57, 65.)

Barros, M. A. M. (1982). Low-noise InSb photodetector preamp for the infrared. *IEEE Journal of Solid-State Circuits*, 17(4):761–768. (In this thesis: page 114.)

Barrow, M. P., Witt, M., Headley, J. V., and Peru, K. M. (2010). Athabasca oil sands process water: Characterization by atmospheric pressure photoionization and electrospray ionization Fourier transform ion cyclotron resonance mass spectrometry. *Analytical Chemistry*, 82(9):3727–3735. (In this thesis: page 16.)

Beynon, J. H. and Morgan, R. P. (1978). The development of mass spectroscopy: An historical account. *International Journal of Mass Spectrometry and Ion Physics*, 27(1):1–30. (In this thesis: page 9, 10.)

Brustkern, A. M., Rempel, D. L., and Gross, M. L. (2008). An electrically compensated trap designed to eighth order for FT-ICR mass spectrometry. *Journal of the American Society for Mass Spectrometry*, 19(9):1281–1285. (In this thesis: page 33, 166.)

Burlingame, A. L., Boyd, R. K., and Gaskell, S. J. (1998). Mass spectrometry. *Analytical Chemistry*, 70(16):647–716. (In this thesis: page 13.)

Canterbury, J. D., Gladden, J., Buck, L., Olund, R., and MacCoss, M. J. (2010). A high voltage asymmetric waveform generator for FAIMS. *Journal of the American Society for Mass Spectrometry*, 21(7):1118–1121. (In this thesis: page 64.)

Caravatti, P. and Allemann, M. (1991). The 'infinity cell': a new trapped-ion cell with radiofrequency covered trapping electrodes for Fourier transform ion cyclotron resonance mass spectrometry. *Organic Mass Spectrometry*, 26(5):514–518. (In this thesis: page 33.)

Cermak, I. (2005). Compact radio-frequency power supply for ion and particle guides and traps. *Review of Scientific Instruments*, 76(6):063302. (In this thesis: page 59, 60, 65.)

Chang, B. T. and Mitchell, T. B. (2006). Frequency stabilized radio-frequency generator for driving ion traps and other capacitive loads. *Review of Scientific Instruments*, 77(6):063101. (In this thesis: page 60, 61, 62, 65.)

Chen, R. Y., Hung, T.-S., and Hung, C.-Y. (2005). A CMOS infrared wireless optical receiver front-end with a variable-gain fully-differential transimpedance amplifier. *IEEE Transactions on Consumer Electronics*, 51(2):424–429. (In this thesis: page 86.)

Chen, T., Kaiser, N. K., Beu, S. C., Hendrickson, C. L., and Marshall, A. G. (2012). Excitation and detection with the same electrodes for improved FT-ICR MS performance. In *60th ASMS Conference on Mass Spectrometry and Allied Topics*, Vancouver, BC, Canada. 20-24 May. (In this thesis: page 89, 164.)

Chien, F.-T. and Chan, Y.-J. (1999). Bandwidth enhancement of transimpedance amplifier by a capacitive-peaking design. *IEEE Journal of Solid-State Circuits*, 34(8):1167–1170. (In this thesis: page 116.)

Comisarow, M. B. (1978). Signal modeling for ion cyclotron resonance. *Journal of Chemical Physics*, 69(9):4097–4104. (In this thesis: page 22, 23, 86, 107.)

Comisarow, M. B. (1993). Fundamental aspects of FT-ICR and applications to chemistry. *Hyperfine Interactions*, 81(1-4):171–178. (In this thesis: page 17.)

Comisarow, M. B., Grassi, V., and Parisod, G. (1978). Fourier transform ion cyclotron double resonance. *Chemical Physics Letters*, 57(3):413–416. (In this thesis: page 31.)

Comisarow, M. B. and Marshall, A. G. (1974a). Fourier transform ion cyclotron resonance spectroscopy. *Chemical Physics Letters*, 25(2):282–283. (In this thesis: page 11, 17.)

Comisarow, M. B. and Marshall, A. G. (1974b). Frequency-sweep Fourier transform ion cyclotron resonance spectroscopy. *Chemical Physics Letters*, 26(4):489–490. (In this thesis: page 17.)

Comisarow, M. B. and Marshall, A. G. (1976). Theory of Fourier transform ion cyclotron resonance mass spectroscopy .I. Fundamental equations and low-pressure line shape. *Journal of Chemical Physics*, 64(1):110–119. (In this thesis: page 17.)

Cui, W., Rohrs, H. W., and Gross, M. L. (2011). Top-down mass spectrometry: recent developments, applications and perspectives. *Analyst*, 136(19):3854–3864. (In this thesis: page 16.)

Dawson, P. H. (1976). *Quadrupole Mass Spectrometry and its Applications*, chapter 1, pages 1–7. American Institute of Physics, Woodbury, New York. (In this thesis: page 48.)

de Hoffmann, E. and Stroobant, V. (2007). *Mass Spectrometry: Principles and Applications*, pages 88–95. John Wiley & Sons. (In this thesis: page 53, 54.)

Deliyannis, T. (1968). High-Q factor circuit with reduced sensitivity. *Electronics Letters*, 4(26):577–579. (In this thesis: page 142.)

Deshpande, N. P. (2008). *Electron Devices & Circuits - Principles & Applications*, page 221. McGraw-Hill Education (India) Pvt Limited. (In this thesis: page 117.)

Douglas, D. J. (2009). Linear quadrupoles in mass spectrometry. *Mass Spectrometry Reviews*, 28(6):937–960. (In this thesis: page 48, 49.)

Douglas, D. J., Frank, A. J., and Mao, D. (2005). Linear ion traps in mass spectrometry. *Mass Spectrometry Reviews*, 24(1):1–29. (In this thesis: page 49.)

El-Diwany, M. H., Roulston, D. J., and Chamberlain, S. G. (1981). Design of low-noise bipolar transimpedance preamplifiers for optical receivers. *IEE Proceedings G, Electronic Circuits and Systems*, 128(6):299–306. (In this thesis: page 86.)

Fabris, L. and Manfredi, P. (2002). Optimization of front-end design in imaging and spectrometry applications with room temperature semiconductor detectors. *IEEE Transactions on Nuclear Science*, 49(4):1978–1985. (In this thesis: page 92, 93.)

Fish, F. H. and Katz, R. S. (1977). Amplifier for fiber optics application. *U.S. Patent*, 4,029,976. (In this thesis: page 114.)

Flora, J. W., Hannis, J. C., and Muddiman, D. C. (2001). High-mass accuracy of product ions produced by SORI-CID using a dual electrospray ionization source coupled with FTICR mass spectrometry. *Analytical Chemistry*, 73(6):1247–1251. (In this thesis: page 31.)

Franceschi, P., Penasa, L., Ascenzi, D., Bassi, D., Scotoni, M., and Tosi, P. (2007). A simple and cost-effective high voltage radio frequency driver for multi-

polar ion guides. *International Journal of Mass Spectrometry*, 265(23):224–229. (In this thesis: page 64.)

Friend, J. J. (1970). A single op amp biquadratic filter section. *IEEE International Symposium on Circuit Theory*, pages 189–90. (In this thesis: page 142.)

Friend, J. J., Harris, C. A., and Hilberman, D. (1975). STAR: An active biquadratic filter section. *IEEE Transactions on Circuits and Systems*, 22(2):115–121. (In this thesis: page 142.)

Gauthier, J. W., Trautman, T. R., and Jacobson, D. B. (1991). Sustained off-resonance irradiation for collision-activated dissociation involving Fourier transform mass spectrometry. Collision-activated dissociation technique that emulates infrared multiphoton dissociation. *Analytica Chimica Acta*, 246(1):211–225. (In this thesis: page 31.)

Gerlich, D. (1992). Inhomogeneous RF fields: A versatile tool for the study of processes with slow ions. *Advances in Chemical Physics*, 82:1–176. (In this thesis: page 48.)

Green, R., Higgins, M., Joshi, H., and Leeson, M. (2008a). Bandwidth extension for optical wireless receiver-amplifiers. *10th Anniversary International Conference on Transparent Optical Networks*, 4:201–204. (In this thesis: page 86, 116.)

Green, R. J. (1986). Experimental performance of a bandwidth enhancement technique for photodetectors. *Electronics Letters*, 22(3):153–155. (In this thesis: page 116.)

Green, R. J., Joshi, H., Higgins, M. D., and Leeson, M. S. (2008b). Recent developments in indoor optical wireless systems. *IET Communications*, 2(1):3–10. (In this thesis: page 134.)

Green, R. J. and McNeill, M. G. (1989). Bootstrap transimpedance amplifier: a new configuration. *IEE Proceedings G, Circuits, Devices and Systems*, 136(2):57–61. (In this thesis: page 86.)

Headley, J. V., Barrow, M. P., Peru, K. M., Fahlman, B., Frank, R. A., Bickerton, G., McMaster, M. E., Parrott, J., and Hewitt, L. M. (2011). Preliminary fingerprinting of Athabasca oil sands polar organics in environmental samples using electrospray ionization Fourier transform ion cyclotron resonance mass spectrometry. *Rapid Communications in Mass Spectrometry*, 25(13):1899–1909. (In this thesis: page 16.)

Hipple, J. A. and Shepherd, M. (1949). Mass spectrometry. *Analytical Chemistry*, 21(1):32–36. (In this thesis: page 13.)

Hiroki, S., Abe, T., and Murakami, Y. (1991). Development of a quadrupole mass spectrometer using the second stable zone in Mathieu's stability diagram. *Review of Scientific Instruments*, 62(9):2121–2124. (In this thesis: page 54.)

Horowitz, P. and Hill, W. (1989). *The Art of Electronics*. Cambridge University Press, Cambridge, UK. (In this thesis: page 149.)

Hsu, C. S., Hendrickson, C. L., Rodgers, R. P., McKenna, A. M., and Marshall, A. G. (2011). Petroleomics: advanced molecular probe for petroleum heavy ends. *Journal of Mass Spectrometry*, 46(4):337–343. (In this thesis: page 16.)

Hullett, J. L. and Moustakas, S. (1981). Optimum transimpedance broadband optical preamplifier design. *Optical and Quantum Electronics*, 13(1):65–69. (In this thesis: page 86.)

Ivanov, B. I., Trgala, M., Grajcar, M., Il'ichev, E., and Meyer, H.-G. (2011). Cryogenic ultra-low-noise SiGe transistor amplifier. *Review of Scientific Instruments*, 82(10):104705. (In this thesis: page 43.)

Jau, Y.-Y., Benito, F. M., Partner, H., and Schwindt, P. D. D. (2011). Low power high-performance radio frequency oscillator for driving ion traps. *Review of Scientific Instruments*, 82(2):023118. (In this thesis: page 63, 64, 65.)

Jefferts, S. R. and Walls, F. L. (1989). A very low-noise FET input amplifier. *Review of Scientific Instruments*, 60(6):1194–1196. (In this thesis: page 41.)

Johnson, J. B. (1925). The Schottky effect in low frequency circuits. *Physical Review*, 26(1):71–85. (In this thesis: page 37.)

Johnson, J. B. (1928). Thermal agitation of electricity in conductors. *Physical Review*, 32(1):97. (In this thesis: page 37.)

Jones, R. M. and Anderson, S. L. (2000). Simplified radio-frequency generator for driving ion guides, traps, and other capacitive loads. *Review of Scientific Instruments*, 71(11):4335–4337. (In this thesis: page 57, 58, 65, 66.)

Jones, R. M., Gerlich, D., and Anderson, S. L. (1997). Simple radio-frequency power source for ion guides and ion traps. *Review of Scientific Instruments*, 68(9):3357–3362. (In this thesis: page 57, 65, 66.)

Kaiser, N. K., Quinn, J. P., Blakney, G. T., Hendrickson, C. L., and Marshall, A. G. (2011a). A novel 9.4 Tesla FTICR mass spectrometer with improved sensitivity, mass resolution, and mass range. *Journal of the American Society for Mass Spectrometry*, 22(8):1343–1351. (In this thesis: page 2, 46, 85.)

Kaiser, N. K., Savory, J. J., McKenna, A. M., Quinn, J. P., Hendrickson, C. L., and Marshall, A. G. (2011b). Electrically compensated Fourier transform ion cyclotron resonance cell for complex mixture mass analysis. *Analytical Chemistry*, 83(17):6907–6910. (In this thesis: page 33.)

Kaur, P. and O'Connor, P. B. (2004). Use of statistical methods for estimation of total number of charges in a mass spectrometry experiment. *Analytical Chemistry*, 76(10):2756–2762. (In this thesis: page 41.)

Kim, S., Choi, M. C., Hur, M., Kim, H. S., Yoo, J. S., Hendrickson, C. L., and Marshall, A. G. (2008). The 'hybrid cell': A new compensated infinity cell for larger radius ion excitation in Fourier transform ion cyclotron resonance mass

spectrometry. *Rapid Communications in Mass Spectrometry*, 22(9):1423–1429. (In this thesis: page 33.)

Kroto, H. (1997). Symmetry, space, stars and C_{60}. *Reviews of Modern Physics*, 69(3):703–722. (In this thesis: page 13.)

Lawrence, E. O. (1934). Method and apparatus for the acceleration of ions. *U.S. Patent*, 1,948,384. (In this thesis: page 11.)

Lawrence, E. O. and Livingston, M. S. (1932). The production of high speed light ions without the use of high voltages. *Physical Review*, 40(1):19–35. (In this thesis: page 11, 12, 17.)

Letzter, S. and Webster, N. (1970). Noise in amplifiers. *IEEE Spectrum*, 7(8):67–75. (In this thesis: page 37, 38, 39, 40, 131.)

Li, H., Lin, T.-Y., Van Orden, S. L., Zhao, Y., Barrow, M. P., Pizarro, A. M., Qi, Y., Sadler, P. J., and O'Connor, P. B. (2011a). Use of top-down and bottom-up Fourier transform ion cyclotron resonance mass spectrometry for mapping calmodulin sites modified by platinum anticancer drugs. *Analytical Chemistry*, 83(24):9507–9515. (In this thesis: page 16.)

Li, H., Zhao, Y., Phillips, H. I. A., Qi, Y., Lin, T.-Y., Sadler, P. J., and OConnor, P. B. (2011b). Mass spectrometry evidence for cisplatin as a protein cross-linking reagent. *Analytical Chemistry*, 83(13):5369–5376. (In this thesis: page 16, 30, 31.)

Li, Y., McIver, R. T., and Hunter, R. L. (1994). High-accuracy molecular mass determination for peptides and proteins by Fourier transform mass spectrometry. *Analytical Chemistry*, 66(13):2077–2083. (In this thesis: page 25.)

Ligon, Woodfin V., J. (1979). Molecular analysis by mass spectrometry. *Science*, 205(4402):151–159. (In this thesis: page 14.)

Limbach, P. A., Grosshans, P. B., and Marshall, A. G. (1993). Experimental determination of the number of trapped ions, detection limit, and dynamic range in Fourier transform ion cyclotron resonance mass spectrometry. *Analytical Chemistry*, 65(2):135–140. (In this thesis: page 41.)

Lin, C., Cournoyer, J. J., and O'Connor, P. B. (2006). Use of a double resonance electron capture dissociation experiment to probe fragment intermediate lifetimes. *Journal of the American Society for Mass Spectrometry*, 17(11):1605–1615. (In this thesis: page 31.)

Lin, T.-Y., Green, R. J., and O'Connor, P. B. (2011). A gain and bandwidth enhanced transimpedance preamplifier for Fourier-transform ion cyclotron resonance mass spectrometry. *Review of Scientific Instruments*, 82(12):124101. (In this thesis: page 33, 80, 83.)

Lin, T.-Y., Green, R. J., and O'Connor, P. B. (2012). A low noise single-transistor transimpedance preamplifier for Fourier-transform mass spectrometry using a T feedback network. *Review of Scientific Instruments*, 83(9):094102. (In this thesis: page 33, 77, 109.)

Little, D. P., Speir, J. P., Senko, M. W., O'Connor, P. B., and McLafferty, F. W. (1994). Infrared multiphoton dissociation of large multiply charged ions for biomolecule sequencing. *Analytical Chemistry*, 66(18):2809–2815. (In this thesis: page 31.)

Lourette, N., Smallwood, H., Wu, S., Robinson, E. W., Squier, T. C., Smith, R. D., and Paša-Tolić, L. (2010). A top-down LC-FTICR MS-based strategy for characterizing oxidized calmodulin in activated macrophages. *Journal of the American Society for Mass Spectrometry*, 21(6):930–939. (In this thesis: page 16.)

Ly, T. and Julian, R. R. (2009). Ultraviolet photodissociation: Developments towards applications for mass-spectrometry-based proteomics. *Angewandte Chemie International Edition*, 48(39):7130–7137. (In this thesis: page 31.)

Makarov, A. (2000). Electrostatic axially harmonic orbital trapping: A high-performance technique of mass analysis. *Analytical Chemistry*, 72(6):1156–1162. (In this thesis: page 133.)

March, R. E. (1997). An introduction to quadrupole ion trap mass spectrometry. *Journal of Mass Spectrometry*, 32(4):351–369. (In this thesis: page 49.)

March, R. E. and Todd, J. F. J. (2005). *Quadrupole Ion Trap Mass Spectrometry*. John Wiley & Sons, Hoboken, NJ, 2nd edition. (In this thesis: page 49, 51.)

March, R. E. and Todd, J. F. J. (2009). *An Appreciation and Historical Survey of Mass Spectrometry*, volume IV of *Practical Aspects of Trapped Ion Mass*

Spectrometry: Theory and Instrumentation, chapter 1, pages 3–168. Taylor & Francis, Boca Raton, FL. (In this thesis: page 49.)

Marshall, A. G., Hendrickson, C. L., and Jackson, G. S. (1998). Fourier transform ion cyclotron resonance mass spectrometry: A primer. *Mass Spectrometry Reviews*, 17(1):1–35. (In this thesis: page 21, 22, 27, 33, 34.)

Marshall, A. G. and Verdun, F. R. (1990). *Fourier Transforms in NMR, Optical, and Mass Spectrometry: A User's Handbook*, pages 144–147. Elsevier, Amsterdam, The Netherlands. (In this thesis: page 24.)

Mathur, R., Knepper, R. W., and O'Connor, P. B. (2007). A low-noise, wideband preamplifier for a Fourier-transform ion cyclotron resonance mass spectrometer. *Journal of the American Society for Mass Spectrometry*, 18(12):2233–2241. (In this thesis: page 41, 43, 44, 80.)

Mathur, R., Knepper, R. W., and O'Connor, P. B. (2008). A low-noise broadband cryogenic preamplifier operated in a high-field superconducting magnet. *IEEE Transactions on Applied Superconductivity*, 18(4):1781–1789. (In this thesis: page 2, 43, 45, 46.)

Mathur, R. and O'Connor, P. B. (2006). Design and implementation of a high power RF oscillator on a printed circuit board for multipole ion guides. *Review of Scientific Instruments*, 77(11):114101. (In this thesis: page 4, 58, 59, 65, 66, 67, 137, 142, 153.)

Mathur, R. and O'Connor, P. B. (2009). Artifacts in Fourier transform mass spectrometry. *Rapid Communications in Mass Spectrometry*, 23(4):523–529. (In this thesis: page 22, 23, 24, 99.)

McDonnell, L. A., Corthals, G. L., Willems, S. M., van Remoortere, A., van Zeijl, R. J. M., and Deelder, A. M. (2010). Peptide and protein imaging mass spectrometry in cancer research. *Journal of Proteomics*, 73(10):1921–1944. (In this thesis: page 16.)

Misharin, A. S., Zubarev, R. A., and Doroshenko, V. M. (2010). Fourier transform ion cyclotron resonance mass spectrometer with coaxial multi-electrode cell ('O-trap'): first experimental demonstration. *Rapid Communications in Mass Spectrometry*, 24(14):1931–1940. (In this thesis: page 33.)

Mohan, S. S., Hershenson, M. D. M., Boyd, S. P., and Lee, T. H. (2000). Bandwidth extension in CMOS with optimized on-chip inductors. *IEEE Journal of Solid-State Circuits*, 35(3):346–355. (In this thesis: page 116.)

Nikolaev, E. N., Boldin, I. A., Jertz, R., and Baykut, G. (2011). Initial experimental characterization of a new ultra-high resolution FTICR cell with dynamic harmonization. *Journal of the American Society for Mass Spectrometry*, 22(7):1125–1133. (In this thesis: page 33.)

Nyquist, H. (1928). Thermal agitation of electric charge in conductors. *Physical Review*, 32(1):110. (In this thesis: page 37.)

O'Connor, P. B. (2002). Considerations for design of a Fourier transform mass spectrometer in the 4.2 K cold bore of a superconducting magnet. *Rapid Communications in Mass Spectrometry*, 16(12):1160–1167. (In this thesis: page 43.)

O'Connor, P. B., Costello, C. E., and Earle, W. E. (2002). A high voltage RF oscillator for driving multipole ion guides. *Journal of the American Society for Mass Spectrometry*, 13(12):1370–1375. (In this thesis: page 50, 57, 65, 66, 67, 68.)

Painter, T. A., Markiewicz, W. D., Miller, J. R., Bole, S. T., Dixon, I. R., Cantrell, K. R., Kenney, S. J., Trowell, A. J., Dong Lak, K., Byoung Seob, L., Yeon Suk, C., Hyun Sik, K., Hendrickson, C. L., and Marshall, A. G. (2006). Requirements and conceptual superconducting magnet design for a 21 T Fourier transform ion cyclotron resonance mass spectrometer. *IEEE Transactions on Applied Superconductivity*, 16(2):945–948. (In this thesis: page 89.)

Paul, W. (1990). Electromagnetic traps for charged and neutral particles. *Reviews of Modern Physics*, 62(3):531–540. (In this thesis: page 48, 49.)

Perez Hurtado, P. and O'Connor, P. B. (2012). Deamidation of collagen. *Analytical Chemistry*, 84(6):3017–3025. (In this thesis: page 16.)

Robbins, M. D., Yoon, O. K., Zuleta, I., Barbula, G. K., and Zare, R. N. (2008). Computer-controlled, variable-frequency power supply for driving multipole ion guides. *Review of Scientific Instruments*, 79(3):034702. (In this thesis: page 63, 65.)

Savory, J. J., Kaiser, N. K., McKenna, A. M., Xian, F., Blakney, G. T., Rodgers, R. P., Hendrickson, C. L., and Marshall, A. G. (2011). Parts-per-billion Fourier transform ion cyclotron resonance mass measurement accuracy with a walking calibration equation. *Analytical Chemistry*, 83(5):1732–1736. (In this thesis: page 30.)

Schmid, D. G., Grosche, P., Bandel, H., and Jung, G. (2000). FTICR-mass spectrometry for high-resolution analysis in combinatorial chemistry. *Biotechnology and Bioengineering*, 71(2):149–161. (In this thesis: page 18, 20.)

Schottky, W. (1918). Über spontane Stromschwankungen in verschiedenen Elektrizitätsleitern. *Annalen Der Physik*, 362(23):541–567. (In this thesis: page 37.)

Schottky, W. (1926). Small-shot effect and flicker effect. *Physical Review*, 28(1):74–103. (In this thesis: page 37.)

Smith, D., Kharchenko, A., Konijnenburg, M., Klinkert, I., Paša-Tolić, L., and Heeren, R. (2012). Advanced mass calibration and visualization for FT-ICR mass spectrometry imaging. *Journal of the American Society for Mass Spectrometry*, 23(11):1865–1872. (In this thesis: page 30.)

Smith, D. F., Robinson, E. W., Tolmachev, A. V., Heeren, R. M. A., and Paša-Tolić, L. (2011). C_{60} secondary ion Fourier transform ion cyclotron resonance mass spectrometry. *Analytical Chemistry*, 83(24):9552–9556. (In this thesis: page 16.)

Taban, I., Altelaar, A., van der Burgt, Y., McDonnell, L., Heeren, R., Fuchser, J., and Baykut, G. (2007). Imaging of peptides in the rat brain using MALDI-FTICR mass spectrometry. *Journal of the American Society for Mass Spectrometry*, 18(1):145–151. (In this thesis: page 16.)

Teloy, E. and Gerlich, D. (1974). Integral cross sections for ion-molecule reactions. I. The guided beam technique. *Chemical Physics*, 4(3):417–427. (In this thesis: page 48.)

Tolmachev, A. V., Robinson, E. W., Wu, S., Kang, H., Lourette, N. M., Pašа-Tolić, L., and Smith, R. D. (2008). Trapped-ion cell with improved DC potential harmonicity for FT-ICR MS. *Journal of the American Society for Mass Spectrometry*, 19(4):586–597. (In this thesis: page 33.)

Tsukakoshi, O., Hayashi, T., Yamamuro, K., and Nakamura, M. (2000). Development of a high precision quadrupole mass filter using the zero-method control circuit. *Review of Scientific Instruments*, 71(3):1332–1336. (In this thesis: page 64.)

Watson, J. T. and Sparkman, O. D. (2008). *Introduction to Mass Spectrometry: Instrumentation, Applications, and Strategies for Data Interpretation*, pages 9–22, 26. John Wiley & Sons, Chichester, UK, 4th edition. (In this thesis: page 9, 10, 11, 13, 27, 28.)

Weisbrod, C. R., Kaiser, N. K., Skulason, G. E., and Bruce, J. E. (2010). Excite-coupled trapping ring electrode cell (eTREC): Radial trapping field control, lin-

earized excitation, and improved detection. *Analytical Chemistry*, 82(14):6281–6286. (In this thesis: page 33.)

Wu, S., Kam, K., Pommerenke, D., Cornelius, B., Shi, H., Herndon, M., and Fan, J. (2010). Investigation of noise coupling from switching power supply to signal nets. In *IEEE International Symposium on Electromagnetic Compatibility*, Fort Lauderdale, FL. 25-30 July. (In this thesis: page 80.)

Xian, F., Hendrickson, C. L., and Marshall, A. G. (2012). High resolution mass spectrometry. *Analytical Chemistry*, 84(2):708–719. (In this thesis: page 89.)

Zhang, L. K., Rempel, D., Pramanik, B. N., and Gross, M. L. (2005). Accurate mass measurements by Fourier transform mass spectrometry. *Mass Spectrometry Reviews*, 24(2):286–309. (In this thesis: page 25.)

Zubarev, R. A., Haselmann, K. F., Budnik, B., Kjeldsen, F., and Jensen, F. (2002). Towards an understanding of the mechanism of electron-capture dissociation: a historical perspective and modern ideas. *European Journal of Mass Spectrometry*, 8(5):337–349. (In this thesis: page 31.)

Zubarev, R. A., Kelleher, N. L., and McLafferty, F. W. (1998). Electron capture dissociation of multiply charged protein cations. A nonergodic process. *Journal of the American Chemical Society*, 120(13):3265–3266. (In this thesis: page 31.)

APPENDIX A

Appendix

Datasheets of the key components used in this work are attached in the following appendices. The datasheet of the JFET BF862, used in both preamplifiers reported in Chapter 5 and 6, is attached in Appendix A.1.

The op amp AD8099 datasheet is attached in Appendix A.2. Such an op amp is the main amplification stage in the preamplifier described in Chapter 5. In Chapter 6, this op amp is also used to test the T feedback network.

Appendix A.3 includes the datasheet of the op amp LT6205, its dual version, LT6206, and its quad version, LT6207. This LT6205/06/07 family of op amps is used in the proposed power supply circuit for a quadrupole mass filter, reported in Chapter 7.

The datasheet of the bipolar power transistor MJE18008 is included in Appendix A.4. Such a power transistor is the main component of the power amplifier used in Chapter 7.

A.1 Datasheet: JFET BF862

The datasheet of the JFET BF862 was downloaded from http://www.nxp.com/pip/BF862.html, accessed 30 August 2012.

DISCRETE SEMICONDUCTORS

DATA SHEET

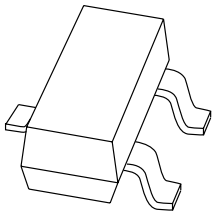

BF862
N-channel junction FET

Product specification 2000 Jan 05
Supersedes data of 1999 Jun 29

Philips
Semiconductors

PHILIPS

N-channel junction FET BF862

FEATURES

- High transition frequency for excellent sensitivity in AM car radios
- High transfer admittance.

APPLICATIONS

- Pre-amplifiers in AM car radios.

DESCRIPTION

Silicon N-channel symmetrical junction field-effect transistor in a SOT23 package. Drain and source are interchangeable.

PINNING SOT23

PIN	DESCRIPTION
1	source
2	drain
3	gate

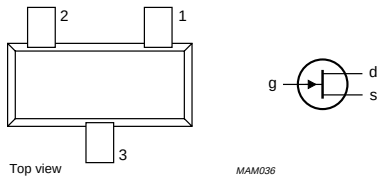

Marking code: 2Ap.

Fig.1 Simplified outline and symbol.

QUICK REFERENCE DATA

SYMBOL	PARAMETER	CONDITIONS	MIN.	TYP.	MAX.	UNIT
V_{DS}	drain-source voltage		–	–	20	V
V_{GSoff}	gate-source cut-off voltage		–0.3	–0.8	–1.2	V
I_{DSS}	drain-source current		10	–	25	mA
P_{tot}	total power dissipation	$T_s \leq 90$ °C	–	–	300	mW
$\lvert y_{fs} \rvert$	transfer admittance		35	45	–	mS
T_j	junction temperature		–	–	150	°C

CAUTION
This product is supplied in anti-static packing to prevent damage caused by electrostatic discharge during transport and handling. For further information, refer to Philips specs.: SNW-EQ-608, SNW-FQ-302A and SNW-FQ-302B.

LIMITING VALUES

In accordance with the Absolute Maximum Rating System (IEC 134).

SYMBOL	PARAMETER	CONDITIONS	MIN.	MAX.	UNIT
V_{DS}	drain-source voltage		–	20	V
V_{DG}	drain-gate voltage		–	20	V
V_{GS}	gate-source voltage		–	–20	V
I_{DS}	drain-source current		–	40	mA
I_G	forward gate current		–	10	mA
P_{tot}	total power dissipation	$T_s \leq 90$ °C; note 1	–	300	mW
T_{stg}	storage temperature		–65	+150	°C
T_j	junction temperature		–	150	°C

Note

1. Main heat transfer is via the gate lead.

THERMAL CHARACTERISTICS

SYMBOL	PARAMETER	CONDITIONS	VALUE	UNIT
$R_{th\ j\text{-}s}$	thermal resistance from junction to soldering point	note 1	200	K/W

Note

1. Soldering point of the gate lead.

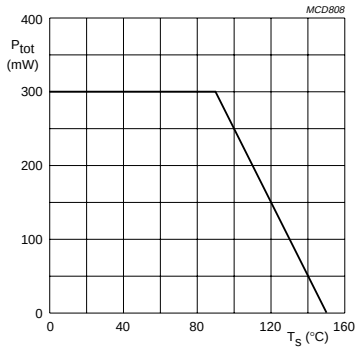

Fig.2 Power derating curve.

STATIC CHARACTERISTICS

T_j = 25 °C; unless otherwise specified.

SYMBOL	PARAMETER	CONDITIONS	MIN.	TYP.	MAX.	UNIT
$V_{(BR)GSS}$	gate-source breakdown voltage	I_{GS} = –1 μA; V_{DS} = 0	–20	–	–	V
V_{GS}	gate-source forward voltage	V_{DS} = 0; I_G = 1 mA	–	–	1	V
V_{GSoff}	gate-source cut-off voltage	V_{DS} = 8 V; I_D = 1 μA	–0.3	–0.8	–1.2	V
I_{GSS}	reverse gate current	V_{GS} = –15 V; V_{DS} = 0	–	–	–1	nA
I_{DSS}	drain-source current	V_{GS} = 0; V_{DS} = 8 V	10	–	25	mA

DYNAMIC CHARACTERISTICS

Common source; T_{amb} = 25 °C; V_{GS} = 0; V_{DS} = 8 V; unless otherwise specified.

SYMBOL	PARAMETER	CONDITIONS	MIN.	TYP.	MAX.	UNIT
$\lvert y_{fs} \rvert$	common source forward transfer admittance	T_j = 25 °C	35	45	–	mS
g_{os}	common source output conductance	T_j = 25 °C	–	180	400	μS
C_{iss}	input capacitance	f = 1 MHz	–	10	–	pF
C_{rss}	reverse transfer capacitance	f = 1 MHz	–	1.9	–	pF
e_n	equivalent noise input voltage	f = 100 kHz	–	0.8	–	nV/√Hz
f_T	transition frequency		–	715	–	MHz

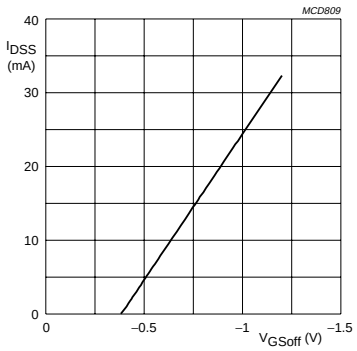

V_{DS} = 8 V; T_j = 25 °C.

Fig.3 Drain saturation current as a function of gate-source cut-off voltage; typical values.

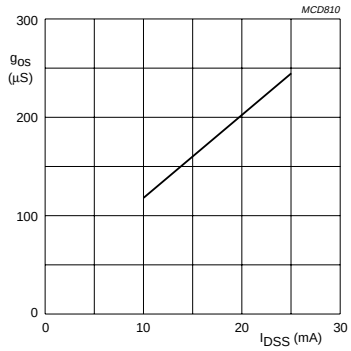

V_{DS} = 8 V; T_j = 25 °C.

Fig.4 Common-source output conductance as a function of drain saturation current; typical values.

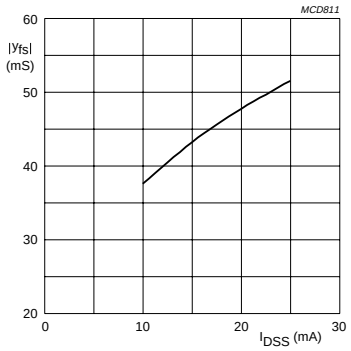

V_{DS} = 8 V; T_j = 25 °C.

Fig.5 Forward transfer admittance as a function of drain saturation current; typical values.

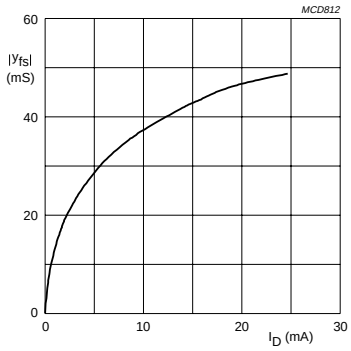

V_{DS} = 8 V; T_j = 25 °C.

Fig.6 Forward transfer admittance as a function of drain current; typical values.

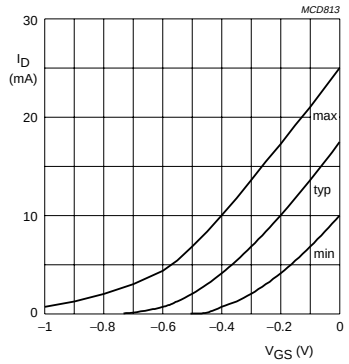

V_{DS} = 8 V; T_j = 25 °C.

Fig.7 Drain current as a function of gate-source voltage; typical values.

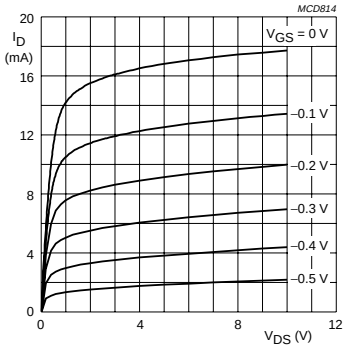

V_{DS} = 8 V; T_j = 25 °C.

Fig.8 Drain current as a function of drain-source voltage; typical values.

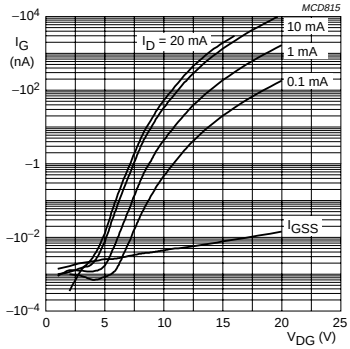

V_{DS} = 8 V; T_j = 25 °C.

Fig.9 Gate current as a function of drain-gate voltage; typical values.

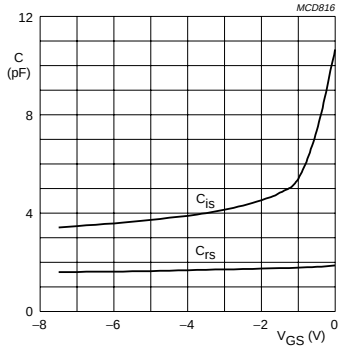

V_{DS} = 8 V; f = 1 MHz; T_j = 25 °C.

Fig.10 Input and reverse transfer capacitance as functions of gate-source voltage; typical values.

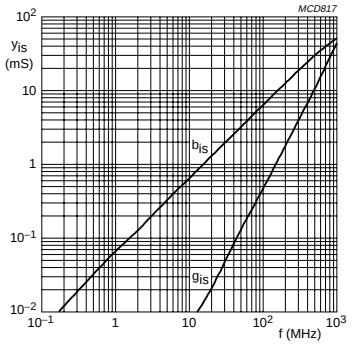

V_{DS} = 8 V; V_{GS} = 0; T_{amb} = 25 °C.

Fig.11 Common-source input admittance as a function of frequency; typical values.

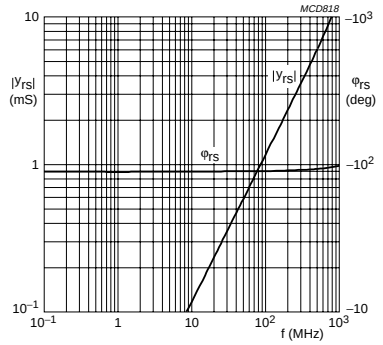

V_{DS} = 5 V; V_{G2} = 4 V.
I_D = 15 mA; T_{amb} = 25 °C.

Fig.12 Common-source reverse admittance as a function of frequency; typical values.

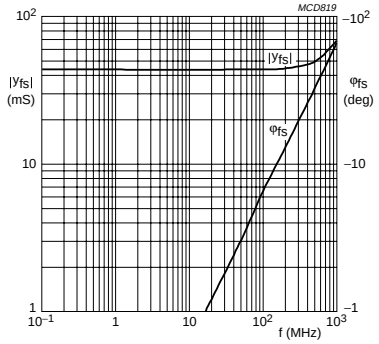

V_{DS} = 8 V; V_{GS} = 0; T_{amb} = 25 °C.

Fig.13 Common-source forward transfer admittance as a function of frequency; typical values.

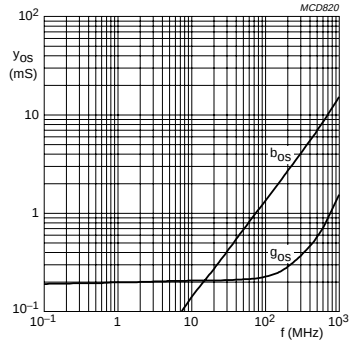

V_{DS} = 8 V; V_{GS} = 0; T_{amb} = 25 °C.

Fig.14 Common-source output admittance as a function of frequency; typical values.

PACKAGE OUTLINE

Plastic surface mounted package; 3 leads **SOT23**

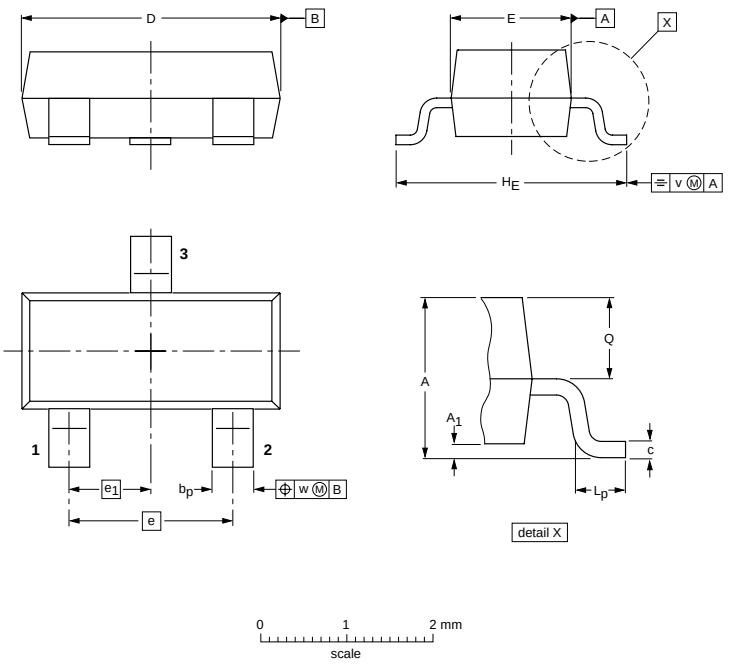

DIMENSIONS (mm are the original dimensions)

UNIT	A	A_1 max.	b_p	c	D	E	e	e_1	H_E	L_p	Q	v	w
mm	1.1 0.9	0.1	0.48 0.38	0.15 0.09	3.0 2.8	1.4 1.2	1.9	0.95	2.5 2.1	0.45 0.15	0.55 0.45	0.2	0.1

OUTLINE VERSION	REFERENCES				EUROPEAN PROJECTION	ISSUE DATE
	IEC	JEDEC	EIAJ			
SOT23		TO-236AB				~~97-02-28~~ 99-09-13

DEFINITIONS

Data sheet status	
Objective specification	This data sheet contains target or goal specifications for product development.
Preliminary specification	This data sheet contains preliminary data; supplementary data may be published later.
Product specification	This data sheet contains final product specifications.
Limiting values	
Limiting values given are in accordance with the Absolute Maximum Rating System (IEC 134). Stress above one or more of the limiting values may cause permanent damage to the device. These are stress ratings only and operation of the device at these or at any other conditions above those given in the Characteristics sections of the specification is not implied. Exposure to limiting values for extended periods may affect device reliability.	
Application information	
Where application information is given, it is advisory and does not form part of the specification.	

LIFE SUPPORT APPLICATIONS

These products are not designed for use in life support appliances, devices, or systems where malfunction of these products can reasonably be expected to result in personal injury. Philips customers using or selling these products for use in such applications do so at their own risk and agree to fully indemnify Philips for any damages resulting from such improper use or sale.

A.2 Datasheet: Operational Amplifier AD8099

The datasheet of the operational amplifier AD8099 was downloaded from http://www.analog.com/en/high-speed-op-amps/low-noise-low-distortion-amplifiers/ad8099/products/product.html, accessed 30 August 2012.

ANALOG DEVICES

Ultralow Distortion, High Speed 0.95 nV/√Hz Voltage Noise Op Amp

AD8099

FEATURES

Ultralow noise: 0.95 nV/√Hz, 2.6 pA/√Hz
Ultralow distortion
2nd harmonic R_L = 1 kΩ , G = +2
−92 dB @ 10 MHz
3rd harmonic R_L = 1 kΩ , G = +2
−105 dB @ 10 MHz
High speed
GBWP: 3.8 GHz
–3 dB bandwidth:
700 MHz (G = +2)
550 MHz (G = +10)
Slew rate:
475 V/µs (G = +2)
1350 V/µs (G = +10)
New pinout
Custom external compensation, gain range –1, +2 to +10
Supply current: 15 mA
Offset voltage: 0.5 mV max
Wide supply voltage range: 5 V to 12 V

APPLICATIONS

Pre-amplifiers
Receivers
Instrumentation
Filters
IF and baseband amplifiers
A-to-D drivers
DAC buffers
Optical electronics

CONNECTION DIAGRAMS

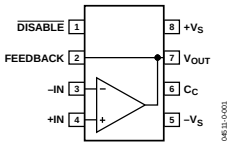

Figure 1. 8-Lead CSP (CP-8)

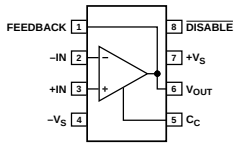

Figure 2. 8-Lead SOIC-ED (RD-8)

GENERAL DESCRIPTION

The AD8099 is an ultralow noise (0.95 nV/√Hz) and distortion (−92 dBc @10 MHz) voltage feedback op amp, the combination of which make it ideal for 16- and 18-bit systems. The AD8099 features a new, highly linear, low noise input stage that increases the full power bandwidth (FPBW) at low gains with high slew rates. ADI's proprietary next generation XFCB process enables such high performance amplifiers with relatively low power.

The AD8099 features external compensation, which lets the user set the gain bandwidth product. External compensation allows gains from +2 to +10 with minimal trade-off in bandwidth. The AD8099 also features an extremely high slew rate of 1350 V/µs, giving the designer flexibility to use the entire dynamic range without trading off bandwidth or distortion. The AD8099 settles to 0.1% in 18 ns and recovers from overdrive in 50 ns.

The AD8099 drives 100 Ω loads at breakthrough performance levels with only 15 mA of supply current. With the wide supply voltage range (5 V to 12 V), low offset voltage (0.1 mV typ), wide bandwidth (700 MHz for G = +2), and a GBWP up to 3.8 GHz, the AD8099 is designed to work in a wide variety of applications.

The AD8099 is available in a 3 mm × 3 mm lead frame chip scale package (LFCSP) with a new pinout that is specifically optimized for high performance, high speed amplifiers. The new LFCSP package and pinout enable the breakthrough performance that previously was not achievable with amplifiers. The AD8099 is rated to work over the extended industrial temperature range, −40°C to +125°C.

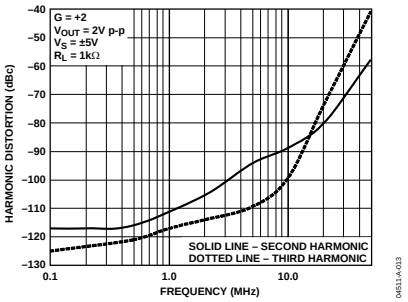

Figure 3 . Harmonic Distortion vs. Frequency and Gain (SOIC)

Rev. B
Information furnished by Analog Devices is believed to be accurate and reliable. However, no responsibility is assumed by Analog Devices for its use, nor for any infringements of patents or other rights of third parties that may result from its use. Specifications subject to change without notice. No license is granted by implication or otherwise under any patent or patent rights of Analog Devices. Trademarks and registered trademarks are the property of their respective owners.

One Technology Way, P.O. Box 9106, Norwood, MA 02062-9106, U.S.A.
Tel: 781.329.4700 **www.analog.com**
Fax: 781.326.8703 **© 2004 Analog Devices, Inc. All rights reserved.**

TABLE OF CONTENTS

Specifications ... 3
Specifications with ±5 V Supply ... 3
Specifications with +5 V Supply ... 4
Absolute Maximum Ratings ... 5
Maximum Power Dissipation ... 5
ESD Caution ... 5
Typical Performance Characteristics ... 6
Theory of Operation ... 15
Applications ... 16
Using the AD8099 ... 16
Circuit Components ... 16
Recommended Values ... 17
Circuit Configurations ... 17
Performance vs. Component values ... 19
Total Output Noise Calculations and Design ... 20
Input Bias Current and DC Offset ... 21
$\overline{\text{DISABLE}}$ Pin and Input Bias Cancellation ... 21
16-Bit ADC Driver ... 22
Circuit Considerations ... 23
Design Tools and Technical Support ... 23
Outline Dimensions ... 25
Ordering Guide ... 26

REVISION HISTORY

6/04—Data Sheet changed from REV. A to REV. B

Change to General Description ... 1
Changes to Maximum Power Dissipation section ... 5
Changes to Applications section ... 16
Changes to Table 7 ... 24
Changes to Ordering Guide ... 26

1/04—Data Sheet changed from REV. 0 to REV. A

Inserted new Figure 3 ... 1
Changes to Specifications ... 3
Inserted new Figures 22 to 34 ... 8
Inserted new Figures 51 to 55 ... 14
Changes to Theory of Operation section ... 16
Changes to Circuit Components section ... 17
Changes to Table 4 ... 18
Changes to Figure 60 ... 18
Changes to Total Output Noise Calculations and Design section ... 21
Changes to Figure 60 ... 22
Changes to Figure 62 ... 23
Changes to 16-Bit ADC Driver section ... 23
Changes to Table 6 ... 23
Additions to PCB Layout section ... 23

11/03—Revision 0: Initial Version

SPECIFICATIONS

SPECIFICATIONS WITH ±5 V SUPPLY

T_A = 25°C, G = +2, R_L = 1 kΩ to ground, unless otherwise noted. Refer to Figure 60 through Figure 66 for component values and gain configurations .

Table 1.

Parameter	Conditions	Min	Typ	Max	Unit
DYNAMIC PERFORMANCE					
−3 dB Bandwidth	G = +5, V_{OUT} = 0.2 V p-p	450	510		MHz
	G = +5, V_{OUT} = 2 V p-p	205	235		MHz
Bandwidth for 0.1 dB Flatness (SOIC/CSP)	G = +2, V_{OUT} = 0.2 V p-p		34/25		MHz
Slew Rate	G = +10, V_{OUT} = 6 V Step	1120	1350		V/µs
	G = +2, V_{OUT} = 2 V Step	435	470		V/µs
Settling Time to 0.1%	G = +2, V_{OUT} = 2 V Step		18		ns
NOISE/DISTORTION PERFORMANCE					
Harmonic Distortion (dBc) HD2/HD3	f_C = 500 kHz, V_{OUT} = 2 V p-p, G = +10		−102/−111		dBc
	f_C = 10 MHz, V_{OUT} = 2 V p-p, G = +10		−84/−92		dBc
Input Voltage Noise	f = 100 kHz		0.95		nV/√Hz
Input Current Noise	f = 100 kHz, $\overline{\text{DISABLE}}$ pin floating		2.6		pA/√Hz
	f = 100 kHz, $\overline{\text{DISABLE}}$ pin = +V_S		5.2		pA/√Hz
DC PERFORMANCE					
Input Offset Voltage			0.1	0.5	mV
Input Offset Voltage Drift			2.3		µV/°C
Input Bias Current	$\overline{\text{DISABLE}}$ pin floating		−6	−13	µA
	$\overline{\text{DISABLE}}$ pin = +V_S		−0.1	−2	µA
Input Bias Current Drift			3		nA/°C
Input Bias Offset Current			0.06	1	µA
Open-Loop Gain		82	85		dB
INPUT CHARACTERISTICS					
Input Resistance	Differential mode		4		kΩ
	Common mode		10		MΩ
Input Capacitance			2		pF
Input Common-Mode Voltage Range			−3.7 to +3.7		V
Common-Mode Rejection Ratio	V_{CM} = ±2.5 V	98	105		dB
$\overline{\text{DISABLE}}$ PIN					
$\overline{\text{DISABLE}}$ Input Voltage	Output disabled		<2.4		V
Turn-Off Time	50% of $\overline{\text{DISABLE}}$ to < 10% of final V_{OUT}, V_{IN} = 0.5 V, G = +2		105		ns
Turn-On Time	50% of $\overline{\text{DISABLE}}$ to < 10% of final V_{OUT}, V_{IN} = 0.5 V, G = +2		39		ns
Enable Pin Leakage Current	$\overline{\text{DISABLE}}$ =+5 V		17	21	µA
$\overline{\text{DISABLE}}$ Pin Leakage Current	$\overline{\text{DISABLE}}$ = −5 V		35	44	µA
OUTPUT CHARACTERISTICS					
Output Overdrive Recovery Time (Rise/Fall)	V_{IN} = -2.5 V to 2.5 V, G =+2		30/50		ns
Output Voltage Swing	R_L = 100 Ω	−3.4 to +3.5	−3.6 to +3.7		V
	R_L = 1 kΩ	−3.7 to +3.7	−3.8 to +3.8		V
Short-Circuit Current	Sinking and sourcing		131/178		mA
Off Isolation	f = 1 MHz, $\overline{\text{DISABLE}}$ = low		−61		dB
POWER SUPPLY					
Operating Range			±5	±6	V
Quiescent Current			15	16	mA
Quiescent Current (Disabled)	$\overline{\text{DISABLE}}$ = Low		1.7	2	mA
Positive Power Supply Rejection Ratio	+V_S = 4 V to 6 V, −V_S = −5 V (input referred)	85	91		dB
Negative Power Supply Rejection Ratio	+V_S = 5 V, −V_S = −6 V to −4 V (input referred)	86	94		dB

SPECIFICATIONS WITH +5 V SUPPLY

V_S = 5 V @ T_A = 25°C, G = +2, R_L = 1 kΩ to midsupply, unless otherwise noted. Refer to Figure 60 through Figure 66 for component values and gain configurations .

Table 2.

Parameter	Conditions	Min	Typ	Max	Unit
DYNAMIC PERFORMANCE					
−3 dB Bandwidth	G = +5, V_{OUT} = 0.2 V p-p	415	440		MHz
	G = +5, V_{OUT} = 2 V p-p	165	210		MHz
Bandwidth for 0.1 dB Flatness (SOIC/CSP)	G = +2, V_{OUT} = 0.2 V p-p		33/23		MHz
Slew Rate	G = +10, V_{OUT} = 2 V Step	630	715		V/µs
	G = +2, V_{OUT} = 2 V Step	340	365		V/µs
Settling Time to 0.1%	G = +2, V_{OUT} = 2 V Step		18		ns
NOISE/DISTORTION PERFORMANCE					
Harmonic Distortion (dBc) HD2/HD3	f_C = 500 kHz, V_{OUT} = 1 V p-p, G = +10		−82/−94		dBc
	f_C = 10 MHz, V_{OUT} = 1 V p-p, G = +10		−80/−75		dBc
Input Voltage Noise	f = 100 kHz		0.95		nV/√Hz
Input Current Noise	f = 100 kHz, $\overline{\text{DISABLE}}$ pin floating		2.6		pA/√Hz
	f = 100 kHz, $\overline{\text{DISABLE}}$ pin = +V_S		5.2		pA/√Hz
DC PERFORMANCE					
Input Offset Voltage			0.1	0.5	mV
Input Offset Voltage Drift			2.5		µV/°C
Input Bias Current	$\overline{\text{DISABLE}}$ pin floating		−6.2	−13	µA
	$\overline{\text{DISABLE}}$ pin = +V_S		−0.2	−2	µA
Input Bias Offset Current			0.05	1	µA
Input Bias Offset Current Drift			2.4		nA/°C
Open-Loop Gain	V_{OUT} = 1 V to 4 V	76	81		dB
INPUT CHARACTERISTICS					
Input Resistance	Differential mode		4		kΩ
	Common mode		10		MΩ
Input Capacitance			2		pF
Input Common-Mode Voltage Range			1.3 to 3.7		V
Common-Mode Rejection Ratio	V_{CM} = 2 V to 3 V	88	105		dB
$\overline{\text{DISABLE}}$ PIN					
$\overline{\text{DISABLE}}$ Input Voltage	Output disabled		<2.4		V
Turn-Off Time	50% of $\overline{\text{DISABLE}}$ to <10% of Final V_{OUT}, V_{IN} = 0.5 V, G = +2		105		ns
Turn-On Time	50% of $\overline{\text{DISABLE}}$ to <10% of Final V_{OUT}, V_{IN} = 0.5 V, G = +2		61		ns
Enable Pin Leakage Current	$\overline{\text{DISABLE}}$ = 5 V		16	21	µA
$\overline{\text{DISABLE}}$ Pin Leakage Current	$\overline{\text{DISABLE}}$ = 0 V		33	44	µA
OUTPUT CHARACTERISTICS					
Overdrive Recovery Time (Rise/Fall)	V_{IN} = 0 to 2.5 V, G = +2		50/70		ns
Output Voltage Swing	R_L = 100 Ω	1.5 to 3.5	1.2 to 3.8		V
	R_L = 1 kΩ	1.2 to 3.8	1.2 to 3.8		V
Short-Circuit Current	Sinking and Sourcing		60/80		mA
Off Isolation	f = 1 MHz, $\overline{\text{DISABLE}}$ = Low		−61		dB
POWER SUPPLY					
Operating Range			±5	±6	V
Quiescent Current			14.5	15.4	mA
Quiescent Current (Disabled)	$\overline{\text{DISABLE}}$ = Low		1.4	1.7	mA
Positive Power Supply Rejection Ratio	+V_S = 4.5 V to 5.5 V, −V_S = 0 V (input referred)	84	89		dB
Negative Power Supply Rejection Ratio	+V_S =5 V, -V_S= −0.5 V to +0.5 V (input referred)	84	90		dB

ABSOLUTE MAXIMUM RATINGS

Table 3.

Parameter	Rating
Supply Voltage	12.6 V
Power Dissipation	See Figure 4
Differential Input Voltage	±1.8 V
Differential Input Current	±10mA
Storage Temperature	−65°C to +125°C
Operating Temperature Range	−40°C to +125°C
Lead Temperature Range (Soldering 10 sec)	300°C
Junction Temperature	150°C

Stresses above those listed under Absolute Maximum Ratings may cause permanent damage to the device. This is a stress rating only; functional operation of the device at these or any other conditions above those indicated in the operational section of this specification is not implied. Exposure to absolute maximum rating conditions for extended periods may affect device reliability.

MAXIMUM POWER DISSIPATION

The maximum safe power dissipation in the AD8099 package is limited by the associated rise in junction temperature (T_J) on the die. The plastic encapsulating the die will locally reach the junction temperature. At approximately 150°C, which is the glass transition temperature, the plastic will change its properties. Even temporarily exceeding this temperature limit may change the stresses that the package exerts on the die, permanently shifting the parametric performance of the AD8099. Exceeding a junction temperature of 150°C for an extended period can result in changes in silicon devices, potentially causing failure.

The still-air thermal properties of the package and PCB (θ_{JA}), the ambient temperature (T_A), and the total power dissipated in the package (P_D) determine the junction temperature of the die. The junction temperature can be calculated as

$$T_J = T_A + (P_D \times \theta_{JA})$$

The power dissipated in the package (P_D) is the sum of the quiescent power dissipation and the power dissipated in the package due to the load drive for all outputs. The quiescent power is the voltage between the supply pins (V_S) times the quiescent current (I_S). Assuming the load (R_L) is referenced to midsupply, the total drive power is $V_S/2 \times I_{OUT}$, some of which is dissipated in the package and some in the load ($V_{OUT} \times I_{OUT}$).

The difference between the total drive power and the load power is the drive power dissipated in the package.

$$P_D = \textit{Quiescent Power} + (\textit{Total Drive Power} - \textit{Load Power})$$

$$P_D = (V_S \times I_S) + \left(\frac{V_S}{2} \times \frac{V_{OUT}}{R_L}\right) - \frac{{V_{OUT}}^2}{R_L}$$

RMS output voltages should be considered. If R_L is referenced to V_S-, as in single-supply operation, then the total drive power is $V_S \times I_{OUT}$. If the rms signal levels are indeterminate, consider the worst case, when $V_{OUT} = V_S/4$ for R_L to midsupply:

$$P_D = (V_S \times I_S) + \frac{(V_S/4)^2}{R_L}$$

In single-supply operation with R_L referenced to V_S-, worst case is $V_{OUT} = V_S/2$.

Airflow will increase heat dissipation, effectively reducing θ_{JA}. Also, more metal directly in contact with the package leads from metal traces, through holes, ground, and power planes will reduce the θ_{JA}. Soldering the exposed paddle to the ground plane significantly reduces the overall thermal resistance of the package. Care must be taken to minimize parasitic capacitances at the input leads of high speed op amps, as discussed in the PCB Layout section.

Figure 4 shows the maximum safe power dissipation in the package versus the ambient temperature for the exposed paddle (e-pad) SOIC-8 (70°C/W), and CSP (70°C/W), packages on a JEDEC standard 4-layer board. θ_{JA} values are approximations.

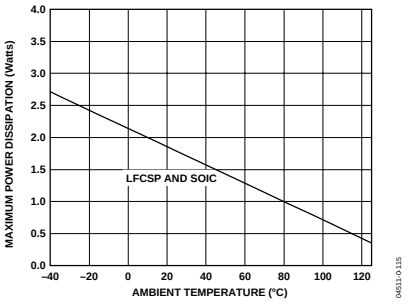

Figure 4. Maximum Power Dissipation

ESD CAUTION

ESD (electrostatic discharge) sensitive device. Electrostatic charges as high as 4000 V readily accumulate on the human body and test equipment and can discharge without detection. Although this product features proprietary ESD protection circuitry, permanent damage may occur on devices subjected to high energy electrostatic discharges. Therefore, proper ESD precautions are recommended to avoid performance degradation or loss of functionality.

TYPICAL PERFORMANCE CHARACTERISTICS

Default Conditions: V_S = ±5 V, T_A = 25°C, R_L = 1 kΩ tied to ground unless otherwise noted. Refer to Figure 63 through Figure 66 for component values and gain configurations.

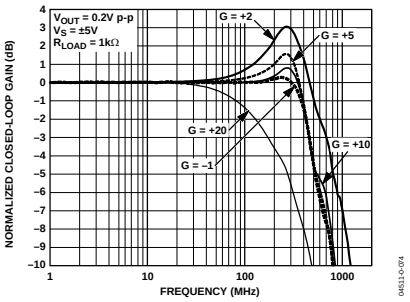

Figure 5. Small Signal Frequency Response for Various Gains (SOIC)

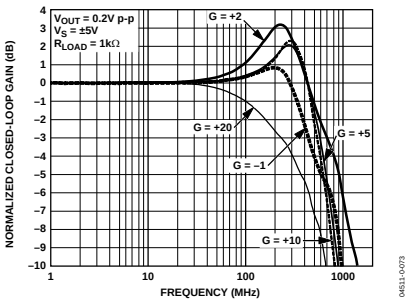

Figure 8. Small Signal Frequency Response for Various Gains (CSP)

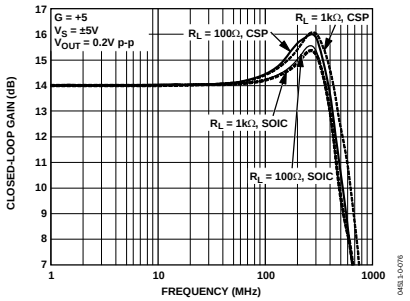

Figure 6. Small Signal Frequency Response for Various Load Resistors

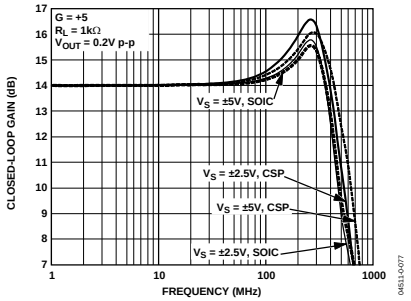

Figure 9. Small Signal Frequency Response for Various Supply Voltages

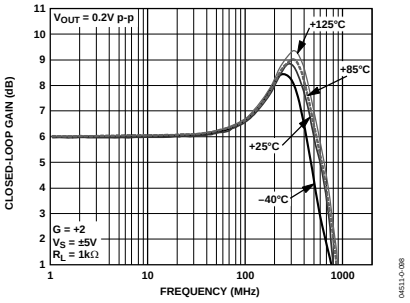

Figure 7. Small Signal Frequency Response for Various Temperatures (SOIC)

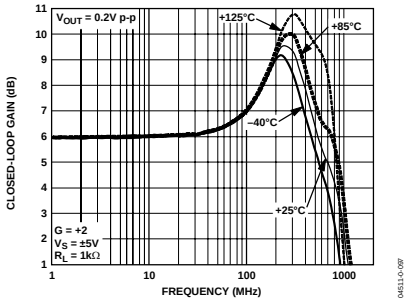

Figure 10. Small Signal Frequency Response for Various Temperatures (CSP)

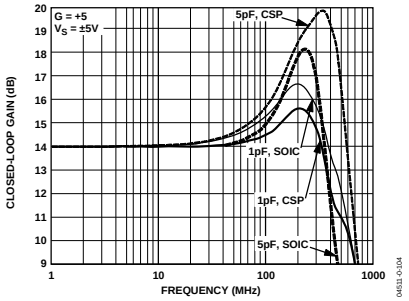

Figure 11. Small Signal Frequency Response for Various Capacitive Loads

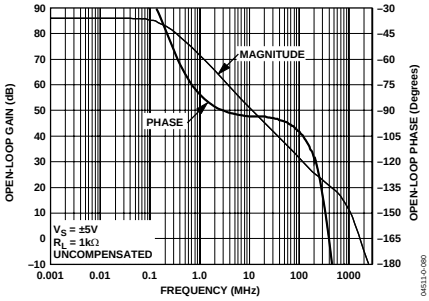

Figure 14. Open Loop Frequency Response

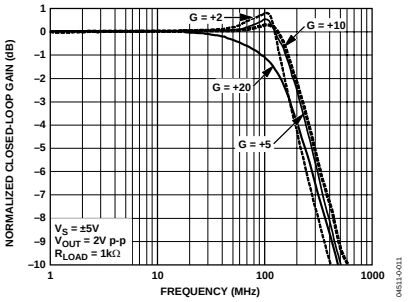

Figure 12. Large Signal Frequency Response for Various Gains (SOIC)

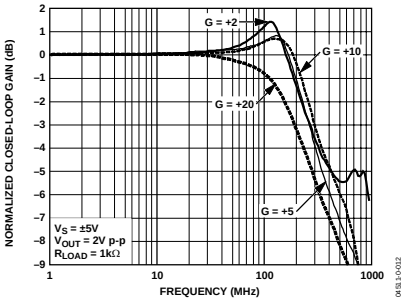

Figure 15. Large Signal Frequency Response for Various Gains (CSP)

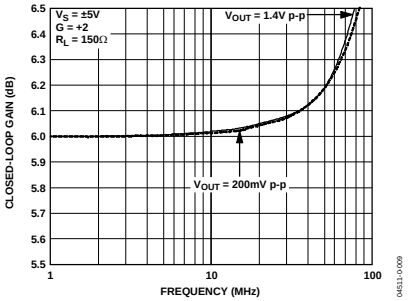

Figure 13. 0.1 dB Flatness (SOIC)

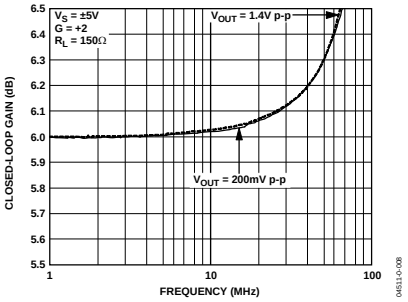

Figure 16. 0.1 dB Flatness (CSP)

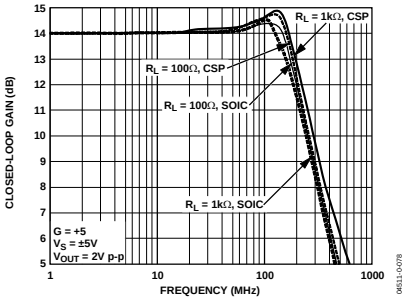

Figure 17. Large Signal Frequency Response for Various Load Resistances

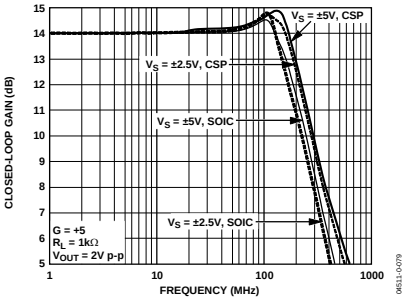

Figure 20. Large Signal Frequency Response for Various Supply Voltages

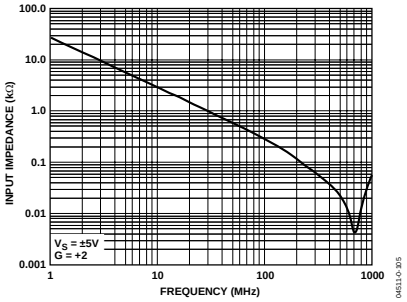

Figure 18. Input Impedance vs. Frequency

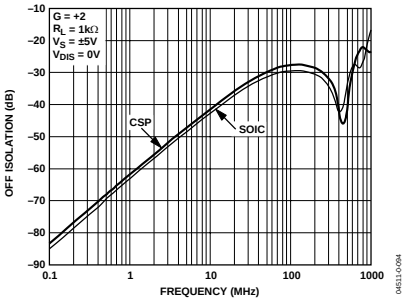

Figure 21. Off Isolation vs. Frequency

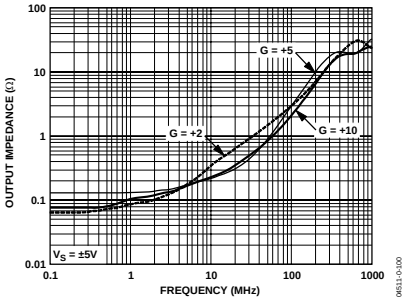

Figure 19. Output Impedance vs. Frequency for Various Gains

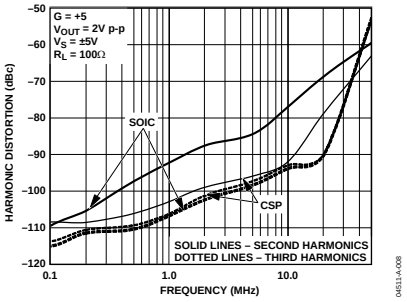

Figure 22. Harmonic Distortion vs. Frequency

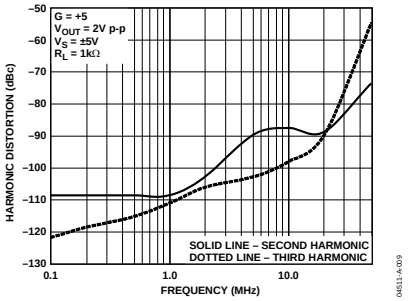

Figure 23. Harmonic Distortion vs. Frequency (SOIC)

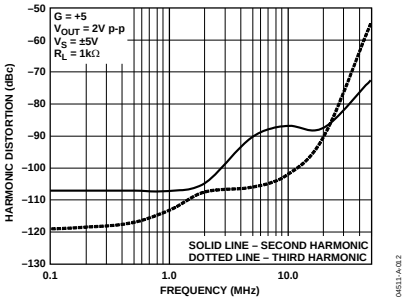

Figure 26. Harmonic Distortion vs. Frequency (CSP)

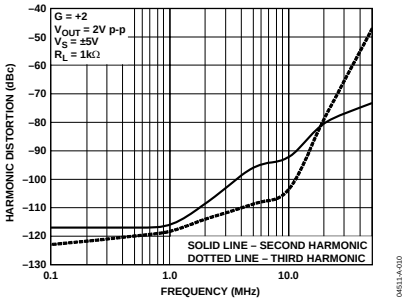

Figure 24. Harmonic Distortion vs. Frequency (SOIC)

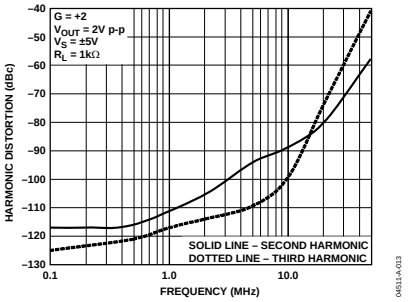

Figure 27. Harmonic Distortion vs. Frequency (CSP)

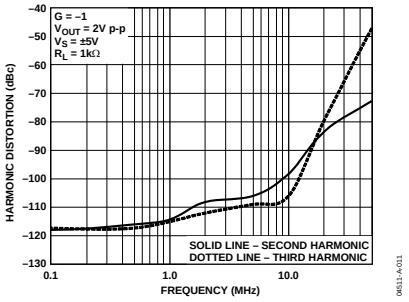

Figure 25. Harmonic Distortion vs. Frequency (SOIC)

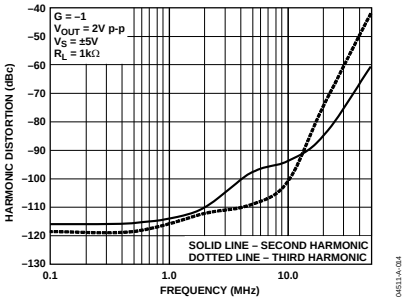

Figure 28. Harmonic Distortion vs. Frequency (CSP)

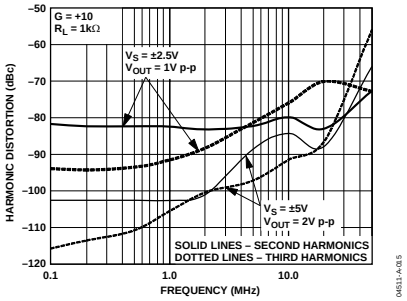

Figure 29. Harmonic Distortion vs. Frequency and Supply Voltage (SOIC)

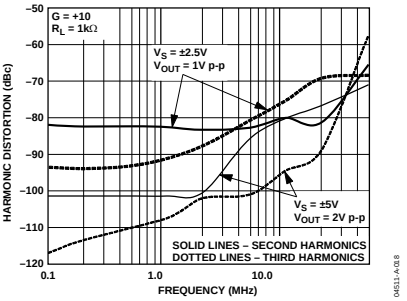

Figure 32. Harmonic Distortion vs. Frequency for Various Supplies (CSP)

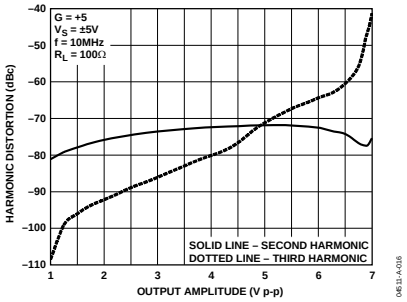

Figure 30. Harmonic Distortion vs. Output Amplitude (SOIC)

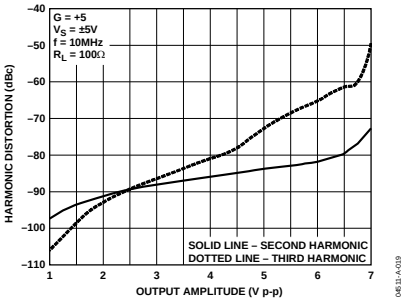

Figure 33. Harmonic Distortion vs. Output Amplitude (CSP)

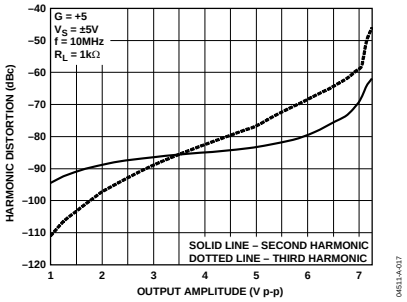

Figure 31. Harmonic Distortion vs. Output Amplitude (SOIC)

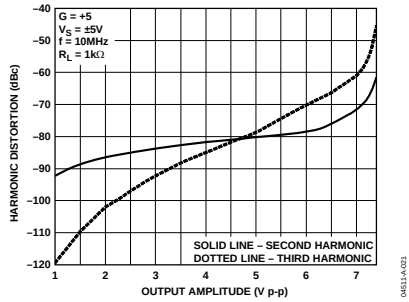

Figure 34. Harmonic Distortion vs. Output Amplitude (CSP)

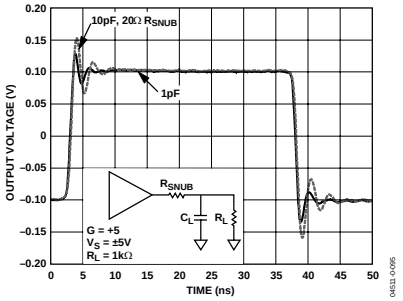

Figure 35. Small Signal Transient Response for Various Capacitive Loads (SOIC)

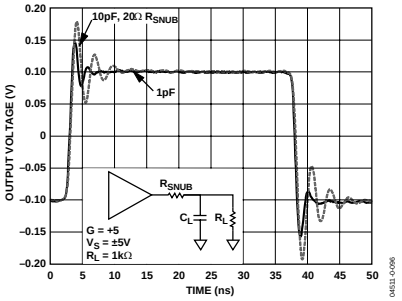

Figure 38. Small Signal Transient Response for Various Capacitive Loads (CSP)

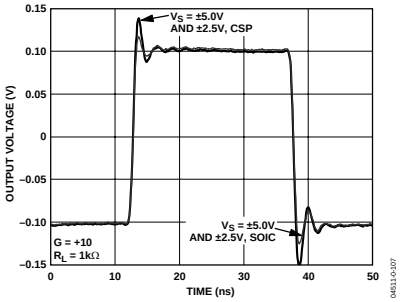

Figure 36. Small Signal Transient Response for Various Supply Voltages

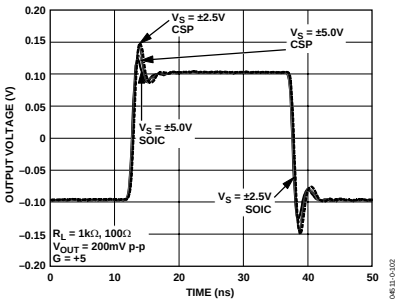

Figure 39. Small Signal Transient Response for Various Supply Voltages

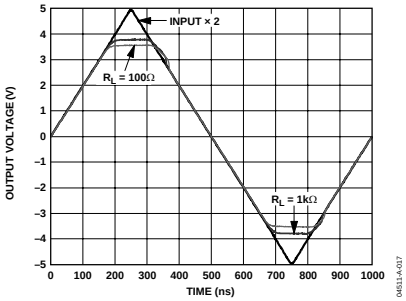

Figure 37. Output Overdrive Recovery for Various Resistive Loads

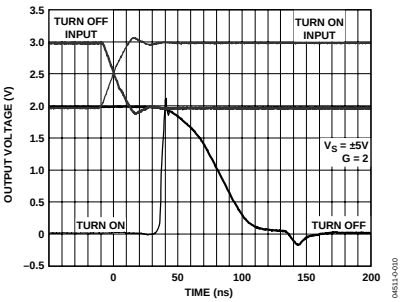

Figure 40. Disable/Enable Switching Speed

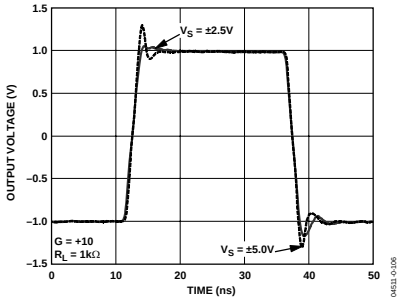

Figure 41. Large Signal Transient Response vs. Supply Voltage (CSP)

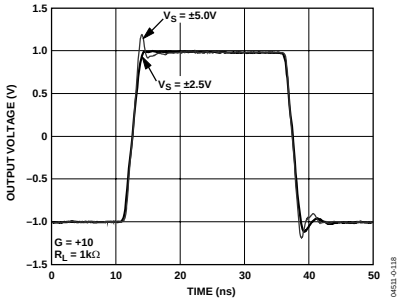

Figure 42. Large Signal Frequency Response vs. Supply Voltage (SOIC)

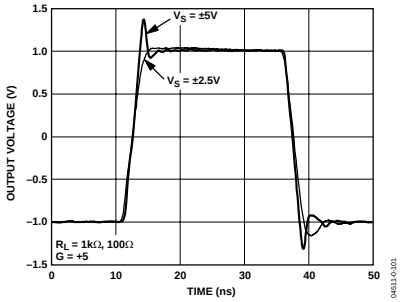

Figure 43. Large Signal Transient Response for Various Supply Voltages and Load Resistances (SOIC and CSP)

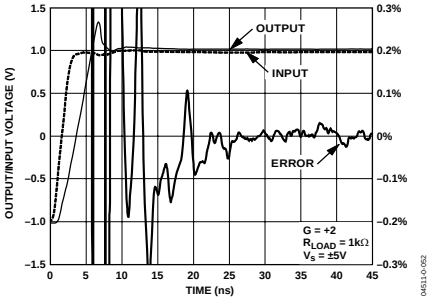

Figure 44. Short Term Settling Time (CSP)

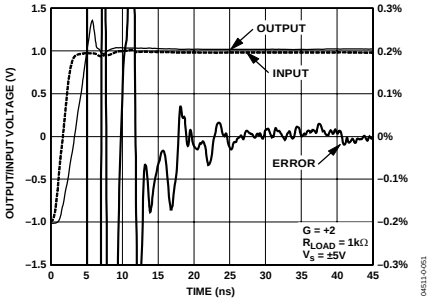

Figure 45. Short Term Settling Time (SOIC)

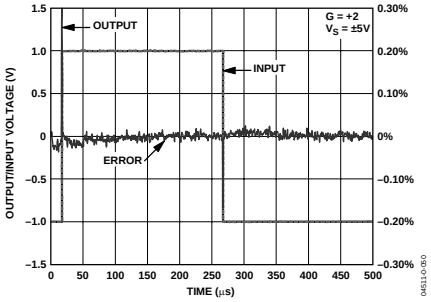

Figure 46. Long Term Settling Time

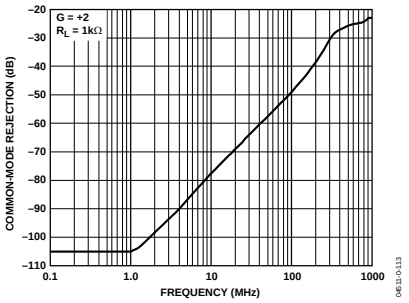

Figure 47. Common-Mode Rejection vs. Frequency

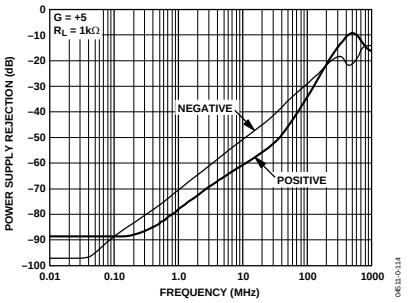

Figure 50. Power Supply Rejection vs. Frequency

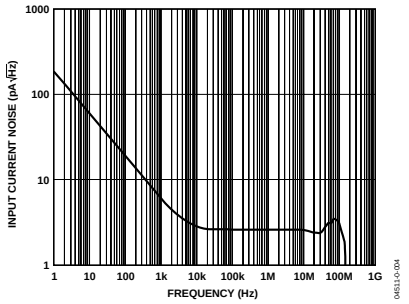

Figure 48. Input Current Noise vs. Frequency ($\overline{DISABLE}$ = Open)

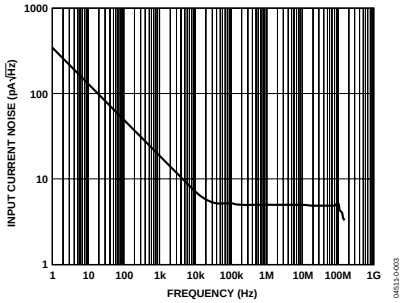

Figure 51. Input Current Noise vs. Frequency ($\overline{DISABLE}$ = $+V_S$)

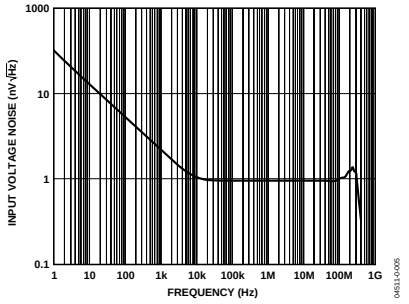

Figure 49. Input Voltage Noise vs. Frequency

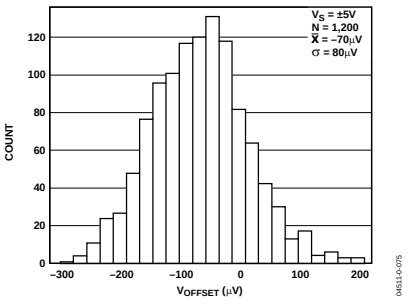

Figure 52. Input Offset Voltage Distribution

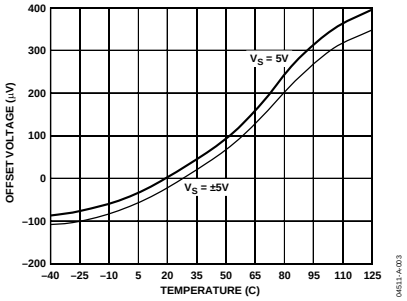

Figure 53. Input Offset Voltage vs. Temperature

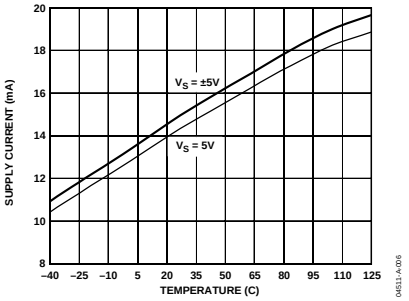

Figure 56. Supply Current vs. Temperature

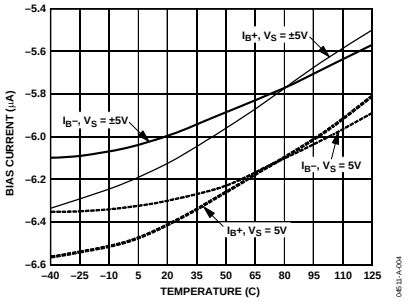

Figure 54. Input Bias Current vs. Temperature ($\overline{DISABLE}$ Pin Floating)

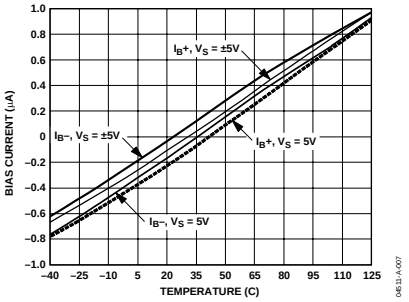

Figure 57. Input Bias Current vs. Temperature ($\overline{DISABLE}$ Pin = $+V_S$)

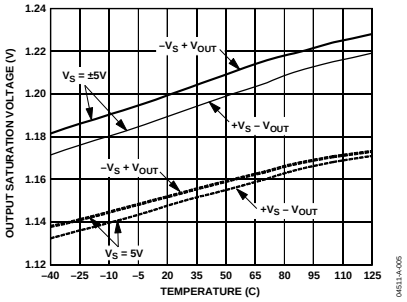

Figure 55. Output Saturation Voltage vs. Temperature

THEORY OF OPERATION

The AD8099 is a voltage feedback op amp that employs a new highly linear low noise input stage. With this input stage, the AD8099 can achieve better than 90 dB distortion for a 2 V p-p, 10 MHz output signal with an input referred voltage noise of less than 1 nV/$\sqrt{\text{Hz}}$. This noise level and distortion performance has been previously achievable only with fully uncompensated amplifiers. The AD8099 achieves this level of performance for gains as low as +2. This new input stage also triples the achievable slew rate for comparably compensated 1 nV/$\sqrt{\text{Hz}}$ amplifiers.

The simplified AD8099 topology is shown in Figure 58. The amplifier is a single gain stage with a unity gain output buffer fabricated in Analog Devices' extra fast complimentary bipolar process (XFCB). The AD8099 has 85 dB of open-loop gain and maintains precision specifications such as CMRR, PSRR, V_{OS}, and $\Delta V_{OS}/\Delta T$ to levels that are normally associated with topologies having two or more gain stages.

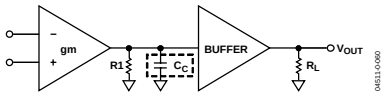

Figure 58. AD8099 Topology

The AD8099 can be externally compensated down to a gain of 2 through the use of an RC network. Above gains of 15, no external compensation network is required. To realize the full gain bandwidth product of the AD8099, no PCB trace should be connected to or within close proximity of the external compensation pin for the lowest possible capacitance.

External compensation allows the user to optimize the closed-loop response for minimal peaking while increasing the gain bandwidth product in higher gains, lowering distortion errors that are normally more prominent with internally compensated parts in higher gains. For a fixed gain bandwidth, wideband distortion products would normally increase by 6 dB going from a closed-loop gain of 2 to 4. Increasing the gain bandwidth product of the AD8099 eliminates this effect with increasing closed-loop gain.

The AD8099 is available in both a SOIC and an LFCSP, each of which has a thermal pad for lower operating temperature. To help avoid this pad in board layout, both packages have an extra output pin on the opposite side of the package for ease in connecting a feedback network to the inputs. The secondary output pin also isolates the interaction of any capacitive load on the output and self-inductance of the package and bond wire from the feedback loop. While using the secondary output for feedback, inductance in the primary output will now help to isolate capacitive loads from the output impedance of the amplifier. Since the SOIC has greater inductance in its output, the SOIC will drive capacitive loads better than the LFCSP. Using the primary output for feedback with both packages will result in the LFCSP driving capacitive load better than the SOIC.

The LFCSP and SOIC pinouts are identical, except for the rotation of all pins counterclockwise by one pin on the LFCSP. This isolates the inputs from the negative power supply pin, removing a mutually inductive coupling that is most prominent while driving heavy loads. For this reason, the LFCSP second harmonic, while driving a heavy load, is significantly better than that of the SOIC.

A three-state input pin is provided on the AD8099 for a high impedance power-down and an optional input bias current cancellation circuit. The high impedance output allows several AD8099s to drive the same ADC or output line time interleaved. Pulling the $\overline{\text{DISABLE}}$ pin low activates the high impedance state. See Table 5 for threshold levels. When the $\overline{\text{DISABLE}}$ pin is left floating, the AD8099 operates normally. With the $\overline{\text{DISABLE}}$ pin pulled within 0.7 V of the positive supply, an optional input bias current cancellation circuit is turned on, which lowers the input bias current to less than 200 nA. In this mode, the user can drive the AD8099 with a high dc source impedance and still maintain minimal output referred offset without having to use impedance matching techniques. In addition, the AD8099 can be ac-coupled while setting the bias point on the input with a high dc impedance network. The input bias current cancellation circuit will double the input referred current noise, but this effect is minimal as long as wideband impedance is kept low (see Figure 48 and Figure 51).

A pair of internally connected diodes limits the differential voltage between the noninverting input and the inverting input of the AD8099. Each set of diodes has two series diodes, which are connected in anti-parallel. This limits the differential voltage between the inputs to approximately ±1.8 V. All of the AD8099 pins are ESD protected with voltage limiting diodes connected between both rails. The protection diodes can handle 5 mA of steady state current. Currents should be limited to 5 mA or less through the use of a series limiting resistor.

APPLICATIONS

USING THE AD8099

The AD8099 offers unrivaled noise and distortion performance in low signal gain configurations. In low gain configurations (less than15), the AD8099 requires external compensation. The amount of gain and performance needed will determine the compensation network.

Understanding the subtleties of the AD8099 gives the user insight on how to exact its peak performance. Use the component values and circuit configurations shown in the Applications section as starting points for designs. Specific circuit applications will dictate the final configuration and value of your components.

CIRCUIT COMPONENTS

The circuit components are referenced in Figure 59, the recommended noninverting circuit schematic for the AD8099. See Table 4 for typical component values and performance data.

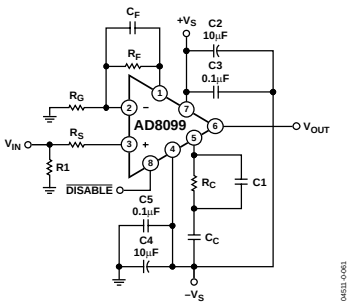

Figure 59. Wideband Noninverting Gain Configuration (SOIC)

R_F and R_G—The feedback resistor and the gain set resistor determine the noise gain of the amplifier; typical R_F values range from 250 Ω to 499 Ω.

C_F—Creates a zero in the loop response to compensate the pole created by the input capacitance (including stray capacitance) and the feedback resistor R_F. C_F helps reduce high frequency peaking and ringing in the closed-loop response. Typical range is 0.5 pF to 1.5 pF for evaluation circuits used here.

R1—This resistor terminates the input of the amplifier to the source resistance of the signal source, typically 50 Ω. (This is application specific and not always required.)

R_S—Many high speed amplifiers in low gain configurations require that the input stage be terminated into a nominal impedance to maintain stability. The value of R_S should be kept to 50 Ω or lower to maintain low noise performance. At higher gains, R_S may be reduced or even eliminated. Typical range is 0 Ω to 50 Ω.

C_C—The compensation capacitor decreases the open-loop gain at higher frequencies where the phase is degrading. By decreasing the open-loop gain here, the phase margin is increased and the amplifier is stabilized. Typical range is 0 pF to 5 pF. The value of C_C is gain dependent.

R_C—The series lead inductance of the package and the compensation capacitance (C_C) forms a series resonant circuit. R_C dampens this resonance and prevents oscillations. The recommended value of R_C is 50 Ω for a closed-loop gain of 2. This resistor introduces a zero in the open-loop response and must be kept low so that this zero occurs at a higher frequency. The purpose of the compensation network is to decrease the open-loop gain. If the resistance becomes too large, the gain will be reduced to the resistor value, and not necessarily to 0 Ω, which is what a single capacitor would do over frequency. Typical value range is 0 Ω to 50 Ω.

C1—To lower the impedance of R_C, C1 is placed in parallel with R_C. C1 is not required, but greatly reduces peaking at low closed-loop gains. The typical value range is 0 pF to 2 pF.

C2 and C3—Bypass capacitors are connected **between** both supplies for optimum distortion and PSRR performance. These capacitors should be placed as close as possible to the supply pins of the amplifier. For **C3, C5**, a 0508 case size should be used. The 0508 case size offers reduced inductance and better frequency response.

C4 and C2—Electrolytic bypass capacitors.

RECOMMENDED VALUES

Table 4. Recommended Values and AD8099 Performance

Gain	Package	Feedback Network Values				Compensation Network Values			−3 dB SS Bandwidth (MHz)	Slew Rate (V/µs)	Peaking (dB)	Output Noise (AD8099 Only) (nV/√Hz)	Total Output Noise Including Resistors (nV/√Hz)
		R_F	R_G	R_S	C_F	R_C	C_C	C1					
−1, 2	SOIC	250	250	50	1.5	50	4	1.5	440/700	515	0.3/3.1	2.1	4
2	CSP	250	250	50	0.5	50	5	2	700	475	3.2	2.1	4
−1	CSP	250	250	50	1.0	50	5	2	420	475	0.8	2.1	4
5	CSP/SOIC	499	124	20	0.5	50	1	0	510	735	1.4	4.9	8.6
10	CSP/SOIC	499	54	0	0	0	0.5	0	550	1350	0.8	9.6	13.3
20	CSP/SOIC	499	26	0	0	0	0	0	160	1450	0	19	23.3

CIRCUIT CONFIGURATIONS

Figure 60 through Figure 66 show typical schematics for the AD8099 in various gain configurations. Table 4 data was collected using the schematics shown in Figure 60 through Figure 66. Resistor R1, as shown in Figure 60 through Figure 66, is the test equipment termination resistor. R1 **is not** required for normal operation, but is shown in the schematics for completeness.

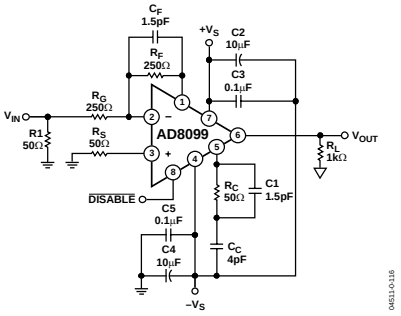

Figure 60. Amplifier Configuration for SOIC Package, Gain = –1

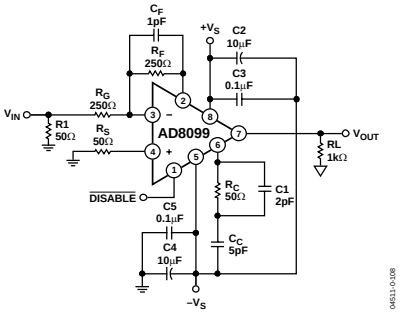

Figure 62. Amplifier Configuration for CSP Package, Gain =–1

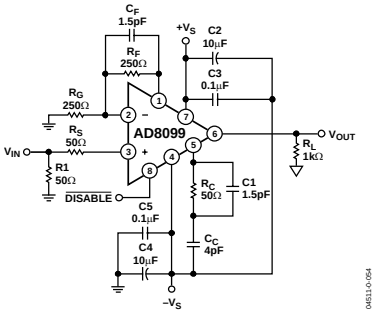

Figure 61. Amplifier Configuration for SOIC Package, Gain = +2

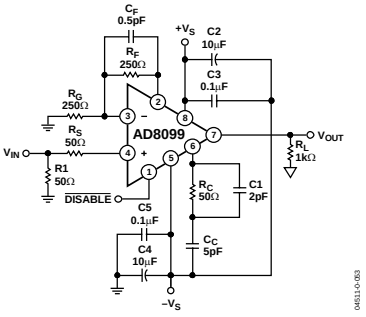

Figure 63. Amplifier Configuration for CSP Package, Gain = +2

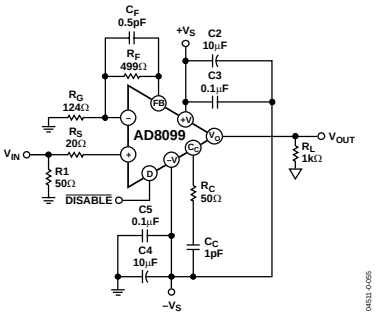

Figure 64. Amplifier Configuration for CSP and SOIC Package, Gain = +5

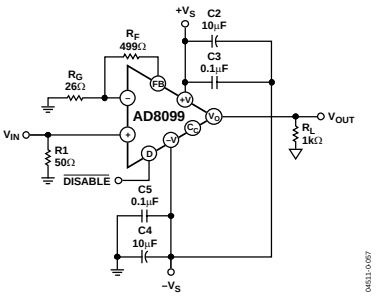

Figure 66. Amplifier Configuration for CSP and SOIC Packages, Gain = +20

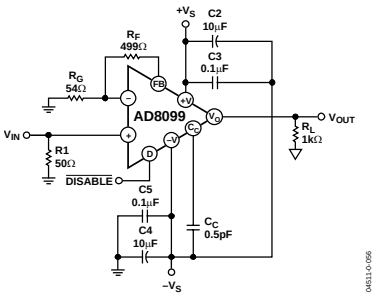

Figure 65. Amplifier Configuration for CSP and SOIC Packages, Gain = +10

PERFORMANCE VS. COMPONENT VALUES

The influence that each component has on the AD8099 frequency response can be seen in Figure 67 and Figure 68. In Figure 67 and Figure 68, all component values are held constant, except for the individual component shown, which is varied. For example, in the R_S performance plot of Figure 68, all components are held constant except R_S, which is varied from 0 Ω to 50 Ω.; and clearly indicates that R_S has a major influence on peaking and bandwidth of the AD8099.

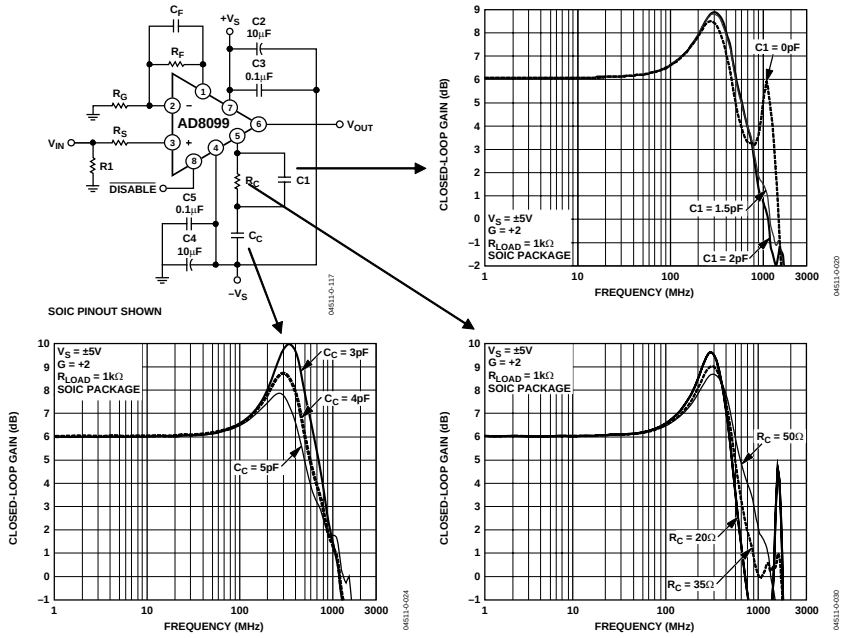

Figure 67. Frequency Response for Various Values of C1, C_C, R_C

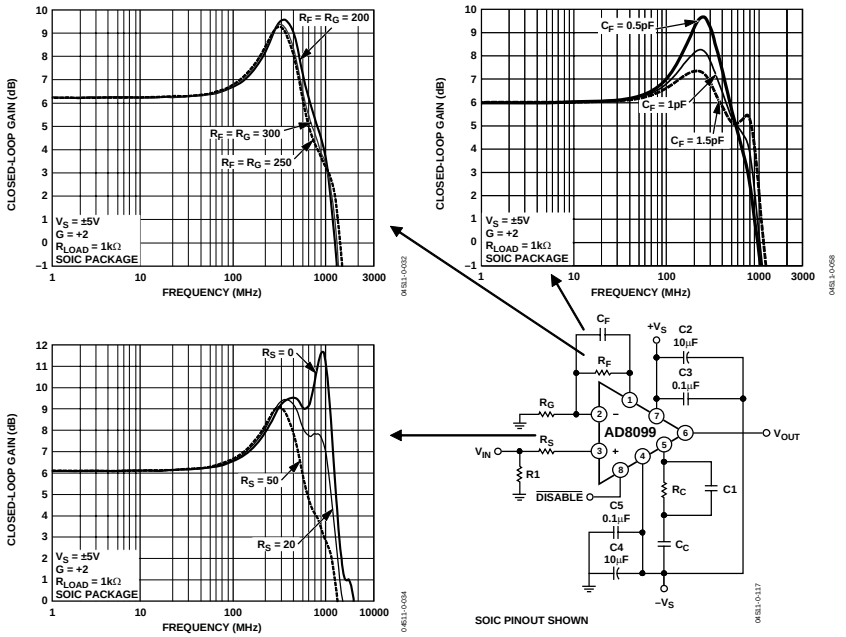

Figure 68. Frequency Response for Various Values of R_F, C_F, R_S

TOTAL OUTPUT NOISE CALCULATIONS AND DESIGN

To analyze the noise performance of an amplifier circuit, the individual noise sources must be identified. Then determine if the source has a significant contribution to overall noise performance of the amplifier. To simplify the noise calculations, we will work with noise spectral densities, rather than actual voltages to leave bandwidth out of the expressions (noise spectral density, which is generally expressed in nV/$\sqrt{\text{Hz}}$, is equivalent to the noise in a 1 Hz bandwidth).

The noise model shown in Figure 69 has six individual noise sources: the Johnson noise of the three resistors, the op amp voltage noise, and the current noise in each input of the amplifier. Each noise source has its own contribution to the noise at the output. Noise is generally specified RTI (referred to input), but it is often simpler to calculate the noise referred to the output (RTO) and then divide by the noise gain to obtain the RTI noise.

All resistors have a Johnson noise of $\sqrt{(4kBTR)}$, where k is Boltzmann's Constant (1.38×10^{-23} J/K), T is the absolute temperature in Kelvin, B is the bandwidth in Hz, and R is the resistance in ohms. A simple relationship, which is easy to remember, is that a 50 Ω resistor generates a Johnson noise of 1 nV$\sqrt{\text{Hz}}$ at 25°C. The AD8099 amplifier has roughly the same equivalent noise as a 50 Ω resistor.

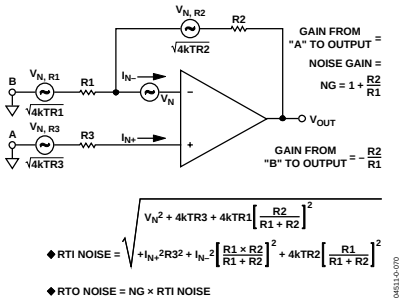

Figure 69. Op Amp Noise Analysis Model

In applications where noise sensitivity is critical, care must be taken not to introduce other significant noise sources to the amplifier. Each resistor is a noise source. Attention to the following areas is critical to maintain low noise performance: design, layout, and component selection. A summary of noise performance for the amplifier and associated resistors can be seen in Table 4.

INPUT BIAS CURRENT AND DC OFFSET

In high noise gain configurations, the effects of output offset voltage can be significant, even with low input bias currents and input offset voltages. Figure 70 shows a comprehensive offset voltage model, which can be used to determine the referred to output (RTO) offset voltage of the amplifier or referred to input (RTI) offset voltage.

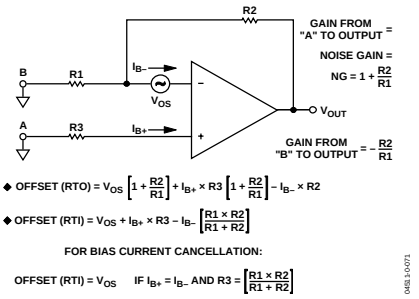

Figure 70. Op Amp Total Offset Voltage Model

For RTO calculations, the input offset voltage and the voltage generated by the bias current flowing through R3 are multiplied by the noise gain of the amplifier. The voltage generated by I_{B-} through R2 is summed together with the previous offset voltages to arrive at a final output offset voltage. The offset voltage can also be referred to the input (RTI) by dividing the calculated output offset voltage by the noise gain.

As seen in Figure 70 if I_{B+} and I_{B-} are the same and R3 equals the parallel combination of R1 and R2, then the RTI offset voltage can be reduced to only V_{OS}. This is a common method used to reduce output offset voltage. Keeping resistances low helps to minimize offset error voltage and keeps the voltage noise low.

$\overline{\text{DISABLE}}$ PIN AND INPUT BIAS CANCELLATION

The AD8099 $\overline{\text{DISABLE}}$ pin performs three functions; enable, disable, and reduction of the input bias current. When the $\overline{\text{DISABLE}}$ pin is brought to within 0.7 V of the positive supply, the input bias current is reduced by an approximate factor of 60. However, the input current noise doubles to 5.2 pA/$\sqrt{\text{Hz}}$. Table 5 outlines the $\overline{\text{DISABLE}}$ pin functionality.

Table 5. $\overline{\text{DISABLE}}$ Pin Truth Table

Supply Voltage	±5 V	+5 V
Disable	–5 to +2.4	0 to 2.4
Enable	Open	Open
Low Input Bias Current	4.3 to 5	4.3 to 5

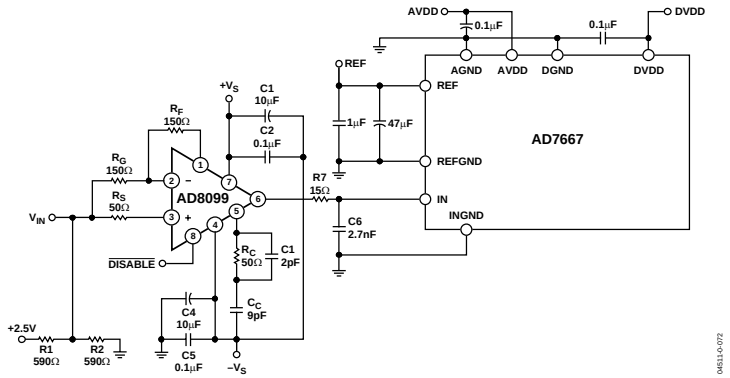

Figure 71. ADC Driver

16-BIT ADC DRIVER

Ultralow noise and distortion performance make the AD8099 an ideal ADC driver. Even though the AD8099 is not unity gain stable, it can be configured to produce a net gain of +1 amplifier, as shown in Figure 71. This is achieved by combining a gain of +2 and a gain of –1 for a net gain of +1. The input range of the ADC is 0 V to 2.5 V.

Table 6 shows the performance data of the AD8099 and the Analog Devices AD7667 a 1 MSPS 16-bit ADC.

Table 6. ADC Driver Performance, f_C = 20 kHz, V_{OUT} = 2.24 V p-p

Parameter	Measurement (dB)
Second Harmonic Distortion	–111.4
Third Harmonic Distortion	–103.2
THD	–101.4
SFDR	102.2
SNR	88.1

CIRCUIT CONSIDERATIONS

Optimizing the performance of the AD8099 requires attention to detail in layout and signal routing of the board. Power supply bypassing, parasitic capacitance, and component selection all contribute to the overall performance of the amplifier. The AD8099 features an exposed paddle on the backs of both the CSP and SOIC packages. The exposed paddle provides a low thermal **resistive** path to the ground plane. For best performance, solder the exposed paddle to the ground plane.

PCB Layout

The compensation network is determined by the amplifier gain requirements. For lower gains, the layout and component placement are more critical. For higher gains, there are fewer compensation components, which results in a less complex layout. With diligent consideration to layout, grounding, and component placement, the AD8099 evaluation boards have been optimized for peak performance. These are the same evaluation boards that are available to customers; see Table 7 for ordering information. The noninverting evaluation board artwork for SOIC and CSP layouts are shown in Figure 72 and Figure 73. Incorporating the layout information shown in Figure 72 and Figure 73 into new designs is highly recommended and helps to ensure optimal circuit performance. The concepts of layout, grounding, and component placement, llustrated in Figure 72 and Figure 73,also apply to inverting configurations. For scale, the boards are 2" × 2".

Parasitics

The area surrounding the compensation pin is very sensitive to parasitic capacitance. To realize the full gain bandwidth product of the AD8099, there should be no trace connected to or within close proximity of the external compensation pin for the lowest possible capacitance. When compensation is required, the traces to the compensation pin, the negative supply, and the interconnect between components (i.e. C_C, C1, and R_C in Figure 59) should be made as wide as possible to minimize inductance.

All ground and power planes under the pins of the AD8099 should be cleared of copper to prevent parasitic capacitance between the input and output pins to ground. A single mounting pad on a SOIC footprint can add as much as 0.2 pF of capacitance to ground as a result of not clearing the ground or power plane under the AD8099 pins. Parasitic capacitance can cause peaking and instability, and should be minimized to ensure proper operation.

The new pinout of the AD8099 reduces the distance between the output and the inverting input of the amplifier. This helps to minimize the parasitic inductance and capacitance of the feedback path, which, in turn, reduces ringing and second harmonic distortion.

Grounding

When possible, ground and power planes should be used. Ground and power planes reduce the resistance and inductance of the power supply feeds and ground returns. If multiple planes are used, they should be "stitched" together with multiple vias. The returns for the input, output terminations, bypass capacitors, and R_G should all be kept as close to the AD8099 as possible. Ground vias should be placed at the very end of the component mounting pad to provide a solid ground return. The output load ground and the bypass capacitor grounds should be returned to a common point on the ground plane to minimize parasitic inductance and improve distortion performance. The AD8099 packages feature an exposed paddle. For optimum performance, solder this paddle to ground. For more information on PCB layout and design considerations, refer to section 7-2 of the 2002 Analog Devices Op Amp Applications book.

Power Supply Bypassing

The AD8099 power supply bypassing has been optimized for each gain configuration as shown in Figure 60 through Figure 66 in the Circuit Configurations section. The values shown should be used when possible. Bypassing is critical for stability, frequency response, distortion, and PSRR performance. The 0.1 µF capacitors shown in Figure 60 through Figure 66 should be as close to the supply pins of the AD8099 as possible and the electrolytic capacitors beside them.

Component Selection

Smaller components less than 1206 SMT case size, offer smaller mounting pads, which have less parasitics and allow for a more compact layout. It is critical for optimum performance that high quality, tight tolerance (where critical), and low drift components be used. For example, tight tolerance and low drift is critical in the selection of the feedback capacitor used in Figure 60. The feedback compensation capacitor in Figure 60 is 1.5pF. This capacitor should be specified with NPO material. NPO material typically has a ±30 ppm/°C change over –55°C to +125°C temperature range. For a 100°C change, this would result in a 4.5 fF change in capacitance, compared to an X7R material, which would result in a 0.23 pF change, a 15% change from the nominal value. This could introduce excessive peaking, as shown in Figure 68, C_F vs. Frequency Response.

DESIGN TOOLS AND TECHNICAL SUPPORT

Analog Devices is committed to the design process by providing technical support and online design tools. ADI offers technical support via free evaluation boards, sample ICs, SPICE models, interactive evaluation tools, application notes, phone and email support—all available at www.analog.com.

A.3 Datasheet: Operational Amplifier LT6205/LT6206/LT6207

The datasheet of the operational amplifier LT6205/LT6206/LT6207 was downloaded from http://www.linear.com/product/LT6205, accessed 30 August 2012.

LINEAR TECHNOLOGY

LT6205/LT6206/LT6207

Single/Dual/Quad Single Supply 3V, 100MHz Video Op Amps

FEATURES

- **450V/µs Slew Rate**
- **100MHz Gain Bandwidth Product**
- **Wide Supply Range 2.7V to 12.6V**
- **Output Swings Rail-to-Rail**
- **Input Common Mode Range Includes Ground**
- High Output Drive: 50mA
- Channel Separation: 90dB at 10MHz
- Specified on 3V, 5V and ±5V Supplies
- Input Offset Voltage: 1mV
- Low Power Dissipation: 20mW per Amplifier on Single 5V
- Operating Temperature Range: –40°C to 125°C
- Low Profile (1mm) SOT-23 (ThinSOT™) Package

APPLICATIONS

- Video Line Driver
- Automotive Displays
- RGB Amplifiers
- Coaxial Cable Drivers
- Low Voltage High Speed Signal Processing

DESCRIPTION

The LT®6205/LT6206/LT6207 are low cost single/dual/quad voltage feedback amplifiers that feature 100MHz gain-bandwidth product, 450V/µs slew rate and 50mA output current. These amplifiers have an input range that includes ground and an output that swings within 60mV of either supply rail, making them well suited for single supply operation.

These amplifiers maintain their performance for supplies from 2.7V to 12.6V and are specified at 3V, 5V and ±5V. The inputs can be driven beyond the supplies without damage or phase reversal of the output. Isolation between channels is high, over 90dB at 10MHz.

The LT6205 is available in the 5-pin SOT-23, and the LT6206 is available in an 8-lead MSOP package with standard op amp pinouts. For compact layouts the quad LT6207 is available in the 16-pin SSOP package. These devices are specified over the commercial, industrial and automotive temperature ranges.

LT, LTC, LTM, Linear Technology and the Linear logo are registered trademarks and ThinSOT is a trademark of Linear Technology Corporation. All other trademarks are the property of their respective owners.

TYPICAL APPLICATION

Baseband Video Splitter/Cable Driver

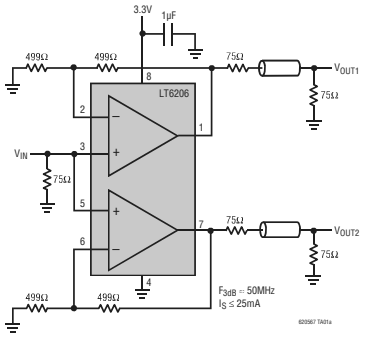

Output Step Response

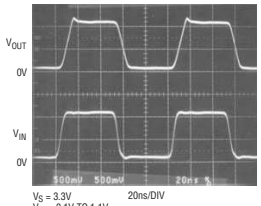

ABSOLUTE MAXIMUM RATINGS (Note 1)

Total Supply Voltage (V^+ to V^-) 12.6V
Input Current ..... ±10mA
Input Voltage Range (Note 2) ..... $\pm V_S$
Output Short-Circuit Duration (Note 3) ..... Indefinite
Pin Current While Exceeding Supplies (Note 9) ... ±25mA
Operating Temperature Range (Note 4)
LT6205C/LT6206C/LT6207C,
LT6205I/LT6206I/LT6207I ..... –40°C to 85°C
LT6205H ..... –40°C to 125°C
Specified Temperature Range (Note 4)
LT6205C/LT6206C/LT6207C ..... 0°C to 70°C
LT6205I/LT6206I/LT6207I ..... –40°C to 85°C
LT6205H ..... –40°C to 125°C
Storage Temperature Range ..... –65°C to 150°C
Maximum Junction Temperature ..... 150°C
Lead Temperature (Soldering, 10 sec) ..... 300°C

PIN CONFIGURATION

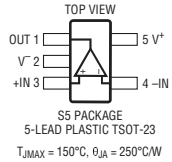

S5 PACKAGE
5-LEAD PLASTIC TSOT-23
T_{JMAX} = 150°C, θ_{JA} = 250°C/W

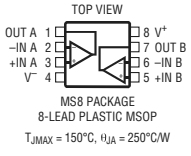

MS8 PACKAGE
8-LEAD PLASTIC MSOP
T_{JMAX} = 150°C, θ_{JA} = 250°C/W

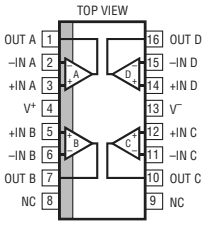

GN PACKAGE
16-LEAD NARROW PLASTIC SSOP
T_{JMAX} = 150°C, θ_{JA} = 135°C/W

ORDER INFORMATION

LEAD FREE FINISH	TAPE AND REEL	PART MARKING*	PACKAGE DESCRIPTION	SPECIFIED TEMPERATURE RANGE
LT6205CS5#PBF	LT6205CS5#TRPBF	LTAEM	5-Lead Plastic TSOT-23	0°C to 70°C
LT6205IS5#PBF	LT6205IS5#TRPBF	LTAEM	5-Lead Plastic TSOT-23	–40°C to 85°C
LT6205HS5#PBF	LT6205HS5#TRPBF	LTAEM	5-Lead Plastic TSOT-23	–40°C to 125°C
LT6206CMS8#PBF	LT6206CMS8#TRPBF	LTH3	8-Lead Plastic MSOP	0°C to 70°C
LT6206IMS8#PBF	LT6206IMS8#TRPBF	LTH4	8-Lead Plastic MSOP	–40°C to 85°C
LT6207CGN#PBF	LT6207CGN#TRPBF	6207	16-Lead Narrow Plastic SSOP	0°C to 70°C
LT6207IGN#PBF	LT6207IGN#TRPBF	6207I	16-Lead Narrow Plastic SSOP	–40°C to 85°C

Consult LTC Marketing for parts specified with wider operating temperature ranges. *The temperature grade is identified by a label on the shipping container.
Consult LTC Marketing for information on non-standard lead based finish parts.

For more information on lead free part marking, go to: http://www.linear.com/leadfree/
For more information on tape and reel specifications, go to: http://www.linear.com/tapeandreel/

ELECTRICAL CHARACTERISTICS

The ● denotes specifications which apply over the specified temperature range, otherwise specifications are at T_A = 25°C. V_S = 3V, 0V; V_S = 5V, 0V; V_{CM} = V_{OUT} = 1V, unless otherwise noted.

SYMBOL	PARAMETER	CONDITIONS		LT6205C/LT6206C/LT6207C LT6205I/LT6206I/LT6207I MIN	TYP	MAX	UNITS
V_{OS}	Input Offset Voltage				1	3.5	mV
			●			5	mV
	Input Offset Voltage Match (Channel-to-Channel) (Note 5)				1	3	mV
			●			4	mV
	Input Offset Voltage Drift (Note 6)		●		7	15	µV/°C
I_B	Input Bias Current		●		10	30	µA
I_{OS}	Input Offset Current		●		0.6	3	µA
	Input Noise Voltage	0.1Hz to 10Hz			2		μV_{P-P}
e_n	Input Noise Voltage Density	f = 10kHz			9		$nV/\sqrt{Hz}$
i_n	Input Noise Current Density	f = 10kHz			4		$pA/\sqrt{Hz}$
	Input Resistance	V_{CM} = 0V to V^+ – 2V			1		MΩ
	Input Capacitance				2		pF
CMRR	Common Mode Rejection Ratio	V_{CM} = 0V to V^+ – 2V	●	78	90		dB
	Input Voltage Range		●	0		V^+ – 2	V
PSRR	Power Supply Rejection Ratio	V_S = 3V to 12V V_{CM} = V_{OUT} = 0.5V	●	67	75		dB
	Minimum Supply Voltage	V_{CM} = 0.5V	●			2.7	V
A_{VOL}	Large-Signal Voltage Gain	V_S = 5V, V_O = 0.5V to 4.5V, R_L = 1k	●	30	100		V/mV
		V_S = 5V, V_O = 1V to 3V, R_L = 150Ω	●	5	20		V/mV
		V_S = 3V, V_O = 0.5V to 2.5V, R_L = 1k	●	20	60		V/mV
V_{OL}	Output Voltage Swing Low (Note 7)	No Load, Input Overdrive = 30mV	●		10	25	mV
		I_{SINK} = 5mA	●		75	150	mV
		V_S = 5V, I_{SINK} = 25mA	●		300	500	mV
		V_S = 3V, I_{SINK} = 15mA	●		200	350	mV
V_{OH}	Output Voltage Swing High (Note 7)	No Load, Input Overdrive = 30mV	●		60	100	mV
		I_{SOURCE} = 5mA	●		150	250	mV
		V_S = 5V, I_{SOURCE} = 25mA	●		650	1200	mV
		V_S = 3V, I_{SOURCE} = 15mA	●		300	500	mV
I_{SC}	Short-Circuit Current	V_S = 5V, Output Shorted to GND		35	60		mA
			●	20			mA
		V_S = 3V, Output Shorted to GND		30	50		mA
			●	20			mA
I_S	Supply Current per Amplifier				3.75	5	mA
			●			5.75	mA
GBW	Gain Bandwidth Product	f = 2MHz	●	65	100		MHz
SR	Slew Rate	V_S = 5V, A_V = 2, R_F = R_G = 1k V_O = 1V to 4V, Measured from 1.5V to 3.5V			450		V/µs
	Channel Separation	f = 10MHz			90		dB
FPBW	Full Power Bandwidth	V_{OUT} = $2V_{P-P}$ (Note 8)			71		MHz
t_s	Settling Time to 3% Settling Time to 1%	V_S = 5V, ΔV_{OUT} = 2V, A_V = –1, R_L = 150Ω			15 25		ns ns
	Differential Gain Differential Phase	V_S = 5V, A_V = 2, R_L = 150Ω, Output Black Level = 1V V_S = 5V, A_V = 2, R_L = 150Ω, Output Black Level = 1V			0.05 0.08		% Deg

ELECTRICAL CHARACTERISTICS

The ● denotes specifications which apply over the specified temperature range, otherwise specifications are at T_A = 25°C. V_S = ±5V; V_{CM} = V_{OUT} = 0V, unless otherwise noted.

SYMBOL	PARAMETER	CONDITIONS		LT6205C/LT6206C/LT6207C LT6205I/LT6206I/LT6207I MIN	TYP	MAX	UNITS
V_{OS}	Input Offset Voltage		 ●		1	4.5 6	mV mV
	Input Offset Voltage Match (Channel-to-Channel) (Note 5)		 ●		1	3 4	mV mV
	Input Offset Voltage Drift (Note 6)		●		10	18	µV/°C
I_B	Input Bias Current		●		18	30	µA
I_{OS}	Input Offset Current		●		0.6	3	µA
	Input Noise Voltage	0.1Hz to 10Hz			2		μV_{P-P}
e_n	Input Noise Voltage Density	f = 10kHz			9		$nV/\sqrt{Hz}$
i_n	Input Noise Current Density	f = 10kHz			4		$pA/\sqrt{Hz}$
	Input Resistance	V_{CM} = –5V to 3V			1		MΩ
	Input Capacitance				2		pF
CMRR	Common Mode Rejection Ratio	V_{CM} = –5V to 3V	●	78	90		dB
	Input Voltage Range		●	–5		3	V
PSRR	Power Supply Rejection Ratio	V_S = ±2V to ±6V	●	67	75		dB
A_{VOL}	Large-Signal Voltage Gain	V_O = –4V to 4V, R_L = 1k	●	50	133		V/mV
		V_O = –3V to 3V, R_L = 150Ω	●	7.5	20		V/mV
	Output Voltage Swing	No Load, Input Overdrive = 30mV I_{OUT} = ±5mA I_{OUT} = ±25mA	● ● ●	±4.88 ±4.75 ±3.8	±4.92 ±4.85 ±4.35		V V V
I_{SC}	Short-Circuit Current	Short to Ground	 ●	±40 ±30	±60		mA mA
I_S	Supply Current per Amplifier		 ●		4	5.6 6.5	mA mA
GBW	Gain Bandwidth Product	f = 2MHz	●	65	100		MHz
SR	Slew Rate	A_V = –1, R_L = 1k V_O = –4V to 4V, Measured from –3V to 3V		350	600		V/µs
	Channel Separation	f = 10MHz			90		dB
FPBW	Full Power Bandwidth	V_{OUT} = $8V_{P-P}$ (Note 8)		14	24		MHz
t_s	Settling Time to 3% Settling Time to 1%	ΔV_{OUT} = 2V, A_V = –1, R_L = 150Ω			15 25		ns ns
	Differential Gain Differential Phase	A_V = 2, R_L = 150Ω, Output Black Level = 1V A_V = 2, R_L = 150Ω, Output Black Level = 1V			0.05 0.08		% Deg

The ● denotes specifications which apply over the full specified temperature range, –40°C ≤ T_A ≤ 125°C, otherwise specifications are at T_A = 25°C. V_S = 3V, 0V; V_S = 5V, 0V; V_{CM} = V_{OUT} = 1V, unless otherwise noted.

SYMBOL	PARAMETER	CONDITIONS		LT6205H MIN	TYP	MAX	UNITS
V_{OS}	Input Offset Voltage		 ●		1	3.5 6	mV mV
	Input Offset Voltage Drift (Note 6)		●			20	µV/°C
I_B	Input Bias Current		●			45	µA

ELECTRICAL CHARACTERISTICS

The ● denotes specifications which apply over the full specified temperature range, –40°C ≤ T_A ≤ 125°C, otherwise specifications are at T_A = 25°C. V_S = 3V, 0V; V_S = 5V, 0V; V_{CM} = V_{OUT} = 1V, unless otherwise noted.

SYMBOL	PARAMETER	CONDITIONS		LT6205H MIN	LT6205H TYP	LT6205H MAX	UNITS
I_{OS}	Input Offset Current		●			5	µA
	Input Noise Voltage	0.1Hz to 10Hz			2		μV_{P-P}
e_n	Input Noise Voltage Density	f = 10kHz			9		$nV/\sqrt{Hz}$
i_n	Input Noise Current Density	f = 10kHz			4		$pA/\sqrt{Hz}$
	Input Resistance	V_{CM} = 0V to V+ – 2V			1		MΩ
	Input Capacitance				2		pF
CMRR	Common Mode Rejection Ratio	V_{CM} = 0V to V+ – 2V	●	72			dB
	Input Voltage Range		●	0		V+ – 2	V
PSRR	Power Supply Rejection Ratio	V_S = 3V to 12V V_{CM} = V_{OUT} = 0.5V	●	62			dB
	Minimum Supply Voltage	V_{CM} = 0.5V	●			2.7	V
A_{VOL}	Large-Signal Voltage Gain	V_S = 5V, V_O = 0.5V to 4.5V, R_L = 1k V_S = 5V, V_O = 1V to 3V, R_L = 150Ω V_S = 3V, V_O = 0.5V to 2.5V, R_L = 1k	● ● ●	25 3.5 15			V/mV V/mV V/mV
V_{OL}	Output Voltage Swing Low (Note 7)	No Load, Input Overdrive = 30mV I_{SINK} = 5mA V_S = 5V, I_{SINK} = 25mA V_S = 3V, I_{SINK} = 15mA	● ● ● ●			40 200 600 400	mV mV mV mV
V_{OH}	Output Voltage Swing High (Note 7)	No Load, Input Overdrive = 30mV I_{SOURCE} = 5mA V_S = 5V, I_{SOURCE} = 25mA V_S = 3V, I_{SOURCE} = 15mA	● ● ● ●			125 300 1400 600	mV mV mV mV
I_{SC}	Short-Circuit Current	V_S = 5V, Output Shorted to GND	 ●	35 20	60		mA mA
		V_S = 3V, Output Shorted to GND	 ●	30 15	50		mA mA
I_S	Supply Current per Amplifier		 ●		3.75	5 6.5	mA mA
GBW	Gain Bandwidth Product	f = 2MHz	●	50			MHz
SR	Slew Rate	V_S = 5V, A_V = 2, R_F = R_G = 1k V_O = 1V to 4V, Measured from 1.5V to 3.5V			450		V/µs
	Channel Separation	f = 10MHz			90		dB
FPBW	Full Power Bandwidth	V_{OUT} = $2V_{P-P}$ (Note 8)			71		MHz
t_s	Settling Time to 3% Settling Time to 1%	V_S = 5V, ΔV_{OUT} = 2V, A_V = –1, R_L = 150Ω			15 25		ns ns
	Differential Gain Differential Phase	V_S = 5V, A_V = 2, R_L = 150Ω, Output Black Level = 1V V_S = 5V, A_V = 2, R_L = 150Ω, Output Black Level = 1V			0.05 0.08		% Deg

The ● denotes specifications which apply over the full specified temperature range, –40°C ≤ T_A ≤ 125°C, otherwise specifications are at T_A = 25°C. V_S = ±5V; V_{CM} = V_{OUT} = 0V, unless otherwise noted.

SYMBOL	PARAMETER	CONDITIONS		LT6205H MIN	LT6205H TYP	LT6205H MAX	UNITS
V_{OS}	Input Offset Voltage		 ●		1.3	4.5 7	mV mV
	Input Offset Voltage Drift (Note 6)		●			25	µV/°C

ELECTRICAL CHARACTERISTICS

The ● denotes specifications which apply over the full specified temperature range, –40°C ≤ T_A ≤ 125°C, otherwise specifications are at T_A = 25°C. V_S = ±5V; V_{CM} = V_{OUT} = 0V, unless otherwise noted.

				LT6205H			
SYMBOL	PARAMETER	CONDITIONS		MIN	TYP	MAX	UNITS
I_B	Input Bias Current		●			50	µA
I_{OS}	Input Offset Current		●			5	µA
	Input Noise Voltage	0.1Hz to 10Hz			2		μV_{P-P}
e_n	Input Noise Voltage Density	f = 10kHz			9		$nV/\sqrt{Hz}$
i_n	Input Noise Current Density	f = 10kHz			4		$pA/\sqrt{Hz}$
	Input Resistance	V_{CM} = –5V to 3V			1		MΩ
	Input Capacitance				2		pF
CMRR	Common Mode Rejection Ratio	V_{CM} = –5V to 3V	●	72			dB
	Input Voltage Range		●	–5		3	V
PSRR	Power Supply Rejection Ratio	V_S = ±2V to ±6V	●	62			dB
A_{VOL}	Large-Signal Voltage Gain	V_O = –4V to 4V, R_L = 1k	●	40			V/mV
		V_O = –3V to 3V, R_L = 150Ω	●	5			V/mV
	Output Voltage Swing	No Load, Input Overdrive = 30mV I_{OUT} = ±5mA I_{OUT} = ±25mA	● ● ●	±4.85 ±4.65 ±3.5			V V V
I_{SC}	Short-Circuit Current	Short to Ground	 ●	±40 ±20	±60		mA mA
I_S	Supply Current per Amplifier		 ●		4	5.6 7.5	mA mA
GBW	Gain Bandwidth Product	f = 2MHz	●	50			MHz
SR	Slew Rate	A_V = –1, R_L = 1k V_O = –4V to 4V, Measured from –3V to 3V		350	600		V/µs
	Channel Separation	f = 10MHz			90		dB
FPBW	Full Power Bandwidth	V_{OUT} = $8V_{P-P}$ (Note 8)		14	24		MHz
t_s	Settling Time to 3% Settling Time to 1%	ΔV_{OUT} = 2V, A_V = –1, R_L = 150Ω			15 25		ns ns
	Differential Gain Differential Phase	A_V = 2, R_L = 150Ω, Output Black Level = 1V A_V = 2, R_L = 150Ω, Output Black Level = 1V			0.05 0.08		% Deg

Note 1: Stresses beyond those listed under Absolute Maximum Ratings may cause permanent damage to the device. Exposure to any Absolute Maximum Rating condition for extended periods may affect device reliability and lifetime.

Note 2: The inputs are protected by back-to-back diodes. If the differential input voltage exceeds 1.4V, the input current should be limited to less than 10mA.

Note 3: A heat sink may be required to keep the junction temperature below absolute maximum. This depends on the power supply voltage and how many amplifiers are shorted.

Note 4: The LT6205C/LT6206C/LT6207C are guaranteed to meet specified performance from 0°C to 70°C and are designed, characterized and expected to meet specified performance from –40°C to 85°C but are not tested or QA sampled at these temperatures. The LT6205I/LT6206I/LT6207I are guaranteed to meet specified performance from –40°C to 85°C. The LT6205H is guaranteed to meet specified performance from –40°C to 125°C.

Note 5: Matching parameters are the difference between the two amplifiers A and D and between B and C of the LT6207; between the two amplifiers of the LT6206.

Note 6: This parameter is not 100% tested.

Note 7: Output voltage swings are measured between the output and power supply rails.

Note 8: Full power bandwidth is calculated from the slew rate measurement: $FPBW = SR/2\pi V_{PEAK}$.

Note 9: There are reverse biased ESD diodes on all inputs and outputs. If these pins are forced beyond either supply, unlimited current will flow through these diodes. If the current is transient in nature and limited to less than 25mA, no damage to the device will occur.

TYPICAL PERFORMANCE CHARACTERISTICS

V_{OS} Distribution

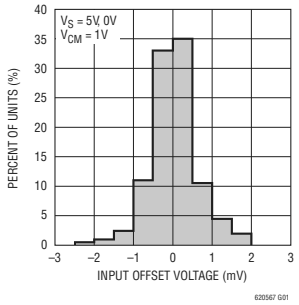

Supply Current per Amplifier vs Supply Voltage

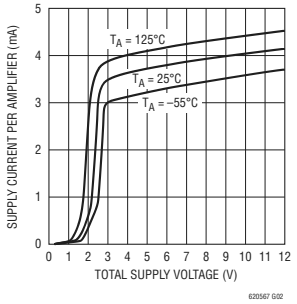

Minimum Supply Voltage

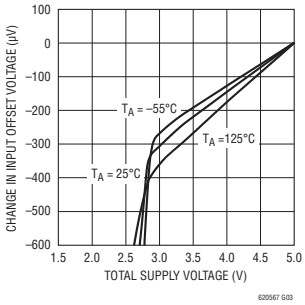

Change in Offset Voltage vs Input Common Mode Voltage

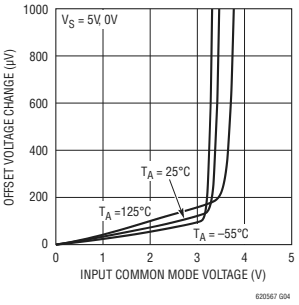

Input Bias Current vs Input Common Mode Voltage

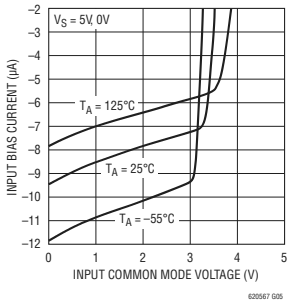

Input Bias Current vs Temperature

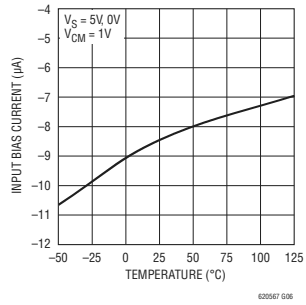

Output Saturation Voltage vs Load Current (Output Low)

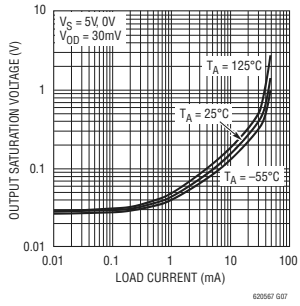

Output Saturation Voltage vs Load Current (Output High)

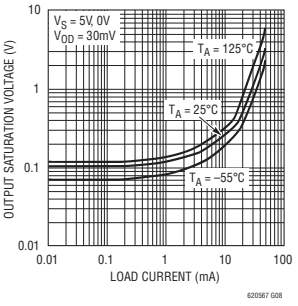

Short-Circuit Current vs Temperature

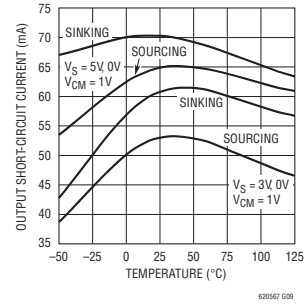

TYPICAL PERFORMANCE CHARACTERISTICS

Short-Circuit Current vs Temperature

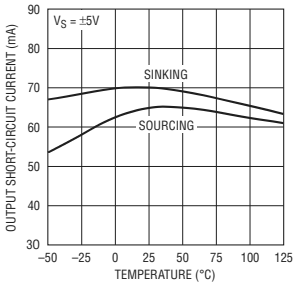

Open-Loop Gain

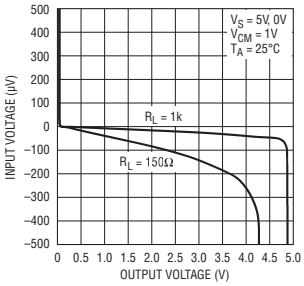

Open-Loop Gain

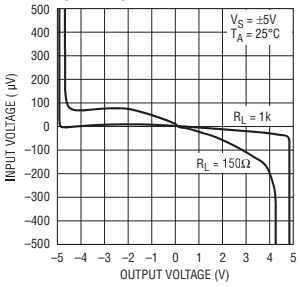

Warm Up Drift vs Time (LT6206)

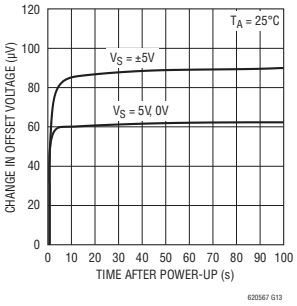

Input Noise Voltage Density vs Frequency

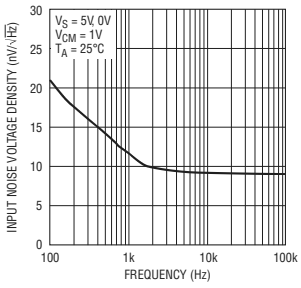

Input Noise Current Density vs Frequency

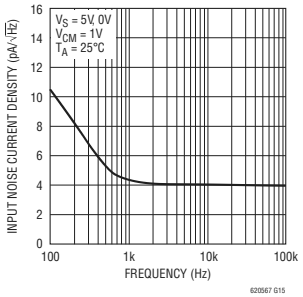

0.1Hz to 10Hz Noise Voltage

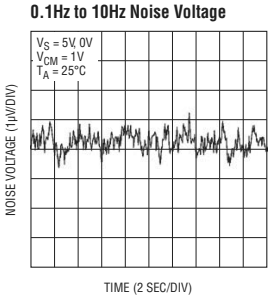

Gain and Phase vs Frequency

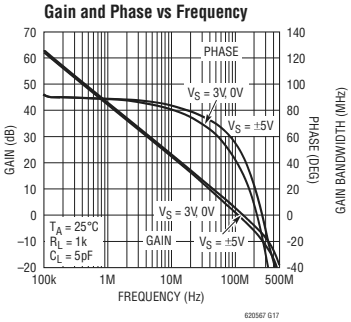

Gain Bandwidth and Phase Margin vs Supply Voltage

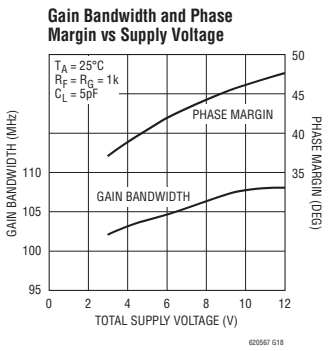

TYPICAL PERFORMANCE CHARACTERISTICS

Gain Bandwidth and Phase Margin vs Temperature

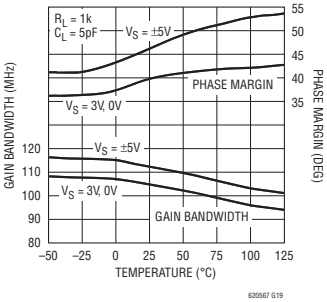

Slew Rate vs Temperature

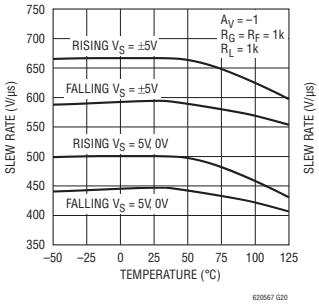

Slew Rate vs Closed-Loop Gain

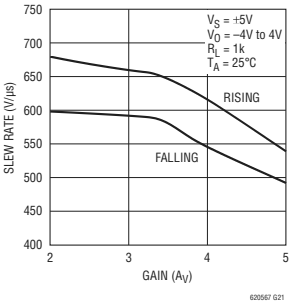

Closed-Loop Gain vs Frequency

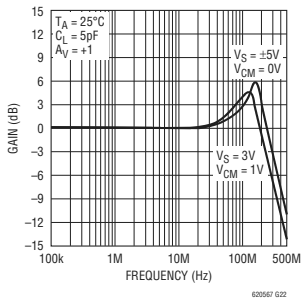

Output Impedance vs Frequency

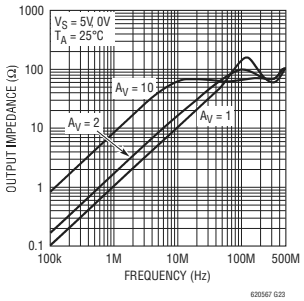

Power Supply Rejection Ratio vs Frequency

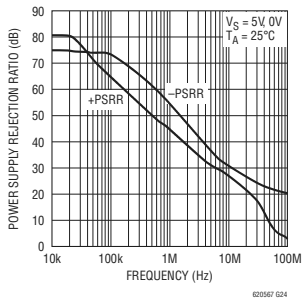

Common Mode Rejection Ratio vs Frequency

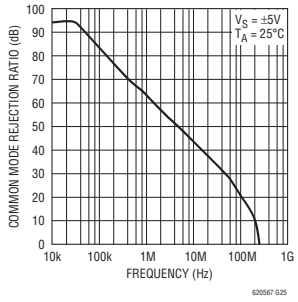

Channel Separation vs Frequency

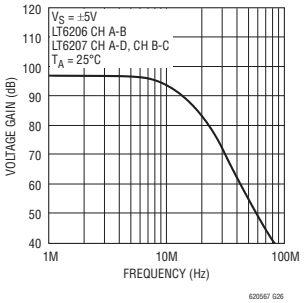

Series Output Resistor vs Capacitive Load

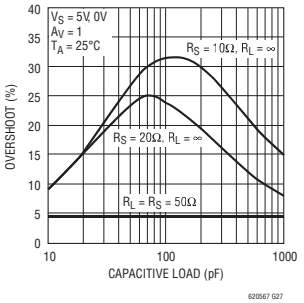

TYPICAL PERFORMANCE CHARACTERISTICS

Series Output Resistor vs Capacitive Load

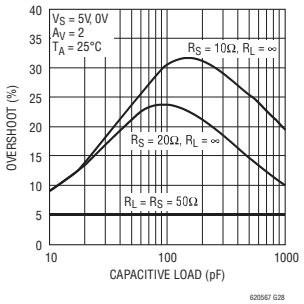

Maximum Undistorted Output Signal vs Frequency

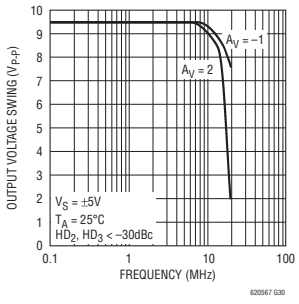

Distortion vs Frequency

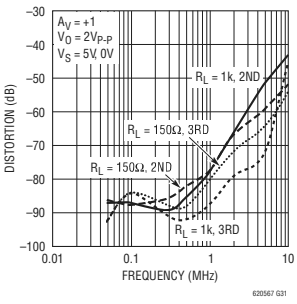

Distortion vs Frequency

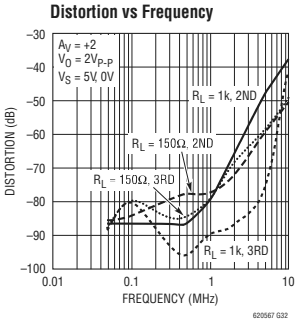

Distortion vs Frequency

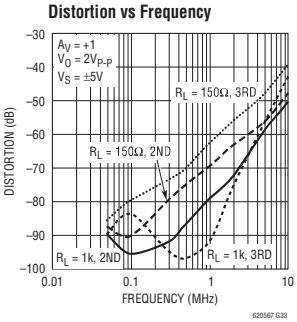

Distortion vs Frequency

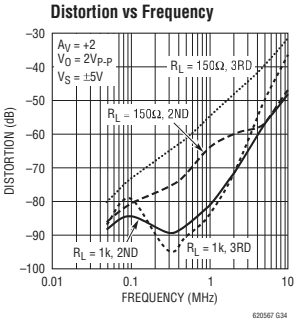

Large Signal Response
V_S = 5V, 0V

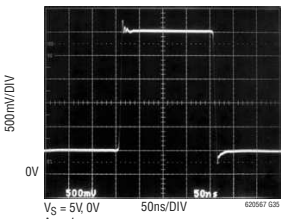

V_S = 5V, 0V
A_V = 1
R_L = 150Ω

Small Signal Response
V_S = 5V, 0V

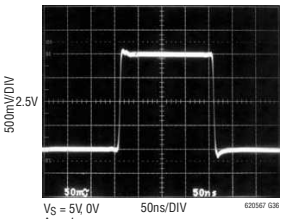

V_S = 5V, 0V
A_V = 1
R_L = 150Ω

TYPICAL PERFORMANCE CHARACTERISTICS

Large Signal Response V_S = ±5V

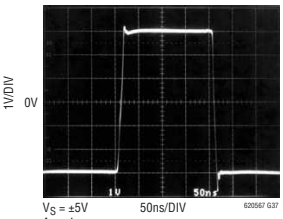

V_S = ±5V
A_V = 1
R_L = 150Ω
50ns/DIV
620567 G37

Small Signal Response V_S = ±5V

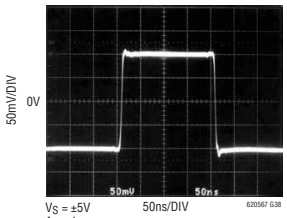

V_S = ±5V
A_V = 1
R_L = 150Ω
50ns/DIV
620567 G38

Output-Overdrive Recovery

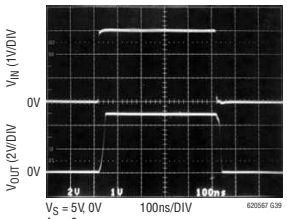

V_S = 5V, 0V
A_V = 2
100ns/DIV
620567 G39

APPLICATIONS INFORMATION

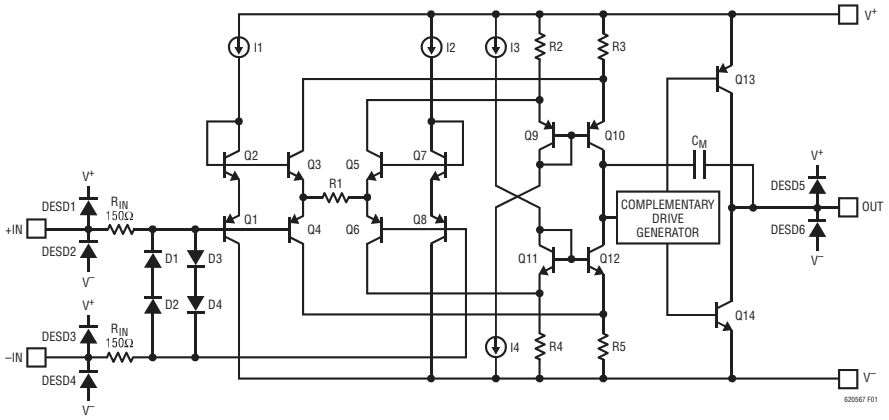

Figure 1. Simplified Schematic

APPLICATIONS INFORMATION

Amplifier Characteristics

Figure 1 shows a simplified schematic of the LT6205/LT6206/LT6207. The input stage consists of transistors Q1 to Q8 and resistor R1. This topology allows for high slew rates at low supply voltages. The input common mode range extends from ground to typically 1.75V from V_{CC}, and is limited by 2 VBEs plus a saturation voltage of a current source. There are back-to-back series diodes, D1 to D4, across the + and – inputs of each amplifier to limit the differential voltage to ±1.4V. R_{IN} limits the current through these diodes if the input differential voltage exceeds ±1.4V. The input stage drives the degeneration resistors of PNP and NPN current mirrors, Q9 to Q12, which convert the differential signals into a single-ended output. The complementary drive generator supplies current to the output transistors that swing from rail-to-rail.

The current generated through R1, divided by the capacitor CM, determines the slew rate. Note that this current, and hence the slew rate, are proportional to the magnitude of the input step. The input step equals the output step divided by the closed loop gain. The highest slew rates are therefore obtained in the lowest gain configurations. The Typical Performance Characteristics curve of Slew Rate vs Closed-Loop Gain shows the details.

ESD

The LT6205/LT6206/LT6207 have reverse-biased ESD protection diodes on all inputs and outputs as shown in Figure 1. If these pins are forced beyond either supply unlimited current will flow through these diodes. If the current is transient, and limited to 25mA or less, no damage to the device will occur.

Layout and Passive Components

With a gain bandwidth product of 100MHz and a slew rate of 450V/µs the LT6205/LT6206/LT6207 require special attention to board layout and supply bypassing. Use a ground plane, short lead lengths and RF quality low ESR supply bypass capacitors. The positive supply pin should be bypassed with a small capacitor (typically 0.01µF to 0.1µF) within 0.25 inches of the pin. When driving heavy loads, an additional 4.7µF electrolytic capacitor should be used. When using split supplies, the same is true for the negative supply pin. For optimum performance all feedback components and bypass capacitors should be contained in a 0.5 inch by 0.5 inch area. This helps ensure minimal stray capacitances.

The parallel combination of the feedback resistor and gain setting resistor on the inverting input can combine with the input capacitance to form a pole which can degrade stability. In general, use feedback resistors of 1k or less.

Capacitive Load

The LT6205/LT6206/LT6207 are optimized for wide bandwidth video applications. They can drive a capacitive load of 20pF in a unity-gain configuration. When driving a larger capacitive load, a resistor of 10Ω to 50Ω should be connected between the output and the capacitive load to avoid ringing or oscillation. The feedback should still be taken from the output pin so that the resistor will isolate the capacitive load and ensure stability. The Typical Performance Characteristics curves show the output overshoot when driving a capacitive load with different series resistors.

Video Signal Characteristics

Composite video is the most commonly used signal in broadcast grade products and includes luma (or luminance, the intensity information), chroma (the colorimetry information) and sync (vertical and horizontal raster timing) elements combined into a single signal, NTSC and PAL being the common formats. Component video for entertainment systems include separate signal(s) for the luma and chroma (i.e., Y/C or YPbPr) with sync generally applied to the luma channel (Y signal). In some instances, native RGB signals (separate intensity information for each primary color: red, green, blue) will have sync included as well. All the signal types that include sync are electrically similar from a voltage-swing standpoint, though various timing and bandwidth relationships exist depending on the applicable standard.

The typical video waveforms that include sync (including full composite) are specified to have nominal $1V_{P-P}$ amplitude. The lower 0.3V is reserved for sync tips that carry timing information, and by being at a lower potential than all the other information, represents blacker-than-

APPLICATIONS INFORMATION

black intensity, thereby causing scan retrace activity to be invisible on a CRT. The black level of the waveform is at (or set up very slightly above) the upper limit of the sync information. Waveform content above the black level is intensity information, with peak brightness represented at the maximum signal level. In the case of composite video, the modulated color subcarrier is superimposed on the waveform, but the dynamics remain inside the $1V_{P-P}$ limit (a notable exception is the chroma ramp used for differential-gain and differential-phase measurements, which can reach $1.15V_{P-P}$).

DC-Coupled Video Amplifier Considerations

Typically video amplifiers drive cables that are series terminated (back-terminated) at the source and load-terminated at the destination with resistances equal to the cable characteristic impedance, Z_0 (usually 75Ω). This configuration forms a 2:1 resistor divider in the cabling that must be accounted for in the driver amplifier by delivering $2V_{P-P}$ output into an effective $2 \bullet Z_0$ load (e.g., 150Ω). Driving the cable can require more than 13mA while the output is approaching the saturation limits of the amplifier output. The absolute minimum supply is: $V_{MIN} = 2 + V_{OH} + V_{OL}$. For example, the LT6206 dual operating on 3.3V as shown on the front page of this data sheet, with exceptionally low $V_{OH} \leq 0.5V$ and $V_{OL} \leq 0.35V$, provides a design margin of 0.45V. The design margin must be large enough to include supply variations and DC bias accuracy for the DC-coupled video input.

Handling AC-Coupled Video Signals

AC-coupled video inputs are intrinsically more difficult to handle than those with DC-coupling because the average signal voltage of the video waveform is effected by the picture content, meaning that the black level at the amplifier wanders with scene brightness. The wander is measured as 0.56V for a $1V_{P-P}$ NTSC waveform changing from black field to white field and vice-versa, so an additional 1.12V allowance must be made in the amplifier supply (assuming gain of 2, so $V_{MIN} = 3.12 + V_{OH} + V_{OL}$). For example, an LT6205 operating on 5V has a conservative design margin of 1.03V. The amplifier output (for gain of 2) must swing +1.47V to –1.65V around the DC-operating point, so the biasing circuitry needs to be designed accordingly for optimal fidelity.

Clamped AC-Input Cable Driver

A popular method of further minimizing supply requirements with AC-coupling is to employ a simple clamping scheme, as shown in Figure 2. In this circuit, the LT6205 operates from 3.3V by having the sync tips control the charge on the coupling capacitor C1, thereby reducing the black level input wander to ≈ 0.07V. The only minor drawback to this circuit is the slight sync tip compression (≈ 0.025V at input) due to the diode conduction current, though the picture content remains full fidelity. This circuit has nearly the design margin of its DC-coupled counterpart, at 0.31V (for this circuit, $V_{MIN} = 2.14 + V_{OH} + V_{OL}$). The clamp diode anode bias is selected to set the sync tip output voltage at or slightly above V_{OL}.

YPbPr to RGB Component Video Converter

The back page application uses the LT6207 quad to implement a minimum amplifier count topology to transcode consumer component video into RGB. In this circuit, signals only pass through one active stage from any input to any output, with passive additions being performed by the cable back-termination resistors. The compromise in using passive output addition is that the amplifier outputs must be twice as large as that of a conventional cable driver. The Y-channel section also has the demanding requirement that it single-handedly drives all three outputs to full brightness during times of white content, so a helper current source is used to assure unclipped video when operating from ±5V supplies. This circuit maps sync-on-Y to sync on all the RGB channels, and for best results should have input black levels at 0V nominal to prevent clipping.

TYPICAL APPLICATION

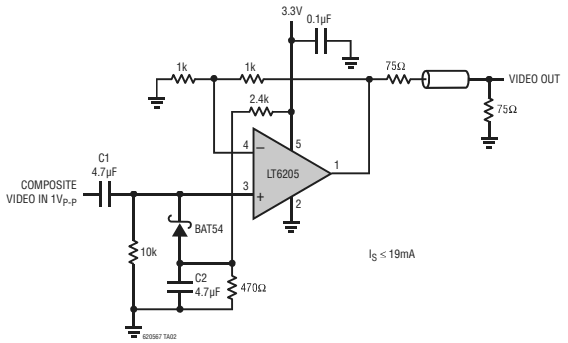

Figure 2. Clamped AC-Input Video Cable Driver

PACKAGE DESCRIPTION

S5 Package
5-Lead Plastic TSOT-23
(Reference LTC DWG # 05-08-1635)

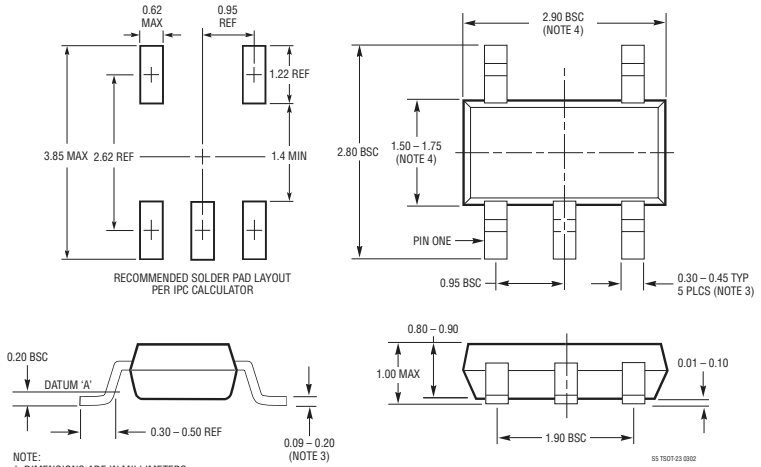

NOTE:
1. DIMENSIONS ARE IN MILLIMETERS
2. DRAWING NOT TO SCALE
3. DIMENSIONS ARE INCLUSIVE OF PLATING
4. DIMENSIONS ARE EXCLUSIVE OF MOLD FLASH AND METAL BURR
5. MOLD FLASH SHALL NOT EXCEED 0.254mm
6. JEDEC PACKAGE REFERENCE IS MO-193

PACKAGE DESCRIPTION

MS8 Package
8-Lead Plastic MSOP
(Reference LTC DWG # 05-08-1660)

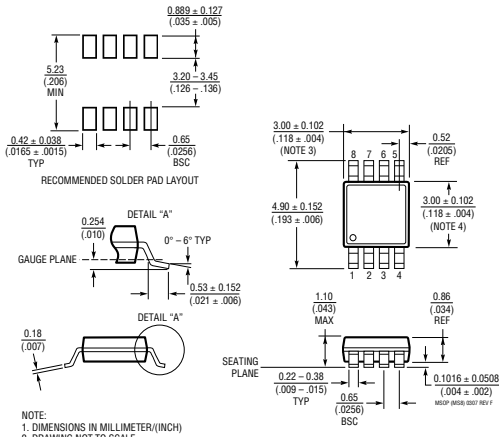

NOTE:
1. DIMENSIONS IN MILLIMETER/(INCH)
2. DRAWING NOT TO SCALE
3. DIMENSION DOES NOT INCLUDE MOLD FLASH, PROTRUSIONS OR GATE BURRS.
   MOLD FLASH, PROTRUSIONS OR GATE BURRS SHALL NOT EXCEED 0.152mm (.006") PER SIDE
4. DIMENSION DOES NOT INCLUDE INTERLEAD FLASH OR PROTRUSIONS.
   INTERLEAD FLASH OR PROTRUSIONS SHALL NOT EXCEED 0.152mm (.006") PER SIDE
5. LEAD COPLANARITY (BOTTOM OF LEADS AFTER FORMING) SHALL BE 0.102mm (.004") MAX

GN Package
16-Lead Plastic SSOP (Narrow .150 Inch)
(Reference LTC DWG # 05-08-1641)

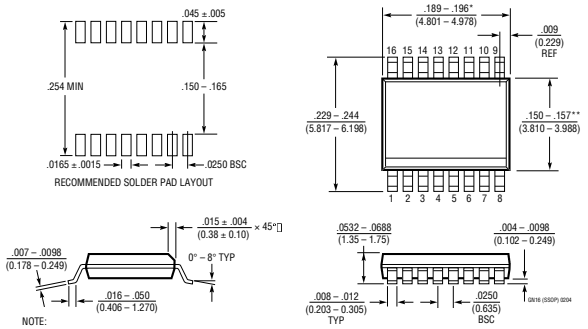

NOTE:
1. CONTROLLING DIMENSION: INCHES
2. DIMENSIONS ARE IN $\frac{\text{INCHES}}{(\text{MILLIMETERS})}$
3. DRAWING NOT TO SCALE
*DIMENSION DOES NOT INCLUDE MOLD FLASH. MOLD FLASH SHALL NOT EXCEED 0.006" (0.152mm) PER SIDE
**DIMENSION DOES NOT INCLUDE INTERLEAD FLASH. INTERLEAD FLASH SHALL NOT EXCEED 0.010" (0.254mm) PER SIDE

REVISION HISTORY (Revision history begins at Rev C)

REV	DATE	DESCRIPTION	PAGE NUMBER
C	3/10	C Grade Specified Temperature Range Changed in the Order Information Section	2

LINEAR TECHNOLOGY

Information furnished by Linear Technology Corporation is believed to be accurate and reliable. However, no responsibility is assumed for its use. Linear Technology Corporation makes no representation that the interconnection of its circuits as described herein will not infringe on existing patent rights.

TYPICAL APPLICATION

YP_BP_R to RGB Converter

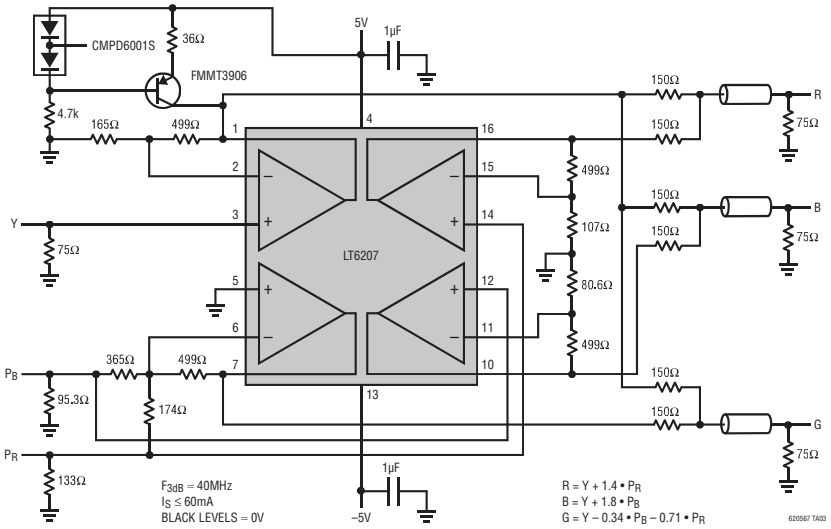

RELATED PARTS

PART NUMBER	DESCRIPTION	COMMENTS
LT1253/LT1254	Low Cost Dual and Quad Video Amplifiers	–3dB Bandwidth = 90MHz, Current Feedback
LT1395/LT1396/LT1397	Single Dual Quad 400MHz Current Feedback Amplifiers	0.1dB Flatness to 100MHz, 80mA Output Drive
LT1675	RGB Multiplexer with Current Feedback Amplifiers	–3dB Bandwidth = 250MHz, 100MHz Pixel Switching
LT1809/LT1810	Single/Dual, 180MHz, Rail-to-Rail Input and Output Amplifiers	350V/µs Slew Rate, Shutdown, Low Distortion –90dBc at 5MHz
LT6550/LT6551	3.3V Triple and Quad Video Amplifiers	Internal Gain of 2, 110MHz –3dB Bandwidth, Input Common Modes to Ground
LT6552	3.3V Single Supply Video Difference Amplifier	Differential or Single-Ended Gain Block, 600V/µs Slew Rate, Input Common Modes to Ground

Linear Technology Corporation
1630 McCarthy Blvd., Milpitas, CA 95035-7417
(408) 432-1900 • FAX: (408) 434-0507 • www.linear.com

LT 0310 REV C • PRINTED IN USA

© LINEAR TECHNOLOGY CORPORATION 2003

A.4 Datasheet: Bipolar Power Transistor MJE18008

The datasheet of the bipolar power transistor MJE18008 was downloaded from http://www.onsemi.com/PowerSolutions/product.do?id=MJE18008, accessed 30 August 2012.

MJE18008, MJF18008

Preferred Device

SWITCHMODE™
NPN Bipolar Power Transistor For Switching Power Supply Applications

The MJE/MJF18008 have an applications specific state−of−the−art die designed for use in 220 V line−operated SWITCHMODE Power supplies and electronic light ballasts.

Features

- Improved Efficiency Due to Low Base Drive Requirements:
  - High and Flat DC Current Gain h_{FE}
  - Fast Switching
  - No Coil Required in Base Circuit for Turn−Off (No Current Tail)
- Tight Parametric Distributions are Consistent Lot−to−Lot
- Two Package Choices: Standard TO−220 or Isolated TO−220
- MJF18008, Case 221D, is UL Recognized at 3500 V_{RMS}: File #E69369
- Pb−Free Packages are Available*

MAXIMUM RATINGS

Rating	Symbol	Value	Unit
Collector−Emitter Sustaining Voltage	V_{CEO}	450	Vdc
Collector−Base Breakdown Voltage	V_{CES}	1000	Vdc
Emitter−Base Voltage	V_{EBO}	9.0	Vdc
Collector Current − Continuous − Peak (Note 1)	I_C I_{CM}	8.0 16	Adc
Base Current − Continuous − Peak (Note 1)	I_B I_{BM}	4.0 8.0	Adc
RMS Isolation Voltage (Note 2) Test No. 1 Per Figure 22a Test No. 1 Per Figure 22b Test No. 1 Per Figure 22c (for 1 sec, R.H. < 30%, T_A = 25°C)	V_{ISOL}	**MJF18008** 4500 3500 1500	V
Total Device Dissipation @ T_C = 25°C MJE18008 MJF18008 Derate above 25°C MJE18008 MJF18008	P_D	 125 45 1.0 0.36	W W/°C
Operating and Storage Temperature	T_J, T_{stg}	−65 to 150	°C

THERMAL CHARACTERISTICS

Characteristics	Symbol	Max	Unit
Thermal Resistance, Junction−to−Case MJE18008 MJF18008	$R_{\theta JC}$	 1.0 2.78	°C/W
Thermal Resistance, Junction−to−Ambient	$R_{\theta JA}$	62.5	°C/W
Maximum Lead Temperature for Soldering Purposes 1/8″ from Case for 5 Seconds	T_L	260	°C

Maximum ratings are those values beyond which device damage can occur. Maximum ratings applied to the device are individual stress limit values (not normal operating conditions) and are not valid simultaneously. If these limits are exceeded, device functional operation is not implied, damage may occur and reliability may be affected.

1. Pulse Test: Pulse Width = 5 ms, Duty Cycle ≤ 10%.
2. Proper strike and creepage distance must be provided.

ON Semiconductor®

http://onsemi.com

POWER TRANSISTOR
8.0 AMPERES
1000 VOLTS
45 and 125 WATTS

MARKING DIAGRAMS

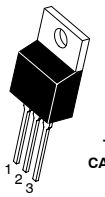

TO−220AB
CASE 221A−09
STYLE 1

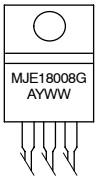

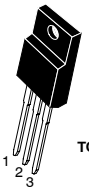

TO−220 FULLPACK
CASE 221D
STYLE 2
UL RECOGNIZED

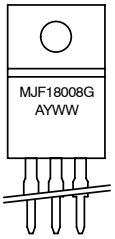

G	= Pb−Free Package
A	= Assembly Location
Y	= Year
WW	= Work Week

ORDERING INFORMATION

See detailed ordering and shipping information in the package dimensions section on page 7 of this data sheet.

Preferred devices are recommended choices for future use and best overall value.

*For additional information on our Pb−Free strategy and soldering details, please download the ON Semiconductor Soldering and Mounting Techniques Reference Manual, SOLDERRM/D.

© Semiconductor Components Industries, LLC, 2006

April, 2006 − Rev. 6
Publication Order Number:
MJE18008/D

MJE18008, MJF18008

ELECTRICAL CHARACTERISTICS (T_C = 25°C unless otherwise specified)

Characteristic				Symbol	Min	Typ	Max	Unit
OFF CHARACTERISTICS								
Collector–Emitter Sustaining Voltage (I_C = 100 mA, L = 25 mH)				$V_{CEO(sus)}$	450	–	–	Vdc
Collector Cutoff Current (V_{CE} = Rated V_{CEO}, I_B = 0)				I_{CEO}	–	–	100	μAdc
Collector Cutoff Current (V_{CE} = Rated V_{CES}, V_{EB} = 0)				I_{CES}	–	–	100	μAdc
			(T_C = 125°C)		–	–	500	
(V_{CE} = 800 V, V_{EB} = 0)			(T_C = 125°C)		–	–	100	
Emitter Cutoff Current (V_{EB} = 9.0 Vdc, I_C = 0)				I_{EBO}	–	–	100	μAdc
ON CHARACTERISTICS								
Base–Emitter Saturation Voltage (I_C = 2.0 Adc, I_B = 0.2 Adc)				$V_{BE(sat)}$	–	0.82	1.1	Vdc
(I_C = 4.5 Adc, I_B = 0.9 Adc)					–	0.92	1.25	
Collector–Emitter Saturation Voltage				$V_{CE(sat)}$				Vdc
(I_C = 2.0 Adc, I_B = 0.2 Adc)					–	0.3	0.6	
			(T_C = 125°C)		–	0.3	0.65	
(I_C = 4.5 Adc, I_B = 0.9 Adc)					–	0.35	0.7	
			(T_C = 125°C)		–	0.4	0.8	
DC Current Gain (I_C = 1.0 Adc, V_{CE} = 5.0 Vdc)				h_{FE}	14	–	34	–
			(T_C = 125°C)		–	28	–	
(I_C = 4.5 Adc, V_{CE} = 1.0 Vdc)					6.0	9.0	–	
			(T_C = 125°C)		5.0	8.0	–	
(I_C = 2.0 Adc, V_{CE} = 1.0 Vdc)					11	15	–	
			(T_C = 125°C)		11	16	–	
(I_C = 10 mAdc, V_{CE} = 5.0 Vdc)					10	20	–	
DYNAMIC CHARACTERISTICS								
Current Gain Bandwidth (I_C = 0.5 Adc, V_{CE} = 10 Vdc, f = 1.0 MHz)				f_T	–	13	–	MHz
Output Capacitance (V_{CB} = 10 Vdc, I_E = 0, f = 1.0 MHz)				C_{ob}	–	100	150	pF
Input Capacitance (V_{EB} = 8.0 V)				C_{ib}	–	1750	2500	pF
Dynamic Saturation Voltage:	(I_C = 2.0 Adc I_{B1} = 200 mAdc V_{CC} = 300 V)	1.0 μs	(T_C = 125°C)	$V_{CE(dsat)}$	–	5.5	–	Vdc
Determined 1.0 μs and 3.0 μs respectively after rising I_{B1} reaches 90% of final I_{B1} (see Figure 18)					–	11.5	–	
		3.0 μs	(T_C = 125°C)		–	3.5	–	
					–	6.5	–	
	(I_C = 5.0 Adc I_{B1} = 1.0 Adc V_{CC} = 300 V)	1.0 μs	(T_C = 125°C)		–	11.5	–	
					–	14.5	–	
		3.0 μs	(T_C = 125°C)		–	2.4	–	
					–	9.0	–	
SWITCHING CHARACTERISTICS: Resistive Load (D.C. ≤ 10%, Pulse Width = 20 μs)								
Turn–On Time	(I_C = 2.0 Adc, I_{B1} = 0.2 Adc, I_{B2} = 1.0 Adc, V_{CC} = 300 V)		(T_C = 125°C)	t_{on}	–	200	300	ns
					–	190	–	
Turn–Off Time			(T_C = 125°C)	t_{off}	–	1.2	2.5	μs
					–	1.5	–	
Turn–On Time	(I_C = 4.5 Adc, I_{B1} = 0.9 Adc, I_{B2} = 2.25 Adc, V_{CC} = 300 V)		(T_C = 125°C)	t_{on}	–	100	180	ns
					–	250	–	
Turn–Off Time			(T_C = 125°C)	t_{off}	–	1.6	2.5	μs
					–	2.0	–	
SWITCHING CHARACTERISTICS: Inductive Load (V_{clamp} = 300 V, V_{CC} = 15 V, L = 200 μH)								
Fall Time	(I_C = 2.0 Adc, I_{B1} = 0.2 Adc, I_{B2} = 1.0 Adc)		(T_C = 125°C)	t_{fi}	–	100	180	ns
					–	120	–	
Storage Time			(T_C = 125°C)	t_{si}	–	1.5	2.75	μs
					–	1.9	–	
Crossover Time			(T_C = 125°C)	t_c	–	250	350	ns
					–	230	–	
Fall Time	(I_C = 4.5 Adc, I_{B1} = 0.9 Adc, I_{B2} = 2.25 Adc)		(T_C = 125°C)	t_{fi}	–	85	150	ns
					–	135	–	
Storage Time			(T_C = 125°C)	t_{si}	–	2.0	3.2	μs
					–	2.6	–	
Crossover Time			(T_C = 125°C)	t_c	–	210	300	ns
					–	250	–	

3. Pulse Test: Pulse Width = 5.0 ms, Duty Cycle ≤ 10%.
4. Proper strike and creepage distance must be provided.

MJE18008, MJF18008

TYPICAL STATIC CHARACTERISTICS

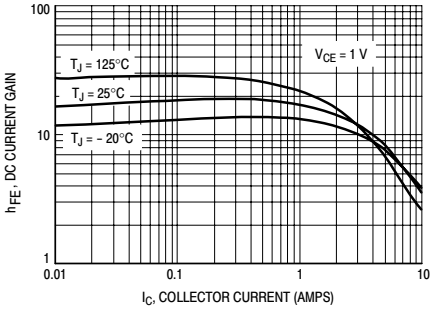

Figure 1. DC Current Gain @ 1 Volt

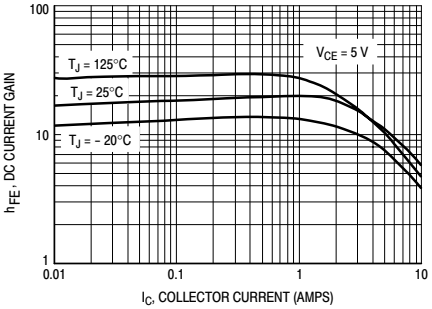

Figure 2. DC Current Gain @ 5 Volts

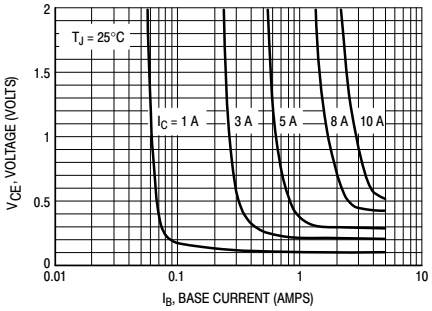

Figure 3. Collector Saturation Region

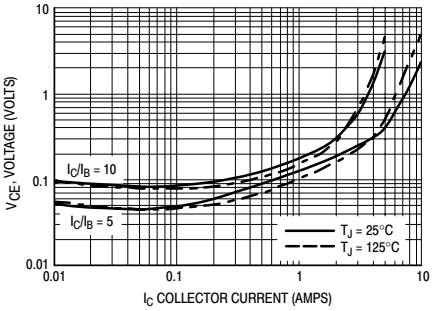

Figure 4. Collector−Emitter Saturation Voltage

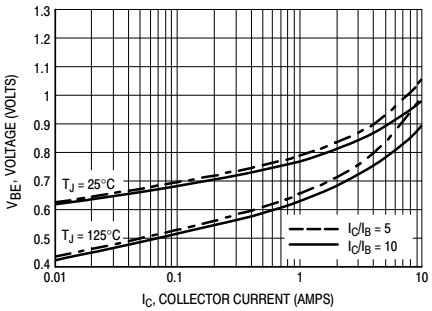

Figure 5. Base−Emitter Saturation Region

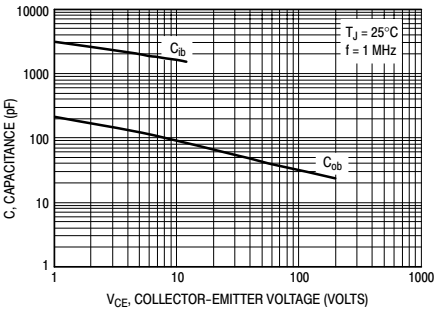

Figure 6. Capacitance

TYPICAL SWITCHING CHARACTERISTICS
($I_{B2} = I_C/2$ for all switching)

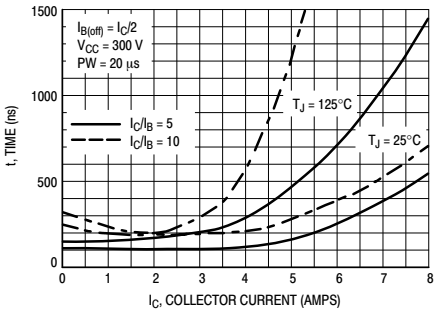

Figure 7. Resistive Switching, t_{on}

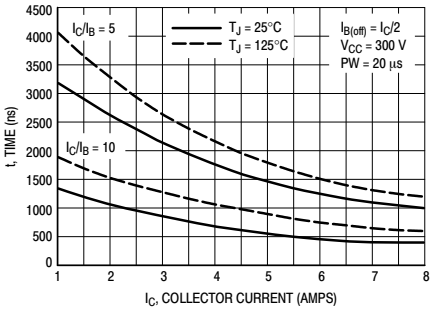

Figure 8. Resistive Switching, t_{off}

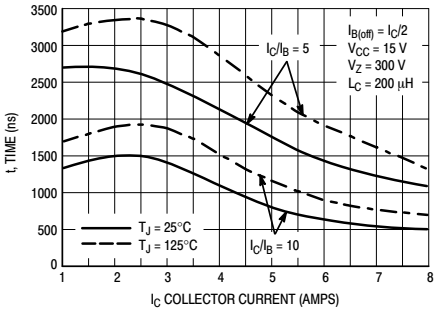

Figure 9. Inductive Storage Time, t_{si}

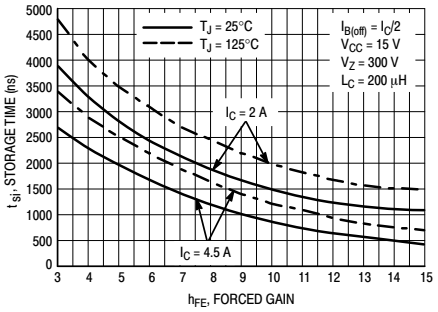

Figure 10. Inductive Storage Time, $t_{si}(h_{FE})$

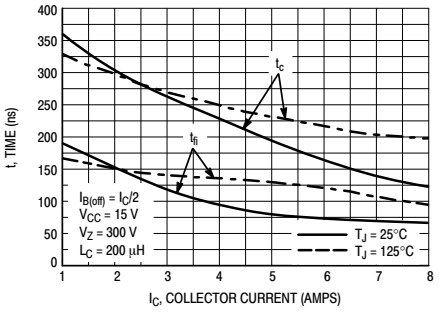

Figure 11. Inductive Switching, t_c and t_{fi}
I_C/I_B = 5

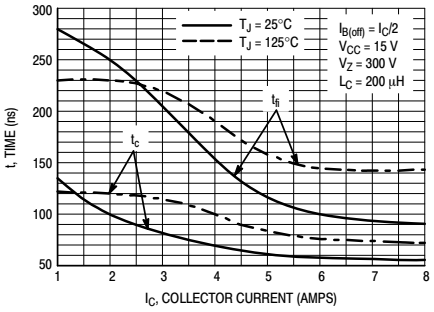

Figure 12. Inductive Switching, t_c and t_{fi}
I_C/I_B = 10

TYPICAL SWITCHING CHARACTERISTICS
($I_{B2} = I_C/2$ for all switching)

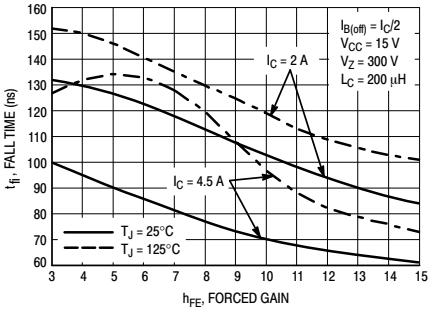

Figure 13. Inductive Fall Time

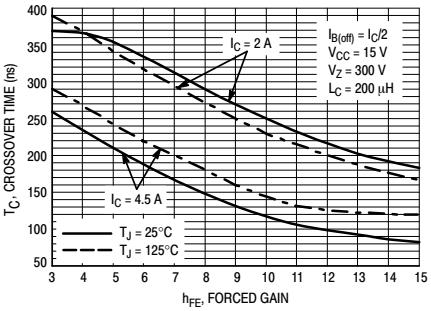

Figure 14. Inductive Crossover Time

GUARANTEED SAFE OPERATING AREA INFORMATION

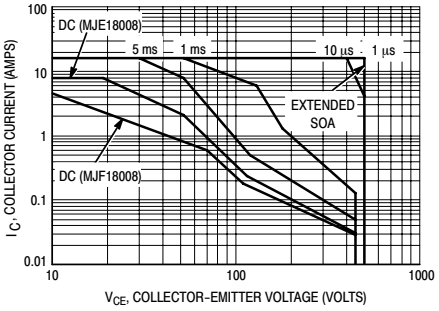

Figure 15. Forward Bias Safe Operating Area

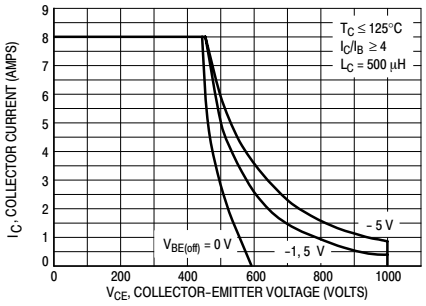

Figure 16. Reverse Bias Switching Safe Operating Area

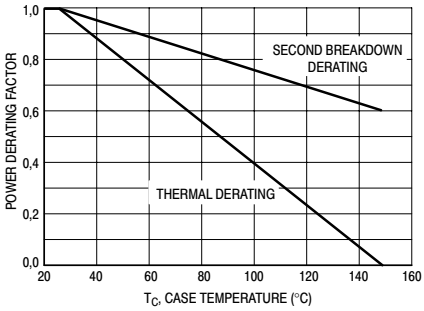

Figure 17. Forward Bias Power Derating

There are two limitations on the power handling ability of a transistor: average junction temperature and second breakdown. Safe operating area curves indicate $I_C - V_{CE}$ limits of the transistor that must be observed for reliable operation; i.e., the transistor must not be subjected to greater dissipation than the curves indicate. The data of Figure 15 is based on T_C = 25°C; $T_{J(pk)}$ is variable depending on power level. Second breakdown pulse limits are valid for duty cycles to 10% but must be derated when T_C > 25°C. Second breakdown limitations do not derate the same as thermal limitations. Allowable current at the voltages shown in Figure 15 may be found at any case temperature by using the appropriate curve on Figure 17. $T_{J(pk)}$ may be calculated from the data in Figure 20 and 21. At any case temperatures, thermal limitations will reduce the power that can be handled to values less than the limitations imposed by second breakdown. For inductive loads, high voltage and current must be sustained simultaneously during turn−off with the base−to−emitter junction reverse−biased. The safe level is specified as a reverse−biased safe operating area (Figure 16). This rating is verified under clamped conditions so that the device is never subjected to an avalanche mode.

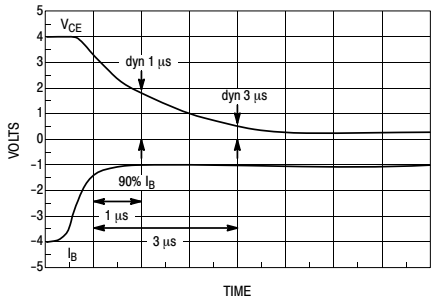

Figure 18. Dynamic Saturation Voltage Measurements

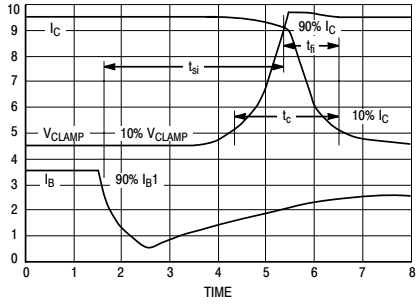

Figure 19. Inductive Switching Measurements

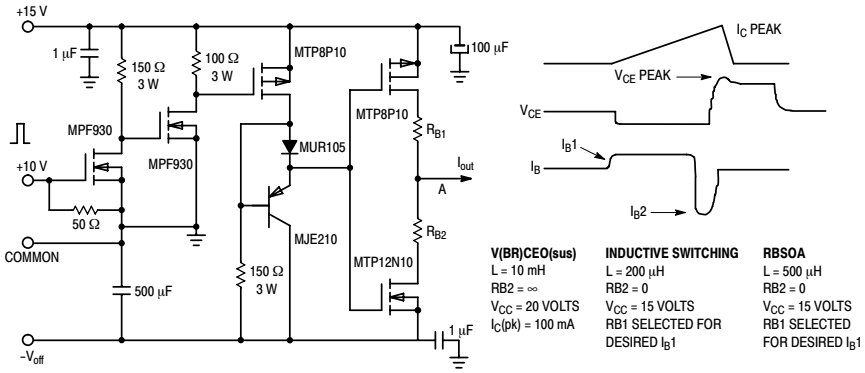

V(BR)CEO(sus)	INDUCTIVE SWITCHING	RBSOA
L = 10 mH	L = 200 μH	L = 500 μH
RB2 = ∞	RB2 = 0	RB2 = 0
V_{CC} = 20 VOLTS	V_{CC} = 15 VOLTS	V_{CC} = 15 VOLTS
I_C(pk) = 100 mA	RB1 SELECTED FOR DESIRED I_{B1}	RB1 SELECTED FOR DESIRED I_{B1}

Table 1. Inductive Load Switching Drive Circuit

MJE18008, MJF18008

TYPICAL THERMAL RESPONSE

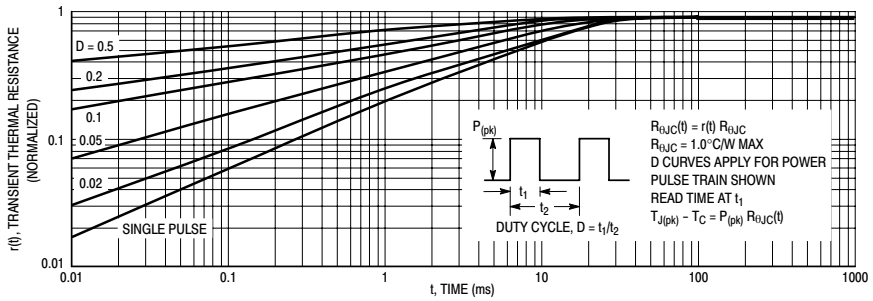

Figure 20. Typical Thermal Response ($Z_{\theta JC}(t)$) for MJE18008

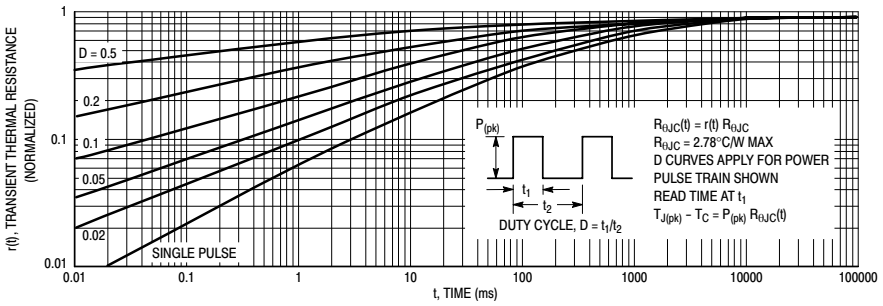

Figure 21. Typical Thermal Response ($Z_{\theta JC}(t)$) for MJF18008

ORDERING INFORMATION

Device	Package	Shipping
MJE18008	TO−220AB	50 Units / Rail
MJE18008G	TO−220AB (Pb−Free)	50 Units / Rail
MJF18008	TO−220 (Fullpack)	50 Units / Rail
MJF18008G	TO−220 (Fullpack) (Pb−Free)	50 Units / Rail

TEST CONDITIONS FOR ISOLATION TESTS*

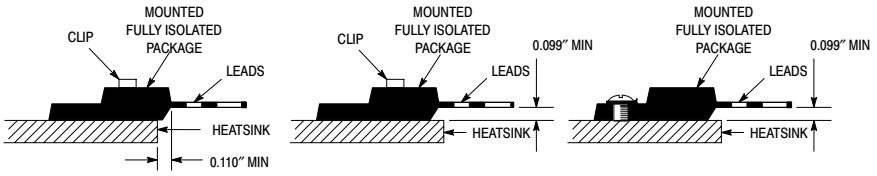

Figure 22a. Screw or Clip Mounting Position for Isolation Test Number 1

Figure 22b. Clip Mounting Position for Isolation Test Number 2

Figure 22c. Screw Mounting Position for Isolation Test Number 3

*Measurement made between leads and heatsink with all leads shorted together

MOUNTING INFORMATION**

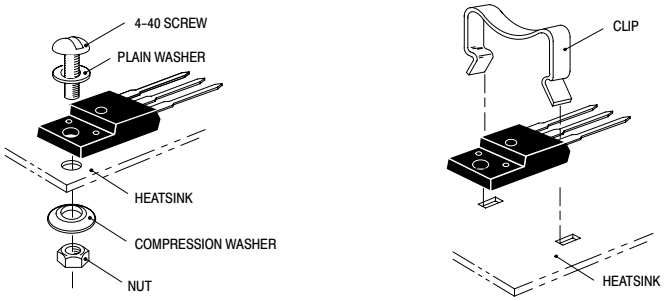

Figure 23a. Screw–Mounted

Figure 23b. Clip–Mounted

Figure 23. Typical Mounting Techniques for Isolated Package

Laboratory tests on a limited number of samples indicate, when using the screw and compression washer mounting technique, a screw torque of 6 to 8 in · lbs is sufficient to provide maximum power dissipation capability. The compression washer helps to maintain a constant pressure on the package over time and during large temperature excursions.

Destructive laboratory tests show that using a hex head 4–40 screw, without washers, and applying a torque in excess of 20 in · lbs will cause the plastic to crack around the mounting hole, resulting in a loss of isolation capability.

Additional tests on slotted 4–40 screws indicate that the screw slot fails between 15 to 20 in · lbs without adversely affecting the package. However, in order to positively ensure the package integrity of the fully isolated device, ON Semiconductor does not recommend exceeding 10 in · lbs of mounting torque under any mounting conditions.

** For more information about mounting power semiconductors see Application Note AN1040.

MJE18008, MJF18008

PACKAGE DIMENSIONS

TO−220AB
CASE 221A−09
ISSUE AA

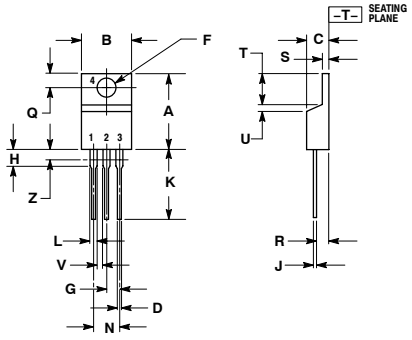

NOTES:
1. DIMENSIONING AND TOLERANCING PER ANSI Y14.5M, 1982.
2. CONTROLLING DIMENSION: INCH.
3. DIMENSION Z DEFINES A ZONE WHERE ALL BODY AND LEAD IRREGULARITIES ARE ALLOWED.

	INCHES		MILLIMETERS	
DIM	MIN	MAX	MIN	MAX
A	0.570	0.620	14.48	15.75
B	0.380	0.405	9.66	10.28
C	0.160	0.190	4.07	4.82
D	0.025	0.035	0.64	0.88
F	0.142	0.147	3.61	3.73
G	0.095	0.105	2.42	2.66
H	0.110	0.155	2.80	3.93
J	0.018	0.025	0.46	0.64
K	0.500	0.562	12.70	14.27
L	0.045	0.060	1.15	1.52
N	0.190	0.210	4.83	5.33
Q	0.100	0.120	2.54	3.04
R	0.080	0.110	2.04	2.79
S	0.045	0.055	1.15	1.39
T	0.235	0.255	5.97	6.47
U	0.000	0.050	0.00	1.27
V	0.045	---	1.15	---
Z	---	0.080	---	2.04

STYLE 1:
PIN 1. BASE
2. COLLECTOR
3. EMITTER
4. COLLECTOR

TO−220 FULLPAK
CASE 221D−03
ISSUE G

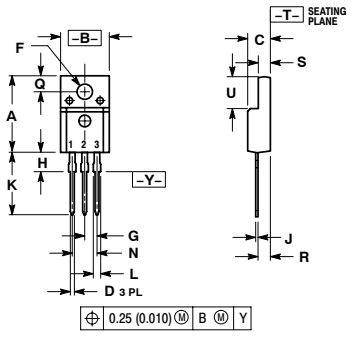

NOTES:
1. DIMENSIONING AND TOLERANCING PER ANSI Y14.5M, 1982.
2. CONTROLLING DIMENSION: INCH
3. 221D−01 THRU 221D−02 OBSOLETE, NEW STANDARD 221D−03.

	INCHES		MILLIMETERS	
DIM	MIN	MAX	MIN	MAX
A	0.625	0.635	15.88	16.12
B	0.408	0.418	10.37	10.63
C	0.180	0.190	4.57	4.83
D	0.026	0.031	0.65	0.78
F	0.116	0.119	2.95	3.02
G	0.100 BSC		2.54 BSC	
H	0.125	0.135	3.18	3.43
J	0.018	0.025	0.45	0.63
K	0.530	0.540	13.47	13.73
L	0.048	0.053	1.23	1.36
N	0.200 BSC		5.08 BSC	
Q	0.124	0.128	3.15	3.25
R	0.099	0.103	2.51	2.62
S	0.101	0.113	2.57	2.87
U	0.238	0.258	6.06	6.56

STYLE 2:
PIN 1. BASE
2. COLLECTOR
3. EMITTER